Debonding of Viscoelastic Materials: From a Viscous Liquid to a Soft Elastic Solid

Dissertation zur Erlangung des Grades
der Doktorin der Naturwissenschaften
der Naturwissenschaftlich-Technischen Fakultät II
- Physik und Mechatronik -
der Universität des Saarlandes
und der
Université Pierre et Marie Curie

von
Julia Nase

Saarbrücken/Paris
2009

Tag des Kolloquiums: 21.09.2009

Dekan: Prof. Dr. Thomas Wichert

Mitglieder des Prüfungsausschusses:

Dr. Anke Lindner, Maître de conférences
Dr. Costantino Creton, Directeur de Recherche
Prof. Dr. Christian Wagner
Prof. Dr. Martine Ben Amar
Dr. Philippe Coussot, Directeur de Recherche
Prof. Dr. Pascal Damman
Prof. Dr. Rolf Pelster
Prof. Dr. Ralf Stannarius

DEBONDING OF VISCOELASTIC MATERIALS: FROM A VISCOUS LIQUID TO A SOFT ELASTIC SOLID

In the present experimental study, we investigate the transition in the debonding mechanism when going from a viscous liquid to a soft elastic solid using a probe tack geometry. We have developed a model system consisting of PDMS with different degrees of crosslinking, ensuring a continuous transition between the material classes. During debonding, a fingering instability with characteristic wavelength evolves. We explain the subsequent coarsening of the pattern for a Newtonian oil by linear stability analysis and identify the influence on the adhesion energy. Over a wide range of properties from liquid to solid, we present a quantitative description of the initially destabilizing wavelength for the observed interfacial and bulk mechanisms. We predict the transition between these mechanisms from linear viscoelastic and surface properties. Furthermore, we investigate the debonding quantitatively in terms of adhesion energy and maximum deformation. For interfacial debonding, we are able to explain the speed dependence in the adhesion energy by bulk properties only and confirm thus over two decades in the elastic modulus an existing empiric law. Adapting a recent 3D technique, we visualize for the first time in situ the contact line between viscoelastic material and rigid probe in three dimensions and provide thus direct access to the boundary conditions.

Keywords: adhesion, elastic instabilities, linear viscoelasticity, pattern formation, soft matter, viscous fingering.

DÉCOLLEMENT DE MATÉRIAUX VISCOÉLASTIQUES : DU LIQUIDE VISQUEUX AU SOLIDE ÉLASTIQUE MOU

Dans le cadre de cette thèse expérimentale, nous étudions le décollement en géométrie de probe tack lors de la transition d'un liquide visqueux vers un solide élastique mou. Nous avons développé un système modèle (du PDMS à différents degrés de réticulation), assurant ainsi une transition continue entre ces classes de matériaux. Au début du décollement, une instabilité de digitation avec une longueur d'onde caractéristique apparaît. Pour une huile newtonienne, nous expliquons le coarsening des structures lors du décollement par une analyse de stabilité linéaire, et nous mettons en évidence leur influence sur l'énergie d'adhésion. Pour une large gamme de propriétés du liquide jusqu'au solide, nous identifions des mécanismes volumiques ou interfaciaux et présentons une analyse quantitative de leur longueur d'onde initiale respective. Nous montrons que le mécanisme de décollement est déterminé par la viscoélasticité linéaire et des propriétés de surface. En outre, nous étudions le décollement quantitativement par l'énergie d'adhésion et la déformation maximale. Pour le mécanisme interfacial, nous arrivons à expliquer la dépendance en vitesse de l'énergie d'adhésion par des propriétés volumiques du matériau. Variant le module élastique sur deux décades, nous confirmons ainsi une loi empirique existante. En adaptant une technique 3D récente, nous visualisons pour la première fois in situ la ligne de contact entre le matériau viscoélastique et le substrat rigide, offrant ainsi un accès direct aux conditions aux limites.

Mots clés : adhésion, digitation visqueuse, formation de structures, instabilités élastiques, matière molle, viscoélasticité linéaire.

ABLÖSEN VISKOELASTISCHER MATERIALIEN:
VON DER VISKOSEN FLÜSSIGKEIT ZUM WEICHEN ELASTISCHEN FESTKÖRPER

Im der vorliegenden experimentellen Studie untersuchen wir den Ablöseprozess in einer Probe-Tack-Geometrie während des Übergangs von einer viskosen Flüssigkeit zum elastischen weichen Festkörper. Wir entwickeln ein Modellsystem (PDMS mit verschiedenen Vernetzungsgraden), das einen kontinuierlichen Übergang zwischen diesen Substanzklassen aufweist. Während des Ablösens entsteht eine Fingerinstabilität mit charakteristischer Wellenlänge. Für ein Newtonsches Öl erklären wir durch lineare Stabilitätsanalyse das nachfolgende Coarsening der Strukturen und zeigen ihren Einfluss auf die Adhäsionsenergie auf. Über einen weiten Bereich der Materialeigenschaften von flüssig zu fest beobachten wir Bulk- oder Grenzflächenmechanismen und präsentieren eine quantitative Analyse der jeweiligen anfänglichen Wellenlänge. Den Übergang zwischen diesen Mechanismen sagen wir anhand linearer Viskoelastizität und Oberflächeneigenschaften voraus. Ferner untersuchen wir das Ablösen quantitativ anhand der Adhäsionsenergie und der maximalen Verformung. Im Falle des Grenzflächenmechanismus erklären wir die Geschwindigkeitsabhängigkeit der Adhäsionsenergie durch Volumeneigenschaften und bestätigen damit ein existierendes empirisches Gesetz. Indem wir eine neue 3D-Technik weiterentwickeln, bilden wir zum ersten Mal in situ die Kontaktlinie zwischen viskoelastischem Material und festem Substrat in drei Dimensionen ab. Damit ermöglichen wir einen direkten Zugang zu den Randbedingungen.

Contents

1. General introduction 1

I. Background 7

2. Viscosity, elasticity, and viscoelasticity 9
- 2.1. Liquids 10
- 2.2. Elasticity 12
- 2.3. Viscoelasticity 14
  - 2.3.1. Modeling viscoelastic liquids and solids 14
- 2.4. Characterization by rheometry 19

3. Theoretical concepts of adhesion 23
- 3.1. Measuring adhesive properties 23
- 3.2. Debonding mechanisms 26
- 3.3. From rheological properties to debonding mechanisms 27

4. Viscous and elastic instabilities in confined geometries 31
- 4.1. Linear stability analysis 31
- 4.2. The Saffman–Taylor instability 32
  - 4.2.1. Circular geometry 39
  - 4.2.2. The lifted Hele–Shaw cell 40
  - 4.2.3. Towards non-Newtonian systems 41
  - 4.2.4. Elastic bulk instability 42
- 4.3. Elastic interfacial instability 43

II. Materials and methods 49

5. Materials 51
- 5.1. Preparation of the PDMS samples 51
- 5.2. Characterizing the samples 54
  - 5.2.1. Measurement of the thickness 54
  - 5.2.2. Linear rheological measurements 55
  - 5.2.3. Traction 59
  - 5.2.4. Sol content 59
- 5.3. Liquid-solid transition varying the number of crosslink points 61

5.4. Varying the rheological properties . . . 63

6. Experimental setup and image treatment 67
6.1. The probe tack test . . . 67
6.2. Image treatment . . . 71

III. Debonding of confined viscoelastic materials 73

7. Pattern formation 75
7.1. Introduction . . . 75
7.2. Experimental . . . 75
7.3. Two regimes of debonding . . . 78
7.3.1. Bulk case . . . 79
7.3.2. Interfacial case . . . 82
7.4. Transition . . . 83
7.5. Nonlinear patterns . . . 86
7.6. Conclusion and discussion . . . 88

8. The complete debonding process 91
8.1. Introduction . . . 91
8.2. Experimental protocol . . . 91
8.3. Force-displacement curves . . . 92
8.4. Quantitative analysis of the stress-strain curves . . . 95
8.4.1. Maximum stress . . . 96
8.4.2. Maximum strain . . . 96
8.4.3. Adhesion energy W_{adh} . . . 97
8.5. Conclusion . . . 102

9. Visualization in three dimensions 105
9.1. Introduction – the need for $3D$-visualization . . . 105
9.2. Setup . . . 107
9.3. First results . . . 109
9.4. Conclusion . . . 113

IV. Debonding of Newtonian oils 115

10. The fingering pattern in a Newtonian oil 117
10.1. Introduction . . . 117
10.2. Materials and methods . . . 118
10.2.1. Materials . . . 119
10.2.2. Experimental protocol . . . 120
10.3. The number of fingers in comparison to linear $2D$ theory . . . 123
10.4. Confinement dependence . . . 127

10.5. Finger growth 132
10.5.1. Controlled perturbation 137
10.6. Lifting force 139
10.7. A viscoelastic shear thinning liquid 142
10.8. Conclusion 147
Appendix to Chapter 10 149

V. Conclusions 153

11. Conclusion 155

Résumé en Français 159
Introduction 159
Matériaux et méthodes 160
Résultats 162
Conclusion 169

Deutsche Zusammenfassung 171

List of Figures

1.1. Surface instabilities in viscoelastic liquids. 3

2.1. Different states of a polymer. 9
2.2. Shear thinning and shear thickening liquids. 11
2.3. Mechanical elements to model viscoelastic materials. 15
2.4. σ and γ versus t in Maxwell and Voigt model. 17
2.5. E' and E'' vs ω for Maxwell and Voigt model 18
2.6. Schemes of different rheometer measurement geometries. 20

3.1. Different techniques to characterize PSA performance 24
3.2. Patterns during the peeling of an adhesive tape 25

4.1. Schematical view of a Hele–Shaw cell 33
4.2. Sinusoidal deformation of the interface between two liquids 34
4.3. The growth rate as a function of the wave vector 37
4.4. Destabilization and finger selection in the liner Hele–Shaw cell 39
4.5. Outward fingering in a circular cell. 40
4.6. Stress distribution under a rigid punch 43
4.7. Contact instabilities in confined elastic systems. 44
4.8. Stability of the contact line in the peeling geometry 46

5.1. Schematical view of the crosslinking process 51
5.2. The sample shape measured in a profilometer 53
5.3. Sample thickness from weighting and from the profilometer 54
5.4. η, G', G'' for the pure oil 55
5.5. G' and G'' versus ω. 57
5.6. Traction curves 60
5.7. Sol content 61
5.8. Moduli and $\tan\delta$ for some chosen materials. 62
5.9. E and $\tan\delta$ versus r 63
5.10. G', G'', $\tan\delta$, $|\eta^\star|$ versus ω for different T 64
5.11. G', G'', $\tan\delta$, $|G^\star|$ versus ω when adding a different oil 66

6.1. Typical force-time and stress-strain curves in the probe tack test. . . . 68
6.2. Schematical view of the µ-tack setup. 69
6.3. Schematical view of probe polishing 70
6.4. Image treatment in *ImageJ* 71

6.5. Image treatment in *Igor* 72

7.1. Linear destabilization in the bulk case 76
7.2. Linear destabilization in the interfacial case 76
7.3. Schematic view of the wavelength λ. 77
7.4. Side view of fibrillation. 78
7.5. Wavelength versus debonding speed. 79
7.6. Comparison to the ST theory. 80
7.7. The wavelength for all experiments in comparison to the ST prediction. 82
7.8. Lambda versus film thickness 83
7.9. Mechanism map 85
7.10. λ compared to the ST prediction 86
7.11. Top view images of the cohesive debonding of a pure viscous oil 86
7.12. Top view images of the debonding of a viscoelastic material 87
7.13. Top view images of the debonding of an elastic material 87

8.1. Typical stress-strain curves of the different materials 93
8.2. Comparison of the stress-displacement curves for different materials . . 94
8.3. Maximum strain versus E 96
8.4. Adhesion energy versus E 97
8.5. W_{adh} compared to the scaling in the Newtonian case 99
8.6. W_{adh} versus v for interfacial debonding. 100
8.7. W_{adh} versus $Eb\epsilon^2_{\mathrm{max}}$ 101
8.8. $W_{\mathrm{adh}}/\tan\delta$ versus ω for predominantly elastic materials. 102

9.1. Peeling of a commercial tape from different substrates 105
9.2. Large strain simulations of the debonding of a soft elastomer 106
9.3. Schematic of the $3D$-setup of Yamagutchi *et al.* 107
9.4. The $3D$ visualization technique, schematical view and setup. 108
9.5. $3D$ snapshots of interfacial and bulk fingering. 110
9.6. Shape of the contact line for different materials. 111
9.7. Estimated contact angle, r = 0.16. 112

10.1. Viscosity versus shear rate 119
10.2. Viscosity versus temperature 120
10.3. Top view of the ST instability in the *LHSC* 121
10.4. Superposition of the contact lines for different t 122
10.5. N versus t', comparison to prediction from linear theory 124
10.6. Growing and dying fingers 125
10.7. N_{grow} versus t', comparison to linear theory 126
10.8. N versus t', gap width color code 127
10.9. N versus t', confinement color code 128
10.10. Images at $\tau_0 = 3.0 \times 10^{-5}$ and $\tau_0 = 4.5 \times 10^{-6}$ 130
10.11. N_{all} and N_{grow} versus t' at three different τ_0 131
10.12. Different growth at one control parameter 132

10.13. Dimensionless perimeter versus dimensionless time 133
10.14. Growth rate and most unstable wave vector at $t' = 0$. 135
10.15. Comparison of the contact line in experiment and simulation 136
10.16. N versus t' from simulations 137
10.17. Mask for soft lithography 138
10.18. Images of a cured polyurethane pastille 138
10.19. Force versus strain 140
10.20. F versus t' from literature 141
10.21. Viscosity of Carbopol solutions 142
10.22. G' and G'' versus ω for the 1% Carbopol solution. 143
10.23. Debonding of 0.1% Carbopol solution 144
10.24. Debonding of 1.0% Carbopol solution, I 144
10.25. Debonding of 1.0% Carbopol solution, II 145
10.26. N versus t for Carbopol 147
10.27. Comparison of experiment, $2D$, and $3D$ theory 151
10.28. Volume loss 152

1. General introduction

The experience of gluing or debonding two bodies is common in everyday life. A large industry is developing and improving the different kinds of glues and adhesives, which are of great importance as well in industrial applications as in workaday life. So-called *pressure sensitive adhesives (PSA)*, are adhering to a substrate upon application of light pressure, and can ideally be detached without leaving traces. The adhesion is generated solely by van der Waals forces, covalent bonds are not involved. Widely spread applications of PSAs are tapes and labels.

PSAs consist of quite complex materials. They have to be liquid enough to form a good contact between two (rough) surfaces one wants to glue together; at the same time, they have to resist strains that occur during debonding. In the last years, much fundamental work was done to understand better the mechanisms of the debonding process. It has been investigated in terms of performance, reflected in quantities such as the adhesion energy or the maximum deformation before complete debonding. Much interest was shown as well to the structures formed during debonding, like cavities or air fingers. These patterns are observed in peel tests as well as in tensile deformation tests.

In the investigation of the patterns as well as in the quantitative analysis of the adhesive performance, the theoretical concepts are well-known for the limiting cases in the material properties. That is, the cases of Newtonian liquids and of elastic solids are well-established, however, the situation is more complex in the crossover region between those limits. To obtain PSAs with good performance, their properties have to be chosen in this crossover region. PSA are thus very complex viscoelastic materials that show simultaneously liquid and solid properties.

Viscoelasticity is a very general property exhibited by many different condensed matter systems, solid or liquid-like. In this work, we are dealing with materials where the elasticity is of entropic origin. Systems such as viscoelastic fluids, more or less crosslinked polymer melts, and polymer networks up to rubber-like materials are typical examples. For these systems the transition from a more liquid-like to a more solid-like behavior can occur very differently depending on the characteristics of the material, as the length of the polymer chains, the number and the nature of crosslink points, or the applied time scale or temperature.

A *polymer melt* consisting of long polymer chains shows elasticity even in the absence of chemical crosslinks. This elasticity originates from entanglements of the polymer chains that act, at short time scales, as crosslink points. At longer timescales, the polymer chains can slide along each other and the behavior is liquid-like. Therefore, an entangled polymer melt acts like a typical *Maxwell* fluid: it displays a liquid-like behavior on long time scales and a solid-like behavior on short time scales. When one starts to crosslink such a melt, the elastic plateau value changes little, as the entanglements are replaced by chemical crosslinks. The relaxation time of the material increases however strongly and it becomes elastic at larger and larger timescales. Typical PSAs are imperfect polymer networks that are swollen with polymer chains of different length. They are characterized by a wide spectrum of relaxation times, maintaining an almost identical level of viscoelasticity over a wide temperature range. *Rubbers* or *elastomers* are characterized by their unique ability to extend to several times their size and recovering their initial shape with (almost) no hysteresis.

When debonding a thin layer of these viscoelastic materials from a substrate, different mechanisms are observed. The modification of the debonding mechanism as a function of the viscoelastic properties has been noted by several researchers, but the existing studies have focused on specific, rather narrowly defined systems such as entangled polymer melts of linear chains [65, 102, 63, 11, 89], polymer melts containing hydrogen bonds [96], Newtonian or lightly viscoelastic fluids [93, 40, 113], complex networks resembling commercial PSAs [76, 130, 38, 32], or well crosslinked rubbers [48, 77, 2]. Many researchers noted the importance of the viscoelastic properties on the adhesive behavior in general [17, 114], and more specifically on the existence and frequency dependence of sharp transitions in mechanisms from cohesive to interfacial failure and from fibrillar deformation to failure by crack propagation [39, 49, 45, 28, 69]. Most of the results obtained in these studies have been discussed from the mechanistic point of view [108] or relating the rheology with adhesive behavior [44]. On the theoretical side, the early work in solid mechanics, which focused on crack propagation in viscoelastic materials [80], has been followed by the insights of de Gennes and coworkers on the modeling of a propagating viscoelastic crack in the bulk or at the interface [34, 35, 70, 101]. Yet a continuous description of adhesion from the Newtonian fluids (sticky honey for example) to the adhesion of elastic rubber has never been investigated within the same material family.

Pattern formation, beside the role it plays in debonding, is also interesting from a more general point of view, as it can be observed in a large variety of systems. It occurs when a so-called homogeneous ground state becomes unstable against small perturbations. The system then passes into a new state, and the formation of periodic patterns ensues. This phenomenon is widely spread in nature; from cloud formation and patterns on animal coats to chemical reactions, pattern formation is a very rich and complex subject. Figure 1.1 reveals the beauty of the resulting structures in two cases. On the left side, we see the instability on a thread of a viscoelastic fluid [100]. The initially straight borders of the jet become unstable towards a sinusoidal deformation whose amplitude is growing in time *(Rayleigh–Plateau instability)*. On complex fluids, droplets on a string are formed at later times. The instability on a vertically shaken fluid layer *(Faraday instability)* is shown in figure 1.1(b) (taken from reference [117]). Vertical shaking results in an oscillatory modulation of the vertical acceleration. Above a certain shaking frequency and amplitude, the liquid layer develops beautiful periodic patterns of different complexity. Here

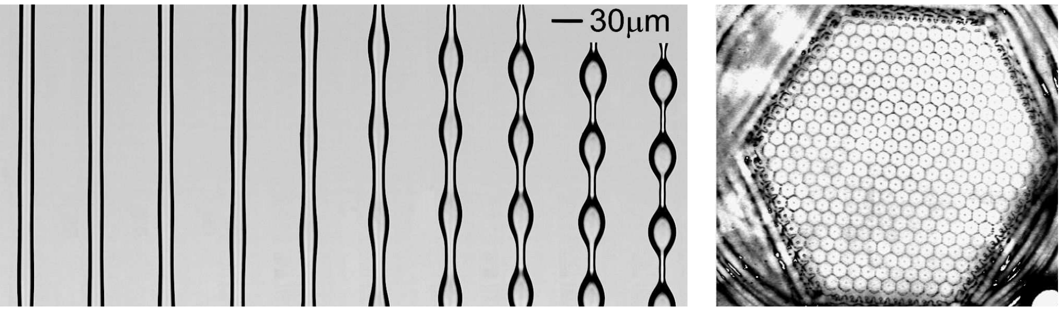

(a) Rayleigh–Plateau instability on a viscoelastic thread. The amplitude grows in time (from the left to the right), and then develops into groups of droplets [100].

(b) Faraday instability: localized stationary surface patterns of harmonic hexagons [117].

Figure 1.1.: Surface instabilities in viscoelastic liquids.

we see stationary hexagons.

Recently, the patterns that are formed during tensile deformation of thin layers in confined geometries have attracted much interest. We consider in this thesis the case of a viscoelastic material confined between two plates which are subsequently separated. Air penetrates from the edges and leads to the formation of bulk or interfacial fingers. The bulk fingering instability is well described by the classical *Saffman–Taylor* instability, where a less viscous liquid pushes a more viscous liquid in a confined geometry [98, 104, 87, 40, 93, 75, 10]. Some studies have focused on complex or yield stress fluids [40, 10, 9], ferromagnetic fluids [85], pastes [71], or considered the role of the substrate [110]. However, instabilities are equally known for elastic materials. A surface instability of a thin layer of a purely elastic material with undulating crack front has been observed experimentally and explained theoretically [1, 79, 42, 47, 105, 46]. Shull *et al.* [109] and Webber *et al.* [118] described a bulk instability for elastic gels.

The transition from the liquid to the solid state is currently a subject of strong interest. The transition between a viscous liquid and a glassy material has been investigated in references [54, 128, 125]. Very recently, Arun *et al.* performed experiments where they approached a flat plate to a thin layer of different viscoelastic materials in an electric field [7]. A change in the wavelength of the resulting surface instability revealed the transition between liquid and solid behavior. However, no systematic study of the pattern formation during tensile deformation of a viscoelastic material focusing on the respective role of the liquid and elastic properties over a wide range of material properties has been undertaken so far.

In this thesis, we investigate here a continuous transition and a large range of properties *within one system* using a model family of Poly(dimethyl siloxane) (PDMS) with different degrees of crosslinking. We study this transition both in terms of initial pattern formation and in terms of adhesive properties during the highly non-linear debonding process over the whole range of viscoelastic properties. Such a study contributes to a better understanding of the instabilities observed in viscoelastic materials, which are important for industrial applications. It is also of importance for any theoretical treatment aiming to bridge the gap between the different formalisms that apply to viscous liquids and elastic solids.

This thesis is divided into four parts. The first part overviews the theoretical background. In Chapter 2, we recall the basic principles of viscosity, elasticity, and viscoelasticity, and explain the concepts of rheometry. The focus of Chapter 3 lies on adhesion and adhesives. The principles of linear stability analysis are introduced in Chapter 4, and examples for pattern formation in liquids and solids are given.

In the second part, we characterize in detail the PDMS model system, mainly by rheometry, (Chapter 5) and we present the “probe tack” setup (Chapter 6).

In the third and forth part, we present the results we obtained in this thesis. Chapter 7 investigates in detail the initial pattern formation during debonding. In the probe tack geometry, we observe an initially circular, smooth contact line between air and viscoelastic material. Soon, the contact line is oscillating and becomes instable. The amplitudes of the oscillations start to grow, and air fingers evolve. We investigate the wavelength of the initial destabilization. Dependent on the material properties, we identify an interfacial regime, where air fingers propagate at the interface between probe and PDMS, and a bulk regime, where the PDMS bulk is deformed and fingers are formed in the volume. In both cases, we predict quantitatively and qualitatively the wavelength in agreement with theory. Additionally, we propose an empiric parameter that determines the transition between bulk and interfacial regime. These results have been published in 2008 [81].

In Chapter 8, we investigate the complete debonding process in terms of stress-strain curves. We describe the change in the curve shape as the viscoelastic properties of the material vary and identify clearly three different debonding mechanisms. For very weakly crosslinked materials, we observe a cohesive bulk mechanism, where the complete fingering process takes place in the volume. For intermediate degrees of crosslinking, the debonding is initiated in the bulk and then becomes interfacial. For well crosslinked materials, the debonding is purely interfacial without bulk deformation. Quantitatively, the change in the curve shape is reflected in the two quantities adhesion energy and maximum deformation before debonding. For the well crosslinked materials we investigate in greater detail the adhesion energy and explain its speed dependence in terms of viscoelastic bulk properties.

A novel visualization technique is presented in Chapter 9. Adapting a recent $3D$-technique that is based on the total reflection in a prism [122], we visualize for the first time directly the contact between probe, air, and viscoelastic material in three dimensions. In this way, we estimate the contact angle and are able to determine the boundary conditions of the advancing contact line *in situ*.

A detailed study of the viscous fingering instability during the debonding of a Newtonian oil completes this work (Chapter 10). We investigate the coarsening of the fingering pattern as the probe is pulled away. We divide the air fingers into growing fingers, which are moving towards the center of the probe, and dying fingers, which are fixed at their position. We show that the number of growing fingers is very well described by linear stability analysis. Furthermore, we investigate the finger amplitude and the force that is needed to debond the probe, and find that both quantities depend on the confinement.

The last part concludes this thesis. An extended résumé in German and French can be found at the end of this manuscript.

Part I.

Background

2. Viscosity, elasticity, and viscoelasticity

The materials we used in this study are all based on polymers. The term *polymer* denotes a large class of materials, including such diverse substances as plastics, rubber, DNA, and cellulose. Their common feature is that they are macromolecules, made of repetition units (monomers), which are typically connected to each other by covalent chemical bonds. Polymers in general show very complex behavior. One of their most striking properties is that they behave as a brittle solid, an elastomer, or a liquid, depending on the temperature and on the experimental time scale. A distinction is made between viscoelastic liquids and viscoelastic solids. Viscoelastic liquids are polymer melts in which the polymer chains can flow freely. At intermediate times, the elastic character is predominant, but at long times, they behave like liquids. This behavior is in contrast to viscoelastic solids where the polymer chains are linked to each other by chemical crosslinks or by strong physical bonds, forming in this way a network. These materials behave like a liquid on short time scales, but the elastic properties predominate at long times. Thereby a analogy between time and temperature exists: the properties at long timescales correspond to those at high temperatures [119].

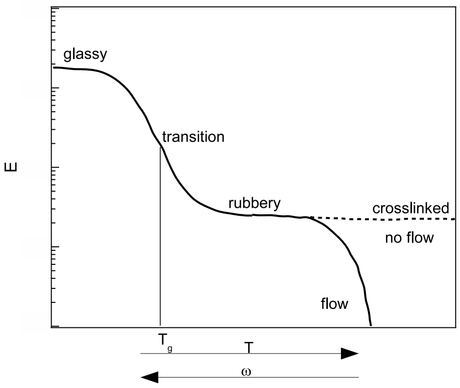

Figure 2.1.: The elastic modulus as a function of temperature T and frequency ω, respectively.

Figure 2.1 displays the change in the elastic modulus as a function of temperature and inverse timescale (frequency) as a polymer experiences typical phase transitions. At low temperatures or high frequencies, the polymeric material behaves like a glassy, brittle solid with very high elastic modulus. Towards higher temperatures and lower frequencies, the material softens. Around the so-called glass transition temperature T_{g}, the modulus drops over several decades. Subsequently, the modulus reaches the so-called rubber plateau. Towards even higher temperatures, the material either gets softer and starts to flow (non-crosslinked polymers), or the modulus stays constant (crosslinked polymers).

In this Chapter, we first present the basic equations of liquids and solids when a force is applied. Then we turn towards viscoelastic materials, which show properties of both liquids and solids simultaneously, and their characterization.

2.1. Liquids

In this section, we briefly review some important aspects of liquids [86]. A liquid is referred to as *Newtonian* if under shear it fulfils Newton's law

$$\sigma = \eta \dot{\gamma} \; . \tag{2.1}$$

The stress σ is proportional to the shear rate $\dot{\gamma}$, which is a velocity gradient. The proportionality constant is the viscosity η. The viscosity quantifies the liquid's ability to dissipate energy due to inner friction of the molecules: the higher the inner friction, the less the liquid wants to flow and the higher is the viscosity. Various liquids though do not have constant viscosity.

Shear thinning and shear thickening liquids

If the viscosity in not constant for all shear rates, it can be either shear thinning or shear thickening. The viscosity of shear thinning liquids decreases with increasing shear rate, see figure 2.2(a). In contrast, the viscosity of shear thickening liquids increases with increasing shear rate, see figure 2.2(b). Their behavior can be described by phenomenological models. A shear thinning liquid is typically characterized by two plateau values: η_0 is the viscosity at vanishing shear rates, η_∞ the viscosity at very high shear rates. Between these two plateaus, the viscosity often follows a simple power law,

$$\eta = \eta_0 (k\dot{\gamma})^{n-1} = m\,\dot{\gamma}^{n-1} \; , \tag{2.2}$$

where k and n are adjustable parameters. The liquid is shear thinning if $n < 1$. Equation 2.2 is called *Ostwald–de Waehle* law.

More sophisticated models, which for example take into account η_∞, exist. A common model is the *Carreau* model,

$$\frac{\eta - \eta_\infty}{\eta_0 - \eta_\infty} = \frac{1}{(1 + (k_1 \dot{\gamma}^2))^{m_1/2}} \; . \tag{2.3}$$

However, the simpler *Ostwald* model (equation 2.2) is in many cases sufficient to describe the liquid's behavior in the relevant range of shear rates.

Typical examples for liquids with shear thinning behavior are melts of short, rigid, rod-like polymers. Think of a solution of rod-like molecules in a solvent, for example

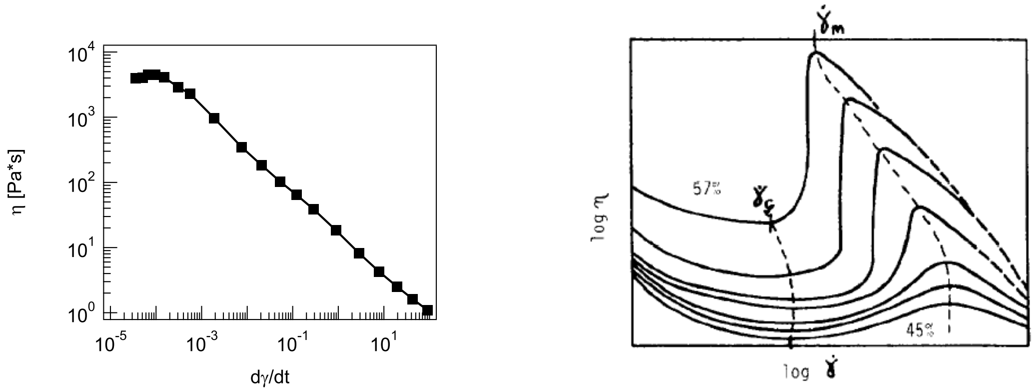

(a) Viscosity versus strain rate for a shear thinning liquid ("Carbopol", see Chapter 10) with plateau at small shear rates.

(b) Viscosity versus strain rate for granular suspensions with different percentages of grains, taken from [8].

Figure 2.2.: Shear thinning and shear thickening liquids.

in water. The polymer-water mixture has a strongly increased viscosity compared to the pure solvent, as the molecules introduce additional internal friction. If this mixture is sheared, one can easily imagine that the rods align in the direction of shear. The friction between the single molecules decreases since they can slip along each other more easily compared to the non-aligned state. That is why the viscosity drops down with increasing shear rate.

Shear thickening liquids are more rare in nature. An example are some suspensions of hard particles. Their behavior depends on the particle concentration and the shear rate and can switch from shear thinning to shear thickening in an appropriate range of parameters. In figure 2.2(b) taken from reference [8], the suspensions are shear thickening between $\dot\gamma_\mathrm{c}$ and $\dot\gamma_\mathrm{m}$.

Yield stress fluids

Some liquids have an inner structure that is stable at very low stresses. It cannot easily be changed, and as a result, these liquids do not flow as long as the applied stress stays below a critical value σ_c. Examples are toothpaste or hair gel. Their behavior can be modeled as follows.

The simplest model is the *Bingham* model, in which the liquid does not flow below the critical stress and behaves as a Newtonian liquid above the critical stress. The corresponding equations are

$$\dot\gamma = 0 \qquad \text{for} \quad \sigma < \sigma_\mathrm{c}\ , \tag{2.4}$$

$$\dot\gamma = \frac{\sigma - \sigma_\mathrm{c}}{\eta} \qquad \text{for} \quad \sigma > \sigma_\mathrm{c}\ . \tag{2.5}$$

Slightly more complicated, the *Herschel–Bulkley* model describes liquids that are shear thinning or shear thickening above σ_c according to the following equations:

$$\begin{aligned} \dot{\gamma} &= 0 && \text{for} \quad \sigma < \sigma_c \,, \\ \sigma &= \sigma_c + k\dot{\gamma}^n && \text{for} \quad \sigma > \sigma_c \,. \end{aligned} \tag{2.6}$$

Having introduced the general concepts of liquids, we now turn to the basic equations of solids, see for example reference [4].

2.2. Elasticity

Solids

We consider a rigid body under deformation. We limit the discussion to a linear response theory, meaning that the material shows a linear response to small deformations. Moreover, we do not consider time dependent phenomena. The initial length of a body shall be l_0. The tensile strain $\epsilon = \Delta l / l_0$ is its dimensionless deformation, resulting in a small tensile stress σ_t (the force per cross section). In the linear regime, the strain is linked to the stress via the tensile modulus

$$E = \frac{\sigma_t}{\epsilon} \,. \tag{2.7}$$

A second modulus used extensively is the shear modulus G. In analogy to equation 2.7, it is defined as

$$G = \frac{\sigma_s}{\gamma} \,, \tag{2.8}$$

with σ_s being the shear stress and γ the shear strain. The linear relationship between the stress and the strain is known as *Hooke's law.* The elastic material behaves as a spring with the elastic spring constant E.

E and G are linked via the compressibility of a material of volume V. It is expressed in the Poisson's ratio ν,

$$\nu = \frac{1}{2} \left[1 - \left(\frac{1}{V} \right) \frac{dV}{d\epsilon} \right] \,. \tag{2.9}$$

From elasticity theory it follows for the relation between tensile and shear modulus

$$E = 2(1+\nu)G \,. \tag{2.10}$$

For incompressible materials, $\nu = 0.5$, and equation 2.10 simplifies to

$$E = 3G \,. \tag{2.11}$$

Rubbers

Polymers soften above their glass transition temperature and behave as very elastic rubbers, as displayed in figure 2.1. They have the unique ability to extend to several times their size. The high extendability and elasticity is of entropic origin: the single polymer chains can coil, stretch, entangle, and are in general very flexible without changing the interatomic distances. A good overview for rubbery states is given for example in references [4] and [97].

A rich variety of different models describe the behavior and the elasticity of polymeric rubbers under stress. These models describe the single polymer chains in different ways, the simplest being the freely jointed chain model [97]. The collective behavior is derived from the behavior of a single chain. We shall only mention the simplest of these models here: the *affine network* model. The main assumption is that the deformation is affine: each network strand on the microscopic level is supposed to be deformed in exactly the same way as the macroscopic sample.

Let a network have the undeformed dimensions l_{x0}, l_{y0}, and l_{z0}. Its deformation along the direction i is then defined as

$$\lambda_i = l_i / l_{i0} \ . \tag{2.12}$$

The affine deformation implies that the end points of the polymer strands in the sample undergo the same deformations as the sample itself. The single polymer chain in this model is assumed to follow Gaussian statistics. Additionally, the sample volume V_0 shall be conserved. Starting from these assumptions, one can derive from the networks' entropy and free energy a relation between an uniaxial deformation and the resulting stress,

$$\sigma_\mathrm{T} = \frac{nkT}{V_0} \left(\lambda^2 - \frac{1}{\lambda} \right) \ . \tag{2.13}$$

σ_T is the true stress, that is, the force per cross section A of the sample. n is the number of polymer chains in the sample, T the temperature, and k the Boltzman constant. Likewise, an equation for the engineering stress σ_E, that is, the force per initial cross section A_0, can be derived:

$$\sigma_\mathrm{E} = \frac{nkT}{V_0} \left(\lambda - \frac{1}{\lambda^2} \right) \ . \tag{2.14}$$

A shear modulus G can be determined from equations 2.13 and 2.14:

$$G = nkT/V_0 = \nu kT = \frac{\rho \mathcal{R} T}{M_\mathrm{s}} \ . \tag{2.15}$$

ρ is the network density, $\mathcal{R}$ the gas constant, and M_s the number-average molar mass of a network strand.

In the affine network model, the end points of the polymer chains are fixed to some elastic background and are not allowed to fluctuate in space. This means that the polymer chains cannot be crosslinked among each other, which is of course not the case in real networks. The simplest model accounting for these fluctuations is the *phantom network* model. The same stress-deformation relations 2.13 and 2.14 as for the affine network model can be derived, with a slight difference in the definition of G: M_s is replaced by an apparent molar mass [97].

Both of the presented models do not account for chain entanglements or defects like loops and dangling chains. A very good agreement is found though between theory and experimental results for deformations up to 50% [4].

2.3. Viscoelasticity

Viscoelastic materials show the viscous properties of liquids as well as the elastic properties of solids. Upon application of a stress, these materials partially recover their original shape. Some of the energy injected into the system is stored elastically and can be recovered after the stress is released, but some energy is also dissipated by inner friction. This dissipation is responsible for the incomplete shape recovery going along with hysteresis. Viscoelasticity is a complex property and not easy to describe. In the following section, we introduce some simple phenomenological models for the viscoelasticity of polymers.

2.3.1. Modeling viscoelastic liquids and solids

As we mentioned before, an elastic solid is characterized by a linear relationship between tensile stress σ and deformation ϵ, the proportionality constant being the elastic modulus:

$$\sigma = E\epsilon \ . \tag{2.16}$$

The simplest model to represent such a behavior is a spring with spring constant E, see figure 2.3(a).

The corresponding equation for a liquid is a linear relationship between the stress σ and the deformation rate $\dot{\epsilon}$, the proportionality constant being the viscosity η:

$$\sigma = \eta\dot{\epsilon} \ . \tag{2.17}$$

Mechanically, equation 2.17 can be represented by a piston moving in a container filled with a liquid of viscosity η. This element is called a dashpot, see figure 2.3(b).

These two elements, spring and dashpot, can be combined in various ways to construct a large number of models for viscoelastic liquids and solids.

The Maxwell model

The simplest model for a viscoelastic liquid is the *Maxwell* model, a serial combination of spring and dashpot, see figure 2.3(c). The total tensile strain in this model is simply the sum of the strain in each element:

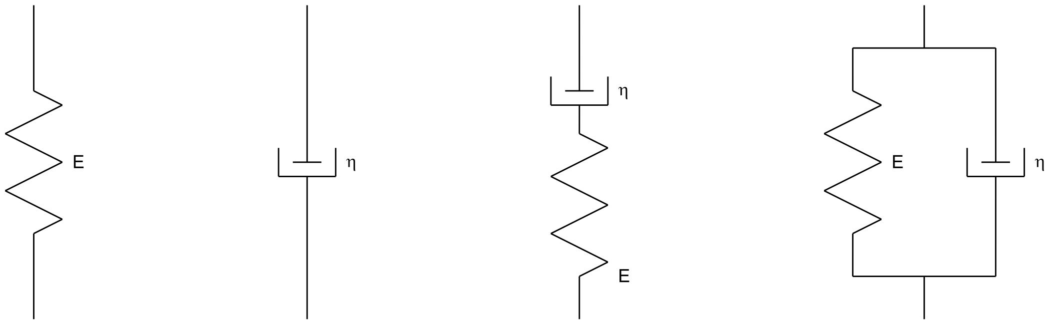

(a) Spring element.

(b) Dashpot element.

(c) Maxwell model.

(d) Voigt model.

Figure 2.3.: Mechanical elements representing solids, liquids, and viscoelastic materials.

$$\epsilon = \epsilon_{\text{spring}} + \epsilon_{\text{dashpot}} \; . \tag{2.18}$$

The stress on the other hand has to be the same in each element as they are connected in series:

$$\sigma = E\,\epsilon_{\text{spring}} = \eta\,\dot{\epsilon}_{\text{dashpot}} \; . \tag{2.19}$$

From equations 2.18 and 2.19, one can write down the equation of motion:

$$\frac{d\epsilon}{dt} = \frac{\sigma}{\eta} + \frac{1}{E}\frac{d\sigma}{dt} \; . \tag{2.20}$$

Now we study how the system reacts when a strain ϵ_0 is imposed instantaneously ("stress relaxation" or "step strain" test). The spring in figure 2.3(c) will follow immediately and the stress jumps to σ_0. Subsequently, the dashpot relaxes and the stress decreases as a function of time. For times $t < 0$, the stress is zero. For times $t \geq 0$, equation 2.20 reduces to

$$\frac{d\sigma}{dt} = -\frac{E}{\eta}\,\sigma(t) \; , \tag{2.21}$$

the solution of which is

$$\sigma = \sigma_0\, \mathrm{e}^{-t/\tau_{\text{Max}}} \tag{2.22}$$

with relaxation time $\tau_{\text{Max}} = \eta/E$. τ_{Max} determines the time scale of the system: for times $t < \tau_{\text{Max}}$, the systems reacts mainly as an elastic spring and answers with a constant stress σ_0. At long times compared to τ_{Max}, the system behaves as a liquid and the stress decays to zero, see figure 2.4(a).

Instead of imposing a constant strain ϵ_0 at $t = 0$, one can also apply a stress σ_0 and study how the strain evolves. This situation is called “creep test”. Equation 2.20 gives

$$\epsilon(t) = \frac{\sigma_0}{\eta} t + \epsilon_0 \; . \tag{2.23}$$

At time $t = 0$ the spring jumps instantaneously at the deformation ϵ_0, then the strain grows steadily as the dashpot relaxes, corresponding to the behavior of a pure liquid with viscosity η, see figure 2.4(b).

The Voigt model

The simplest model for a viscoelastic solid is a parallel combination of dashpot and spring, known as the *Voigt* model, see figure 2.3(d).

In this parallel connection, the constraint for the total tensile strain is

$$\epsilon = \epsilon_{\text{spring}} = \epsilon_{\text{dashpot}} \; . \tag{2.24}$$

The total stress in the system is the sum of the stresses of each element, so that

$$\sigma(t) = \sigma_{\text{spring}} + \sigma_{\text{dashpot}} = E\,\epsilon + \eta\,\frac{d\epsilon}{dt} \; . \tag{2.25}$$

We now discuss how the strain follows an instantly applied constant stress σ_0. From equation 2.25 it follows that

$$\sigma_0 = E\,\epsilon(t) + \eta\,\frac{d\epsilon}{dt} \; , \tag{2.26}$$

the solution of which is

$$\epsilon(t) = \frac{\sigma_0}{E}\left(1 - \mathrm{e}^{-t/\tau_{\text{Voigt}}}\right) \; . \tag{2.27}$$

τ_{Voigt} is again a relaxation time as defined for the Maxwell model. The strain increases slowly in this model and reaches the value γ_0 after a typical time determined by the viscoelastic relaxation time. Unlike the viscoelastic liquid, the viscoelastic solid behaves like a liquid at times $t < \tau$, where the system is deformed and the dashpot relaxes. On long times $t > \tau$ on the other hand, the system has reached its maximum strain γ_0 that stays constant as long as the stress σ_0 is imposed. This behavior is displayed in figure 2.4(c).

Oscillatory experiments

A question of great importance is how the system reacts to dynamic experiments where the imposed stress depends on the time. We assume an oscillating tensile stress of the form

$$\sigma = \sigma_0 \mathrm{e}^{i\omega t} \tag{2.28}$$

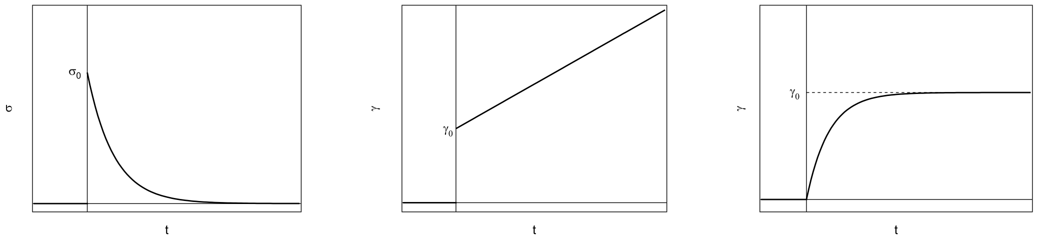

(a) Stress versus time predicted by the Maxwell model when a step strain is applied at $t = 0$.

(b) Strain versus time predicted by the Maxwell model when a step stress is applied at $t = 0$.

(c) Strain versus time predicted by the Voigt model when a step stress is applied at $t = 0$.

Figure 2.4.: σ and γ versus t in Maxwell and Voigt model.

with amplitude σ_0 and frequency ω.

First we investigate the Maxwell model. Substituting the oscillating stress into the underlying differential equation 2.20 gives

$$\frac{\epsilon(t)}{dt} = \frac{\sigma_0}{E} i\omega \mathrm{e}^{i\omega t} + \frac{\sigma_0}{\eta} \mathrm{e}^{i\omega t} . \tag{2.29}$$

Integrating equation 2.29 between t_1 and t_2 yields an expression for the difference in strain between these two times:

$$\epsilon(t_2) - \epsilon(t_1) = \frac{\sigma_0}{E} (\mathrm{e}^{i\omega t_2} - \mathrm{e}^{i\omega t_1}) + \frac{\sigma_0}{\eta i\omega} (\mathrm{e}^{i\omega t_2} - \mathrm{e}^{i\omega t_1}) . \tag{2.30}$$

The complex modulus $E^\star$ is defined as

$$E^\star = E' + iE'' = \frac{\sigma(t_2) - \sigma(t_1)}{\epsilon(t_2) - \epsilon(t_1)} . \tag{2.31}$$

It represents the proportionality constant between the total stress and the total strain in the system. Substituting equations 2.30 and 2.28 into equation 2.31 and dividing into real- and imaginary part leads to the following expressions for E' and E'':

$$E' = \frac{E\tau^2\omega^2}{1 + \omega^2\tau^2} , \tag{2.32}$$

$$E'' = \frac{E\tau\omega}{1 + \omega^2\tau^2} . \tag{2.33}$$

E' is called the *storage modulus* and represents the in-phase part measuring the elastic response of the material. E'' is called the *loss modulus* and represents the out-of-phase part, a measure for the dissipation in the material and therefore for

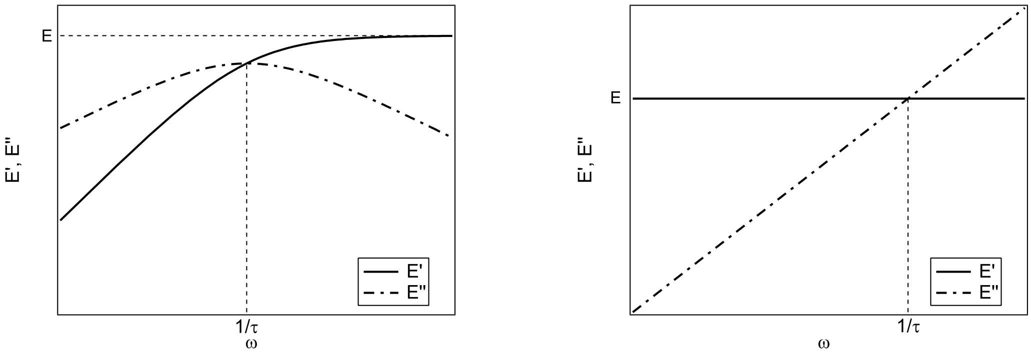

(a) Maxwell model equations 2.32 and 2.33.

(b) Voigt model equations 2.34 and 2.35.

Figure 2.5.: Storage modulus E' and loss modulus E'' as a function of frequency ω for simple viscoelastic models.

its viscous properties.[1] Figure 2.5(a) shows the storage and the loss modulus as a function of frequency for the Maxwell model.

In the same manner as for the Maxwell model one can investigate the reaction of the Voigt model to oscillatory elongations and calculate the elongational storage and loss modulus. Assuming a oscillatory stress as in equation 2.28, it follows from equation 2.25 for E' and E'', that

$$E' = E \ , \tag{2.34}$$

$$E'' = \omega\eta \ . \tag{2.35}$$

The two figures 2.5(a) and 2.5(b) reveal some interesting features. At small frequencies, the loss modulus is higher than the storage modulus in the Maxwell model, meaning that the viscous character prevails. At a frequency corresponding to one over the typical relaxation time τ, both moduli are equal. For higher frequencies, the storage modulus increases and reaches a plateau value E, whereas the loss modulus gets smaller and smaller: the system behaves as a solid. These regimes are characteristic for a viscoelastic liquid. A different behavior is found for the Voigt model system. Here, the storage modulus is constant and equal to E. The loss modulus however increases linearly with slope η. The behavior is divided into a regime at frequencies smaller than $1/\tau$, where the elastic properties predominate, and a regime at frequencies higher than $1/\tau$, where the viscous properties are more important. Thus the Voigt model represents a simple model for a viscoelastic solid.

These two models have in common that they use only two elements, a dashpot with viscosity η and a spring with modulus E. They have one relaxation time τ and can only describe a transition between a liquid-like and a solid-like regime. In reality, polymers can exhibit many different relaxation times and also have more

---

[1] The concept of storage and loss modulus will be explained in more detail in section 2.4.

than one phase transition (liquid – rubber – glassy). More sophisticated models for polymer viscoelasticity include the superposition of several Maxwell or Voigt elements, with a finite or continuous distribution of relaxation times, or they go down to the molecular size to model the dynamics of melts and networks. We shall not discuss these models here.

2.4. Characterization by rheometry

We will see in this section how to measure the viscosity and the storage and loss modulus in a rheometer. These concepts will be very important for characterizing our materials.

Constant shear measurements

A common method of determining the viscosity of a liquid with high precision is using a rheometer. The principle is either to impose a strain rate and measure the stress necessary to maintain it, or, in the inverse case, to impose a constant stress and measure the resulting deformation. We performed most of our measurements in the strain controlled configuration. We are working exclusively with shear deformations and shear stresses in the following. Figure 2.6 schematically displays the two measurement geometries we used to characterize our materials: a plate-plate and a cone-plate geometry [86].

The plate-plate geometry consists of two metal plates of the same radius a at distance b from each other. In some cases, the lower plate has a bigger radius than the upper plate, and a denotes then the radius of the upper plate. The lower plate shall be fixed, whereas the upper plate is allowed to rotate at a controlled angular speed Ω. The gap of variable width b is filled with the measurement substance. To determine the shear viscosity η, one has to establish equations for the shear rate $\dot{\gamma}$ and the stress σ.

The shear rate between the two rotating parallel plates is not constant, but an average can be expressed as

$$\dot{\gamma} = \frac{a\,\Omega}{b} \,. \tag{2.36}$$

The measured torque C can be calculated from the shear stress via

$$C = \int_0^a 2\pi\sigma(r) r^2 dr \tag{2.37}$$

with r being the position along the plate radius. Using equations 2.1 and 2.36, it follows from integration that

$$\eta = \frac{2\,b\,C}{\pi\Omega\,a^4} \,. \tag{2.38}$$

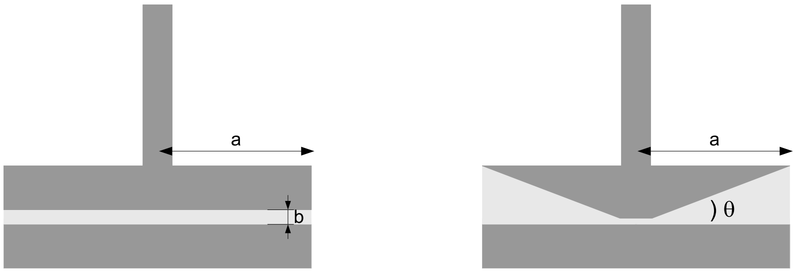

(a) Plate-plate geometry. (b) Cone-plate geometry.

Figure 2.6.: Schemes of different rheometer measurement geometries.

In the cone-plate geometry, a upper cone is situated at distance b from a lower plate of the same radius a. The cone is allowed to rotate with angular speed Ω. The gap b between cone and plate is defined by the cone's opening angle θ. The local velocity at distance r from the center of the cone is equal to $\Omega\, r$. Assuming a linear velocity profile between the plate and the cone, the velocity gradient is

$$\dot{\gamma} = \frac{\Omega\, r}{h(r)} = \frac{\Omega}{\tan\theta}\ , \tag{2.39}$$

with $h(r)$ the local position in the vertical direction (note that this approximation is only valid for small angles θ). Consequently the shear rate is independent of the position in the radial direction and all fluid elements experience the same shear rate. The relation between the total torque C on the axis and the stress σ is

$$\sigma = \frac{3\, C}{2\pi\, a^3}\ . \tag{2.40}$$

From equations 2.39 and 2.40 follows for the viscosity

$$\eta = \frac{\sigma}{\dot{\gamma}} = \frac{3\, C \tan\theta}{2\pi\, a^3\, \Omega}\ . \tag{2.41}$$

Oscillatory measurements of linear viscoelasticity

For viscoelastic materials with complex properties it can become impossible to perform constant shear measurements as described above. The structure of a polymeric network is most likely to be destroyed in a steady shear experiment as chemical or physical crosslinks between the polymer chains will break up (or the experiment will be stopped by overload of the instrument). In this case, one still can gain insight into the material properties if one submits the material to oscillatory shear at different amplitudes and frequencies [86]. We discuss here *linear* rheological properties, meaning that we stay in a regime of small deformations where the material's stress response to deformation is linear.

We consider now an imposed deformation γ of the form

$$\gamma = \gamma_0 \cos \omega t \ , \tag{2.42}$$

with ω the angular velocity and γ_0 the maximum deformation, which has to be chosen small enough to stay in the linear regime. For an elastic material, the stress is proportional to γ and in phase with it. For a liquid, the stress is proportional to the strain rate,

$$\dot{\gamma} = -\omega \gamma_0 \sin \omega t \ , \tag{2.43}$$

and stress and strain are 90 ° out of phase. A material with elastic and viscous properties can consequently experience an arbitrary phase shift δ between strain and stress. Therefore, the measured total torque C exhibits a part C', which is in phase with the excitation, and a part C'', which is out of phase with the excitation:

$$C = C' \cos \omega t - C'' \sin \omega t \ . \tag{2.44}$$

We discuss the plate-plate geometry. Equation 2.37 stays valid if one introduces the complex notation

$$C = \frac{\pi a^4}{2\, b} \eta^\star \ \Omega_0 i \, \omega \mathrm{e}^{i\omega t} \tag{2.45}$$

with

$$\eta^\star = G^\star / i\omega = (G' \cos \omega t + i \, G'' \sin \omega t) \ . \tag{2.46}$$

Comparing the real part of equation 2.45 to equation 2.44 and identifying the terms in sine and cosine yields

$$G' = \frac{2\, b}{\pi a^4 \, \Omega_0} C', \ G'' = \frac{2\, b}{\pi \, a^4 \Omega_0} C'' \ . \tag{2.47}$$

In conclusion, one imposes an oscillating strain $\gamma = \gamma_0 \cos \omega t$ and measures the oscillating response of the stress $\sigma = \sigma_0 \cos(\omega t + \delta)$. The phase difference δ is given by

$$\tan \delta = \frac{G''}{G'} \ . \tag{2.48}$$

One can deduce from the measured phase shift and measured amplitude how elastic or viscous a material is. The following quantities are calculated:

- The storage modulus $G' = \frac{\sigma_0}{\gamma_0} \cos \delta$ measures the in-phase elastic properties of the material.
- The loss modulus $G'' = \frac{\sigma_0}{\gamma_0} \sin \delta$ measures the out-of-phase viscous properties of the material.
- The complex modulus $G^\star = \frac{\sigma_0}{\gamma_0} = \sqrt{G'^2 + G''^2}$ measures the material's total resistance to deformation.

In later chapters, we will make extensive use of these rheological techniques.

3. Theoretical concepts of adhesion

Having introduced the basic concepts of elasticity and viscoelasticity, we now turn to adhesion and the question of how bodies stick together and debond again. We restrict the discussion to so-called *pressure sensitive adhesives (PSA)*, which are common in industry and everyday life applications. The most common application for PSAs are tapes and labels. PSAs are viscoelastic materials that adhere to a substrate after application of a low pressure, and they debond ideally without leaving any residues on the substrate. The adhesion is generated only by van der Waals forces, covalent bonds are not involved. This means that these adhesives do not undergo a transition between liquid and solid during the bonding process like other adhesives do. As an example, two compound epoxy adhesives come as two liquid compounds that start to react chemically upon mixing. After some waiting time, these liquids have transformed into a brittle solid.

Many studies have been dedicated to the investigation of PSAs. Especially the improvement of performance, the investigation of different materials, and the study of different debonding mechanisms have been at the center of interest. A review article of Shull and Creton has recently described the different mechanisms in some detail [108]. In this Chapter, we first present some classical methods of measuring the properties of PSAs, then we describe different debonding mechanisms, and finally we introduce typical adhesive properties and their influence on the debonding behavior. An overview of the properties and the application of PSAs in general can be found, for example, in references [99], [41], and [91].

3.1. Measuring adhesive properties

Soft adhesives can be characterized with various techniques probing different properties. A crucial quantity is the adhesion energy, that is, the energy needed to debond an adhesive from a substrate. It depends on many factors, like the testing geometry, the sample geometry, the material properties of the adhesive, and also the interactions between the adhesive and the probing surface.

The thermodynamic work of adhesion is defined as the minimum energy per unit area required to separate two bodies and to create new free surface. It is calculated adding the two free surface energies from each body and subtracting the interfacial free energy $\gamma_{\mathrm{S}_{12}}$,

$$W_{\mathrm{adh}_{\mathrm{thermo}}} = \gamma_{\mathrm{S}_1} + \gamma_{\mathrm{S}_2} - \gamma_{\mathrm{S}_{12}} \ . \tag{3.1}$$

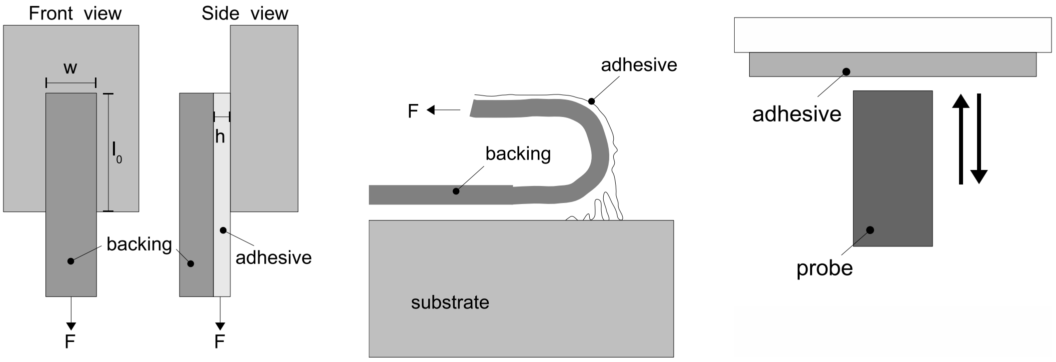

(a) Shear test.
(b) Peel test.
(c) Probe test.

Figure 3.1.: Different techniques to characterize the performance of pressure sensitive adhesives, see reference [41].

If two surfaces of the same elastic solid material are put together, the adhesion energy corresponds to two times the surface energy γ_S,

$$W_{\mathrm{adh}_{\mathrm{thermo}}} = 2\gamma_S \ . \tag{3.2}$$

In the case of PSAs, the practical adhesion energy is much higher than the thermodynamic work of adhesion (equation 3.1). As the materials are viscoelastic, they are deformed a lot and much energy is dissipated during the debonding process. The debonding mechanisms are very complex and involve cavitation and fibrillation, see section 3.2.

Now we introduce some experimental techniques to characterize the performance of an adhesive.

Shear test

The demands on a PSA's performance depend on the application. The load they are supposed to sustain and the period of time over which to sustain this load are very variable. In shear tests, one therefore measures the material's resistance to a constant moderate shear stress over a certain period in time. Such a "shear holding power test" is depicted in figure 3.1(a). A PSA is bonded partially to a rigid vertical substrate in such way that the contact area is known. Then a mass of known weight is fixed to the dangling end and the time between the attachment of the weight and the moment when failure occurs in the PSA and the weight drops is measured. The weight and the time give access to the "shear holding power". The resistance to shear obtained in this way is commonly used as a measure of the material's ability to resist to flow.

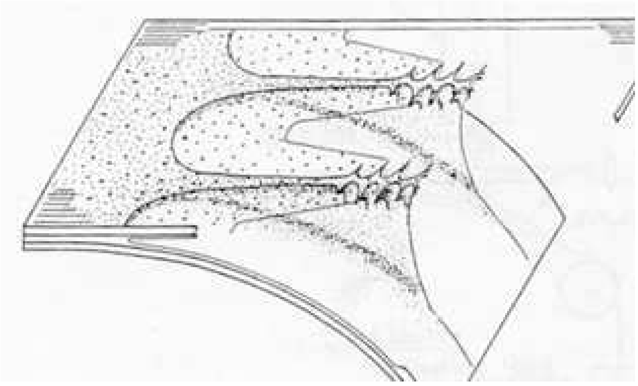

Figure 3.2.: Typical patterns observed during the peeling of an adhesive tape, from [115].

Peel test

A peel test probes the adhesive's behavior when it is peeled away from a substrate. The "peel adhesion" is defined as the force required to remove a PSA tape of known width from a standard test surface at a given velocity. Initially, the adhesive, which is bonded to a backing tape, wets a thick, rigid substrate. Then the tape is peeled off at fixed peeling angle and fixed peeling rate. The force is measured during the test. The peeling angle can differ: common tests are performed in a 90 ° or 180 ° geometry. In the 180 ° test, the PSA is folded back over itself, see figure 3.1(b), and then peeled at a fixed rate. In the 90 ° geometry, the substrate with the adhesive is fixed on a trolley that is allowed to move freely perpendicular to the direction of the peeling, so that the angle is kept constant during the test. During a peel test, one observes typically the lateral propagation of interfacial fractures as well as the formation and stretching of bulk fibrils as shown in figure 3.2 from reference [115].

Tack test

The term "tack" refers to the adhesive's ability to bond to a substrate upon light contact (that is, upon a pressure not higher than finger pressure) and to resist debonding. The classical way to test it is called "probe tack test". A probe is brought into contact with an adhesive layer, and after a certain waiting time it is pulled away from the surface at a fixed speed. The probe is usually a cylindrical flat or slightly convex punch. The force and the displacement of the probe are recorded during the whole test, so it is possible to trace characteristic curves for the complete debonding process and to calculate the energy per unit area needed to debond the probe from the adhesive. A schematical view of the setup is given in figure 3.1(c). As the deformation is well controlled in this test, it is often used for fundamental studies. The probe tack setup will be described in further detail in Chapter 6.

We shall only mention that, aside from the probe tack test, a family of other tests to determine a material's tack exist, such as the *the rolling ball test* or the *loop tack test*.

3.2. Debonding mechanisms

It has been observed in many studies that confined soft adhesive materials debond in different ways under an applied tensile stress, as carried out in the probe tack test geometry for example. As a function of the material parameters and the probe surface, the debonding can be mainly interfacial (at the interface between the probe and the polymeric layer), or in the material's bulk. The complex deformation mechanisms involve the formation of short or long fibrils, air fingers that penetrate at the edge of the adhesive layer, and the formation of cavities. In fact, the nucleation of cavities breaking the confinement of the layer is crucial for the performance of pressure sensitive adhesives, since it allows the large deformations of the layer that are necessary to dissipate much energy during debonding. It is desirable for most of the applications that the PSA eventually debonds adhesively, which means without leaving residues on the substrate. This requires a mechanism of strain hardening of the highly stretched layer. We now describe in more detail the mechanisms of debonding as they typically occur during a probe test.

Fracture – interfacial failure

In the case of fracture, the debonding is very fast and does not involve large deformations of the layer. Cavities nucleate at the probe/polymer interface and grow with a disk shape during debonding. Finally, they merge and the failure is complete at very small strains. As no residues are left on the probe, the debonding is called adhesive.

Fibrillation – adhesive failure

A second mechanism frequently observed is an adhesive mechanism that involves a large deformation of the polymeric layer. The mechanism starts by the nucleation of cavities or fingers. Subsequently, the material is stretched to several times the initial layer thickness. The final failure occurs by detachment of the fibrils from the probe surface. In this case, the cavities or fingers do not necessarily merge before failure occurs. Although the debonding mechanism is adhesive, an important bulk deformation is involved. A condition for the stretched fibrils to detach from the probe surface is that the material displays so-called *strain hardening*, meaning that the material becomes stiffer with increasing strain.

Fibrillation – cohesive failure

In the case of cohesive failure, the cavities or air fingers are initiated in the bulk of the confined layer. No direct contact between air and probe surface occurs. Subsequently, long fibrils are formed and stretched until they break up in the middle. The material undergoes deformations of several times its initial thickness. The failure in this case is called *cohesive*: the fibrils break up in the middle and residues are left on the probe at the end of the test.

3.3. From rheological properties to debonding mechanisms

Some criterions have to be fulfilled to obtain a pressure sensitive adhesive with good performance. The first one established was the so-called *Dahlquist* criterion [33], stipulating that the elastic shear modulus at the bonding frequency must be lower than 0.1 MPa. Otherwise the layer is not able to form a good contact with the substrate within the contact time. Even if this criterion is not always correct, it is clear that G' must not be too high to be able to wet the substrate and form a good molecular contact over a rough surface [30]. An empiric "viscoelastic window of performance" determining the material properties for which the PSA's performance is optimal has been proposed by Chang [17, 18]. If G' lies in the right range, the debonding mechanism is determined by an interplay of different factors. The interfacial energy plays a role as well as the deformability of the layer. We present first some concepts for elastomers (a good overview is given in reference [88]), before we approach the more complicated situation of viscoelastic adhesives.

Interfacial crack propagation explained by an energy balance

Based on thermodynamic considerations, Kendall [60] and Johnson [56] applied the concepts of energy balance and energy minimization to gain a better understanding of adhesion between elastic bodies. We consider two elastic bodies in contact. A is the contact area, P an applied force, and d an applied displacement. The system's total energy $U = U(S,\, d,\, A)$ depends on the independent parameters entropy, displacement, and contact area. It can be separated into an elastic energy U_E and a surface energy U_S. The surface energy is

$$U_\mathrm{S} = -(\gamma_1 + \gamma_2 - \gamma_{12}) = -\mathcal{G}_0\, A\ , \tag{3.3}$$

where $\mathcal{G}_0$ is the thermodynamic work of adhesion per unit area that arises from van der Waals forces and is also known as the *Dupré* work w.

We write down the total derivative of the system's energy,

$$\mathrm{d}U = \left(\frac{\partial U}{\partial S}\right)_{d,\,A} \mathrm{d}S + \left(\frac{\partial U}{\partial d}\right)_{S,\,A} \mathrm{d}d + \left(\frac{\partial U}{\partial A}\right)_{S,\,d} \mathrm{d}A\ . \tag{3.4}$$

Using thermodynamical relationships and neglecting thermic effects, one obtains the following equations for the thermodynamic potentials. The derivative of *Helmholtz' free energy* is given by

$$\mathrm{d}F = P\ \mathrm{d}d + (\mathcal{G} - \mathcal{G}_0)\ \mathrm{d}A = \mathrm{d}(U_\mathrm{E} + U_\mathrm{S})\ , \tag{3.5}$$

and the derivative of *Gibb's free energy* by

$$\mathrm{d}G = -d\ \mathrm{d}P + (\mathcal{G} - \mathcal{G}_0)\ \mathrm{d}A = \mathrm{d}(U_\mathrm{E} + U_\mathrm{S} + U_\mathrm{P})\ , \tag{3.6}$$

with the system's potential energy $U_\mathrm{P} = -Pd$. $\mathcal{G} = \left(\frac{\partial U_\mathrm{E}}{\partial A}\right)_d$ is the *energy release rate*. It denotes the variation in the elastic energy with varying contact area for a given displacement. From these thermodynamical consideration follows that the system is at equilibrium at a given displacement d, if

$$\mathcal{G} = \mathcal{G}_0 \; . \tag{3.7}$$

Equation 3.7 is called *Griffith's criterion* [52]. It can be interpreted in the following way: if $\mathcal{G} < \mathcal{G}_0$, it follows from equations 3.5 and 3.6 that a minimization of the thermodynamic potentials ($\mathrm{d}F < 0$ and $\mathrm{d}G < 0$) leads to an increase in the contact area, $\mathrm{d}A > 0$: the crack is closing. In contrast, if $\mathcal{G} > \mathcal{G}_0$, it follows in the same manner that $\mathrm{d}A < 0$ and the crack advances to the center of the contact area. In the latter case, the energy $\mathcal{G}\,\mathrm{d}A$ is given back to the system. The energy $\mathcal{G}_0\,\mathrm{d}A$ is needed to break the interfacial bonds and create new surface. The energy difference $(\mathcal{G} - \mathcal{G}_0)\,\mathrm{d}A$, in the absence of any dissipation, is converted into kinetic energy that makes the crack advance faster. $\mathcal{G} = \mathcal{G}_0$ is the minimum energy needed to propagate a crack at zero velocity. The energy equilibrium equation 3.7 can be stable, unstable, or neutral. A stable situation is given for $\left(\frac{\partial \mathcal{G}}{\partial A}\right)_d > 0$. The quasi-static force P_c is the force that corresponds to a controlled debonding at the stability limit $\mathcal{G} = \mathcal{G}_0$, $\left(\frac{\partial \mathcal{G}}{\partial A}\right)_d = 0$.

The influence of dissipation

When a crack propagates, the energy equilibrium situation becomes unstable as soon as $\left(\frac{\partial \mathcal{G}}{\partial A}\right)_d = 0$, and the crack accelerates until complete debonding. Viscoelastic dissipation in the material stabilizes the crack velocity at the limiting velocity V. Viscoelastic losses of course vary with the speed and the temperature.

In peeling experiments, it has been shown first in 1964 that temperature-frequency superposition [119] works well and that a single master curve can be obtained for the adhesion energy as a function of $a_\mathrm{T}V$ [59]. Maugis and Barquins proposed an empirical equation for the kinetics of an interfacial crack that propagates at velocity V [77],

$$\mathcal{G}_\mathrm{c} - \mathcal{G}_0 = \mathcal{G}_0\,\Phi(a_\mathrm{T}V) \; . \tag{3.8}$$

In a stationary state, the energy $\mathcal{G}$ that is supplied to the system corresponds to the energy $\mathcal{G}_\mathrm{c}$ that is dissipated during the crack propagation at velocity V. $\mathcal{G}_\mathrm{c} - \mathcal{G}_0$ is then the driving force of the crack, whereas $\mathcal{G}_0\,\Phi(a_\mathrm{T}V)$ stabilizes the crack velocity at V and acts thus as a brake in the system. Maugis *et al.* proposed that for elastomers, the dissipation function Φ takes at constant temperature the empirical form [77],[3]

$$\Phi \propto \left(\frac{V}{V^\star}\right)^n \; . \tag{3.9}$$

$V^\star$ is a characteristic crack velocity. Furthermore, for high velocities or high dissipation, $\mathcal{G}_0 \ll \mathcal{G}_\mathrm{c}$ and equation 3.8 yields

$$\mathcal{G}_{\mathrm{c}} \approx \mathcal{G}_0 \, \Phi(a_{\mathrm{T}} V) \; . \tag{3.10}$$

Different authors have been proposing an estimate for $\Phi(a_{\mathrm{T}}V)$ as a function of the linear viscoelastic properties. Saulnier *et al.* developed a rather complex analytic expression for $\mathcal{G}_{\mathrm{c}}/\mathcal{G}_0$. They considered G' and G'' and integrated over the range of frequencies over which the material is excited [101]. They found

$$\frac{\mathcal{G}_{\mathrm{c}}}{\mathcal{G}_0} \cong G_\infty \int_{\omega_{\mathrm{min}}}^{\omega_{\mathrm{max}}} \frac{G''(\omega)}{G'(\omega)^2 + G''(\omega)^2} \frac{d\omega}{\omega} \; . \tag{3.11}$$

Therein, ω_{min} and ω_{max} are the upper and lower cut-off frequencies, respectively, determined by the layer thickness and the crack front speed. G_∞ is a plateau value of the modulus at high frequencies.

Gent showed experimentally in peel tests for simple elastomers that the increase in the fracture energy with the peel rate resembles the increase in the dynamic modulus G' with frequency ω [44]. However, Ramond *et al.* found that the frequency dependence of the loss modulus G'' dominates Φ [94]. For PSAs though, the loss *and* the storage modulus depend strongly on the frequency, so that the total frequency dependence is rather reflected in $\tan\delta = G''/G'$ than in G'' alone. Deplace *et al.* thus approximated Φ as a linear function of $\tan\delta(\omega)$ [36]. Equation 3.10 reads with this approximation

$$\mathcal{G}_{\mathrm{c}} \approx \mathcal{G}_0 \; \tan\delta \; . \tag{3.12}$$

Interfacial versus bulk propagation

Within the transition from the interfacial propagation of a crack to a bulk deformation of the layer, several parameters play a role. On the one hand, energy is required to make an interfacial crack move at a certain speed. As discussed previously, this energy cost is determined by $\mathcal{G}_{\mathrm{c}}(V)$ for elastomers. On the other hand, elastic energy is necessary to deform a layer of thickness b and elastic modulus E. The higher the elastic modulus E, the more difficult it is to deform the bulk. Crosby *et al.* [31], and also Creton *et al.* [29], considered the case of a an elastic layer confined between a punch of radius R and an undeformable surface. The contact area is assumed to be radial with radius a. The authors investigated the conditions for the propagation of an axisymmetric fracture. If the fracture does not propagate, bulk deformation ensues. They showed that the relevant parameter describing the competition between bulk and interfacial mechanisms at a given confinement is

$$\frac{\mathcal{G}_{\mathrm{c}}}{Ea} \; . \tag{3.13}$$

Webber *et al.* investigated later the stability of an interfacial fracture for a given contact area and different degrees of confinement [118]. They showed that for a high degree of confinement, the layer thickness b is a more natural length than a, and the relevant parameter is rather

$$\frac{\mathcal{G}_\mathrm{c}}{Eb}\ . \tag{3.14}$$

These are results for elastic rubbers. To extend them to the case of viscoelastic soft materials, dissipation has to be taken into account. One of the main results of the thesis of Deplace [36], see also reference [16], is the determination of an expression for the parameter equation 3.14 that is valid for viscoelastic materials. They proposed the empirical parameter

$$\mathcal{G}_\mathrm{c}/E \approx G''/G'^2\ , \tag{3.15}$$

originating from the combination of equations 3.12 and 3.14. It was shown that this parameter is appropriate for predicting the debonding mechanism for a model viscoelastic adhesive system [36]. The advantage of this approach is that the complicated quantity $\mathcal{G}_\mathrm{c}$, which depends on many parameters and is very difficult to calculate for complex materials, can be approximated by linear rheological properties, which are rather simple to measure. We shall refer again to this parameter in Chapter 7.

4. Viscous and elastic instabilities in confined geometries

4.1. Linear stability analysis

Pattern formation can be observed in a large variety of systems in nature. It occurs when a so-called homogeneous ground state becomes unstable against small perturbations. The system then passes into a new state, and the formation of periodic patterns ensues. This phenomenon is widely spread in nature; from cloud formation and patterns on animal coats to chemical reactions, pattern formation is a very rich and complex subject. We will outline in the following how the stability or instability of the ground state can be investigated by mathematical means.

Let a system be described by differential equations for the relevant quantities. In general, a homogeneous solution, called the ground state, for this set of differential equations exists. Introducing an adequate control parameter, the equations can be written in a dimensionless way. The control parameter is a dimensionless number that combines the relevant physical quantities in the system. These quantities can be for instance the pressure field, the velocity field, the density field, and so on.

The ground state is stable in time towards perturbations or not. Small perturbations are always present in nature or in the laboratory framework. Possible origins are the roughness of a wall supposed to be smooth, small dust particles, thermal fluctuations, and so on. The system in its ground state is thus permanently "tickled" by a small noise. These perturbations can be damped by the system. In this case, the disturbing amplitude becomes smaller and the perturbations finally die out: the ground state is stable. A second possibility is that the amplitude of the perturbation is growing, and a new disturbed state arises. The new state again can be stable or unstable. To investigate the stability of a system, the concept of linear stability analysis has been established. It consists in assuming sinusoidal perturbations of all possible wavelengths and investigating how the system reacts subsequently to them.[1]

The procedure consists in adding a small disturbing field of sinusoidal shape to the initial ground state. These disturbed fields are substituted into the system's underlying equations. The resulting equations are linearized and the corresponding boundary conditions applied. One assumes that the amplitude of the perturbation with wavelength λ and corresponding wave vector $k = 2\pi/\lambda$ changes in time via an exponential factor $\mathrm{e}^{\sigma_k t}$. σ_k is the growth rate of the mode k and is here assumed to be

---

[1] A perturbation of arbitrary shape can be represented as superposition of sinusoidal perturbations.

a real number. An evaluation of the resulting linearized differential equations yields for a fixed control parameter the function $\sigma_k(k)$, that is, the dispersion relation. If σ_k is negative, the amplitude of the corresponding perturbing mode k is damped away and the ground state is stable against this perturbation. If σ_k is positive for one or more k, these modes are growing exponentially and the system is unstable. In general, a fastest growing mode exists and this mode is the most unstable or destabilizing mode. Subsequently, $\sigma_k(k)$ can be studied as a function of the control parameter. For many systems, there exists a critical control parameter below which the system is stable to all perturbating modes, and above which a destabilizing mode exists.

In the following sections, we will discuss several systems exhibiting instabilities and we will see how they can be investigated using linear stability analysis.

4.2. The Saffman–Taylor instability

The Saffman–Taylor instability, or viscous fingering instability, has first been described by Saffman in 1958 [98], and has been one of the flagships of pattern formation since then. It was widely studied and is a beautiful example to illustrate the pattern formation processes that are overall present in nature. In addition, it has a huge impact in the oil industrie. In fact, the Saffman–Taylor instability was discovered during the recovery of oil from porous rocks. To recover the oil from the rock pores, it was pushed with water. During this process, oil workers observed the formation of air fingers limiting the oil yield: An important oil layer was left behind on both sides of the air finger.

In this thesis, we study on the one hand pattern formation in viscoelastic materials, in particular the linear instability. On the other hand, we are interested in the time evolution of the number of air fingers during the debonding of a Newtonian liquid. The understanding of the Saffman–Taylor instability is therefore crucial and this section is devoted to the explanation of its principles.

The Navier–Stokes equations

To describe completely the motion of a flowing liquid, it is necessary to know the velocity $\boldsymbol{u} = \boldsymbol{u}(x, y, z, t)$ and two thermodynamic parameters, for example the pressure field $p = p(x, y, z, t)$ and the density $\rho = \rho(x, y, z, t)$. The coordinates (x, y, z, t) here are related to a fixed coordinate system, not to the moving fluid particle. These parameters are related to each other through two equations: a continuity equation and the Navier–Stokes equations, which originate from a balance of momentum and were first in 1827 by C. L. Navier and then in 1845 by G. G. Stokes [67]. Presuming an incompressible fluid with constant density ρ, the Navier–Stokes equations have the form

$$\frac{\partial \boldsymbol{u}}{\partial t} + (\boldsymbol{u} \cdot \boldsymbol{\nabla})\boldsymbol{u} = -\frac{1}{\rho}\,\boldsymbol{\nabla}\,p + \left(\frac{\eta}{\rho}\,\nabla^2 \boldsymbol{u}\right) . \tag{4.1}$$

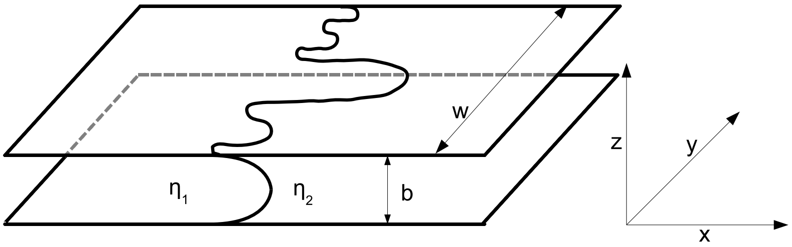

Figure 4.1.: Schematical view of a Hele–Shaw cell filled with two liquids of different viscosities. The thickness b is much smaller than the width w, the cell can thus be approximated as a $2D$ system.

The left side of equation 4.1 describes the change in the velocity $\boldsymbol{u}$ of a volume particle. $\boldsymbol{u}$ is on the one hand determined by a change in the velocity at a fixed point in space during the time $\mathrm{d}t$, on the other hand by a convective contribution originating from the difference in the velocities at a fixed moment t at two different points in space. The change in the velocity in equation 4.1 is balanced by the forces in the system. The first term on the right side corresponds to the force induced by a pressure gradient in the liquid. The second term describes dissipation due to the inner friction in a viscous liquid.
The continuity equation from mass conservation

$$\frac{\partial \rho}{\partial t} + \boldsymbol{\nabla} \cdot (\rho \boldsymbol{u}) = 0 \tag{4.2}$$

reduces for an incompressible fluid with constant density to

$$\boldsymbol{\nabla} \cdot \boldsymbol{u} = 0 \,. \tag{4.3}$$

The Hele–Shaw cell

The Saffman–Taylor instability may arise when a less viscous fluid is pushing a fluid of higher viscosity in a confined geometry under applied pressure. In the laboratory, this confined geometry is called a *Hele–Shaw* cell. It consists of two plates separated by a small gap of well-known thickness. Figure 4.1 shows the classical linear cell. The upper and lower plates are usually glass plates, which are thick enough to sustain the pressure differences. The gap width is controlled using spacers. As long as the gap width b is much smaller than the channel width w, the system can be approximated as a $2D$ system. We suppose a horizontally placed cell for the following considerations, so any influence due to gravity can be neglected.

We consider now the case of of air pushing a viscous liquid in the cell under a pressure gradient. The speed V of the liquid and the contact line is proportional to the pressure gradient ∇p. We presume a straight contact line at the beginning of the experiment. This straight line is subject to small perturbations by the underlying noise that is present in every experiment. A deformation of the contact line changes

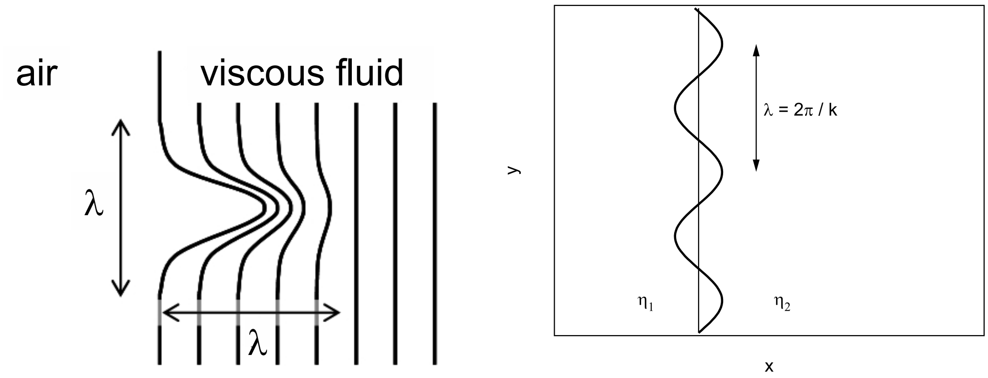

(a) (b)

Figure 4.2.: A sinusoidal perturbation with wavelength λ of the initially linear contact between fluid 1 and 2.

the boundary conditions and therefore influences the pressure field in the liquid. The pressure gradient is increased just in front of the maximum deformation: Figure 4.2(a) displays the deformation of the lines of constant pressure. As the $V \propto \nabla p$, the "tip" of the perturbation is moving faster into the fluid, and the perturbation is growing.
We now investigate in more detail the equations describing the system.

Darcy's law

The "motor" of motion in this situation is the pressure gradient; the motion is limited by viscous friction. The motion of a viscous liquid is described by the Navier–Stokes equations 4.1. Neglecting inertial effects gives

$$\nabla p = \eta \nabla^2 \boldsymbol{u} \ . \tag{4.4}$$

As the gap width $b \ll w$, we consider only velocity components parallel to the plates. As the dominant variation of the velocity is along the z-axis, the derivatives in x and y-direction are small, and $\nabla^2 \boldsymbol{u}$ is approximated by $\partial^2/\partial z^2 \ \boldsymbol{u}$. Equation 4.4 then reads

$$\nabla p = \eta \frac{\partial^2 \boldsymbol{u}}{\partial z^2} \ . \tag{4.5}$$

We are interested in the velocity field. Integrating equation 4.5 and applying no slip boundary conditions $[\boldsymbol{u}(z=0) = \boldsymbol{u}(z=b) = 0]$ yields the parabolic velocity field of a plane Poiseuille flow

$$\boldsymbol{u} = \frac{1}{2\eta} z(z-b) \nabla p \ . \tag{4.6}$$

Integrating over the cell thickness b leads to an expression for the mean velocity,

$$\boldsymbol{u}_{\mathrm{mean}} = -\frac{b^2}{12\eta}\nabla p \,. \tag{4.7}$$

With $K = b^2/12\eta$, equation 4.7 represents a particular case of Darcy's law for porous media

$$\boldsymbol{u}_{\mathrm{mean}} = -K\,\nabla p \,, \tag{4.8}$$

an equation that connects the mean velocity of a flow to the pressure gradient via a constant K, which is the permeability of the porous medium.

Combining equation 4.7 with the condition of incompressibility leads to the Laplacian equation,

$$\nabla^2 p = 0 \,. \tag{4.9}$$

Linear stability analysis

The stability of the straight interface towards sinusiodal perturbations as depicted in figure 4.2(b) is investigated by means of linear stability analysis. For the Saffman-Taylor instability, this analysis was performed first by Chuoke in 1959 [22].

For each of the two liquids 1 and 2, Darcy's law equation 4.7

$$\boldsymbol{u}_i = -\frac{b^2}{12\eta_i}\nabla p_i \tag{4.10}$$

as well as the Laplace equation 4.9

$$\nabla^2 p_i = 0 \tag{4.11}$$

are valid on both sides of the interface.

In the non-disturbed flow state, the linear interface is moving with velocity V in the x-direction, and has no components in the other directions. The position of the contact line is $\xi = Vt$. The pressure can be calculated integrating equation 4.10. The boundary condition is zero pressure at the moving interface $x = \xi = Vt$. Therefore one finds

$$p = \frac{V}{K}(x - Vt) \,. \tag{4.12}$$

Now the linear interface is disturbed by a sinusoidal perturbation of wavelength λ and small initial amplitude, see figure 4.2(b). The amplitude depends on time as $\epsilon \mathrm{e}^{\sigma t}$. The moving interface is then described by

$$\xi = Vt + \epsilon\,\mathrm{e}^{\sigma_k t}\sin ky \,. \tag{4.13}$$

The disturbed interface leads to a perturbation in the velocity and pressure fields. The resulting disturbed fields can be written as as superposition of the ground state and a small perturbation field:

$$p_i^{\text{res}} = p_i^{\text{ground}} + p_i \tag{4.14}$$

$$\boldsymbol{u}_i^{\text{res}} = \boldsymbol{u}_i^{\text{ground}} + \boldsymbol{u}_i \tag{4.15}$$

The disturbed fields and the ground state fields both fulfil Darcy's law 4.10 and the incompressibility constraint 4.3. Therefore, they must hold also for the small disturbing fields. There are some requirements for the form of the solutions. First, the perturbation in the pressure field must have the same periodicity in the spatial y-direction as the initial perturbation of the contact line. Second, the perturbation should be growing or decreasing exponentially in time with a typical growth rate σ_k depending on the wavelength of the perturbation. Third, the perturbation should vanish when moving away from the contact line, so it is supposed to decay exponentially over a typical length, which is the size of the perturbation itself. Therefore the solutions for the pressure field must have the form

$$p_1 = A_1\, \mathrm{e}^{\sigma_k t + kx} \sin ky \ , \ \ p_2 = A_2\, \mathrm{e}^{\sigma_k t - kx} \sin ky \ . \tag{4.16}$$

For small deformations, one can assume that the velocity in x-direction at the interface must be the same for both fluids, that is,

$$u_{x_1} = u_{x_2} = \frac{\partial \xi}{\partial t} - V = \sigma_k \epsilon\, \mathrm{e}^{\sigma_k t} \sin ky \ . \tag{4.17}$$

So far, we have not considered the effect at the interface due to capillarity. As the pressure field is Laplacian, the surface tension γ induces a pressure jump δp at the interface between the two liquids:

$$\delta p = \gamma \left(\frac{1}{R_1} + \frac{1}{R_2} \right) \ . \tag{4.18}$$

R_1 and R_2 are the radii of curvature of the interface in the z-direction and in the xy-plane, respectively. An assumption generally made is that the curvature in the z-direction is of the order of $b/2$ and constant along the interface [98]. Thus equation 4.18 simplifies to

$$\delta p = \gamma \left(\frac{2}{b} + \frac{1}{R_2} \right) \ . \tag{4.19}$$

Note that in this approximation the dynamical effects are neglected. It disregards as well the fact that the more viscous fluid, oil in general, is wetting the cell and leaving a thin liquid layer behind. It has been shown that the approximation of no wetting layer is not always valid [112].

However, using the boundary conditions at the interface equations 4.10 and 4.18, it is possible to determine the amplitudes A_1 and A_2. Linearizing the resulting

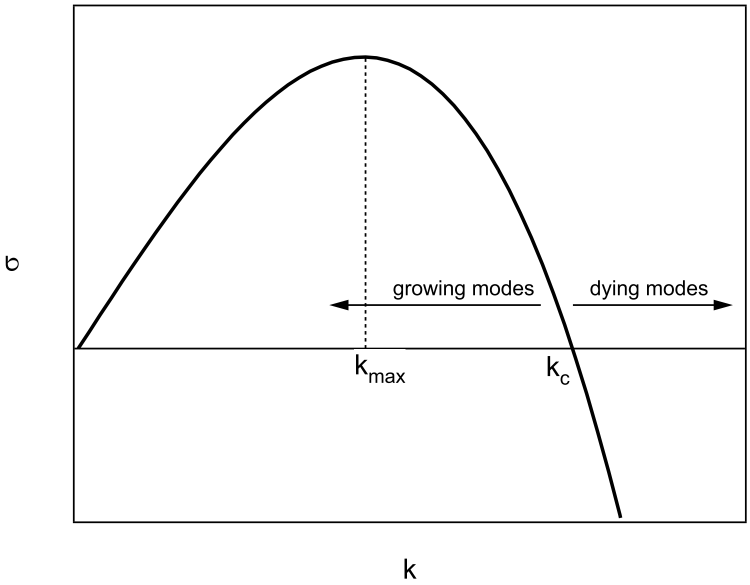

Figure 4.3.: The growth rate as a function of the wave vector k. k_{c} is the critical mode, $k_{\max}$ the fastest growing mode.

equations by suppressing all terms of higher orders in combination with the boundary conditions leads to an expression for the growth rate σ_k of a perturbation with wave vector k:

$$\sigma_k = \frac{1}{\eta_1 + \eta_2}\left[-V(\eta_1 - \eta_2)k - \frac{\gamma b^2 k^3}{12}\right] . \tag{4.20}$$

Closer inspection of equation 4.20 reveals that the growth rate is negative for all $\eta_1 > \eta_2$. The amplitude $A_0 \mathrm{e}^{\sigma_k t}$ of a perturbation decreases exponentially for all wavelengths. The linear interface is thus stable when a more viscous fluids pushes a less viscous fluids, as for example oil pushing water.

For $\eta_1 < \eta_2$ there exists a critical wave vector below which the growth rate becomes positive: a small perturbation is exponentially growing and the interface becomes instable. The dispersion relation in this case is plotted in figure 4.3. The critical wave vector is

$$k_{\mathrm{c}} = \frac{2}{b}\sqrt{\frac{3V(\eta_2 - \eta_1)}{\gamma}} . \tag{4.21}$$

The interface is unstable to all perturbations with wave vectors $0 < k < k_{\mathrm{c}}$. $\sigma(k)$ has a maximum. The wave vector for which the growth rate is maximal is the fastest growing mode and the system will be unstable to this perturbation. It is

$$k_{\max} = k_{\mathrm{c}}/\sqrt{3} , \tag{4.22}$$

and the corresponding fastest growing (or most unstable) wavelength is thus

$$\lambda_{\max} = \pi b \sqrt{\frac{\gamma}{V(\eta_2 - \eta_1)}} \ . \tag{4.23}$$

The fastest growing wavelength is also called the capillary length of the instability.

For the situation that $\eta_1 \ll \eta_2 = \eta$, for example the very common laboratory situation of a gas pushing an oil, equations 4.20 and 4.23 reduce to

$$\sigma_k = Vk \left[1 - \frac{\gamma b^2}{12 V \eta} \, k^2 \right] \tag{4.24}$$

and

$$\lambda_{\max} = \pi b \sqrt{\frac{\gamma}{V\eta}} \ , \tag{4.25}$$

respectively. The term

$$Ca = \frac{V\eta}{\gamma} \tag{4.26}$$

is called capillary number. It is a dimensionless number that compares viscous forces to capillary forces.

An upper bound for the destabilizing wavelength is introduced naturally in the experimenal situation: the undulation has to fit into the actual cell, the wavelength $\lambda_{\max}$ cannot exceed twice the channel width,

$$\lambda_{\max} \leq 2w \ . \tag{4.27}$$

This implies that the interface is stable if $\lambda_{\max} > 2w$.

Non-linear finger selection

So far, we discussed the wavelength right at the onset of the instability. But many researchers have been interested in the non-linear evolution of the pattern at later times.

Figure 4.4 shows an experiment where water pushes oil [112]. The initially linear interface begins to undulate at early times. The typical distance of the undulations is determined by the linear mode selection discussed previously. Then the amplitudes begin to grow and evolve into competing fingers. A stronger deformation of the contact line leads to a higher pressure gradient in front of the finger tip and therefore to a higher velocity. Thus, the biggest finger grows faster than its neighbours. It screens all other fingers, and finally one single finger is left. The parameter controlling the width of the persisting finger in a cell of width w and thickness b was determined by Saffman and Taylor [98] as

$$\frac{1}{B} = 12 \frac{\eta V}{\gamma} \left(\frac{w}{b} \right)^2 \ . \tag{4.28}$$

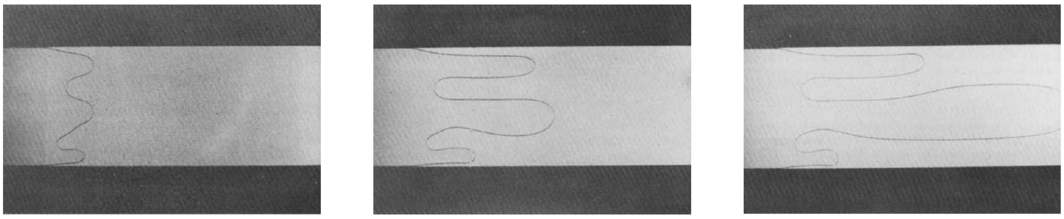

(a) (b) (c)

Figure 4.4.: The interface between water and oil is initially destabilized [4.4(a)]. Subsequently, the amplitudes grow and evolve into competing fingers [4.4(b)]. Finally one finger wins [4.4(c)]. At late times, it covers half the channel width w (not shown here). Taken from reference [112].

Investigating the dimensionless fingerwidth, that is the fingerwidth divided by the cell width, as a function of the control parameter equation 4.28, they found that the dimensionless fingerwidth saturates at a value of 0.5 for higher values of $1/B$. This phenomenon was not understood for many years until in 1986 three groups showed independently that the surface tension introduces an additional condition at the finger tip [23, 55, 106]. This condition leads to an analytical equation for the dimensionless fingerwidth as a function of $1/B$ that tends to 0.5 for high values of $1/B$.

4.2.1. Circular geometry

Viscous fingering was not only observed in the classical linear geometry. A circular setup has for example been studied by Paterson in 1981 [87]. For the circular cell, the relevant length scales are the gap width b between the glass plates and the radius R of the cell. Experiments can be performed in two variants. One fills the cell with a high viscosity liquid and pushes in the first variant air through a hole at the center, resulting in outward fingering. In the second variant, the filling liquid is sucked out of the hole in the center, and inward fingering ensues. In the latter case, the liquid is pushed at the outer cell radius by the ambient air.

Paterson found that both in the case of inward and outward fingering, the most unstable wavelength $\lambda_{\mathrm{max}} = 2\pi R/k_{\mathrm{max}}$ is

$$\lambda_{\mathrm{max}} = \frac{2\sqrt{3}\pi R}{\sqrt{\frac{12 V_{\mathrm{R}} R^2 \eta}{b^2 \gamma} + 1}} \,, \tag{4.29}$$

where V_R is the radial velocity [87]. From volume conservation, V_R is linked to the lifting speed v as $V_R = vR/2\,b$. For $R \gg b$, equation 4.29 recovers the result for the linear geometry (equation 4.25) with capillary number

$$Ca = \frac{\eta V_{\mathrm{R}}}{\gamma} \,. \tag{4.30}$$

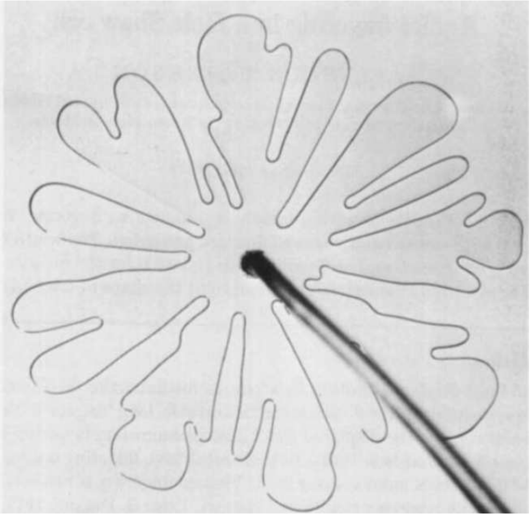

Figure 4.5.: Outward fingering in a circular cell. Air injected into glycerine, taken from reference [87]

Figure 4.5 shows outward fingering in a radial cell when air is injected into glycerine [87]. Of course even if the initial destabilizing wavelength is the same in the linear and circular cell, the late time behavior differs strongly, as the mechanisms of finger competition are not the same.

4.2.2. The lifted Hele–Shaw cell

This thesis is concerned with pattern formation in the probe tack experiment. This setup can be interpreted as a circular Hele–Shaw cell with changing gap width in the inward fingering geometry. It is called the lifted Hele–Shaw cell. In this setup, the control parameter varies as the gap width b is changing as a function of time. At $t = 0$, the initial control parameter from linear stability analysis is

$$\tau_0 = \frac{\gamma {b_0}^3}{12 v_0 \eta {R_0}^3} \,, \tag{4.31}$$

with b_0 the initial plate spacing, v_0 the lifting speed, and R_0 the radius of the Hele–Shaw cell.

The finger number N_0 is linked to τ_0 via

$$N_0 = \sqrt{\frac{1}{3}\left(1 + \frac{1}{2\tau_0}\right)} \,. \tag{4.32}$$

The time dependence can be introduced as follows. $t' = t\, v_0/b_0$ is the dimensionless time variable. The varying gap width is

$$b(t) = b_0 + v_0 t = b_0(1 + t') \,, \tag{4.33}$$

and the mean radius of the more viscous liquid at time t'

$$R(t') = R_0/\sqrt{1+t'}\ . \tag{4.34}$$

Equation 4.34 follows from volume conservation.

Replacing each quantity in equation 4.31 by their time dependent analogue allows for writing a time dependent control parameter τ [104, 10]. It can be written as

$$\tau(t) = \frac{\gamma b(t)^3}{12 v_0 \eta R(t)^3}\ . \tag{4.35}$$

Substituting equations 4.33 and 4.34 into equation 4.35 yields

$$\begin{aligned}\tau(t) &= \frac{\gamma b(t)^3}{12 \eta v_0 R(t)^3}\\ &= \frac{\gamma {b_0}^3}{12 \eta v_0 {R_0}^3} \frac{(1+t')^3}{(1+t')^{-3/2}}\\ &= \tau_0 (1+t')^{9/2}\ .\end{aligned}$$

In the framework of a linear 2D theory, the number of fingers as a function of time reads thus

$$N(t') = \sqrt{\frac{1}{3}\left(1+\frac{1}{2\tau(t')}\right)} \tag{4.36}$$

$$= \sqrt{\frac{1}{3}\left(1+\frac{1}{2\tau_0(1+t')^{9/2}}\right)}\ . \tag{4.37}$$

One single growing finger in a circular cell is physically not possible. The lower bound for the number of fingers is thus

$$2 \leq N \leq \sqrt{\frac{1}{3}\left(1+\frac{1}{2\tau_0(1+t')^{9/2}}\right)}\ . \tag{4.38}$$

Lindner, Derks, and Shelley compared experiments and numerical simulations based on the time dependent $2D$ Navier–Stokes equations to the prediction from the linear theory equation 4.37 [75]. They found that the number of fingers in experiments and simulations is always higher than calculated by linear stability analysis. We shall refer again to these results in Chapter 10.

4.2.3. Towards non-Newtonian systems

The Saffman–Taylor instability has been the subject of many studies. Basic principles and current research have been reviewed for example by Couder [24]. Great interest has been devoted to the study of more complex systems going away from Newtonian liquids. In fact, the calculations given in the previous section can in many cases be modified and expanded to non-Newtonian systems in such a way that the calculations start from the Newtonian results, but yield a modified control parameter.

Lindner *et al.* investigated the Saffman–Taylor instability in a linear channel filled with different non-Newtonian liquids [72, 74, 73]. For shear thinning liquids [72], they studied the influence of the non-Newtonian character on the finger size at late times by two different approaches. For slightly shear thinning liquids, they replaced the viscosity in Darcy's law (equation 4.7) by the shear thinning viscosity and found good agreement with experimental results. In the case of strongly shear thinning liquids, this approach was not sufficient and a new selection mechanism was uncovered. Based on the techniques for Newtonian liquids, the authors obtained a modified control parameter that determines the fingerwidth at late times. Going even further away from Newtonian liquids, Coussot and Lindner investigated yield stress fluids. They derived a modified control parameter that contained the yield stress and allowed to describe their experimental results [25, 74].

4.2.4. Elastic bulk instability

Shull *et al.* went even further and considered purely elastic gels where no material flow was involved [109]. They studied a bulk fingering instability in confined layers of an elastic gel that was rigidly bonded to a lower and an upper substrate. They pulled on one of the plates, imposing in this way a traction stress with large deformations to the gel layer. During cyclic traction experiments, they observed reproducible bulk fingers.

The authors investigated in more detail the stress distribution under a rigid punch of radius a in contact with an elastic layer of thickness h as a function of the confinement a/h, see figure 4.6. From the literature the asymptotic behavior is known. In the limit of an infinitely thick layer, that is, for confinement $a/h = 0$, the stress is maximal at the borders of the punch and has a minimum at the center. For $a/h \to \infty$, the situation is inverted, the stress distribution has a maximum at the center and tends to 0 at the borders. For intermediate values of a/h, the stress has a minimum close to the borders and increases towards the center. This means that the stress gradient is pointing in the direction of the moving interface when pulling, a criterion that has been established for the Saffmann–Taylor instability in section 4.2. The authors subsequently argued that the wavelength of the observed bulk instability can be estimated following the Saffman–Taylor prediction,

$$\lambda = 2\pi\sqrt{\gamma/(\mathrm{d}\sigma/\mathrm{d}x)} \approx 4\pi\sqrt{\gamma h/\sigma_{\mathrm{avg}}}. \tag{4.39}$$

$\mathrm{d}\sigma/\mathrm{d}x$ is therein the stress gradient, γ the surface tension, and σ_{avg} the average applied tensile stress. The observed wavelength is in agreement with the one calculated from equation 4.39, but also in the order of magnitude of the film thickness. In

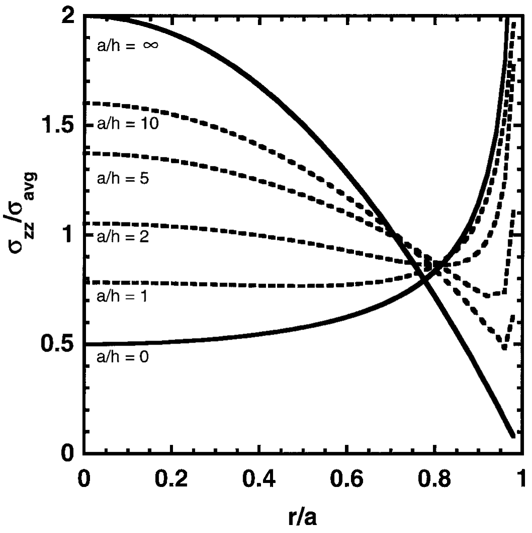

Figure 4.6.: The distribution of the normal stress σ_{zz} in a elastic layer of thickness h under a flat rigid punch with radius a for different confinements a/h. σ_{avg} is the applied tensile stress.

conclusion, the authors observed an elastic bulk instability, triggered by a pressure gradient and inhibited by surface tension. No material flow was involved.

4.3. Elastic interfacial instability

In section 4.2, we have introduced the Saffman–Taylor instability, a classical bulk instability observed in a variety of liquids. In the following section, we present interfacial instabilities observed in elastic media.

Peeling of thin elastic films – interfacial instabilities

In 2000, Ghatak *et al.* found for the first time evidence for an instability of the contact line in thin elastic films in a peel geometry [47]. Their experimental set-up was the following: elastic PDMS films with different shear moduli G and controlled thickness b were prepared on a glass substrate. Then a glass cover slip of variable flexural rigidity D was brought into contact with the PDMS. D is defined as

$$D = \frac{\mu b'^3}{6(1-\nu)} \tag{4.40}$$

with μ the shear modulus of the cover plate, b' its thickness, and ν its Poisson's ratio. A spacer was put on one side between the cover glass and the elastic film so that the plate and the film formed a wedge. The authors observed that the contact line spontaneously moved to its equibrium position. Below a critical film thickness, the contact line started to undulate. These undulations remained stable after the crack

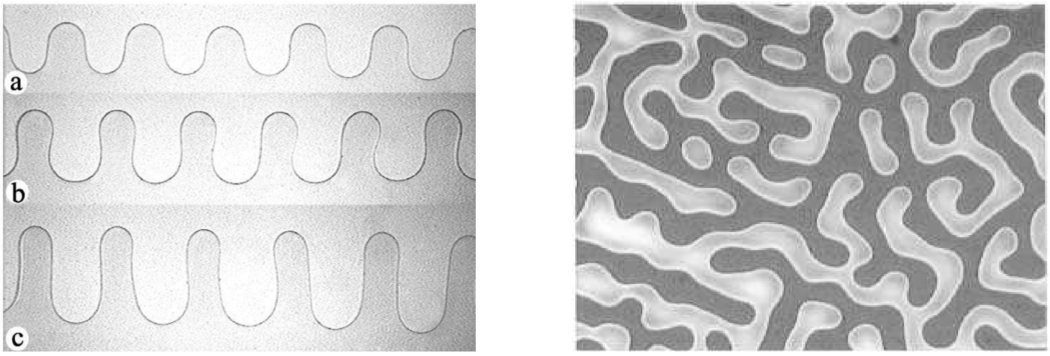

(a) The meniscus instability of a thin elastic film in a peel geometry. $b = 150\,\mu\mathrm{m}$, $G = 1 \times 10^6\,\mathrm{Pa}$. The flexural rigidity of the cover glass increases from top ($0.02\,\mathrm{Nm}$) to bottom ($0.2\,\mathrm{Nm}$). From reference [47].

(b) $2D$ ripple pattern observed upon contact when approaching a thin elastomeric layer ($b = 12.1\,\mu\mathrm{m}$) to a parallel glass slide. From reference [79].

Figure 4.7.: Contact instabilities in confined elastic systems.

came to rest. Figure 4.7(a) shows the wavelength and amplitude of the undulations for fixed thickness b and shear modulus G but for different flexural rigidities D of the cover slip.

The main result of this study was that the wavelength of the instability increases linearly with the film thickness, but stays independent both of the flexural rigidity of the cover slip and the shear modulus of the elastic layer. This elastic instability involves no material flow.

A similar situation was investigated by Mönch and Herminghaus in 2001 [79]. They studied the pattern formation when a very thin layer of a soft polymer is fixed on a lower rigid glass substrate and approached to an upper rigid glass substrate. The elastomeric film and the contactor were parallel in this study. Film thicknesses ranged from $7\,\mu\mathrm{m}$ to $60\,\mu\mathrm{m}$. From a critical distance on, the authors observed a $2D$ ripple pattern with a typical wavelength λ. As in the study by Ghatak *et al.*, λ depended solely on the film thickness.

A mathematical model for the plane strain case has been developed by Mönch *et al.* [79] as well as by Shenoy and Sharma in 2001 [105]. We give here the basic principles and main results as reported in [105]. An elastomeric film of thickness b is strongly bonded to a rigid substrate. A flat rigid contactor is placed in the distance d from the free film surface, and the free surface of the film is allowed to deform. The interaction forces between the two surfaces, which tend to destabilize the stystem, are in competition with the elastic restoring forces in the film. The authors draw the energy balance upon approach of the contactor,

$$E_{\text{total}} = E_{\text{elastic}} + E_{\text{interaction}} + E_{\text{surface}} \,. \tag{4.41}$$

The interaction energy is not specified in their model and can originate for example from van der Waals interactions between the free surface and the contactor. The authors show that a homogeneous solution for the displacement field $\boldsymbol{u}$ in the elastomeric film exists, so that the stresses in the film are equal everywhere. This equilibrium stress field minimizes the total system energy equation (4.41) in a linearized form. Subsequently, they test the stability of this homogeneous solution to disturbing displacement fields of the form $u_j = \mathrm{e}^{ikx_1} u_j(x_2)$. They find that for sufficiently small distances d, the homogeneous solution is unstable and undulations of the contact line appear. The critical wavenumber k_c is determined by a rather complex function of the thickness b, the Poisson's ratio ν, the surface tension γ and the film's shear modulus G. For the relevant experimental conditions for elastomers $\nu \to 0.5$ and $\gamma/Gh \ll 1$ though, this function reduces to the simpler form

$$b\, k_\mathrm{c} = 2.12 - 2.86(1 - 2\nu) - 2.42\, \frac{\gamma}{Gh}\ . \tag{4.42}$$

It is obvious that the wavelength $\lambda_\mathrm{c} = 2\pi/k_\mathrm{c}$ does solely depend on the film thickness for common elastomeric films with the typical values $\nu \approx 0.5$, $G \approx 1\,\mathrm{MPa}$, $b > 1\,\mu\mathrm{m}$, and $\gamma \approx 0.1\,{}^{\mathrm{J}}\!/\!{}_{\mathrm{m}^2}$.[2]

The main results of the model are:

- The destabilizing wavelength λ is independent of all system parameters but the film thickness.
- The wavelength does not depend on the exact nature of the interaction. The destabilization is triggered by the interaction energy but the mode selection is not influenced.
- The surface tension has a stabilizing influence, but is negligible in common experimental situations.
- If one includes viscous stresses into the stability analysis, the critical viscoelastic mode recovers the critical elastic mode for the typical experimental parameters.

A broader study involving different setups such as circular and rotating geometries has been published in 2003 [46]. As mentioned before, there exists a critical film thickness b_c below which the contact line in the peeling geometry is instable and starts to undulate. Performing a systematic study with different rigidities of the cover plate and shear moduli of the elastic film, Ghatak and Chaudhury found experimentally that

$$b_\mathrm{c} \propto \left(\frac{D}{G}\right)^{1/3}\ , \tag{4.43}$$

---

[2] Very recently, Arun *et al.* investigated the contact instability upon approach of an upper glass plate to a viscoelastic material in an electrical field [7]. In this study, the parameters are chosen in such way that the additional terms in equation 4.42 become important compared to $bk_\mathrm{c} = 2.12$. A transition from viscous to elastic behavior is reflected in a change of the wavelength of this surface instability.

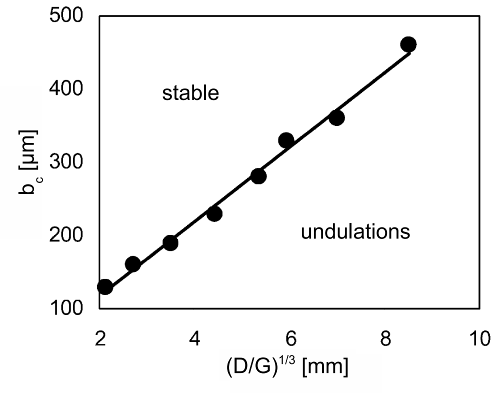

Figure 4.8.: In the peeling geometry, the critical thickness depends on the bending stiffness of the cover plate D and on the shear modulus of the film G, taken from [46].

as displayed in figure 4.8. This dependence has been explained theoretically in 2005 by Ghatak *et al.* [48] and in 2006 by Adda-Bedia and Mahadevan [1]. We follow here the line of argumentation of the latter reference, in which the peel geometry is investigated and not, as before, the plain strain geometry.

We consider again a peeling geometry where a plate with rigidity D is in contact with an elastomer with shear modulus G. For a relatively thick film, the peeling front is a straight line and does not show undulations. The cover plate shall be deformed by the small length δ over a lengthscale l_p. The deformations decay exponentially into the bulk of the elastomer, also with the typical lengthscale l_p. The penetration depth can be determined studying the energy balance in this situation. When the contact line is not moving, the bending energy per unit area in the plate is balanced by the bending energy per unit area in the elastomer,

$$D\frac{\delta^2}{l_\mathrm{p}^3} = G\left(\frac{\delta}{l_\mathrm{p}}\right)^2 l_\mathrm{p}^2\,. \tag{4.44}$$

From equation 4.44 it follows for the penetration depth that

$$l_\mathrm{p} \propto \left(\frac{D}{G}\right)^{1/3}\,. \tag{4.45}$$

If the film thickness b is decreased, at some point the deformations cannot decay over l_p anymore but are forced to decay over $b < l_\mathrm{p}$. This introduces a confinement parameter α:

$$\alpha = \left(\frac{D}{Gb^3}\right)^{1/3}\,. \tag{4.46}$$

For $\alpha \ll 1$, the system is unconfined, the film can relax deformations over l_p along its thickness and a straight peeling front is possible. On the other hand, for $\alpha \gg 1$, the penetration depth is b instead of l_p. This creates large stresses around the crack and the contact line explores other configurations to relieve the stored elastic energy. It turns out that shear formations are favored over normal (bulk) deformations. The energy cost for the creation of surface is compensated by the elastic energy released in the film, and the contact line prefers to undulate [1]. Performing a linear stability analysis, the authors were able to determine a critical wavenumber $k_c b \approx 1.85$ and a critical confinement $\alpha_c \approx 21$ above which the crack front is unstable. These values are in good agreement with experimental results from reference [46], $\alpha_c \approx 18$ and $k_c b \approx 1.57$.

The instabilities described above are observed in a *static* peeling geometry. However, the observation of fingering instabilities in a dynamic debonding situation has also been reported, for example in the situation of an adhesive layer debonded from a silicone substrate [57], a layer of latex (PEHA) debonded from steel [19], or in dynamic peeling [115].

Part II.

Materials and methods

5. Materials

In this Chapter, we present the sample preparation protocol and characterize in detail the properties of our model system, mainly by rheometry.

5.1. Preparation of the PDMS samples

The material we chose as a model system for this study is the *"Sylgard© 184 Silicone Elastomer Kit"* purchased at *Dow Corning*. It consists of a silicone oil (Poly(dimethylsiloxane) - PDMS) and a crosslinker (curing agent). Mixing the base with the crosslinker and curing under heat activation leads to the formation of chemical crosslink points between the polymer chains, see a schematic view in figure 5.1. Using 10% of curing agent yields a transparent, elastic material. Its conventional use is to be found in microfluidics. It is perfectly adapted to be cast into molds to produce channels on a micrometer scale, and also to make stamps and PDMS molds [124]. Since *"Sylgard 184"* is a commercial product, the exact formulation is not given by the manufacturer. This type of two component system however is typically composed of a polydisperse low molecular weight PDMS oil, functionalized with vinyl groups, and a crosslinking agent containing Si-H functions [5]. The reaction requires temperature and the presence of a Platinum catalyst. Using this system with an under-stoichiometric ratio of crosslinker allows us to make chemically stable networks with different degrees of crosslinking.

Preparation protocol

We used different percentages of crosslinker for our study. Percentages are given in weight percent relative to the absolute mass, as

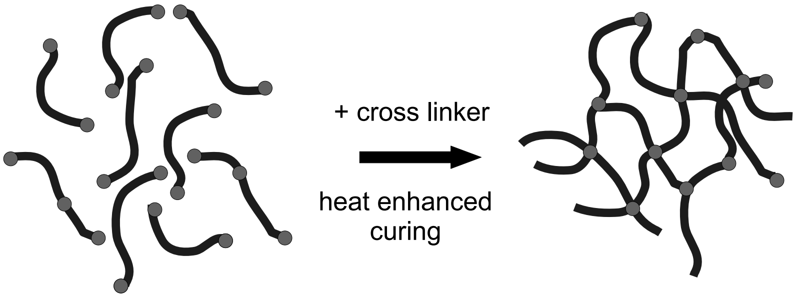

Figure 5.1.: Adding the curing agent to the oil base leads to the formation of crosslink points (covalent bonds) between the polymer chains.

$$\% = 100 \frac{m[\text{curing agent}]}{m[\text{curing agent}] + m[\text{silicone oil}]} \,. \tag{5.1}$$

We also defined a stoichiometry parameter r. 10% of curing agent corresponds to $r = 1$, that is, the fully cured material as defined by the manufacturer. It should be noted that this amount does probably not correspond to a true stoichiometric ratio since this type of silicone systems typically requires an excess of crosslinker [68]. The glass transition temperature of chemically pure PDMS lies well below room temperature ($T_\mathrm{g} \approx -120\,^\circ\mathrm{C}$). For Sylgard 184, we found $T_\mathrm{g} \approx -125\,^\circ\mathrm{C}$.[1] In the following we describe the exact protocol that has been established during the present work.

Weighing A certain amount of oil and curing agent are weighed using a precision scale to define a percentage following equation 5.1.

Mixing The oil and the curing agent are mixed with a magnetic mixer during 5 to 10 minutes, taking care to avoid any inhomogeneities.

Degassing As air is trapped in the sample during mixing, it is placed under vacuum at room temperature during about 30 minutes to degas until no bubbles are visible anymore.

Cleaning Microscope glass slides with dimensions 10 cm × 2.6 cm × 0.2 cm are precleaned with acetone and ethanol. Then a primer coat (*"Dow Corning 1200 OS"*) is applied on the glass slides. The coating enhances the PDMS's adherence to the glass and ensures for well defined conditions at the glass-PDMS contact.

Weighing The glass slides are weighed on a precision scale.

Depositing Applicators made of stainless steel by *Erichsen* with different gaps are used to deposit polymeric films on the precleaned glass slides.

Curing The samples are cured in a desiccator at 80 °C during five hours, again under vacuum to remove any air that has possibly been trapped when depositing the layer. It is important to control the curing time exactly to achieve reproducible material parameters. A longer curing time could influence the material properties at least for the less crosslinked PDMS.

Reweighing After cooling down, we reweigh the glass slides with the PDMS layer and measure the length and width of the layer to obtain its thickness.

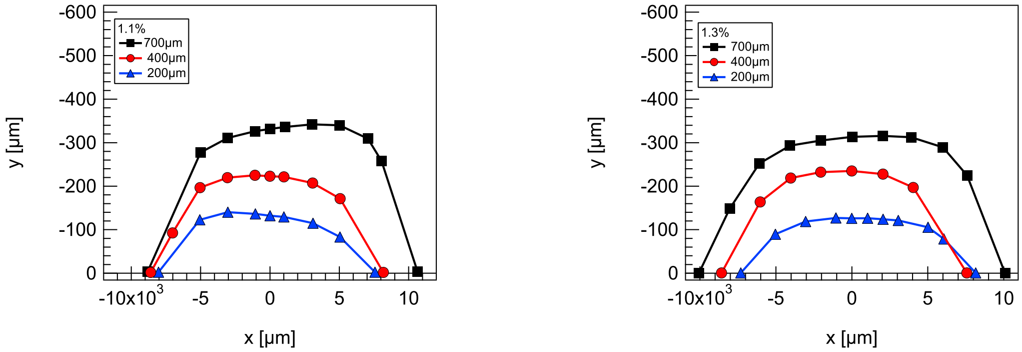

(a) 1.1% of curing agent.

(b) 1.3% of curing agent.

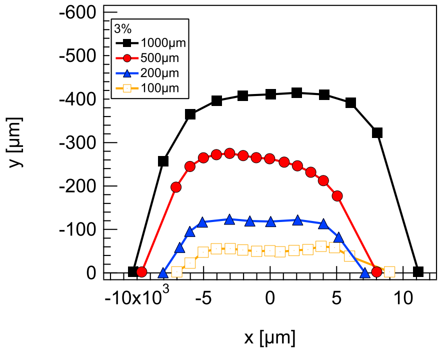

(c) 3.0% of curing agent.

Figure 5.2.: The sample shape as measured in a profilometer for different percentages and different applicator gaps. Note the different scalings in the width (x-direction) and height (y-direction).

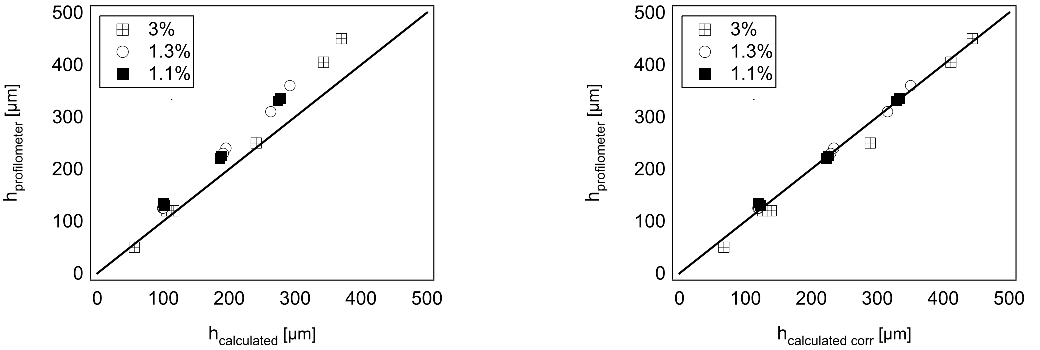

(a) Measured thickness versus calculated thickness.

(b) Measured thickness versus corrected calculated thickness.

Figure 5.3.: Comparison of the mean sample thickness from profilometer and weight measurements.

5.2. Characterizing the samples

5.2.1. Measurement of the thickness

To determine the sample thickness, we used first an optical profilometer, a technique exploiting interference fringes to determine height profiles.[2] Figure 5.2 shows the sample profiles as they were measured in the profilometer. x represents to the width of the samples, y the height. This method is very precise, but also laborious for a systematic examination of many samples. We decided instead to calculate the thickness from the polymer layer's mass and dimensions. Therefore, we weighted the glass slides with and without the PDMS layer. Measuring the layer's width w and length l, and presuming a density of 1000 kg/m³ for PDMS, we calculated the thickness following[3]

$$h[\mathrm{m}] = \frac{m_{\mathrm{PDMS}}[\mathrm{kg}]}{l[\mathrm{m}] \times w[\mathrm{m}] \times \rho_{\mathrm{PDMS}}[\mathrm{kg/m^3}]} . \tag{5.2}$$

Figure 5.3(a) shows the relation between the mean thickness measured in the profilometer and calculated from the sample weight. Systematically, the calculated values are too small. For the calculation in equation 5.2, the section of the PDMS layer was assumed as rectangular. This is not true as the edges are smoothed out, and the height is underestimated. We included in equation 5.2 an empirical correction factor $h_{\mathrm{corr}} = 1.2\, h_{\mathrm{calc}}$. Figure 5.3(b) shows that this correction yields calculated thicknesses in accordance with the results from profilometer measurements.

---

[1] Differential Scanning Calorimetry (DSC) at a cooling rate of 10 °C/min. In collaboration with F. Martin, PPMD, ESPCI.

[2] In collaboration with A. Prevost, ENS.

[3] The specific gravity is 1.03 following the datasheet provided by the manufacturer.

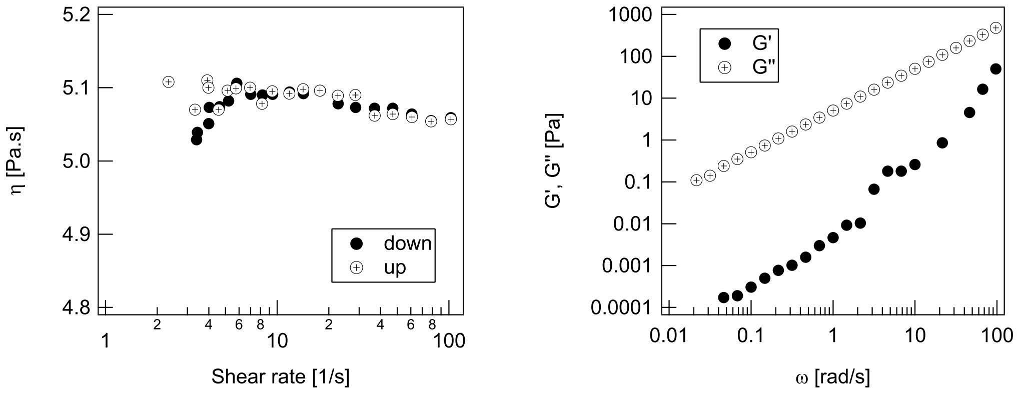

(a) The viscosity does not depend on the shear rate.

(b) Storage and loss modulus as a function of the frequency ω.

Figure 5.4.: The shear viscosity, storage, and loss modulus for the non-cured silicone oil (cone-plate geometry, $d = 60\,\mathrm{mm}, \theta = 1°$).

5.2.2. Linear rheological measurements

To characterize the samples further, we determined their linear rheological characteristics.

The non-crosslinked silicone oil Sylgard 184

We measured the rheological characteristics of the pure silicone oil Sylgard 184 without curing agent in a *Haake RS 100 Rheostress* rheometer. The measurement geometry was plate-cone, with a cone diameter $a = 60\,\mathrm{mm}$ and an angle $\theta = 1°$. The shear viscosity was measured as a function of the shear rate. The shear viscosity is independent of the shear rate and equal to 5.1 Pa s, see figure 5.4(a). To have an estimate of the oil's elasticity, we performed oscillatory strain and frequency sweeps. Figure 5.4(b) shows that the storage modulus G' lies one to three decades under the loss modulus G'' in the investigated range of frequencies $0.02\,{}^{\mathrm{rad}}\!/\mathrm{s} < \omega < 100\,{}^{\mathrm{rad}}\!/\mathrm{s}$. G' becomes more important for higher frequencies $\omega \approx 100\,{}^{\mathrm{rad}}\!/\mathrm{s}$, but still the liquid behavior dominates the system. G'' follows clearly a power law. A fit yields $G'' = (5.31 \pm 0.05)\,\omega^{0.98 \pm 0.002}$. The prefactor 5.31 is close to the shear viscosity 5.1 Pa s from constant shear measurements, the exponent is $0.98 \approx 1$ as expected for a Newtonian liquid.

Crosslinked materials

We performed shear oscillatory measurements on all materials to determine the storage modulus G' and the loss modulus G''. We used a strain controlled *TA ARES* rheometer equipped with a Peltier heating unit and a water cooling system to provide a constant measurement temperature.[4] The measurement geometry was plate-plate with a diameter $a = 25\,\mathrm{mm}$ and a gap width $b = 0.5\,\mathrm{mm}$. The measurement protocol was as follows.

The rheometer was heated at 80 °C during at least 30 minutes to be sure to have reached the curing temperature. We mixed and degassed the PDMS as described in section 5.1 and put then a small volume of the material on the lower rheometer plate. The upper plate was instantly lowered to the measurement position $b = 0.5\,\mathrm{mm}$. Then we cured the material for five hours. Afterwards, we decreased the temperature to the measurement temperature $T = 25\,^\circ\mathrm{C}$ and waited again at least 45 minutes to reach a homogeneous temperature in the sample volume. First we performed a strain sweep: We measured G' and G'' at constant frequency ($\omega = 6.28\,\mathrm{rad/s}$) for different values of the maximum strain amplitude γ_0. This measurement is necessary to place oneself in the region of linear response where G' and G'' do not depend on the strain amplitude. In this way we chose for the frequency sweep the maximum strain value $\gamma_0 = 10\%$ that lies in the linear region for all materials. Finally we performed a frequency sweep, starting at $\omega = 100\,\mathrm{rad/s}$ and going down to $\omega = 0.01\,\mathrm{rad/s}$. In this way, we had access to the material properties as a function of the frequency.

Figure 5.5 shows some typical curves for G' and G'' from frequency sweep tests for materials with curing agent content from 0.9% up to 10%. From these curves, one can follow the change in the viscoelastic properties. The materials with 0.9% and 1.0% have a G'' that is higher than G', however the difference between them is less than a decade. Adding 1.1% of curing agent, G'' is only slightly higher than G' ($G'' \approx 1.6G'$). The two moduli are parallel over the whole range of frequencies, indicating that the system is very close to the gel point [121]. At a percentage of 1.2% of curing agent, the system is clearly above the gel point. G' reaches a plateau value at small frequencies. Adding more curing agent increases the value of the plateau modulus ever more. At around 1.6% of curing agent, the gap between G' and G'' becomes more important. From 2% on, G' is practically constant over the whole range of tested frequencies and increases strongly with the amount of curing agent. G'' however remains frequency-dependent. For all materials from 1.2% of curing agent on, the dissipation is more important with increasing frequency.

For practical application, G' and G'' can be fitted with a power law. We fitted the storage modulus with $G'(\omega) = \mathrm{y}_0 + \mathrm{A}\,\omega^{\mathrm{pow}}$ and the loss modulus with $G''(\omega) = \mathrm{A}\,\omega^{\mathrm{pow}}$. Table 5.1 gives a reference of the fit parameters and the error as $+/-$ one standard variation for all viscoelastic materials. Note that the data for the PDMS with 10% of curing agent have not been obtained in the *ARES* rheometer, since the stresses were too high. We used a DMA technique instead. This technique involves oscillatory elongational measurements. In figure 5.5, G' and G'' for 10% of curing agent have been calculated from the elongational moduli supposing an incompressible material and a Poisson's ratio of 0.5. Then, the corresponding value of the shear modulus is obtained dividing the elongational moduli by 3.

---

[4] In collaboration with G. Ducouret, PPMD, ESPCI.

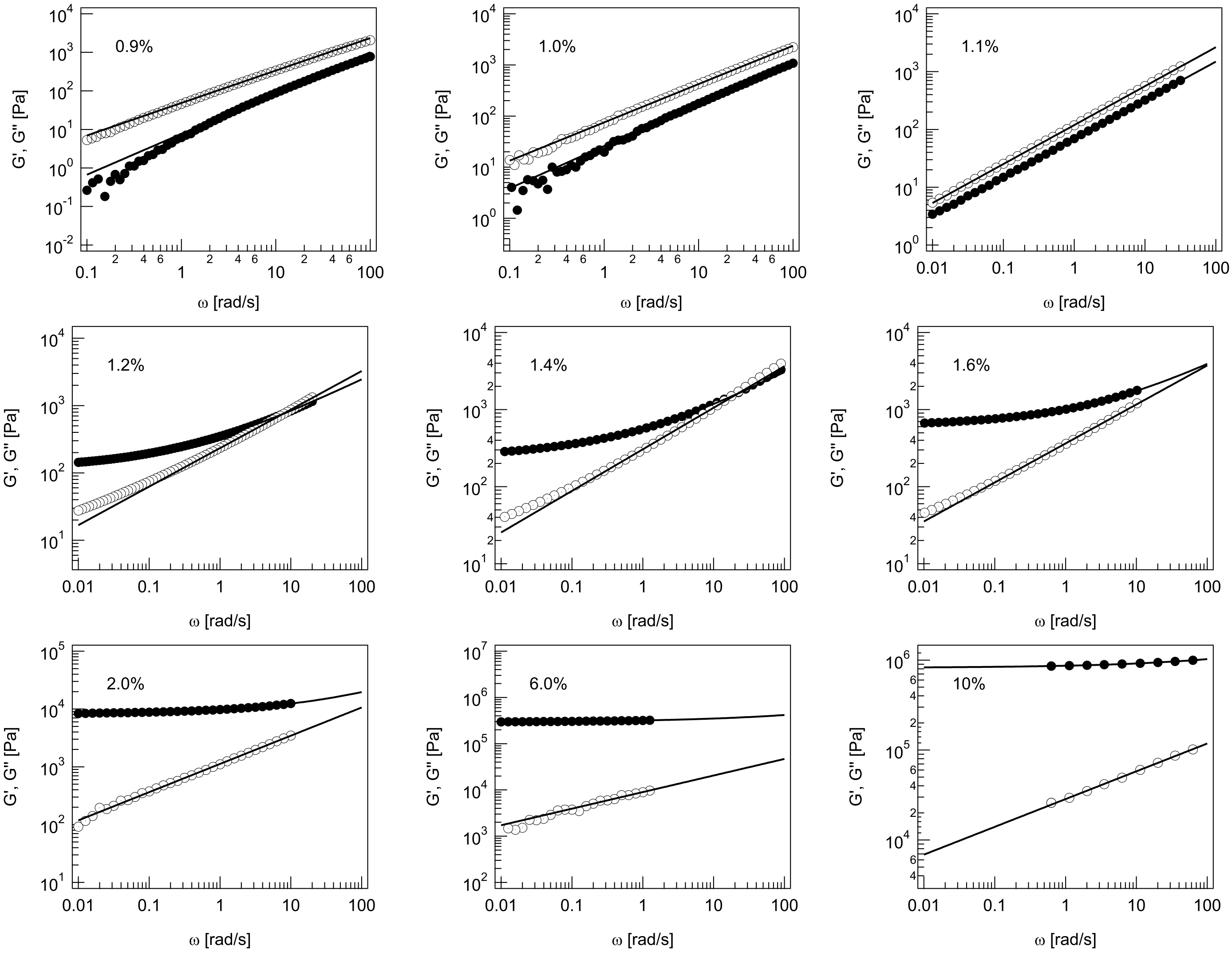

Figure 5.5.: Storage modulus and loss modulus versus frequency for different degrees of crosslinking.

Percentage		y_0	stdv y_0	A	stdv A	pow	stdv pow
0.9%	G'	0	0	7.66	0.0601	1.059	0.0034
	G''	0	0	48.47	0.106	0.8424	0.001
1.0%	G'	0	0	25.92	0.157	0.827	0.0024
	G''	0	0	75.23	0.164	0.749	0.0009
1.1%	G'	0	0	69.312	0.043	0.665	0.0005
	G''	0	0	118.67	0.0712	0.674	0.0005
1.2%	G'	130.65	0.537	215.95	0.62	0.515	0.0009
	G''	0	0	233.49	0.754	0.572	0.0014
1.3%	G'	202.22	0.196	287.7	0.281	0.483	0.0004
	G''	0	0	290.8	0.706	0.533	0.0014
1.4%	G'	250.61	0.936	310	1.35	0.479	0.0017
	G''	0	0	304.77	2.05	0.539	0.0033
1.6%	G'	624.14	1.05	385.35	1.58	0.466	0.0019
	G''	0	0	363.31	2.1	0.506	0.0037
1.8%	G'	7903.4	35.1	1287.6	41.9	0.396	0.0091
	G''	0	0	1422.3	35.5	0.29	0.011
2.0%	G'	8248.7	6.26	1515.1	7.82	0.438	0.002
	G''	0	0	1121.5	2.72	0.488	0.0015
2.5%	G'	16500	18.2	2171.1	24.9	0.403	0.005
	G''	0	0	973.43	15.5	0.578	0.0102
3.0%	G'	48076	61.7	5168.9	67	0.384	0.0036
	G''	0	0	2564.2	23.4	0.452	0.0055
6.0%	G'	291300	691	27249	686	0.332	0.0128
	G''	0	0	8977.5	90.3	0.359	0.0089
10.0%	G'	820350	1620	45491	1450	0.327	0.0058
	G''	0	0	28476	342	0.309	0.0037

Table 5.1.: Fit parameters to a power law $y = \mathrm{y}_0 + \mathrm{A}\omega^{\mathrm{pow}}$ for the storage and loss modulus of all materials.

5.2.3. Traction

We performed traction experiments on the PDMS samples to gain information about the non-linear behavior and also to have an additional measure of the elastic modulus. We used an *Instron 5565* traction machine on the predominantly elastic samples, that is, on PDMS with 2%, 3%, 6%, and 10% of curing agent, corresponding to $r = 0.2,\ 0.3,\ 0.6$, and 1. It was not possible to produce samples for the traction machine from the less crosslinked materials, as they were simply too soft and sticky to be removed from the molds. The sample size was about $15\,\mathrm{mm} \times 5\,\mathrm{mm} \times 0.5\,\mathrm{mm}$. The traction tests were performed at an initial elongational frequency of $1\,{}^{1}\!/\!_{\mathrm{s}}$ until rupture of the sample. For $r = 0.6$ and $r = 1$, the test was stopped before rupture, as the sample was gliding out of the sample holder. Figure 5.6 shows the nominal stress (the force divided by the initial cross section) versus the relative deformation. The linear elastic modulus can be determined from the initial slope. At higher deformations, the traction curves yield information about the non-linear behavior of the samples. For 6% and 10% of crosslinker, we observe an important strain hardening behavior for small deformations $\epsilon \approx 100\%$. In other terms, the force increases strongly with the deformation. This is a typical signature of well crosslinked materials.

We also performed hysteresis tests where the sample was stretched until a maximum deformation and then brought back to the initial deformation. For these tests, the deformation frequency was $0.1\,{}^{1}\!/\!_{\mathrm{s}}$ with $\epsilon_{\mathrm{max}} = 200\%$ for $r = 0.3$ and $\epsilon_{\mathrm{max}} = 80\%$ for $r = 0.3$, $r = 0.6$, and $r = 1$. The last three graphs in figure 5.6 show the very weak hysteresis, which corresponds to the small dissipation in these elastic materials.

5.2.4. Sol content

In an elastomer, not all polymer chains are necessarily crosslinked with each other. The term “gel” denotes the fraction of crosslinked chains. The uncrosslinked chains form the soluble part, the so-called “sol”. We determined the sol content of the elastic materials according to the following protocol. We cut small PDMS pieces of mass m_0 and let them swell in toluol for several days to rinse out the non-crosslinked chains. Afterwards, we collected all the material in a paper filter and let it dry at ambient temperature for several days again. Afterwards, short heating at 80 °C made sure that all the solvent had evaporated. We weighed the PDMS samples again and calculated the relative mass loss as

$$\frac{\Delta m}{m_0} = \frac{m_{\mathrm{after}} - m_0}{m_0}\,. \tag{5.3}$$

Figure 5.7 shows the relative amount of soluble polymer for different amounts of curing agent. For the fully cured material with 10% of curing agent, about 3% of the chains can be washed out, confirming that most of the chains are crosslinked. For $r = 0.2$, about 42% of the initial mass is lost, meaning that only about 50% of all polymer chains are attached to the network.

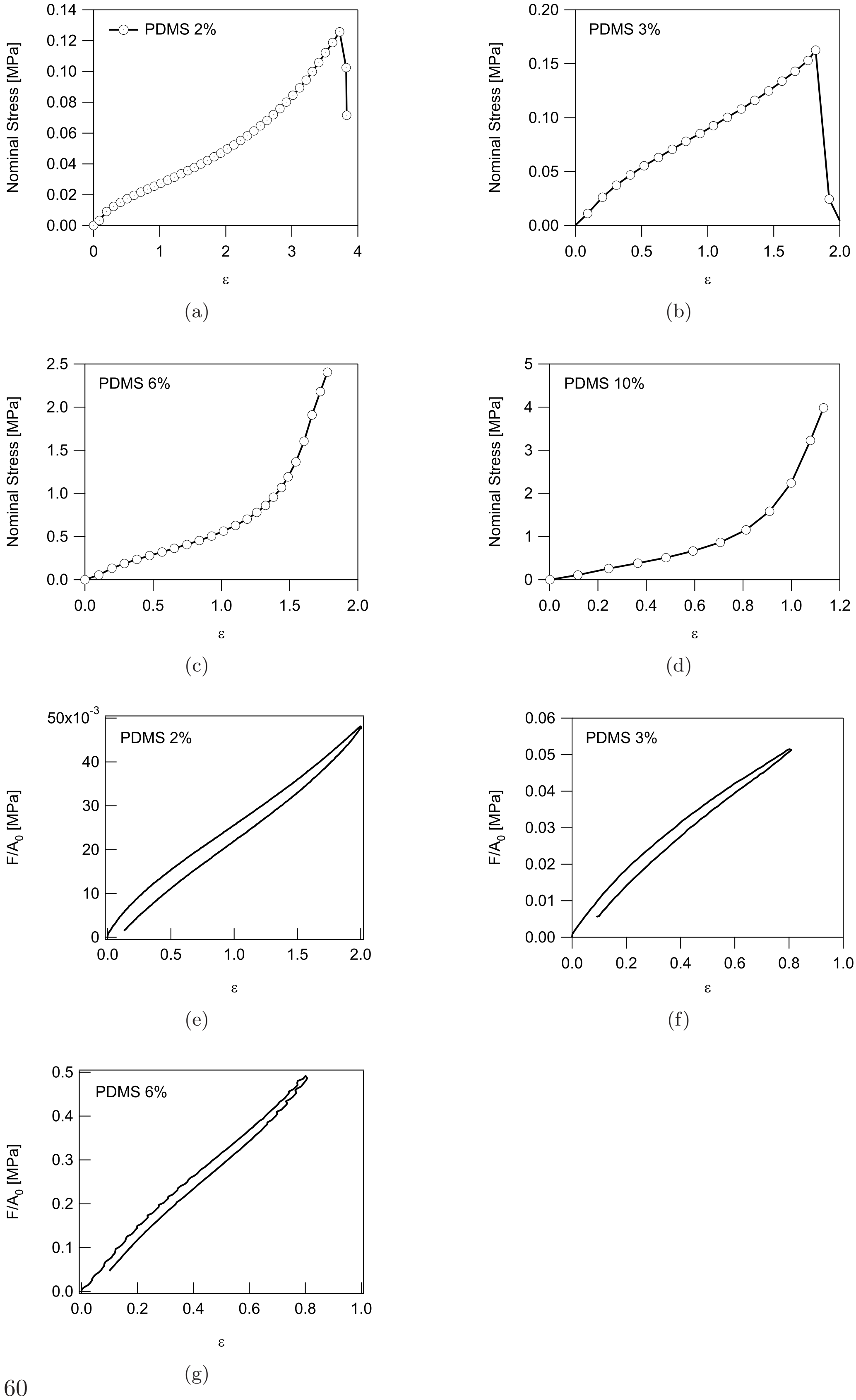

(a) (b) (c) (d) (e) (f) (g)

Figure 5.6.: Nominal stress versus deformation in traction and hysteresis experiments on PDMS with different amounts of curing agent.

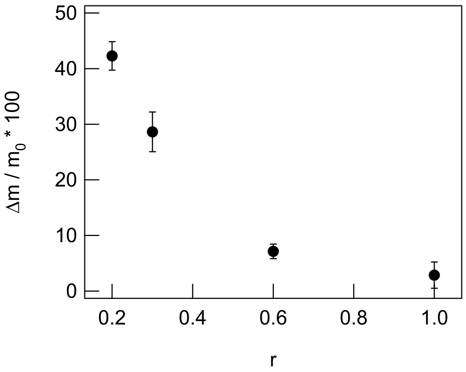

Figure 5.7.: The relative amount of soluble polymer as a function of the crosslinker amount r.

5.3. Liquid-solid transition varying the number of crosslink points

Summarizing our results so far, we prepare layers of PDMS with different degrees of crosslinking on microscope glass slides. The PDMS model system we use consists of short polymer chains. In its non-crosslinked state, it behaves essentially as a Newtonian liquid, with almost no viscoelasticity. When adding the crosslinker, a network is formed. Adding more and more curing agent increases the number density of crosslink points and introduces viscoelasticity. Figure 5.8 displays storage and loss modulus, complex modulus, and $\tan\delta$ for three typical percentages of curing agent. Adding only a small amount of curing agent, namely 1.1%, the material reaches its gel point, indicated by the fact that the storage and loss moduli are almost the same and parallel over a large range of frequencies. When the crosslinker content is increased, small interconnected “patches” of crosslinked networks are formed, and the material stops flowing since the network percolates. Above the percolation threshold, the PDMS becomes a network swollen by short polymer chains. The more crosslinker is added, the more polymer chains contribute to the network elasticity, thus the elastic modulus increases strongly. The elastic modulus remains nearly independent of the frequency above a curing agent content of about 2%. The loss modulus increases however strongly with the frequency. Since the starting PDMS chains are short, they never formed entangled chains, which provide specific dissipation mechanisms and nonlinear behavior when high molecular weight polymers are crosslinked as in PSAs.

Figures 5.9(a) and 5.9(b) show the change in the elastic modulus and in $\tan\delta$ with increasing curing agent amount. The elastic modulus was determined from oscillatory shear measurements. Assuming a Poisson’s ratio of 0.5, the elastic modulus was calculated as $E = 3G_0$, G_0 being the plateau value at low frequencies. Figure 5.9(a) includes only materials that display this plateau at low frequencies, that is, materials with $r \geqslant 0.12$. E increases strongly with r until $r \approx 0.3$, afterwards

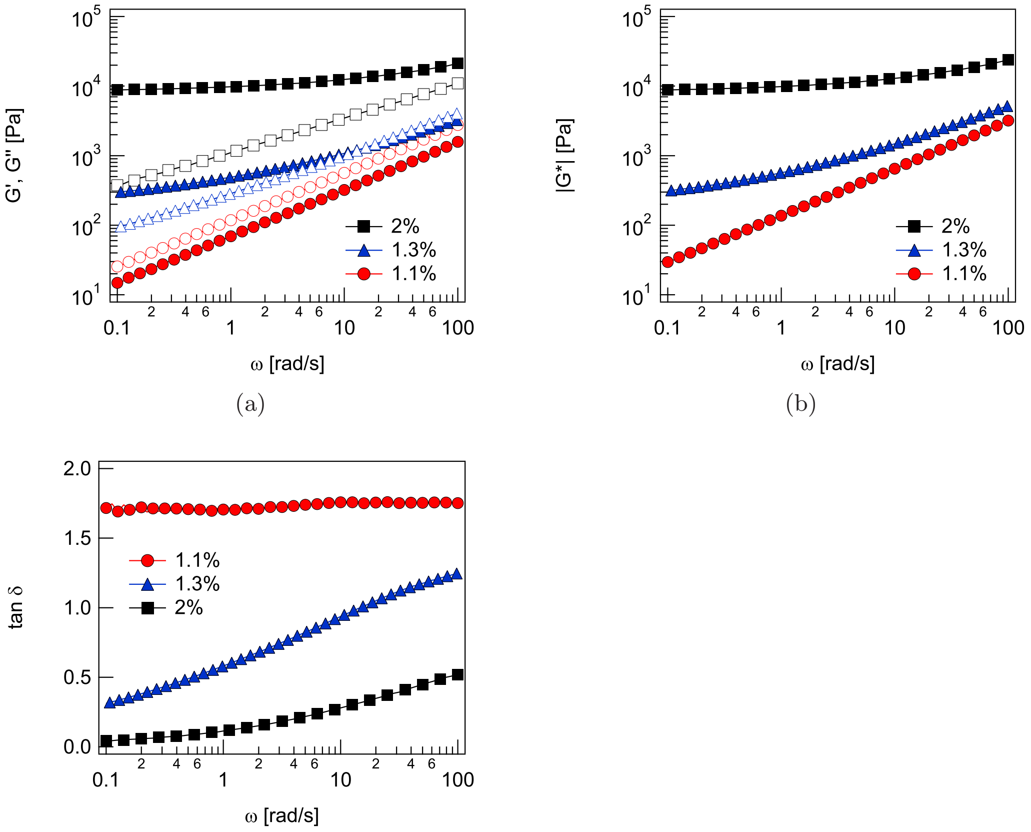

(a)

(b)

(c)

Figure 5.8.: Comparison of G' (full symbols) and G'' (open symbols), $G^\star$, and $\tan\delta$ for different percentages of curing agent.

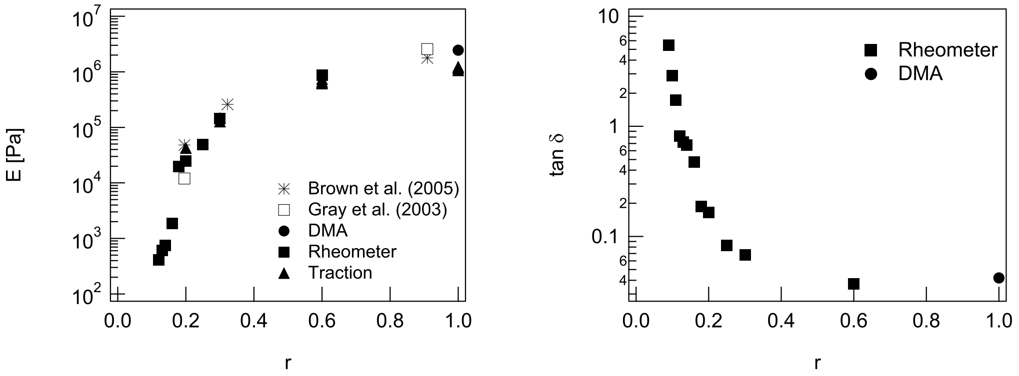

(a) The elastic modulus as a function of the crosslinker amount from different sources.

(b) $\tan\delta$ as a function of the crosslinker amount.

Figure 5.9.: Elastic modulus and $\tan\delta$ as a function of the curing agent content.

the increase slows down and E finally saturates. This graph combines results from traction measurements, oscillatory shear measurements, and traction measurements from the literature [51, 15]. Figure 5.9(b) shows how $\tan\delta = G''/G'$ varies with increasing crosslinker amount. We represent $\tan\delta$ at fixed frequency $\omega = 2.36\,\mathrm{rad/s}$. $\tan\delta$ is close to 1 at the gel point. It decreases strongly for $r \lesssim 0.2$ and evolves little for $r \gtrsim 0.2$.

5.4. Varying the rheological properties

To access a larger range of moduli and vary the storage and the loss modulus independently, we tempted to change the rheological properties of two chosen materials by different means. First, we investigated the temperature dependence in a range between 5 °C and 60 °C, second we added lower viscosity oils into the preparation. Both approaches are discussed in the following.

Dependence on the temperature

We performed rheological measurements as a function of temperature for two specific materials, PDMS with 1.1% and 1.3% of curing agent. The protocol for these measurements was as described before, but we performed several frequency sweeps at different temperatures on the same sample. First we cured the sample in the rheometer at 80 °C. Then we cooled down to 60 °C, waited for the sample to adapt to the new temperature, and performed a first frequency sweep. In this way, we went down to $T = 5\,^\circ\mathrm{C}$ in several steps, measuring G' and G'' at each temperature step. To exclude changes in the sample conformation during the temperature changes, we then heated up again comparing the results at each temperature. The data when cooling down and heating up were in perfect agreement.

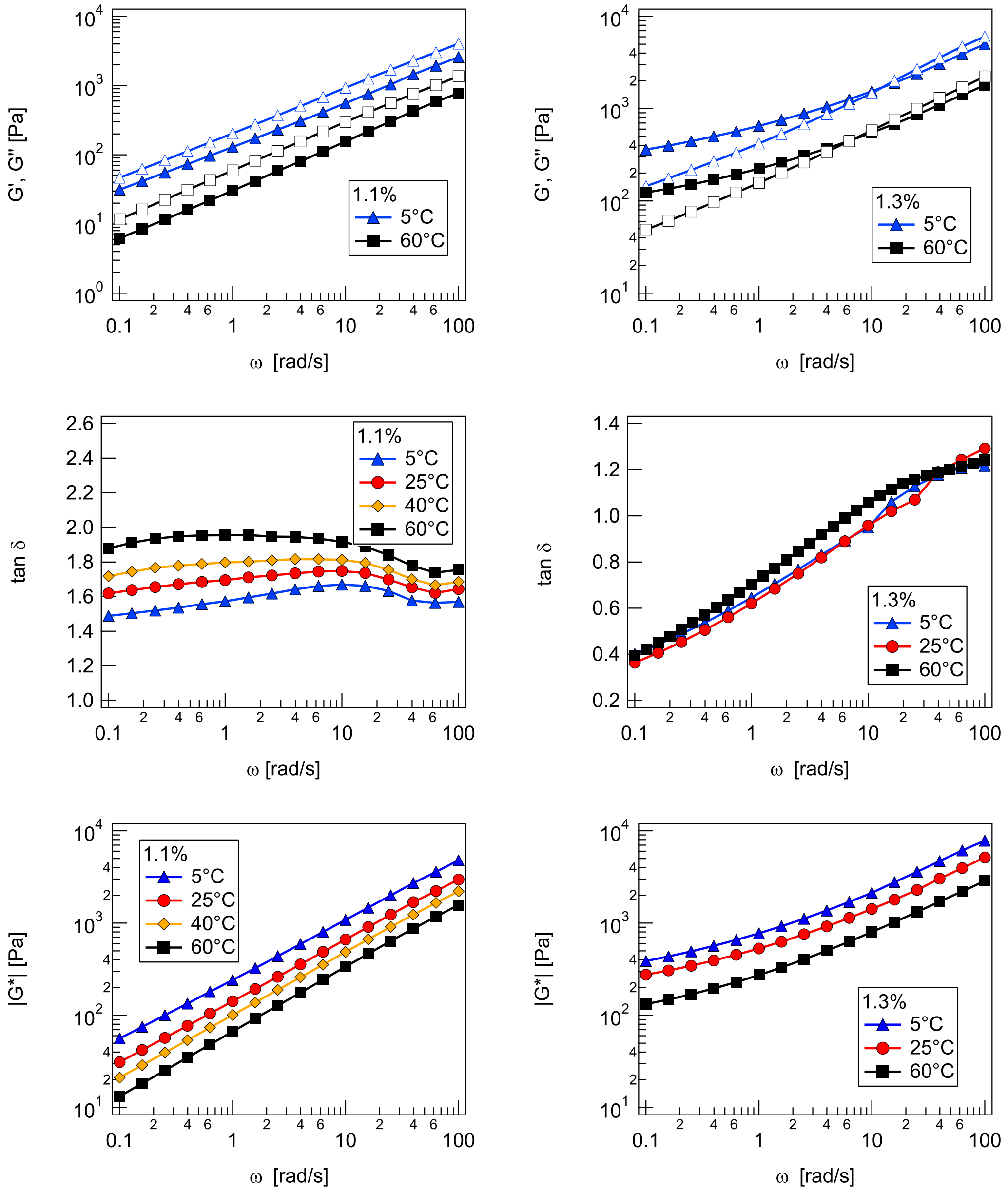

Figure 5.10.: G', G'' (filled and open symbols in the top row), $\tan\delta$, and $|G^\star|$ as a function of ω in a temperature range between 5 °C and 60 °C.

Figure 5.10 shows the results for G', G'', $\tan\delta$, and $|G^\star|$ as a function of ω in a temperature range between 5 °C and 60 °C. The complex modulus decreases with increasing temperature for both of the investigated materials, albeit weakly. For $r = 0.13$, $\tan\delta$ shows virtually no dependence on the temperature in the studied range, indicating that the storage and the loss modulus are shifted in parallel. For $r = 0.11$, $\tan\delta$ increases slightly with increasing temperature, the material becomes slightly more dissipative for higher temperatures. To conclude, for $r = 0.13$, the complex modulus can be changed by about a factor of 4 while keeping $\tan\delta$ constant if the temperature is varied between 5 °C and 60 °C. For $r = 0.11$, the complex modulus changes as well by a factor of 4, but $\tan\delta$ varies at the same time. Note that, even though the data are reproducible, the time-temperature superposition does not work for these materials. This indicates that the formula of the commercial Sylgard 184 has additional compounds that might induce internal changes in the structure of the polymer network.

Mixing different oils

We wanted to vary G' and G'' of an elastic material independently and investigated thus the changes the material experiences when adding a silicone oil of different viscosity to the preparation. In the following, we are studying a material with 2% of curing agent (CA) relative to the total mass. We partially replaced the silicone oil from the commercial kit ($\mathrm{oil}_{\mathrm{Sylgard}}$, $\eta = 5.1\,\mathrm{Pa\,s}$). We added to the oil part of the mixture two different oils ($\mathrm{oil}_{\mathrm{add}}$) with viscosities $\eta_1 = 1\,\mathrm{Pa\,s}$ and $\eta_2 = 0.1\,\mathrm{Pa\,s}$, respectively. The following relations were respected,

$$\frac{m[\mathrm{CA}]}{m[\mathrm{CA}] + m[\mathrm{oil}_{\mathrm{Sylgard}}] + m[\mathrm{oil}_{\mathrm{add}}]} = 2\% \tag{5.4}$$

and

$$\frac{m[\mathrm{oil}_{\mathrm{add}}]}{m[\mathrm{oil}_{\mathrm{Sylgard}}] + m[\mathrm{oil}_{\mathrm{add}}]} = 20\%\ . \tag{5.5}$$

Figure 5.11 shows how G', G'', $|G^\star|$, and $\tan\delta$ vary with the addition of lower viscosity oils. We find that G' stays constant. A constant plateau value of G' at low frequencies is attributed to the fact that the number of crosslink points is not changed by the addition of the lower viscosity oils. The loss modulus G'' however decreases with decreasing viscosity of the added oil, as less energy is dissipated. Since G' is about two decades higher than G'', the complex modulus is not influenced by the changes in G'' and varies only slightly. On the contrary, $\tan\delta$ varies by about a factor of 4.

In conclusion, partly replacing the oil by a less viscous oil modifies the loss modulus but not the storage modulus. Put in other terms, the complex modulus stays constant and the dissipation in the material is changed. Stronger variations might be achieved by replacing a higher fraction of the oil.

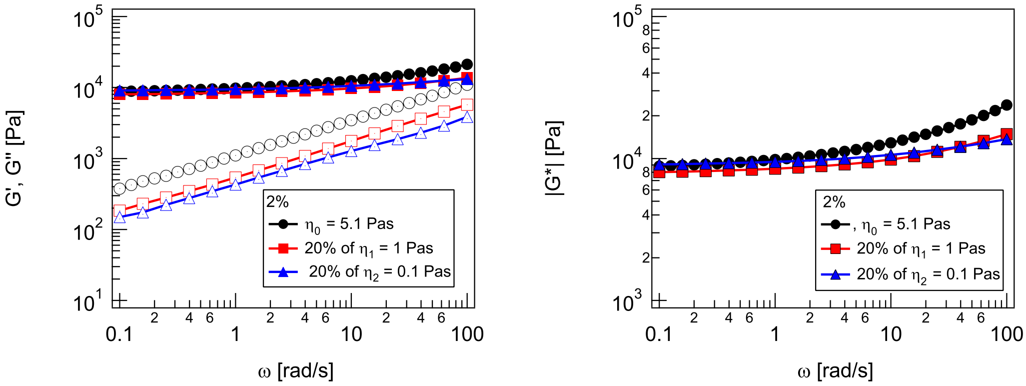

(a) G' and G'' versus ω.

(b) $|\eta^\star|$ versus ω.

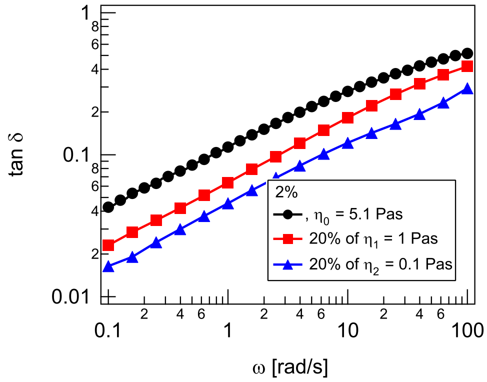

(c) $\tan\delta$ versus ω

Figure 5.11.: The rheological properties G' (filled symbols), G'' (open symbols), $|G^\star|$, and $\tan\delta$ of PDMS with $r = 0.2$ when the silicone oil $\eta = 5.1$ Pa s is partially replaced with lower viscosity oils.

6. Experimental setup and image treatment

In this Chapter, we present in more detail the experimental setup and the techniques of image analysis.

6.1. The probe tack test

We performed most of the experiments on a custom-made "probe tack" machine that has been designed in the laboratory [58]. The principles of the probe tack test have been developed by Hammond in 1964 [53] and in 1985 by Zosel [129]. It is a strong tool for characterizing the performance of a soft adhesive. The principle of the test is to approach a flat-ended cylinder (or a hemisphere with a large radius of curvature), called the probe, to an adhesive or viscoelastic layer of thickness b_0. After a certain contact time, the probe is retracted at a controlled debonding speed v. During the test, the normal force on the probe as well as the probe displacement are monitored. Figure 6.1(a) shows the force as a function of time during the experiment, figure 6.1(b) the convenient representation as stress-strain curves. The stress σ is the nominal stress, that is, the normal force on the probe divided by the maximum contact area before the probe is pulled away. The strain ϵ is defined as the probe displacement d divided by the initial film thickness b_0.

The typical test protocol is described in the following. In the case of solid samples, the probe is approached to the layer at speed v_{approach} until the force $F_{\max}$ is reached. The contact between probe and adhesive takes place when the force gets negative for the first time. During the contact time, the force can change due to relaxation processes. When the probe pulls on the adhesive layer, the force increases, reaches zero and then becomes positive. As the mechanical setup has necessarily a certain compliance, the apparatus itself is stretched first before the material starts to move. The peak in the force curve is caused by an overlay of the increasing force due to the stretching of machine and adhesive, and a decrease in the force as stresses are relaxed in the sample. The stretching of the apparatus has been investigated for example by Francis and Horn [43]. Somewhere around the peak value, the adhesive starts to be deformed, air penetrates into the layer, and patterns are formed. These patterns can be cavities or air fingers penetrating into the bulk of the adhesive or at the interface between probe and adhesive. Cavities have been the topic of many studies, [66, 21, 92, 20], but are not investigated in the present thesis. As the patterns appear, stresses are relaxed in the layer and the force decreases. During debonding, fibrils, that is, material bridges between probe and adhesive, can be

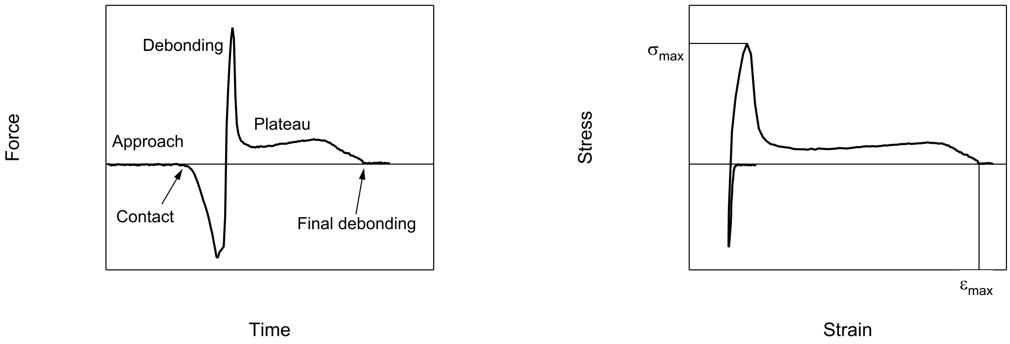

(a) The force as a function of time in the probe tack test.

(b) The stress as a function of strain in the probe tack test.

Figure 6.1.: Typical force-time and stress-strain curves in the probe tack test.

formed and stretched over a long distance. The final debonding can be *adhesive*, meaning a complete detachment from the probe without any residues on the probe surface, or *cohesive*, meaning a break up in the middle of the fibrils with residues on the probe surface. This final debonding marks the end of the test. By means of the stress-strain curves, the adhesion energy W_{adh} of a material can be determined under well-defined conditions. W_{adh} is the energy per unit area needed to debond the probe from an adhesive layer with thickness b_0,

$$W_{\mathrm{adh}} = b_0 \int_0^{\epsilon_{\max}} \sigma(\epsilon)\, d\epsilon \ . \tag{6.1}$$

The force and displacement is not the only information gathered during the experiment. The whole debonding process is visualized from above via a camera. This additional information allows for a qualitative characterization of the pattern formation during the debonding. Furthermore, the $2D$ projection the contact area can be determined.

Setup

The "µ-tack" setup has been developed in the laboratory by Josse *et al.* [58]. It has a slightly different approach concerning the testing protocol. In this set up, the contact of probe and sample is established in the conventional way by moving a circular indenter towards an adhesive layer at a constant speed v_{approach} until $F_{\max}$ is reached. After the contact time t though, the probe is not lowered but instead, the table holding the sample is moved upwards. Of course the relative motion of probe and tested layer is the same in both protocols. Yet the "alternative" protocol has two advantages. First, the motion is realized here with step motors, which have a certain slack. Moving the motors only in one direction prevents uncertainties in the displacement measurement caused by the mechanical slack when the motor changes

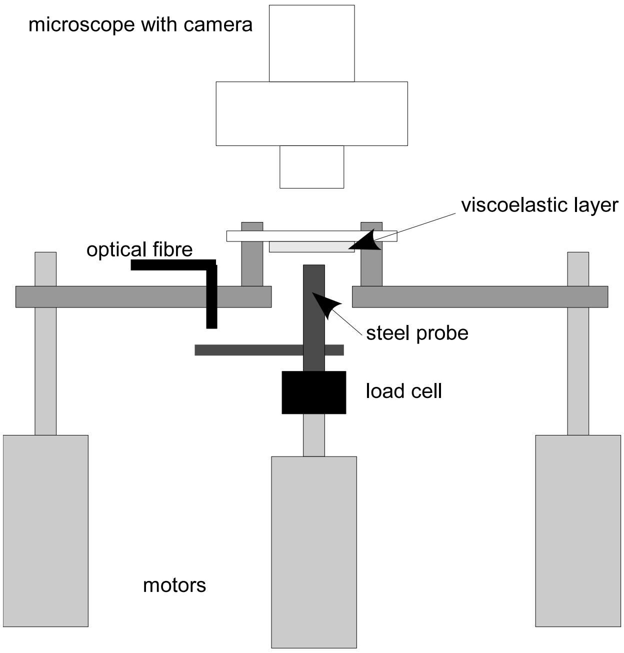

Figure 6.2.: Schematical view of the μ-tack setup.

direction. The second advantage of moving the sample holder during the debonding is that the camera focus remains fixed on the probe surface. In that way, sharp pictures are provided during the whole test. Figure 6.2 shows a schematical view of the apparatus. It features a stepping motor in the middle that moves the probe and three stepping motors that move the table on which the sample is fixed. An optical fibre measures the relative displacement of probe and table, and a load cell the force on the probe. Finally, a camera mounted on a microscope ensures good visualization quality. The table with the fixed sample can be tilted via three screws to align the probe surface and the adhesive layer. Good alignment is crucial for having a maximum contact area between probe and adhesive.

The displacement is measured by an optical fibre that measures intensity variations in the reflection of infrared light. In the present setup, the optical fibre is fixed to the sample holder, and the reflecting silicone waver is fixed directly to the probe. In this way, the measured displacement corresponds to the distance between probe and sample table. The displacement has three contributions: the deformation of the adhesive layer, the deformation of the glass slide, and the deformation of the sample holder. The net displacement of the adhesive can be calculated measuring the compliance of the apparatus and the bending of the glass slide. More details of the apparatus and in-depth considerations concerning its compliance are given in references [57] and [19]. We shall only recall here the specifications of the material:

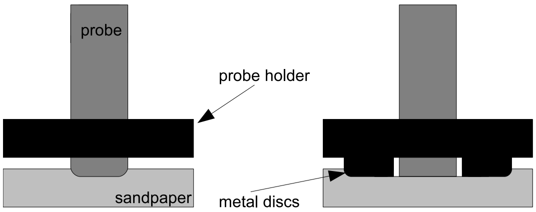

Figure 6.3.: The probe edges are protected with small metal discs during the polishing.

- microscope glass slides (10 cm × 2.6 cm × 0.2 cm) with a bending compliance of 0.3 µm/N purchased at *Preciver*,
- a *Zeiss* microscope with a *Zeiss Epiplan Neofluar* x1.25 objective,
- a *Philtec D63 LPT* optical fibre (equipped with an infrared laser) with a resolution of 0.4 µm,
- *Physik Instrumente* step motors with optical encoders and a resolution of about 100 nm,
- a *Entran* load cell working between −50 N and +50 N with a precision of 0.02 N,
- two different cameras: a digital *Marlin Allied Vision Technologies* camera with an acquisition rate of 12 frames/s and an image resolution of 1392 x 1040 pixel, and a *Pulnix* CCD camera with 25 frames/s and an image resolution of 768 x 567 pixel.

Probes

We used probes made of stainless steel and mostly with a diameter of 6 mm. In Chapter 10, we also used probes with a diameter of 3 mm and 10 mm. A crucial part in the probe preparation process was the polishing. The probes were polished in a *Mecapol P 220U* polishing machine with sandpaper with roughnesses going gradually down to a mirror surface. The last grain size was about 5 µm. The probes have to fulfil several requirements. First, the surface has to be normal to the probe axis and absolutely flat. The flatness is important for a good contact to the adhesive layer. In Chapter 7 we study the pattern formation that takes place at the very edge of the probe. Therefore, a high quality of the probes was crucial. We needed very sharp edges and borders with no roughnesses to prevent any influence on the pattern formation. The sharp edges are important as the probe is illuminated from above through the microscope. Any curvature at the borders leads to a reflection of the light at an angle $\neq 90\,^\circ$, the light cannot be collected by the microscope lens, and the visual information right at the borders is lost. Polishing the probes without protection entails rounded edges as the polishing plate with the sandpaper is not perfectly rigid, see figure 6.3. For protection we glued small metal discs around the

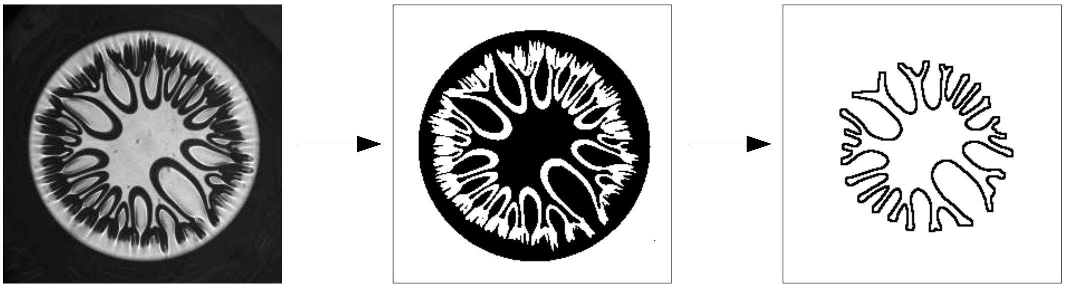

Figure 6.4.: The original image is binarized applying a threshold. Thereafter, the outline is saved as pairs of xy-values.

probes during the polishing. The discs stretch the sandpaper over the whole probe surface; the resulting probe edges are at an angle of almost 90 °.

The final polishing protocol is described in the following. We put 6 probes in a costum-made probe holder. Then we glued small metal discs around the probes with a commercial cyanoacrylate glue. After drying, we polished with the roughest sandpaper with a grain size of about 150 µm until the disc level was reached, then we went gradually down to smaller grain sizes until 5 µm. We polished about 4×2.5 minutes per sandpaper, using two papers per roughness, and rinsed abundantly with water before going to a smaller grain size. After the polishing, the whole probe holder was put in acetone over night so that the small discs could be removed easily without damaging the probe surfaces.

6.2. Image treatment

In this section, we present briefly our methods of images treatment. First, an image sequence is opened using the free software *ImageJ*.[1] The functions of this software can be expanded as it is possible to write *macros* in an implemented macro language or *plugins* in the common programming language *Java*. The plugin that has been developed in this thesis opens an image sequence, applies a previously defined threshold value on each image to binarize it, and then saves the contour line between the black and the white area as pairs of x and y values. At the same time, the length of the perimeter (in pixel) and the area inside the contour line (in pixel^2) are measured. Figure 6.4 shows how the contour line is extracted from an image. The adequate value of the threshold has to be determined manually for each image sequence before the plugin is run. This value and the path of the corresponding image sequence can be saved in a special parameter file. Then it is possible to treat many image sequences in a row.

In a second step, the data of the contour line is loaded into the data analysis software *Igor*. Here as well, a small programm has been developed. It determines the images center from the center on the first image, which is a circle, smoothes

---

[1] Available on the web site `http://rsb.info.nih.gov/ij/`

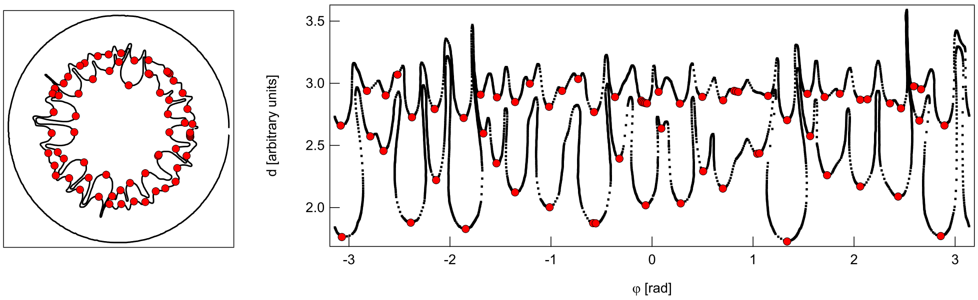

Figure 6.5.: The contour lines and the position of the minima in x-y and φ-d representation at two different times.

the contour line, and calculates for each point along the contour line the distance d to the center. The number of fingers is then determined by means of a so-called built-in `FindPeak`-algorithm. It searches a data set for a minimum or maximum by analyzing the smoothed first and second derivatives. The distance to the image center is, in the most cases, not a function of the angle φ from 0° to 360°, as the fingers are soon bulging in, see figure 6.5. Thus, we determine the minima on the distance to the center as a function of i, the internal order number of each point in a data set provided by *Igor*. The bulging in of the fingers is also the reason why we could not apply a Fourier transformation to determine the destabilizing wavelength. After having found the minima, they can be attributed again to their position (φ/d) or (x/y). The total number of minima corresponds to the number of fingers.

From such an image treatment, we gain information about the contact area, the perimeter length, and the number of fingers for a large number of experiments. Note that the automated finger counting works reliably only from a certain finger amplitude on. Thus, we counted the number of fingers on the very first images by hand.

Part III.

Debonding of confined viscoelastic materials

7. Pattern formation

7.1. Introduction

In this Chapter, we study the formation of the fingering pattern occurring during tensile deformation of confined viscoelastic layers. This situation is familiar from everyday life, when a soft adhesive is debonded from a substrate. As we stated before, a good adhesive should combine viscous and elastic properties that allow on the one hand to have good molecular contact with the substrate and on the other hand resistance to a certain stress level during debonding. The debonding mechanisms when detaching from a rigid substrate, which involves the formation of complex patterns such as bulk fingering or interfacial crack propagation [108], is determined by the adhesive's viscoelastic properties and the interplay between the adhesive material and the substrate.

In this thesis, we are interested in the question of how these instabilities evolve when smoothly changing material parameters *within one material family* as the material turns from a viscous liquid into a very soft viscoelastic solid, finally becoming a soft elastic solid where the dissipation is less and less important.

7.2. Experimental

We perform debonding experiments in the probe tack geometry on a model family of PDMS with different degrees of crosslinking. The material as well as the sample preparation were presented in detail in Chapter 5, and the set up in Chapter 6. We use crosslinker percentages from 0.9% up to 6%. The resulting materials range from very weakly crosslinked viscoelastic liquids to viscoelastic materials around the gel point, and end up with soft elastic solids. The material properties are overviewed in section 5.3. To summarize the experimental protocol, we approach a well polished circular indenter made of stainless steel with a diameter $R = 3\,\mathrm{mm}$ to a layer of PDMS with thickness b until contact is complete. In this protocol, we do not use a maximum force criterion to stop the approach of the probe. Instead, we manually approach the probe until the maximal possible contact area for a sample, which is generally not completely flat, is established. Afterwards, we lift the sample at a well defined speed v. We observe the debonding process from above via a camera mounted on a microscope. The parameters varied in our experiments, besides the viscoelastic properties, are the layer thickness b and the debonding speed v. Typical values are $b = 50 - 500\,\mu\mathrm{m}$ and $v = 1 - 200\,{}^{\mu\mathrm{m}}/_{\mathrm{s}}$. During a typical experiment, air penetrates from the edge of the confined layer. It can penetrate either in the

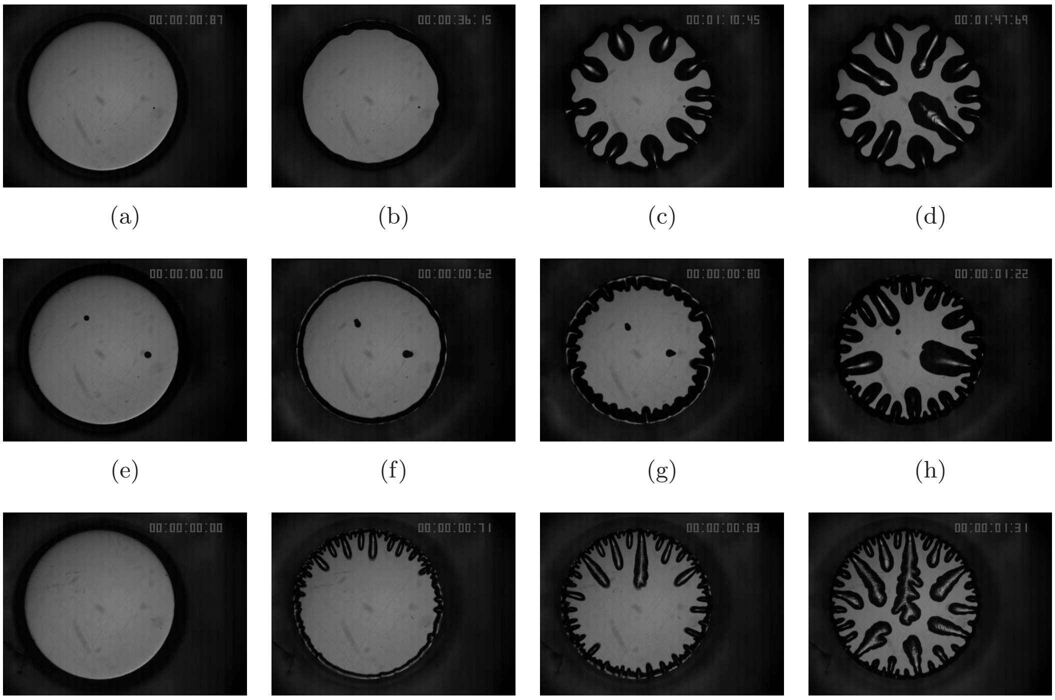

(a) (b) (c) (d)

(e) (f) (g) (h)

(i) (j) (k) (l)

Figure 7.1.: Formation of air fingers in the bulk deformation case, $r = 0.11$. Upper row: $b = 220\,\mu\mathrm{m}$, $v = 20\,{}^{\mu\mathrm{m}}\!/\!{}_{\mathrm{s}}$; middle row: $b = 220\,\mu\mathrm{m}$, $v = 200\,{}^{\mu\mathrm{m}}\!/\!{}_{\mathrm{s}}$; lower row: $b = 130\,\mu\mathrm{m}$, $v = 100\,{}^{\mu\mathrm{m}}\!/\!{}_{\mathrm{s}}$.

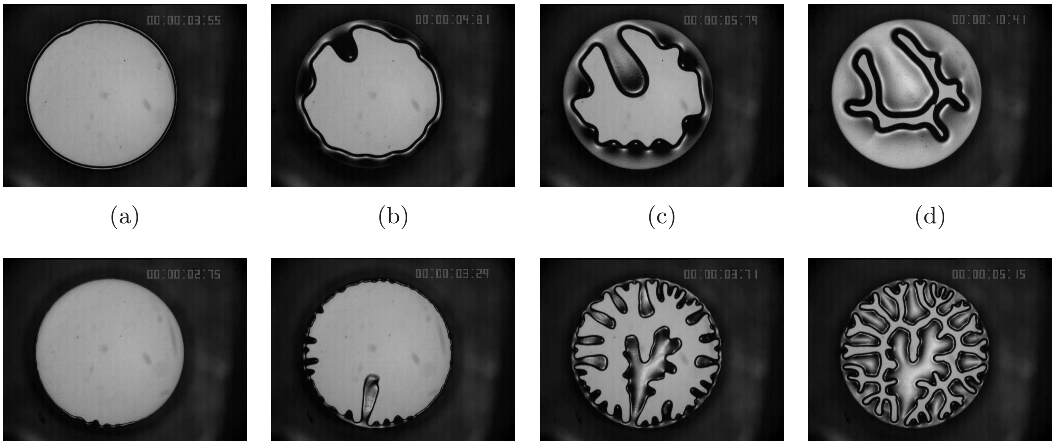

(a) (b) (c) (d)

(e) (f) (g) (h)

Figure 7.2.: Formation of air fingers in the interfacial case, $r = 0.20$. Upper row: $b = 390\,\mu\mathrm{m}$, $v = 10\,{}^{\mu\mathrm{m}}\!/\!{}_{\mathrm{s}}$; lower row: $b = 110\,\mu\mathrm{m}$, $v = 10\,{}^{\mu\mathrm{m}}\!/\!{}_{\mathrm{s}}$.

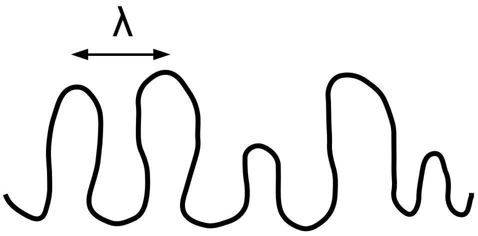

Figure 7.3.: Schematic view of the wavelength λ.

bulk, followed by a strong deformation and the subsequent formation of thin material "bridges" between the probe and the viscoelastic layer, called fibrils; or it can propagate at the interface between the probe surface and the polymer film, leading to fast debonding by interfacial crack propagation. Typical images of the debonding process are displayed in figure 7.1 and 7.2. Figure 7.1 shows three experiments in three lines for a only slightly crosslinked material ($r = 0.11$) with bulk mechanism. The time progresses from the left to the right. The parameters we varied between those three experiments were the debonding speed and the layer thickness. Figure 7.2 shows two experiments for a more crosslinked material ($r = 0.2$), where an interfacial mechanism is observed. Between these two experiments, we varied the layer thickness. In both the bulk and the interfacial case, we observe an initially circular contact line between air and PDMS. As the circle retracts, it is destabilized by small undulations. Subsequently, their amplitude grows, air fingers evolve, and propagate towards the center of the cell. The number of fingers depends on the experimental parameters: thinner layers produce more and thinner fingers; in the bulk case, higher velocities lead as well to more and thinner fingers.

An important point is that the pattern undergoes a coarsening process. As time goes on, the number of fingers becomes smaller and the wavelength increases. This process will be investigated in more detail for a Newtonian oil in Chapter 10, but is also observed for the viscoelastic and elastic materials, albeit less distinctive. The coarsening process has some important implications for the determination of the initial destabilizing wavelength λ. The amplitude of each finger is growing in time but is very small at the onset of the instability. Therefore, it is inherent to every dynamic fingering experiment that the instability can be observed only after the amplitudes have been growing for some time. At onset, a destabilizing wavelength, which corresponds to a linear destabilization process, can be clearly defined, but as the time and debonding process go on, highly non-linear patterns evolve, showing features like lateral undulations, side branching, and tip splitting, see figure 7.1 and 7.2. In a first step we restrict our interest to the analysis of the linear destabilization process at the very beginning. In the following, λ will always denote the first destabilizing wavelength that we were able to observe. We determine the number of fingers n of the first undulations and calculate their mean wavelength $\lambda = 2\pi R/n$. A schematical view of λ is given in figure 7.3.

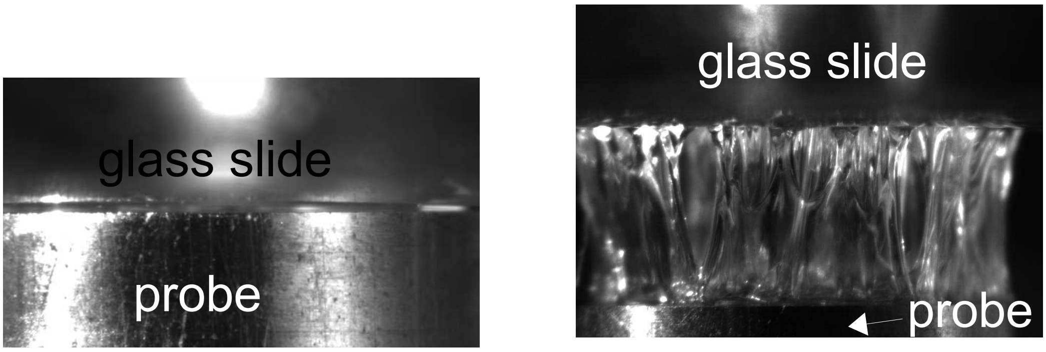

(a) 3.0% of curing agent, interfacial debonding.

(b) 1.1% of curing agent, important bulk deformation.

Figure 7.4.: The formation of fibrils seen from the side.

7.3. Two regimes of debonding

We characterize now in more detail the two cases of interfacial and bulk mechanisms introduced above. Although the patterns look quite similar in the top view pictures in figure 7.1 and 7.2, two different mechanisms are at their origin. Figure 7.4 shows a sideview of the fibril formation between the polymeric layer on the microscope glass slide and the steel probe. The different extend of fibrillation is obvious. On the one hand, we observe an interfacial debonding process [figure 7.2 and 7.4(a)] where the sample's bulk is not deformed. On the other hand, we observe a mechanism involving a large bulk deformation with formation of fibrils [figure 7.1 and 7.4(b)].

We stated that the visual observation of the experiments indicates on the one hand a bulk, on the other hand an interfacial debonding mechanism. In the following, we discuss these two cases separately, aiming to investigate and understand the dependence of the observed patterns on the relevant parameters for each case. To do so, we compare the pattern formation to typical examples for instabilities in two limits of material properties. A typical elastic interfacial instability is the contact instability discovered by Ghatak *et al.* [47], which we described in Chapter 4.

The patterns that we observed depend on the sample thickness in all the experiments. In the case of interfacial debonding, the wavelength depends on the sample thickness, but not on the debonding velocity or on the modulus. Figure 7.5(a) displays that the wavelength is constant over three decades in v for 2% of curing agent. In the bulk case, the wavelength depends on the sample thickness and the debonding speed. Figure 7.5(b) shows λ as a function of v for 1.2% of curing agent. The speed and modulus dependence excludes the elastic mechanism as an explanation for the bulk instability. We compare it in the following to a typical, well-known bulk instability for liquids, the *Saffman–Taylor* instability, which we introduced in Chapter 4.

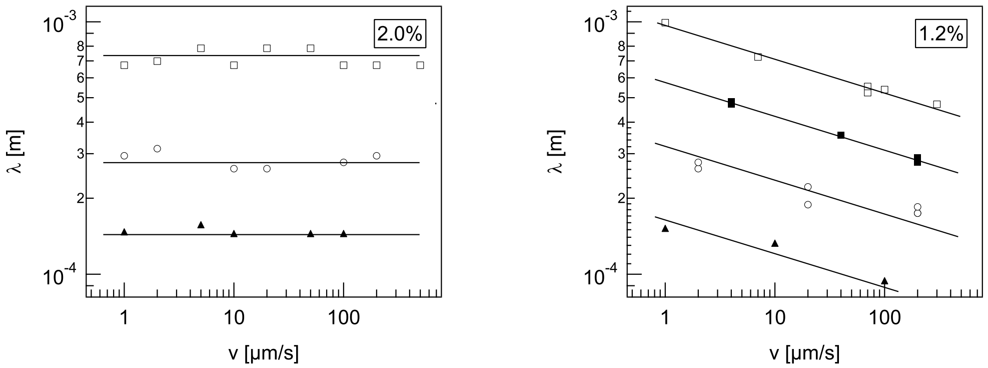

(a) 2% of curing agent, interfacial debonding. □ = 300 µm, ○ = 130 µm, ▲ = 70 µm.

(b) 1.2% of curing agent, bulk deformation. □ = 350 µm, ■ = 230 µm, ○ = 120 µm, ▲ = 60 µm.

Figure 7.5.: Wavelength versus debonding speed. Black lines are a guide for the eye.

7.3.1. Bulk case

The **bulk regime** is characterized by fibrillation and a bulk deformation mechanism. Again, the pattern formation is sensitive to both the initial film thickness and the debonding speed for a given material. The wavelength decreases with the debonding speed and increases with the initial film thickness [figure 7.5(b)]. The situation of air entering into the bulk of a very soft viscoelastic material can be seen as an analogy to the classical *Saffman–Taylor* (*ST*) instability [98, 87]. Instead of the Newtonian viscosity, we introduce the complex modulus into the equation for the most unstable wavelength. In this way, we can compare the destabilizing wavelength from experiments to the Saffman–Taylor prediction from linear stability analysis. A similar approach was adopted to explain fingering in complex fluids [72, 74, 73] and in completely elastic gels [109].

The destabilizing wavelength from the linear stability analysis is given as [98]

$$\lambda = \pi b / \sqrt{Ca}\ . \tag{7.1}$$

$Ca = U\eta/\gamma$ is the dimensionless capillary number comparing viscous to capillary forces, η the viscosity, $\gamma = 20\,\mathrm{mN/m}$ the surface tension between PDMS and air, and U the radial velocity of the circular interface. Presuming an incompressible fluid, $U = Rv/2b$ can be determined from volume conservation. We use this assumption to estimate the radial velocity for small times at the beginning of the destabilization staying in the framework of a viscous instability. Unlike for fluids, a steady shear viscosity η cannot be determined for soft viscoelastic solids, as the material's structure would be destroyed in a constant shear measurement. It is however possible to perform oscillatory frequency measurements and determine a complex viscosity, directly linked to the complex modulus via

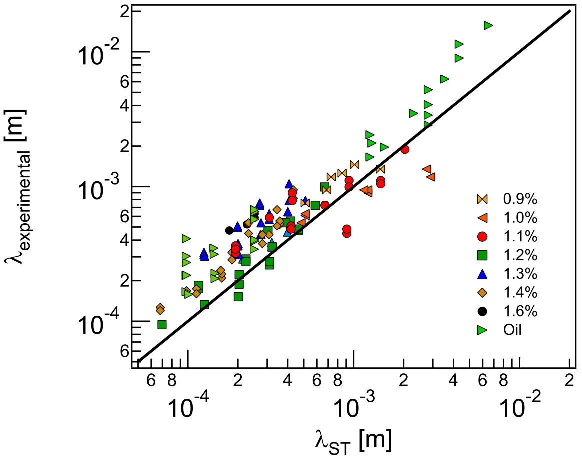

Figure 7.6.: Comparison of the experimentally measured wavelength to the *ST* prediction.

$$|\eta^\star| = \frac{|G^\star|}{\omega} \ . \tag{7.2}$$

In the following, we refer to $|G^\star|$ as $G^\star$ and to $|\eta^\star|$ as $\eta^\star$. For polymer melts, the steady shear viscosity η is related to the complex viscosity $\eta^\star$ via the *Cox–Merz* rule, an empirical relationship that has been established in 1958 [27]. It states that the complex dynamic viscosity at frequency ω is equal to the steady shear viscosity at corresponding shear rate $\dot\gamma$,

$$|\eta^\star(\omega)| = \eta(\dot\gamma)|_{\omega=\dot\gamma} \ . \tag{7.3}$$

Though it is not clear that equation 7.3 is valid for crosslinked materials, it provides a possibility to estimate the complex viscosity of such materials at a certain shear rate. This approach was used for adhesives in many studies aiming to attribute a certain value of the modulus to an experiment at a given strain rate (see for example references [76, 16]).

The strain rate $\dot\gamma$ has to be determined for each experiment. As the strain rate is a velocity gradient, it is clear that it can be approximated by the ratio of a suitably chosen velocity to a given length scale, here the sample thickness b. In the framework of a viscous instability, the pertinent velocity is the radial velocity U. Hence, we estimate the strain rate via the ratio of the radial velocity U and the sample thickness b for each experiment, $\dot\gamma = U/b$, and we calculate

$$\eta^\star(\omega) = \frac{G^\star(\omega)}{\omega} = \frac{G^\star(\dot\gamma)}{\dot\gamma} = \frac{G^\star(U/b)}{(U/b)} = \frac{b\,G^\star}{U} \ . \tag{7.4}$$

We replacing the value of the steady shear viscosity in equation 7.1 by the value of the complex viscosity at the corresponding shear rate. In this way, we can compare the wavelength measured in the experiments to the wavelength theoretically predicted from the Saffman–Taylor theory. Figure 7.6 shows that the experimental results and the theoretical prediction are in good quantitative agreement, despite some scattering. We show here data for viscoelastic materials below the gel point (0.9% and 1.0% of curing agent), in the immediate neighborhood of the gel point (1.1% of curing agent), and above the gel point ($\geq 1.2\%$ of curing agent). The limit of a purely viscous liquid is represented by horizontal triangles obtained for a Newtonian silicone oil. For technical reasons, we did not perform tests with the Sylgard 184 oil, but used a higher viscosity oil ($\eta = 100\,\mathrm{Pa\,s}$). Note that the data for oil yielding high wavelengths of about $0.001-0.01\,\mathrm{m}$ have been measured in a different apparatus with a cell radius $R = 2\,\mathrm{cm}$.[1] The Saffman–Taylor prediction holds, in the limits of the experimental resolution, for all those materials, covering a wide range of properties. Note that the results for a pure silicone oil show important scattering as well.

As we stated before, we use two criterions to determine in which regime a material falls, namely whether the bulk is deformed by visual observation and the dependence on the debonding speed v. The question of the v-dependence needs to be discussed in more detail due to the specific rheological characteristics of the model family. We explained before that we determine the viscosity at a certain shear rate, see equation 7.4. For the most unstable wavelength it follows thus that

$$\lambda_{\mathrm{ST}} = \frac{\pi b}{\sqrt{\frac{U\eta}{\gamma}}} = \frac{\pi b}{\sqrt{\frac{UG^\star}{\omega\gamma}}} = \frac{\pi b}{\sqrt{\frac{UbG^\star}{U\gamma}}} = \frac{\pi b}{\sqrt{\frac{G^\star b}{\gamma}}}\,. \tag{7.5}$$

Therefore, the following subtle problem occurs: the v-dependence of the wavelength is solely included in the v-dependence of $G^\star$. $G^\star$ though is speed-independent for elastic materials, as their properties are dominated by the constant storage modulus. In the case of a speed-independent wavelength two different possibilities therefore exist.

1. The wavelength does not depend on $G^\star$.

2. The wavelength does depend on $G^\star$, which itself is speed independent.

Case 1 represents a wavelength that does not depend on the material parameters and thus clearly not corresponds to a ST mechanism. In case 2 however, the ST prediction could still be valid, even with no speed dependence observed. We thus tested whether the speed-independent wavelength could be described by the ST prediction and we plotted the experimental wavelength versus a hypothetical ST prediction for *all* the experiments, even the elastic case. Results are given in figure 7.7. This graph shows that ST prediction fails for the interfacial and speed independent experiments. We will show in the following section that these results are indeed independent of $G^\star$.

---

[1] Courtesy of D. Derks and A. Lindner.

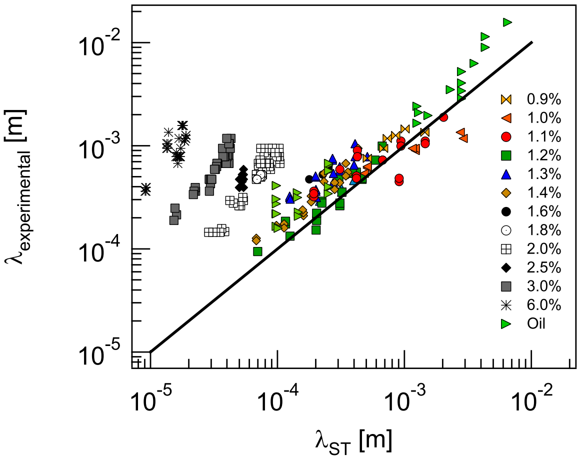

Figure 7.7.: The wavelength for all experiments in comparison to the ST prediction.

7.3.2. Interfacial case

The **interfacial regime** is characterized by interfacial crack propagation and debonding without bulk deformation. The linear wavelength does not depend on the debonding speed over three orders of magnitude, see figure 7.5(a). Figure 7.8(a) displays λ as a function of the film thickness b. All data fall onto one curve for a large range of the elastic modulus. For the materials with interfacial debonding the storage modulus varied over almost three orders of magnitude, that is, $1\,\mathrm{kPa} \lesssim G' \lesssim 0.5\,\mathrm{MPa}$.

We compare our results to theoretical predictions and experimental observations in a static peeling geometry (see [47] and references in Chapter 4). We have already introduced the confinement parameter equation 4.46

$$\alpha = \left(D/Gb^3\right)^{1/3} \tag{7.6}$$

from reference [1], D being the bending stiffness of the cover plate, G the film's elastic shear modulus, and b the film thickness. Above a critical confinement $\alpha_c \approx 20$, shear deformations are more beneficial for the system's energy than normal deformations, leading to undulations of the contact line. Considering the bending stiffness of the microscope glass slides, our experiments represent a dynamic variant of the static peeling situation. For a glass slide of $b_{\mathrm{glass}} = 2\,\mathrm{mm}$, $E_{\mathrm{glass}} \simeq 100\,\mathrm{GPa}$, and $\nu_{\mathrm{glass}} \simeq 0.25$, the bending stiffness is $D \simeq 71\,\mathrm{Nm}$. We calculate $\alpha_{\mathrm{min}} = \left(D/G_{\mathrm{max}}{b_{\mathrm{max}}}^3\right)^{1/3}$. Using the limiting values $G_{\mathrm{max}} \approx 0.5\,\mathrm{MPa}$ and $b_{\mathrm{max}} \simeq 500\,\mu\mathrm{m}$ for our samples, we find that $\alpha \gtrsim 100$ in all experiments. Thus, our experiments are always in the regime of an unstable crack front.

The wavelength as a function of film thickness (figure 7.8(a)) can be fitted by a straight line yielding

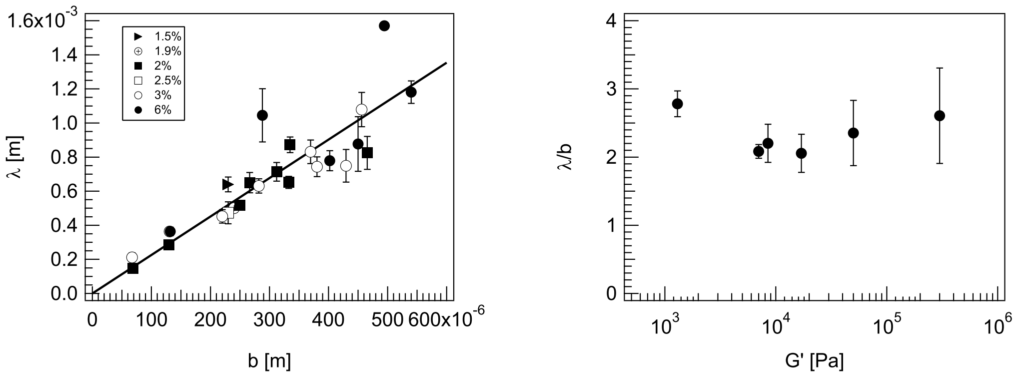

(a) λ scales with the thickness b. The solid line is a straight line fit to the data yielding $\lambda = 2.3\,b$.

(b) λ does not vary with the storage modulus over three decades.

Figure 7.8.: The wavelength in the regime of interfacial crack propagation.

$$\lambda = (2.27 \pm 0.1)\; b\;. \tag{7.7}$$

The critical wavelength calculated in reference [1] $\lambda_c \simeq 3.4\,b$ scales only with the film thickness and is independent of all material parameters. Figure 7.8(b) confirms that λ does not depend on the storage modulus over almost three decades in G'. Our result $\lambda = 2.3\,b$ is in good quantitative agreement with theory. Deviations might be attributed to the fact that calculations are done for $\alpha = \alpha_c$ whereas our experiments are placed far beyond the critical value. The higher scattering for larger b can be explained by the increasing difficulty to determine the wavelength for higher thicknesses; the less fingers evolve along the perimeter, the more it is difficult to count them. Furthermore, the relative error increases with decreasing number of fingers. Table 7.1 compares results for the critical mode $k_c = 2\pi/\lambda_c$ from theory and experiments. All authors agree on the fact that the wavelength does not depend on any material parameters. The absolute values of k_c differ however about a factor of 1.16 for calculations and about a factor of 1.45 for experiments. Again, note that we are working beyond the instability threshold in our study and thus do not observe the *critical* mode.

7.4. Transition

After having identified the two regimes of interfacial and bulk instabilities, we now investigate which parameters determine into which regime an experiment falls and whether it is possible to predict these mechanisms from adhesive theory. Therefore, we compare the energy that is needed to propagate an interfacial fracture in a system and the energy one has to provide to the system to deform an elastic material's bulk. Based on theoretical and experimental work by Maugis *et al.* [77, 94], the empirical

Authors	kb experiment	$k_c b$ theory
Adda-Bedia *et al.* 2006	–	1.85
Ghatak *et al.* 2000	1.59	–
Mönch *et al.* 2001	2.3	2.12
Nase *et al.* 2008	2.73	–
Shenoy *et al.* 2001	–	2.14

Table 7.1.: Comparison of the proportionality constant from experiments and linear stability analysis.

parameter

$$\mathcal{G}_c/E \propto G''/G'^2 \tag{7.8}$$

was established by Deplace *et al.* [36]. They showed that it is a valid approximation for predicting the debonding mechanism in soft adhesive systems for constant conditions at the probe surface and constant film thickness, see Chapter 3. We apply this approximation to our system and modify equation 7.8 in a way that it is suitable for different $\mathcal{G}_0$ and sample thicknesses b. Substituting equation 3.12 into equation 3.14 then yields

$$\frac{\mathcal{G}_c}{Eb} \approx \frac{\mathcal{G}_0 \tan\delta}{Eb} \, . \tag{7.9}$$

Again, the critical energy release rate $\mathcal{G}_c$ is a measure for the energy per unit area one has to provide to the system to make an interfacial crack move. Eb represents the elastic energy per unit area that is necessary to deform the bulk of a sample of thickness b and elastic modulus E. As the elastic modulus E scales with the shear storage modulus G', the right side of equation 7.9 can be rewritten as

$$\frac{\mathcal{G}_0 \, \tan\delta}{b\, G'} \, . \tag{7.10}$$

For cases where the energy cost to propagate a crack is high, bulk mechanisms are expected, while interfacial crack propagation should be observed when the elastic deformation of the layer requires a lot of energy. From equation 7.10 it is possible to trace a “mechanism map” spanned by $\mathcal{G}_0 \, \tan\delta$ on the y-axis and $b\,G'$ on the x-axis. Note that these parameters cannot be varied independently within one material system. For example, a variation in the frequency entails a change in G' as well as in $\tan\delta$.

Figure 7.10(a) represents the debonding mechanism of each experiment as a function of its parameters. Full symbols indicate interfacial, open symbols bulk deformation mechanisms. Close to the transition (at $\approx 1.6\%$ of curing agent), both mechanisms were observed, very likely explained by fluctuations in the sample preparation. The two regimes are nicely separated in figure 7.10(a). The solid line represents $y = 0.18\,x$. We use an estimation of $\mathcal{G}_0$ to draw this mechanism map and

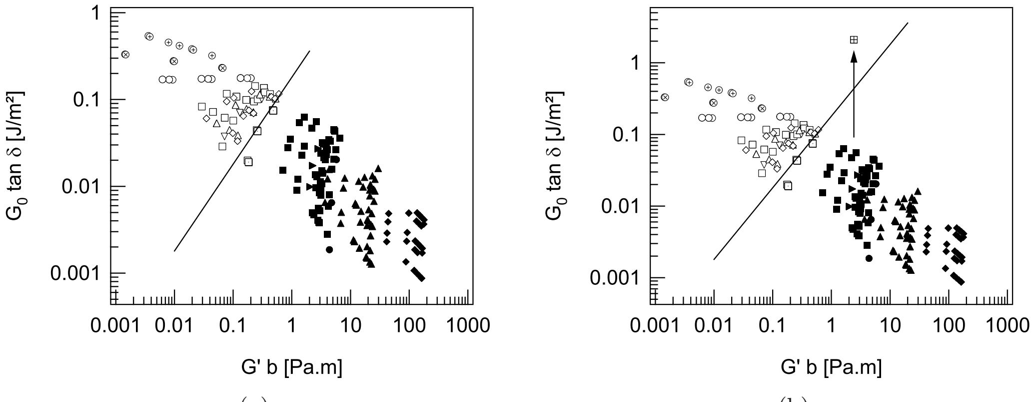

(a) (b)

Figure 7.9.: Mechanism map of bulk and interfacial debonding. Open symbols represent bulk deformation, full symbols interfacial crack propagation. Experiments right at the transition can show both mechanisms due to fluctuations in the sample preparation.

succeed in predicting the correct dependence. Calculating the absolute value of the slope however requires an exact knowledge of all system parameters and all physical processes on a local, microscopic level and is beyond today's understanding of adhesion processes.

Following the theory it should be possible to switch between interfacial and bulk mechanisms by changing $\mathcal{G}_0$, that is, by changing the adhesion of the PDMS to the probe surface. As an example, we performed an experiment by replacing the steel probe with a glass surface previously subjected to plasma treatment. For the polished steel probe, the adhesion energies are very low, see also Chapter 8. We estimated $\mathcal{G}_0$ performing a probe tack test at the experimentally lowest possible debonding speed $v = 0.1\,{}^{\mu m}/_{s}$ on the fully cured PDMS and found for steel $\mathcal{G}_0 \simeq 0.1\,{}^{J}/_{m^2}$. The adhesion on glass treated with plasma is considerably higher, as the plasma treatment activates chemical sites which increase the adhesion. Measuring $\mathcal{G}_0$ as before, we found a value of $\mathcal{G}_0 \simeq 15\,{}^{J}/_{m^2}$.

We were indeed able to change the debonding mechanism from interfacial to bulk deformation for a sample with 2% of crosslinker. This experiment is represented by the symbol ⊞ in figure 7.9(b). The change in the mechanism was visible in the distinct formation of fibrils. We were measuring the wavelength of the plasma experiment and compared it to the *ST* prediction. The value is represented by the symbol ⊞ in figure 7.10. Unfortunately, λ does not change a lot for the investigated conditions. We can however state that λ for the 2% bulk case falls on the *ST* prediction within the experimental error. However, the change in the wavelength is not very distinct.

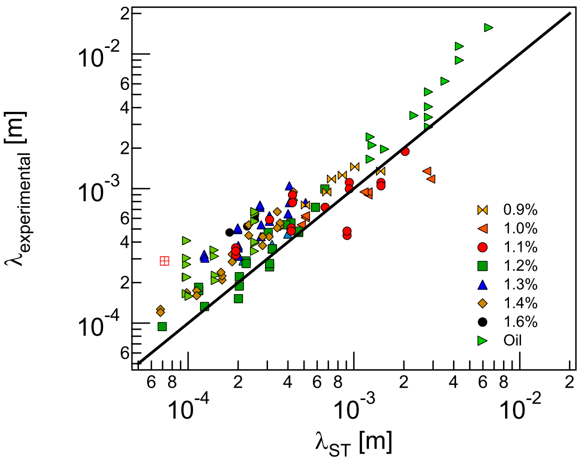

(a)

Figure 7.10.: The wavelength of the experiment with 2% of curing agent and plasma treatment is represented by the symbol ⊞.

7.5. Nonlinear patterns

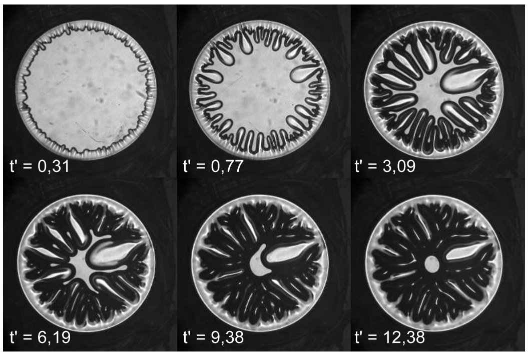

Figure 7.11.: Top view images of the cohesive debonding of a pure viscous oil, $\eta = 95.6\,\mathrm{Pa\,s}$, $b_0 = 50\,\mu\mathrm{m}$, $v = 8\,{}^{\mu\mathrm{m}}/{}_{\mathrm{s}}$.

So far, we were investigating the destabilization process at the onset of the instability. In this section, we discuss briefly the subsequent debonding process. As it is visible on the pictures in figures 7.11, 7.12, and 7.13, the later stages of the pattern formation exhibit more complex features like coarsening, tip splitting, or side branching. The dimensionless time is defined as $t' = v/b_0\,t$. We first compare the debonding process for a pure Newtonian oil and the viscoelastic material at $r = 0.11$.

In both cases, the debonding mechanism is cohesive, meaning that the late fibrils eventually broke up in the middle. For the Newtonian oil in figure 7.11, we observed

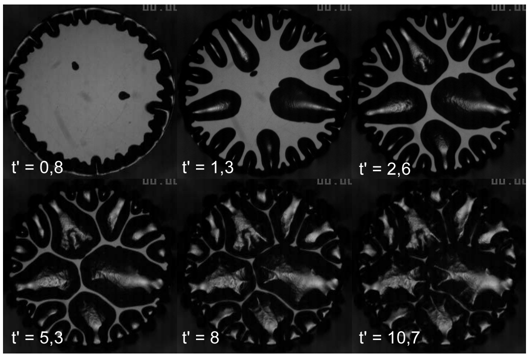

Figure 7.12.: Top view images of the debonding of a viscoelastic material, cohesive debonding. $r = 0.11$, $b_0 = 223\,\mu\text{m}$, $v = 200\,{}^{\mu\text{m}}/\text{s}$.

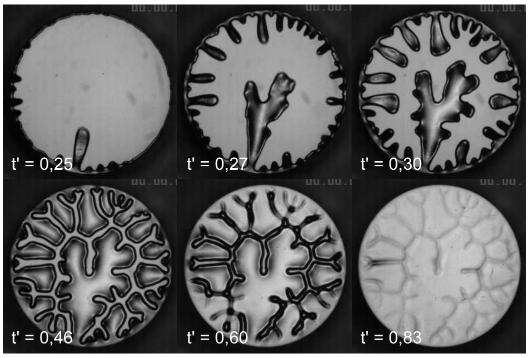

Figure 7.13.: Top view images of the debonding of an elastic material, adhesive debonding. $r = 0.2$, $b_0 = 129\,\mu\text{m}$, $v = 10\,{}^{\mu\text{m}}/\text{s}$.

strong finger growth, followed by subsequent contraction of the “oil bridges” between the fingers back to a circular shape. Strong coarsening of the pattern is observed and will be investigated in detail in Chapter 10. For different speeds and initial thicknesses of the oil layer, we always found one single final fibril.

For the viscoelastic material with $r = 0.11$, we observed a different behavior at late times, see figure 7.12. At the beginning of the debonding, the circular interface recedes and then becomes instable. Later though, the behavior differs substantially from the Newtonian oil. The material bridges between the air fingers cannot recede completely as they are pinned to the probe surface. They persist up to the end of the test, multiple fibrils are formed, and eventually break up in the middle without being detached from the probe. The number of fingers evolves less in time than in the oil experiment.

Figure 7.13 shows the debonding of an elastic material with $r = 0.2$, corresponding to the interfacial adhesive mechanism with no fibrillation. As in the two preceding cases, air fingers are formed. They merge, leading to a complete debonding with no residues left on the steel probe. The debonding is very fast; complete debonding is achieved at $t' < 1$, in contrast to the fibrillation case. The last picture in figure 7.13 shows remaining traces on the polymer film. They disappeared completely a short time after the test.

Note that the general three dimensional shape of the air fingers in the direction of the layer thickness significantly differs in these three cases, see Chapter 9.

7.6. Conclusion and discussion

In conclusion, we investigated in this Chapter the pattern formation when a circular indenter is retracted from a thin PDMS layer. In particular, we were interested in the wavelength λ when the contact line is initially destabilized. We changed the material properties systematically over a wide range staying within the same material family: we started from the uncrosslinked Newtonian oil, and subsequently changed to slightly crosslinked materials below and right at the gel point. Above the gel point, the material ceases to flow and becomes a very soft viscoelastic solid. Crosslinking ever more leads to elastomers where the dissipation gets less and less important. We identified a regime of interfacial crack propagation where the wavelength does not depend on any material parameters but scales linearly with the film thickness. In a bulk regime, we found that the wavelength at the onset of the instability is well described by a Saffman–Taylor equation if we account for the complex modulus.

The transition between the interfacial and bulk regime is governed by an empirical reduced parameter that allows to draw a “mechanism map” spanned by the parameters $\mathcal{G}_0 \tan\delta$ and $G'b$. This graph separates nicely the different mechanisms and therefore allows to predict the debonding behavior of our system from the adhesion energy $\mathcal{G}_0$ and from the linear rheological properties. Increasing the adhesion between the PDMS and the probe, we were able to change the debonding mechanism from interfacial to bulk in accordance with the theoretical prediction. Yet testing the transition between both regimes within one material by changing b and v was not possible. The experimental conditions that are necessary to perform such a test were not feasible due to the technical restrictions of the setup.

One point that stays somewhat unsatisfying in this study is that the wavelengths in the interfacial case and in the bulk case lie in the same order of magnitude. Notably in the region around the transition, the modulus of the viscoelastic materials is such that the resulting wavelength differs not considerably from $\lambda_{\text{interfacial}} = 2.3\,b$. Thus we cannot observe a clear change in the wavelength as the systems changes its mechanism from one regime to another. A possible way to understand better the transition region would be to use another type of materials, like for example gels with very low moduli. In this way, it is possible to investigate the regions of the wavelength space that cannot be accessed with our materials and our experimental parameters. Using a low or high modulus material, the bulk wavelength is expected to by much smaller or much higher than the interfacial wavelength, resulting in a clearer identification of the change in the mechanism.

It also would be illustrative to perform a more detailed study of the exact scaling of the wavelength with the film thickness in the viscoelastic case. The drawback in our setup here is that we experience a large scatter on our data, which can be attributed to the measurement geometry. Namely for large wavelengths it is more difficult to count the fingers. A small error in the finger counting yields a large error in λ if the total number of fingers is very small. Thus the circular geometry is not ideal to investigate the linear instability. A setup in a peeling geometry with a large width might allow to observe a longer wavefront at the onset of the instability and therefore to determine the wavelength with a higher precision. However, the peeling geometry imposes problems for the alignment and imposes a stress field that is less controlled. The interest of the circular system lies in the fact that it is intensely used for the study of commercial adhesives. Understanding the mechanisms of pattern formation in the exact testing geometry is crucial for gaining a more profound knowledge of the very complex debonding mechanisms, and therefore for improving the research on commercial adhesive systems.

8. The complete debonding process – force curves and adhesion energies

8.1. Introduction

Commercial pressure-sensitive-adhesives are complex materials combining elastic properties from solids and viscous properties from liquids. The viscous properties allow the adhesive to conform to the roughness of the substrates, increasing in this way the contact area and guaranteeing thus a better adhesion through van der Waals forces. The elastic properties are important for the adhesive to be able to resist stresses during debonding. A fine tuning of the viscous and elastic properties leads to an optimization of the adhesive's performance [37]. We study the debonding of the model system introduced in Chapter 5, which can behave from a purely viscous Newtonian fluid to a soft elastic solid. It is thus well suited to study systematically within one family of materials the modification of the debonding mechanisms as the material properties change from a liquid to a viscoelastic solid and to an elastomer.

In Chapter 7, we investigated the initial stages of debonding of these materials using a probe tack geometry. We characterized the patterns that are formed by the air penetrating from the edges and identified two different mechanisms. The initiation of the debonding could either occur at the interface between the material and the substrate or in the bulk of the material. In the present Chapter, we investigate the complete highly non-linear debonding mechanism in the same geometry. The whole debonding process is visually observed while force-displacement curves are acquired [58]. This setup provides a very controlled geometry with two stiff parallel plates moving apart from each other at constant velocity. It is ideal to investigate the full range of materials from the viscous liquid to the elastic rubber.

8.2. Experimental protocol

The debonding tests were carried out in the custom-made probe tack setup described in more detail in Chapter 6. The setup mainly consists of a flat circular indenter (probe) that can be brought into contact and debonded from a tacky adhesive sample with thickness b at a controlled speed v via a step motor. During the test, the probe displacement and the normal force on the probe are measured. The debonding process is observed from above via a camera mounted on a microscope, providing insights into the debonding mechanisms. The probe is made of stainless steel and has a radius $R = 3\,\mathrm{mm}$. It was carefully polished to ensure a smooth surface. The testing conditions in the following are $v = 10\,{}^{\mu\mathrm{m}}/_{\mathrm{s}}$ and $b \approx 200\,\mu\mathrm{m}$.

8.3. Force-displacement curves

In this section we investigate the change in the shape of the force curves with varying material properties. A convenient representation are stress-strain curves, see figure 8.1. The stress σ always denotes here the nominal stress $\sigma = F/A_0$. The strain ϵ is the displacement d divided by the initial film thickness b. We study the stress-strain curves of a few selected materials that are representative for each type of behavior.

In the following, we describe the characteristics of the different stress-strain curves for the whole debonding process. Their different shape can be interpreted including the visual observation of the experiment. Observation in a top view gives more information about the evolution of the patterns, whereas the side view helps categorizing the mechanism of the final detachment. In general, we did not observe cavitation in the debonding of all our materials, except for rare cases of air trapped in pockets on the probe surface during the approach. Instead we invariably observed air fingers entering into the adhesive from the sides. Cavitation is controlled by the ratio of air pressure and elastic modulus. It is favored by high moduli, high adherence, and thin layers relative to the debonding speed [118]. As the materials investigated in this study were rather soft, the film thicknesses high, and the interaction between silicone and steel weak, cavitation was mostly suppressed.

Figure 8.1(a) shows the typical stress-strain curve for a pure silicone oil $\mathbf{r} = \mathbf{0}$. As the forces were too weak for the experimental resolution with the Sylgard 184 oil, we performed tests with a higher viscosity PDMS oil ($\eta = 100\,\mathrm{Pa\,s}$) and different testing conditions ($v = 8\,\mathrm{\mu m/s}$ and $b_0 = 50\,\mathrm{\mu m}$). The results stay qualitatively the same. The force first reached a peak value due to the stretching of the machine [43, 40], then it decayed rapidly to forces below the experimental resolution. The oil-probe contact area formed a contracting circle that became smaller and smaller until only one thin fibril was left. This fibril was stretched in the tensile direction and became thinner until it finally broke up triggered by the Rayleigh–Plateau instability [90, 95]. The force however was very early in the process so low that is was not possible to monitor the actual break-up. The maximum deformation was higher than 20.

Figure 8.1(b) displays the stress-strain curve for a material with $\mathbf{r} = \mathbf{0.10}$. This material is below the gel point. The peak shape resembles the case of the non-crosslinked oil. However, a very low force plateau is formed. The test was stopped before the actual break-up of the fibrils; the maximum strain value is expected to be very high ($\epsilon_{\max} > 20$).

Next we consider the material with $\mathbf{r} = \mathbf{0.11}$ [figure 8.1(c)]. G' and G'' are parallel over the whole range of frequencies, indicating that this material is close to its gel point. Such a material is typical of an under-crosslinked PSA , albeit with a much too low T_g to show high adhesion [130, 38]. Unlike before, the force did not decay continuously to zero, but a distinct force plateau was observed after a first strong decay. The plateau value was slightly increasing until it dropped slowly to very small values. The maximum deformation was very high ($\epsilon_{\max} > 20$). The experiment was stopped before the actual debonding was complete because the displacement of the probe was limited to $d = 5\,\mathrm{mm}$ in our set-up. The plateau force in figure 8.1(c)

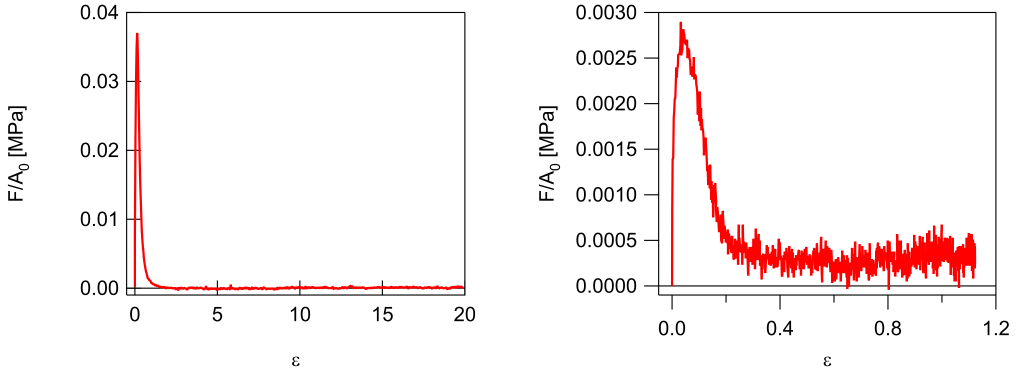

(a) Silicone oil, $\eta = 100\,\mathrm{Pa\,s}$, $b = 50\,\mu\mathrm{m}$, $v = 8\,{}^{\mu\mathrm{m}}/_{\mathrm{s}}$.

(b) $r = 0.10$, $b = 230\,\mu\mathrm{m}$, $v = 10\,{}^{\mu\mathrm{m}}/_{\mathrm{s}}$.

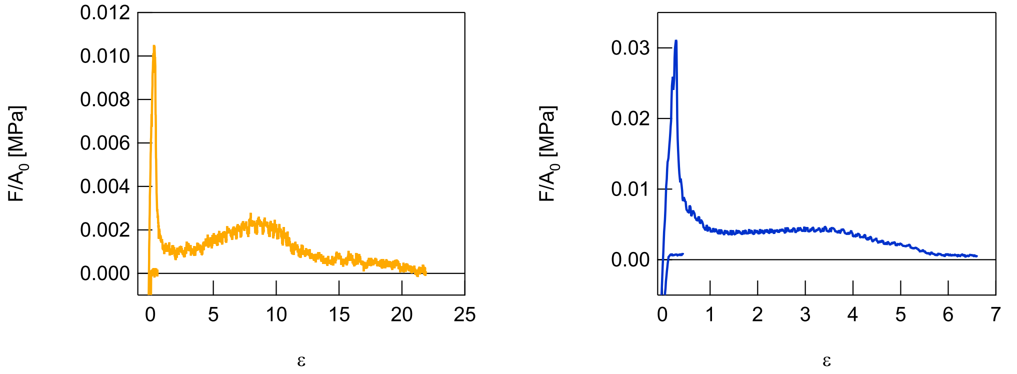

(c) $r = 0.11$, $b = 215\,\mu\mathrm{m}$, $v = 10\,{}^{\mu\mathrm{m}}/_{\mathrm{s}}$.

(d) $r = 0.13$, $b = 215\,\mu\mathrm{m}$, $v = 10\,{}^{\mu\mathrm{m}}/_{\mathrm{s}}$.

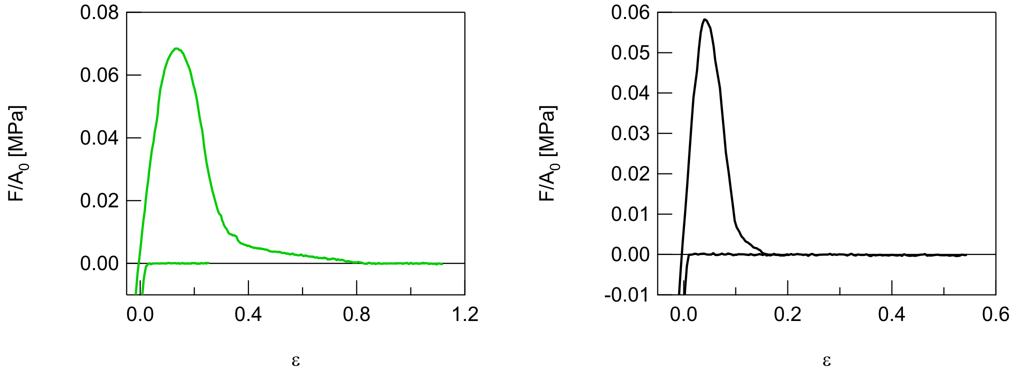

(e) $r = 0.16$, $b = 230\,\mu\mathrm{m}$, $v = 10\,{}^{\mu\mathrm{m}}/_{\mathrm{s}}$.

(f) $r = 0.3$, $b = 238\,\mu\mathrm{m}$, $v = 10\,{}^{\mu\mathrm{m}}/_{\mathrm{s}}$.

Figure 8.1.: Typical stress-strain curves of the different materials. Note the different scaling for each graph.

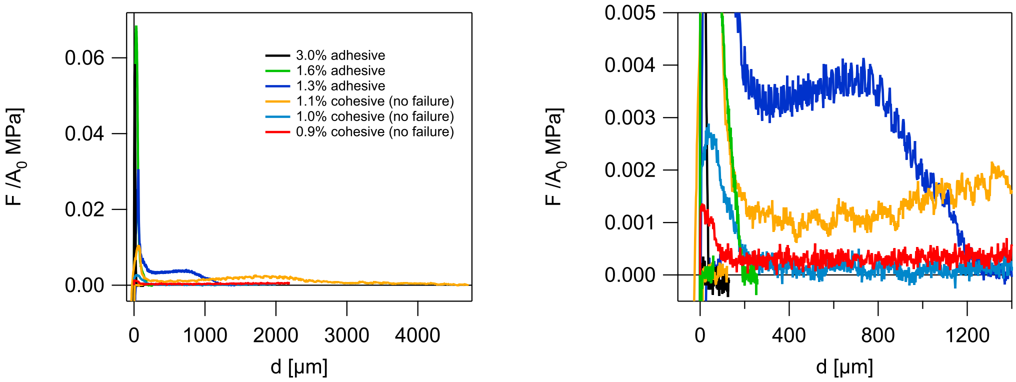

Figure 8.2.: Comparison of the stress-displacement curves for different materials between 0.9% and 3.0% of curing agent. Right side: zoom.

corresponds to a very pronounced formation and stretching of fibrils, as observed visually. The fibrils were very likely to break up in the middle as the force was almost zero when we had to stop the test.

Increasing the crosslinker amount, here $\mathbf{r} = \mathbf{0.13}$, had an obvious influence on the stress-strain curve [figure 8.1(d)]. It still exhibited a strong force plateau, but the force dropped to zero at much smaller strains, and the debonding was complete at a smaller $\epsilon_{\text{max}} \approx 6$. The force plateau was again linked to the formation and stretching of fibrils. In contrast to $r = 0.11$, where the fibrils were breaking up in the middle, they eventually detached from the steel probe without leaving residues. Such a cohesive to adhesive failure transition while forming fibrils is typical of lightly crosslinked networks and cannot occur for polymer melts since it requires strain hardening in the fibrils [66, 50].

At $\mathbf{r} \approx \mathbf{1.6}$ [figure 8.1(e)], the stress-strain curves again changed their shape. We did not observe a plateau, but a continuous decrease in the force. The maximum deformation was smaller than 100%, indicating an interfacial process. Visual observation showed that the material detached from the steel surface deforming the bulk only very weakly. The adhesion energy became very low. We did not observe any fibrils, the detachment was quite fast and without leaving traces on the probe. The more curing agent was added, the smaller the maximum strain became. Figure 8.1(f) shows a typical curve for $\mathbf{r} = \mathbf{0.3}$. These last two stress-strain curves are typical of what has been observed for weakly adhering systems [69, 58].

Figure 8.2 shows the stress-displacement curves and a zoom on the plateau region on one graph for all materials. The differences in in the force plateau and in the absolute values of maximum stress and maximum displacement are distinct.

Combining the shape of the stress-strain curves and visual observation of the debonding process, it was possible to discriminate three different types of debonding mechanisms. *First*, the debonding can be *cohesive*, involving the formation of fibrils that eventually break up in the middle. In this situation, residues of the polymeric film can be found on the probe surface after the test. This mechanism corresponds to the stress-strain curves in figure 8.1(a) to figure 8.1(c) with $r = 0$, $r = 0.01$, and $r = 0.11$, respectively. *Second*, the debonding can involve a large bulk deformation with formation of fibrils, but the fibrils will eventually detach and no residues are left on the probe surface (*adhesive* debonding) as for $r = 0.13$ [figure 8.1(d)]. We call this mechanism in the following *adhesive-bulk*. *Third*, we observed adhesive debonding involving a maximum deformation smaller than 100% ($\epsilon_{\max} < 1$) and interfacial fracture propagation between the adhesive and the probe as for $r \geq 0.16$ [figures 8.1(e), 8.1(f)]. This mechanism is called *adhesive interfacial*.

The initiation of the debonding has been studied in Chapter 7. We found that the debonding involving finger patterns can be initiated at the interface or in the bulk. An initially interfacial mechanism will stay interfacial during the whole debonding. In this case, the wavelength depends solely on the film thickness. On the other hand, an initiation of the debonding in the bulk of the material entails the formation of fibrils that finally can break up in the middle or detach from the probe. The initial wavelength is described by the *Saffman-Taylor* prediction in this bulk case.

The question of whether the mechanism is adhesive-bulk or adhesive-interfacial is answered by an interplay of material parameters and surface characteristics, as discussed in Chapters 3 and 7. When the probe is moved away, volume must be created due to the incompressibility of the adhesive. If it is more costly to create this volume by deforming in the bulk, the system creates new volume by debonding at the interface, conversely if the resistance to crack propagation is too high, the bulk is deformed and fibrils are formed. A stretched fibril can, at the end of the debonding process, detach from the probe or break up in the middle. If the material strain-hardens in tension, then the fibrils can detach from the probe [50]. On the other hand, if the material starts to flow, the force decreases ever more, and the fibril becomes thinner until it breaks up triggered by the Rayleigh–Plateau instability [90, 95].

8.4. Quantitative analysis of the stress-strain curves

In this section, we proceed to a more quantitative analysis of the stress-strain curves. Relevant quantitative parameters are the maximum strain $\epsilon_{\max}$, the maximum stress $\sigma_{\max}$, and the adhesion energy W_{adh}. As we discuss the whole material family from the viscous oil up to the completely cured elastomer, it was difficult to find a single parameter describing the global characteristics of the viscoelastic system. We decided to represent the data as a function of the elastic modulus E determined by linear rheology. E is of course not a control parameter for the system and does not capture all of the very complex non-linear material properties that come into play during the debonding. However, it is possible to represent the data as a function of E for the whole material family on a single curve. The materials that did not exhibit a plateau value a low frequencies are represented by $E' = 3G'$ at the frequency $\omega = U/b = 0.38\,\text{Hz}$. $U = Rv/2b$ is the radial velocity of the circular interface between air and adhesive. This frequency estimates the average shear rate at the propagating debonding front during the initial stages of an experiment with $v = 10\,\mathrm{\mu m/s}$, $b_0 = 200\,\mathrm{\mu m}$, and $R_0 = 0.003\,\mathrm{m}$.

8.4.1. Maximum stress

The maximum normal force on the probe divided by the maximum surface area is called the maximum stress. This quantity depends in a very complex manner on the apparatus itself and its rigidity [93, 43], on the patterns formed, on the testing geometry, on the surface roughness of the probe [21, 20], and finally on the material properties [123]. Therefore the maximum stress is not a very simple parameter to gain information concerning the physics of the debonding and we omit the discussion.

8.4.2. Maximum strain

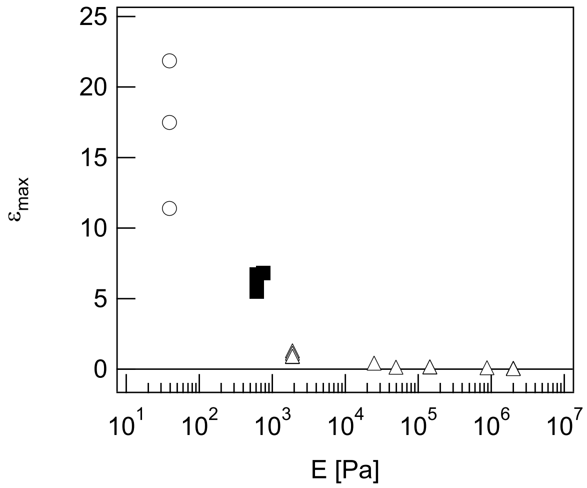

Figure 8.3.: Maximum deformation $\epsilon_{\max}$ versus elastic modulus E for materials between $r = 0.11$ and $r = 1.01$. ○ = cohesive, ■ = adhesive-bulk, △= adhesive-interfacial.

Figure 8.3 shows the maximum deformation before debonding as a function of the elastic modulus. It is important to mention that the maximum strain values of materials for which no break-up during the test occurred are minimum values. For a better understanding, the three different mechanisms that we have defined in section 8.3 are represented by different symbols in figure 8.3 and 8.4. Open circles (○) represent the cohesive mechanism, filled squares (■) the adhesive bulk mechanism, and open triangles (△) the adhesive interfacial mechanism. For the non-crosslinked oil it was not possible to determine the maximum strain $\epsilon_{\max}$ from the force curves. The force dropped soon to very low values and the actual break up of the last fibril remained hidden in the noise of the force measurement.

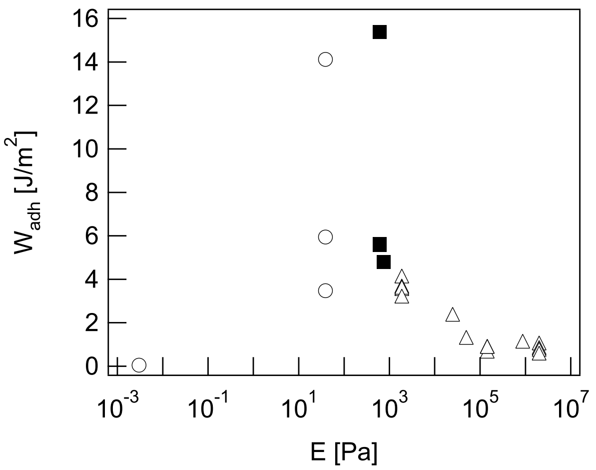

Figure 8.4.: Adhesion energy W_{adh} versus elastic modulus E for materials between $r = 0$ and $r = 1.01$. ○ = cohesive, ■ = adhesive-bulk, △= adhesive-interfacial.

As shown in figure 8.3, the maximum deformation decreases continuously with increasing modulus: the material becomes less and less deformable as it is crosslinked. This corresponds to the fact that the debonding becomes more and more interfacial. The decrease is very important around the gel point and ϵ_{max} changes less when the mechanism becomes interfacial.

8.4.3. Adhesion energy W_{adh}

The adhesion energy is the energy needed per unit area to separate two plates that are bonded together at a certain lifting speed. It can be measured from the area under the stress-strain-curve between $\epsilon = 0$ and $\epsilon = \epsilon_{\mathrm{max}}$ multiplied by the film thickness b,

$$W_{\mathrm{adh}} = b \int_0^{\epsilon_{\mathrm{max}}} \sigma(\epsilon) \mathrm{d}\epsilon \ . \tag{8.1}$$

We investigate in the following how the adhesion energy changes with the material properties. The normal force on the probe was below the experimental resolution for the non-crosslinked silicone oil Sylgard 184. W_{adh} could thus not be measured. However, it can be calculated for the case of a retracting circle following[1] [12]

$$F_{\mathrm{Newtonian}}(t) = \frac{3\pi\eta {R_0}^4 {b_0}^2 v}{2b(t)^5} \ , \tag{8.2}$$

with R_0 the initial circle radius and $b(t) = b_0 + vt$ the changing layer thickness. Integrating equation 8.2 from b_0 to infinity yields the viscous contribution to the

---

[1] In Chapter 10, we show that the calculated and measured values are actually very close, especially in situations with little fingering.

energy needed to separate the plates from the initial distance b_0 to infinity [40]. Dividing by the initial surface area gives

$$W_{\mathrm{visc}} = \frac{3\eta {R_0}^2 v}{8{b_0}^2} \,. \tag{8.3}$$

To obtain the adhesion energy, one has to add the thermodynamic work of adhesion, which is two times the surface energy γ. For silicone oil and air, $\gamma = 20\,\mathrm{mN}/\mathrm{m}$. Therefore, the adhesion energy is

$$\begin{aligned} W_{\mathrm{adh}} &= W_{\mathrm{visc}} + W_{\mathrm{thermo}} \\ &= (0.00443 + 0.04)\,\mathrm{J}/\mathrm{m}^2 \qquad (8.4) \\ &\approx 0.044\,\mathrm{J}/\mathrm{m}^2 \qquad (8.5) \end{aligned}$$

Obviously, the viscous contribution to W_{adh} is much smaller than the thermodynamic work of adhesion and W_{adh} is essentially equal to 2γ for this low viscosity oil.

Figure 8.4 displays the adhesion energy for the whole material family from the viscous oil to the completely cured elastomer as a function of E. As already pointed out, W_{adh} equals the thermodynamic work of adhesion in the viscous limit. In the elastic limit, W_{adh} is as low as $1\,\mathrm{J}/\mathrm{m}^2$. Performing the test at a lower velocity we found an even lower W_{adh} close to the thermodynamic value. Going from the viscous to the elastic limit, the adhesion energy increases as crosslinks are formed. It goes through a maximum at $E \approx 0.5\,\mathrm{kPa}$ and decreases again when the elastic modulus becomes higher and the deformation lower. Such a maximum in dissipation has already been noted by other authors on a much narrower range of material properties [65, 39, 45]. Obviously there is an optimum in the degree of crosslinking for having a large adhesion energy. Compared to typical adhesive materials however, the adhesion energies in our system are very low, as the thermodynamic adhesion and the dissipation at small and large strains are low.

In the following, we compare the adhesion energy to the scaling in the cases of pure liquids and well crosslinked elastomers.

Comparison of W_{adh} to the scaling in the Newtonian case

For a pure liquid, the adhesion energy W_{adh} scales like $\eta v/{b_0}^2$ for constant probe radius, see equation 8.3. In figure 8.5 we compare the theoretical and experimental values for a pure silicone oil and a slightly crosslinked material ($r = 0.12$). The oil has a viscosity $\eta \approx 100\,\mathrm{Pa\,s}$. We used different values of the initial gap width b_0 and the debonding speed v. The experimental values for the un-crosslinked oil stay slightly below the theoretical prediction, which can be attributed to the influence of fingering on the force curves.[2] In contrast, the measured value for the viscoelastic material deviates very strongly from the value that is predicted for a Newtonian oil

---

[2] This effect is discussed in more detail in Chapter 10.

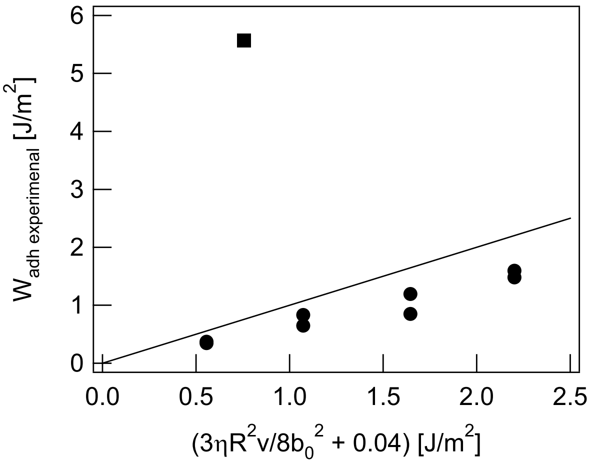

Figure 8.5.: The measured adhesion energy versus the adhesion energy calculated for a retracting circle of a Newtonian oil. ■ = viscoelastic material, $r = 0.12$, ● = Newtonian oil $\approx 100\,\mathrm{Pa\,s}$.

at the same experimental conditions ($b_0 = 61\,\mu\mathrm{m}$, $v = 10\,{}^{\mu\mathrm{m}}/_{\mathrm{s}}$, $\eta = 79\,\mathrm{Pa\,s}$). The presence of crosslinks directly leads to the stabilization of fibrils in extension. Unlike in the case of a Newtonian liquid, the relaxation times are high and the forces can not relax immediately. The force stays distinctly over zero in the plateau region, so that the adhesion energy exceeds the value calculated following the Newtonian theory. Note that the material parameters of the viscoelastic materials change during the experiment. The complex modulus depends on the strain rate and for large deformations also on the strain amplitude. The modulus determined by rheometry refers to a linear, steady state situation, whereas the debonding experiment is a dynamic situation.

Comparison of W_{adh} to the scaling in the elastic case

Now we focus on the adhesion energy in the predominantly elastic materials with interfacial debonding. We studied in more detail $r = 0.2$, $r = 0.3$, $r = 0.6$, and $r = 1$. We tested several thicknesses that yielded qualitatively the same results, but different absolute values. For a clearer view, we present here only experiments with constant thickness $b \approx 230\,\mu\mathrm{m}$. The debonding speed varied between $0.1\,{}^{\mu\mathrm{m}}/_{\mathrm{s}}$ and $100\,{}^{\mu\mathrm{m}}/_{\mathrm{s}}$.

Figure 8.6 shows the adhesion energy as a function of the debonding speed. W_{adh} increases with increasing v. The adhesion energy for the completely crosslinked material ($r = 1$) reaches for very low speeds ($v = 0.1\,{}^{\mu\mathrm{m}}/_{\mathrm{s}}$) values of about $0.1\,{}^{\mathrm{J}}/_{\mathrm{m}^2}$. The thermodynamic work of adhesion for PDMS on itself was found in a *JKR* test to be about $0.04\,{}^{\mathrm{J}}/_{\mathrm{m}^2}$ [48]. For less crosslinked materials, we observe higher adhesion energies. The more these materials are crosslinked, the less they dissipate, although their loss modulus increases. The loss modulus measures the ability to dissipate

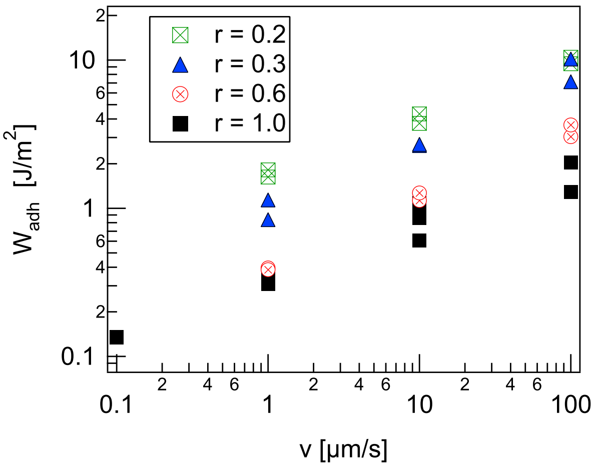

Figure 8.6.: The adhesion energy W_{adh} versus the debonding speed v for elastic materials.

energy per unit volume. The more crosslinked a material is, the higher its G'' is, but at the same time, the absolute dissipative volume decreases, so that we measure higher adhesion energies for less crosslinked material with lower G''.

For a purely elastic material without any dissipation, the adhesion energy equals the thermodynamic energy. This case has been studied by Webber *et al.* who investigated the adhesion energy of soft elastic gel layers in different confinements [118]. They showed that the square root of the quantity $\mathcal{G}_c/Eb$ predicts well the maximum strain that can be applied to a sample before it detaches from a circular indenter,

$$\epsilon_{\text{max}} = \left(\frac{\mathcal{G}_{\text{c}}}{Eb_0}\right)^{1/2} . \tag{8.6}$$

Again, $\mathcal{G}_{\text{c}}$ is the critical energy release rate. Eb measures the elastic energy per unit area that is stored in the sample's bulk for a given applied strain. Webber's theory has been established for elastic gels without dissipation. In their case, $\mathcal{G}_{\text{c}}$ was constant and independent of the elastic modulus. We applied this analysis to our system of weakly dissipating PDMS elastomers and verified the following equation:

$$W_{\text{adh}} = Eb_0 {\epsilon_{\text{max}}}^2 . \tag{8.7}$$

Figure 8.7(a) shows the scaling from equation 8.7 for the completely cured material. We tested two different thicknesses. Although we found speed dependence implying some dissipation in the material, the scaling works well. The speed dependence of W_{adh} is included in the value of the maximum strain ϵ_{max}. The too low values for higher speeds can be attributed to the limited resolution of the experiment: the debonding happens for this hard material too fast for the acquisition of force and displacement to keep up.

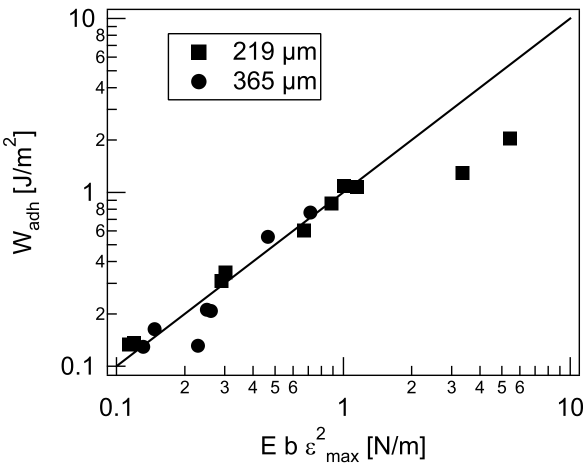

Figure 8.7.: W_{adh} versus $Eb\epsilon^2_{max}$ for the completely cured sample. The continuous line represents the theoretical prediction following equation 8.7.

The speed dependence of $\mathrm{W}_{\mathrm{adh}}$ explained in terms of bulk properties

We now investigate the speed dependence of W_{adh} that we observed for materials with interfacial debonding, see figure 8.6. Maugis and Barquins established a phenomenological viscoelastic theory in 1978 [77], see also Chapter 3. We briefly repeat that for interfacial crack propagation on elastomers with dissipation, the authors split up $\mathcal{G}_{\mathrm{c}}$ into a constant value $\mathcal{G}_0$, which is the energy release rate for a crack propagating at vanishing rate, and a dissipative function $\Phi(V)$. $\Phi(V)$ accounts for the viscous dissipation and depends on the temperature and on the crack velocity V,

$$\mathcal{G}_{\mathrm{c}} = \mathcal{G}_0 \left(1 + \Phi(a_{\mathrm{T}}V)\right) \ . \tag{8.8}$$

The authors also showed that $\Phi \propto V^n$ at constant temperature. Some different approaches have been taken to estimate the dissipative function. Gent showed experimentally for simple elastomers in peel tests that the increase in the fracture energy with peel rate resembles the increase in the dynamic modulus G' with frequency ω [44]. Saulnier *et al.* developed a full theory to predict the energy dissipated by crack propagation as a function of crack velocity with the linear viscoelastic properties of the material [101]. However, the quantitative comparison of this theory to our experimental data is difficult since we control the probe debonding speed and not the crack velocity, which varies spatially and temporally during the debonding process.

Ramond *et al.* showed that the frequency dependence and $\tan\delta$ are solely included in $\Phi(a_{\mathrm{T}}V)$ [94]. We approximated therefore the dissipative function Φ by $\tan\delta = G''/G'$. If this approximation is valid, W_{adh} should show the same speed dependency as $\tan\delta$, as long as we use a reasonable approximation for the equiva-

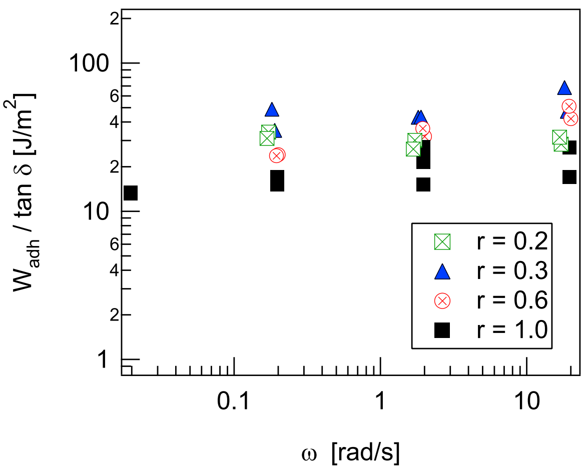

Figure 8.8.: $W_{\mathrm{adh}}/\tan\delta$ versus ω for predominantly elastic materials.

lence between frequency in the steady-state measurements and debonding velocity. Figure 8.8 shows $W_{\mathrm{adh}}/\tan\delta$ as a function of ω. The pronounced dependence on the velocity that is visible in figure 8.6 disappears: we obtained constant value lines for each material. Although the values for $r = 1$ were slightly lower than for the rest of the data, the data scaled well with this theory. In this way, we confirm the theory of Ramond *et al.* for materials that span two decades in the elastic modulus. Differences in the absolute value for each material might be explained by a different overall geometry of the dissipative zone. This geometry is influenced by the boundary conditions at the fingertip-probe boundary. Recent studies have reported differences in the adhesion energy and contact line geometry that were attributed to the role of friction and slippage at the interface [82, 127, 83, 6]. This point will be addressed in Chapter 9.

8.5. Conclusion

In conclusion, we present in this Chapter a complete study of debonding of soft viscoelastic PDMS with varying degrees of crosslinking. The debonding process from a circular steel indenter in a "probe tack" geometry was investigated with synchronized images and stress-strain curves. In a first step, we describe in detail the shape of the stress-strain curves. Adding information from visual observation, we identify three different debonding mechanisms as the material properties change from viscous to viscoelastic solids, finally being soft elastic solids: a pure bulk mechanism with cohesive debonding, an initiation of the debonding in the bulk followed by adhesive debonding, and finally a purely interfacial mechanism leading to adhesive debonding. We observe a clear decrease in extensibility of the adhesive material as it is crosslinked and identify a maximum in the adhesion energy for intermediate amounts of curing agent. W_{adh} is close to the thermodynamic value for the uncrosslinked PDMS oil and for the fully cured elastomer and goes through a maximum for materials around the gel point.

Furthermore, we accomplished a first systematic investigation of the velocity dependence of the adhesion energy for a series of viscoelastic elastomers. Their low frequency modulus spans two decades. For predominantly elastic materials, we showed that the speed dependence of the adhesion energy can be rescaled via the dissipative function $\tan\delta$, which measures a steady state material bulk property. However, the absolute value of W_{adh} depends on the degree of crosslinking and on the sample thickness and can not be quantitatively predicted yet.

In the next Chapter, we present a novel technique that makes it possible to visualize directly the contact line between viscoelastic material and air. As an outlook, it would be of great interest to investigate the speed dependence of the adhesion energy, gaining at the same time clearer information about the contact angle. In this way, we might be able to explain the change in absolute value of the adhesion energy for materials with different degrees of crosslinking by a change in the boundary conditions.

A second interesting perspective is the investigation of the influence that structured probe surfaces have on the adhesion energy. A study is currently starting in the laboratory, probing the influence of regular patterns on the adhesion energy. The structured surfaces with controlled amplitudes and wavelengths are produced using a technique that was developed recently by Vandeparre and Damann [116].

9. A novel technique for direct visualization of the contact line

9.1. Introduction – the need for $3D$-visualization

Evidence for slippage at the adhesive-substrate contact line

The influence of slippage of the contact line on the adhesion energy during debonding has been investigated in some recent studies. Newby *et al.* measured the adhesion energy of a standard commercial viscoelastic adhesive on various substrates (PDMS, alkylsilane, fluoroalkylsilane) in a peeling geometry [84]. From the trend in the surface tension, the peel adhesion should be highest on PDMS and lowest on a fluoroalkylsilane. However, they obtained the contrary result. Figure 9.1 (taken from their study) shows top view images of the instability at the contact line where the adhesive detaches from the substrate. On the PDMS substrate, the "debonding region" is a clear black line. On the fluoroalkylsilane, one observes an important distance between the finger tips (dark contact line) and the region that is actually detached from the substrate (bright regions).

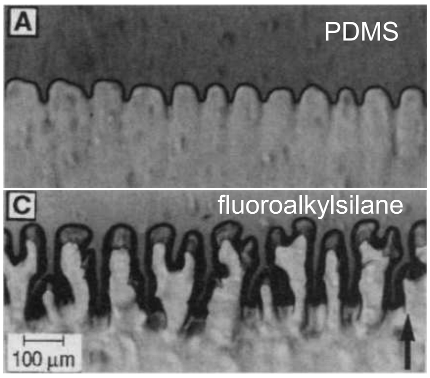

Figure 9.1.: Top view of the debonding line in a peeling geometry, from reference [84]. A standard tape is peeled from different substrates. The arrow (lower right) shows the direction of crack propagation.

From these images it is highly likely that the contact line slips freely on PDMS with a contact angle close to 90 °, and that the contact line experiences friction on the fluoroalkylsilane. The contact angle in the latter case supposedly differs strongly from 90 °. The authors showed that the very low adhesion on the PDMS substrate can be explained accounting for slippage of the adhesive on the substrate.

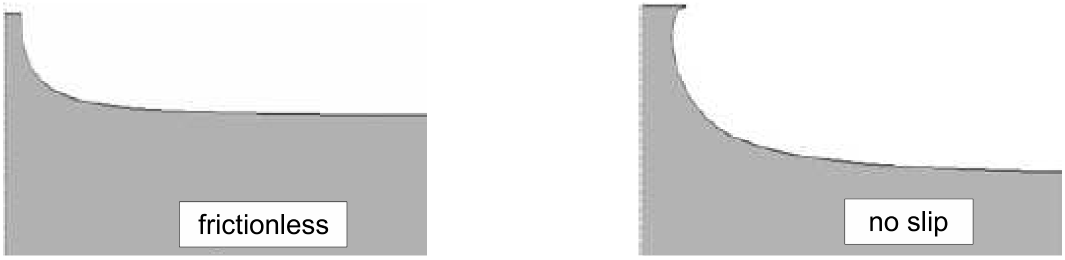

(a) Free slip boundary conditions, contact angle = 90 °

(b) No slip boundary conditions, contact angle ≠ 90 °

Figure 9.2.: Large strain simulations of the debonding of a soft elastomer for free slip and no slip boundary condition. Grey color represents the elastomer, white color the advancing fracture. The images are adapted from reference [64].

In a later study, the slippage phenomenon between a standard commercial adhesive and different substrates has been clearly demonstrated by Newby *et al.* [82]. They placed fluorescent tracer particles at the contact line and determined their position. The net movement of these particles was considerably larger on PDMS substrates, demonstrating the large slippage. Their subsequent study elucidated in more detail the connection between slippage at the interface and a decrease in the work of adhesion [83]. Amouroux *et al.* investigated the peel of an acrylic adhesive tape from PDMS with different filler contents of a resin [6]. They showed that interfacial slip could be directly associated to a small peel energy, while a limited slip leads to a development of important shear stresses and to viscoelastic dissipation in the bulk, resulting in higher peel forces.

The change in the shape of the contact line

The shape of the contact line during debonding in the probe tack geometry has been addressed from a theoretical point of view for solids. Classically, the problem of the debonding of a rigid indenter from a soft material has been studied in the approximation of a small strain linear elastic theory, as for example in the review article by Shull [107]. However, this assumption breaks down rapidly, as the deformations of soft materials are not described correctly by small strain theory and the material properties no longer stay within the linear regime [64]. Krishnan and Hui thus performed a finite strain analysis to investigate the case of a rigid indenter debonded from a soft incompressible elastomer [64]. In particular, they studied the shape of the contact line between air and elastomer when an interfacial crack is propagating. Right at the contact line, one can investigate two opposed boundary conditions. *Free slip* describes a situation in which the contact line can move over the substrate without experiencing friction. *No slip* on the other hand describes a pinned contact line that cannot move. A pinned contact line has been observed in many experiments [66]. In the classical linear elastic approximation, the boundary

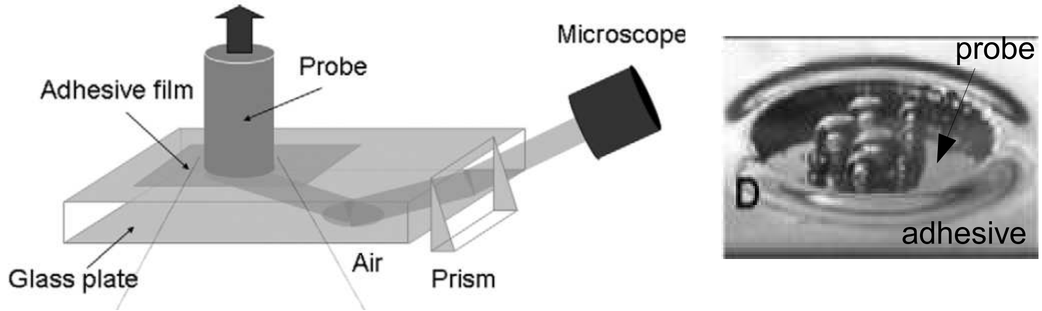

Figure 9.3.: A schematic of the $3D$-setup of Yamagutchi *et al.*, and a $3D$ view of cavity formation, both taken from reference [122].

conditions have no influence on the shear and normal force as long as the strains stay small enough. The influence of *free slip* and *no slip* boundary conditions is very pronounced in the large strain simulations of Krishan and Hui. Figure 9.2 shows results from their simulations for both boundary conditions at a given displacement of the indenter. Obviously, the shape of the contact line differs strongly in both situations. In the frictionless case, the contact line moves freely over the substrate and the contact angle is always $90\,°$. Friction at the contact line leads to the formation of shear stresses, the crack tip bends in, and the contact angle deviates strongly from $90\,°$.

All these studies witness the importance of a clearer understanding of the exact shape of the contact line and the contact angle. A major step was the recent design and development of a novel $3D$-technique by Yamaguchi and co-workers [122]. Their technique uses the total reflection in a prism to gain information on cavity formation in soft adhesive layers. The authors prepared adhesive layers on a thick glass plate. Looking through the glass plate and a prism, they obtained images of the cavity formation in acrylic adhesives, see a schematic view of the setup and a picture of cavity formation in figure 9.3. However, this setup is not suitable for a direct observation of the contact line between adhesive and probe since one looks at the cavities from the adhesive side and not from the probe side.

9.2. Setup

We adapted the mentioned $3D$-technique in collaboration with T. Yamaguchi, L. Olanier, and L. Sonnenberg and modified the setup of a tensile machine (*MTS 810*), which is usually used in the probe tack configuration [66]. The probe displacement in this machine is realized via a hydraulic system. The overall stiffness of the apparatus is much higher than in the case of the μ-tack and does not need to be accounted for. The probe diameter is $D = 10\,\text{mm}$, so that the confinement R/b in this setup is slightly higher than in the μ-tack machine for a given thickness b.

Figure 9.4(a) gives a schematic view of the adapted setup and the optical path.

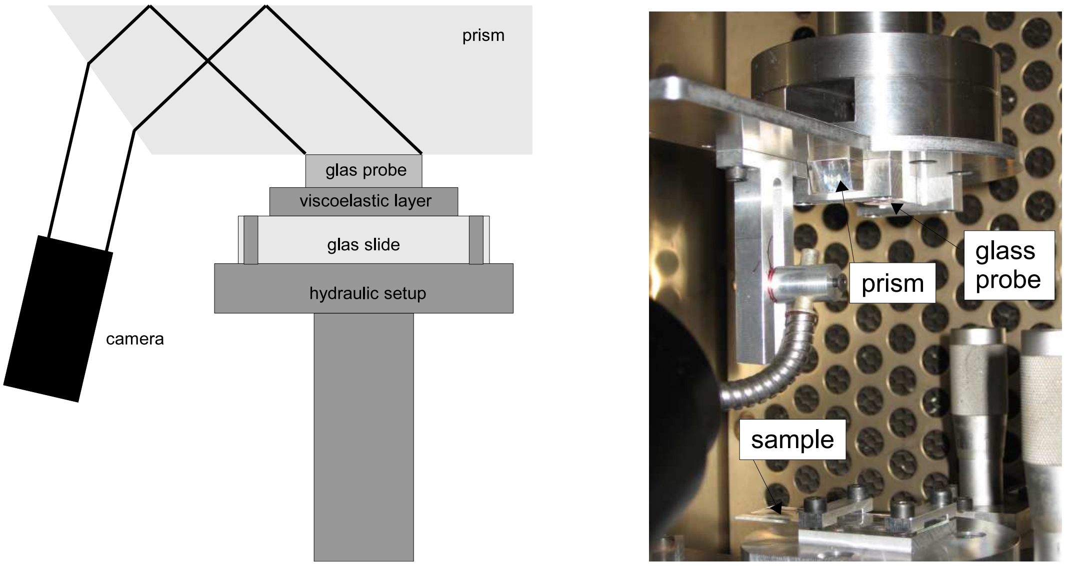

(a) Schematic view of the $3D$-setup (not to scale).

(b) The experimental setup in the laboratory.

Figure 9.4.: The $3D$ visualization technique, schematical view and setup.

The usual steel probe is not used in this setup. Instead, a glass disk with diameter $d = 10\,\mathrm{mm}$ and thickness $h = 1\,\mathrm{mm}$ is glued onto a glass prism with dimensions $10\,\mathrm{mm} \times 15\,\mathrm{mm} \times 74.7\,\mathrm{mm}$. The prism is tapered at an angle of $25\,°$. The small glass disc replaces the steel probe and acts as a contactor.[1] The illumination is realized via an optical fibre that is placed in such way that the light is directed into the prism. The probe surface is observed in total refection “from behind” through the prism and the probe itself. As soon as a contact between the probe surface and the sample is established, the setup yields $3D$ images of the interface between probe and sample. As the camera is looking *through* the probe, we have direct access to the probe-sample interface and can thus observe the exact shape of the advancing contact line.

In the following, we give some more details concerning the setup and some instructions for its use. The $3D$-setup has to be handled with great care. Currently, the setup is not permanently fixed to the traction machine but can be removed. Thus one has to pay attention to several aspects when performing experiments.

Camera position and angle The camera is fixed on a movable metal plate manufactured for this purpose. As the setup is movable, it is of utmost importance to note the exact position of the optical fibre and the camera holder, as well as the camera angle by marking their positions on the metal plate. The image quality depends

---

[1] Note that due to the different probe surfaces in the $3D$ and µ-setup, the debonding mechanisms for one material can sightly differ in both setups.

strongly on the camera position and lightning conditions. For a good image quality with well visible structures the camera has to be put in a steep angle relative to the beveled prism surface. A blunt angle results in very “flat” images with less resolution in the z-direction along the sample thickness. Due to the optical path, part of the contact area cannot be visualized in $3D$. The information in the area right behind the probe edge that faces the camera is lost. In the schematic in figure 9.4(a), this blind area is situated next to the left border of the glass probe. A steep angle reduces the blind area. In the current setup, the optimization of the camera position is hindered by the position of the optical fibre. If one intends to perform *quantitative* measurements on the images or to compare different experimental runs, it is recommended to compare only experiments that have been performed in one session without changing the tensile machine back to the usual setup in the meantime.

Lightning The lightning conditions have to be tested for each series of experiments. We stated that the optimal conditions can depend on the sample. Sometimes, we observed reflections of unknown origin that made it necessary to adapt the camera aperture and the power of the optical fibre. Mostly, strong light yielded the best results.

Image sharpness Another critical point is the image sharpness. The optical path differs a lot for the different beams in this setup, so that the camera focus is concentrated on a very small region and the depth of field is limited. Of course, before the test has started, one does not know where exactly in the sample the patterns will emerge. Therefore, finding the right camera focus is a demanding task. We eventually decided to put a small pen mark on the surface of the glass probe. Then we adjusted the focus on this pen mark. This method yielded in general a satisfying image quality.

9.3. First results

In this section, we present first results we obtained from the $3D$ visualization. Figures 9.5(a) and 9.5(b) show snapshots of interfacial and bulk fingering as taken in this configuration. The darker color indicates a direct air-probe contact. In the case of the well crosslinked material, here 2% of curing agent shown in figure 9.5(a), one sees the very flat interfacial fingering leading to a fast adhesive debonding. In the bulk case, figure 9.5(b), the fingers are thick, and no direct contact between air and probe is observed. Here, the debonding was cohesive. The qualitative difference between the bulk and interfacial case is very clear. Special care though has to be taken when interpreting these images quantitatively. The absolute distances are deformed due to the camera's angle of view. An idea of the real dimensions can be obtained recalling that the probe is a perfect circle with $R = 5\,\text{mm}$. More difficult is estimating the size in the z-direction along the film thickness. There are

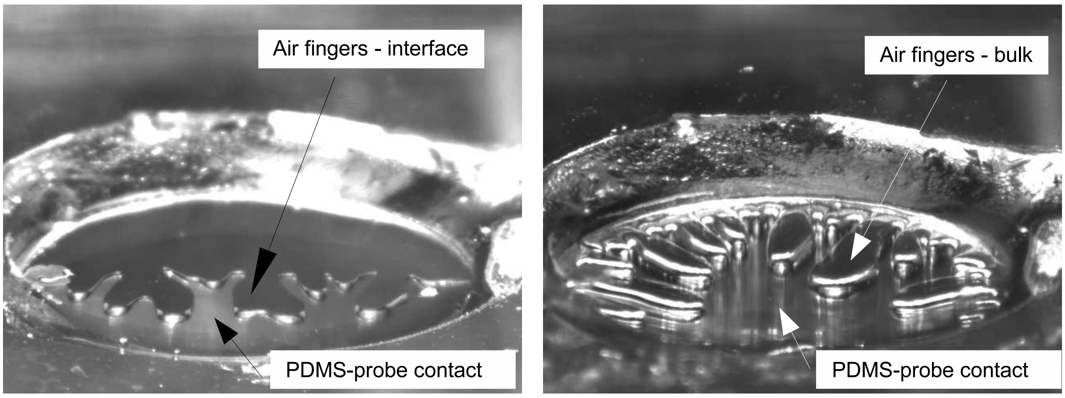

(a) Interfacial fingering at 2% of curing agent. (b) Bulk fingering at 1.1% of curing agent.

Figure 9.5.: $3D$ snapshots of interfacial and bulk fingering. The direct air-probe interface (dark color) is clearly visible in the interfacial case.

unknown deformation effects that are furthermore not necessarily linear with the position in the z-direction. To introduce a reference length, we included small glass beads with diameter $d_{\text{bead}} = 250\,\mu\text{m}$ in the PDMS samples before curing. Adding the glass beads favors the trapping of air during the sample preparation, and even after degassing, the system was very likely to grow cavities on the “bead spots”. In these experiments, the samples had a thickness $b \approx 370 - 540\,\mu\text{m}$, and the debonding speed varied between $10\,{}^{\mu\text{m}}/_{\text{s}}$ and $100\,{}^{\mu\text{m}}/_{\text{s}}$.

Finger shape

We investigated the shape of the contact line for materials with different amounts of curing agent. In figure 9.6, three dimensional views are compared to schematics and top view images. In addition, the corresponding stress-strain curves are given. The $3D$ views reveal clearly the important change in the finger shape concerning the finger thickness and the contact angle φ. Note the analogy to the shape of the contact line from simulations in figure 9.2.

Although it is difficult to extract reliable and reproducible quantitative data from the images for the moment, we estimated the finger thickness in comparison to the known bead diameter. We measured the finger thickness at the moment when the contact line started to move first. The images that are shown in figure 9.6 are, for a better illustration, taken at later (different) times.

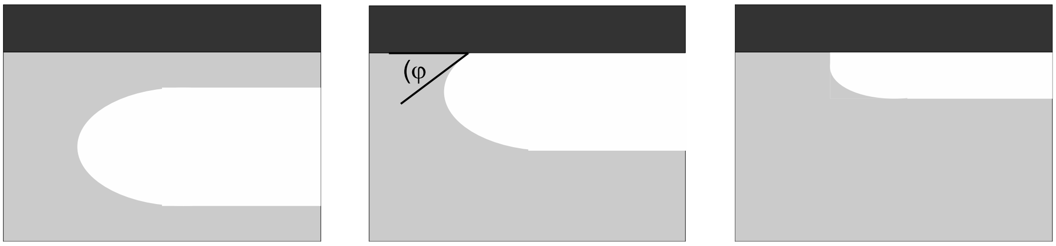

(a) Bulk finger (b) Tip blunting (c) Interfacial fracture

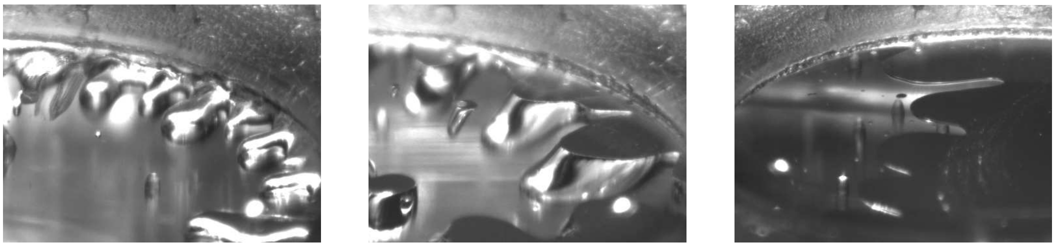

(d) $r = 0.11$. (e) $r = 0.16$ (f) $r = 0.3$.

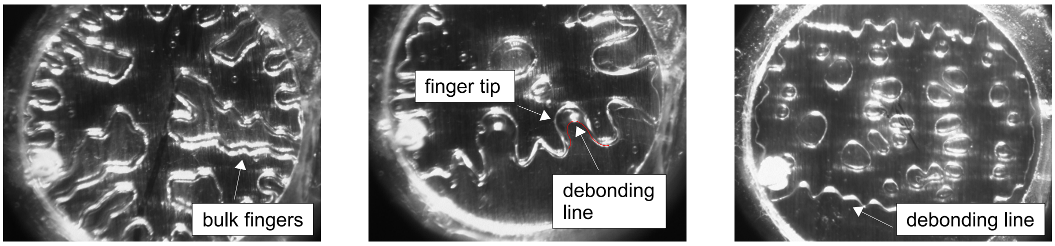

(g) $r = 0.11$. (h) $r = 0.16$ (i) $r = 0.3$.

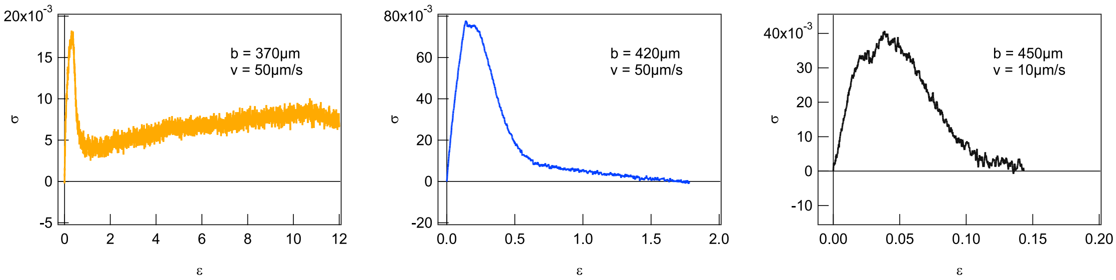

Figure 9.6.: The shape of the air-polymer interface for different mechanisms. On the schematics, white = air, grey = viscoelastic layer, black = probe surface. Bottom row: corresponding stress-displacement curves.

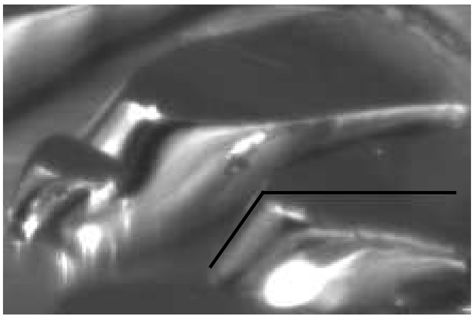

Figure 9.7.: Estimated contact angle, r = 0.16.

We now describe the finger shape in more detail for three different materials.

3% **of curing agent** The threedimensional view on figure 9.6(f) shows clearly that the contact angle φ is close to 90 ° in the case of a well cured PDMS. Comparing the finger thickness to the bead size, we estimated the height of the fingers to be about $1/20\, d_{\text{bead}}$, that is 25 µm on a layer with a thickness $b_0 = 451$ µm. It is important to note that the debonding here is clearly playing at the interface between the probe and the PDMS layer, visible from the color difference between direct air-probe contact (dark area) and PDMS-probe contact (greyish area) and from the sharp line between these two areas.

1.6% **of curing agent** This sample exhibits a more complex finger shape, see figure 9.6(e). At the borders of the probe, the dark air-probe contact area is clearly visible. At the tip however, the air fingers bend in and form a bulk finger part (tip blunting). Later, complete detachment from the probe led to adhesive debonding. The finger thickness as the contact line started to move was in the order of 170 µm for a layer thickness of $b_0 = 423$ µm. It is obvious that the exact contact angles cannot be measured from these pictures without a mathematical analysis of the deformation. However, the angle $\varphi \approx 40\,°$ can be roughly estimated from figure 9.7. Even if this value is not exact, φ is visibly different from 90 ° for this softer and more dissipating material.

1.1% **of curing agent** In contrast to the elastic case, we observed no contact angle for the material at the gel point, see figure 9.6(d). The absence of the darker color (direct air-probe contact) indicates that the air fingers are formed in the very bulk of the PDMS sample and that a thin layer of PDMS remains on the probe during the complete debonding. A contact angle therefore is not defined. The failure in this case is cohesive.

9.4. Conclusion

As shown in the introduction, the variation of the contact angle with varying viscoelastic properties has important consequences on the mechanics of debonding and on the adhesion energy. We present here for the first time a technique that visualizes *in situ* the contact line between viscoelastic material and and rigid probe in three dimensions. Thus, direct access to the boundary conditions at the advancing debonding line is provided. We believe that these images will help modeling such a complex process in the future. Furthermore, the $3D$ view confirms the description of the debonding mechanisms that we obtained from the investigation of the force curves and the initial instability. This study completes thus our previous work.

Some improvements are desirable for future work. In general, a fixed $3D$-setup will increase the reproducibility and will also avoid the lengthy adjustment procedure before every series of experiments. A high resolution camera with a high depth of focus could improve the image quality. Finally, a mathematical procedure for the image treatment, reconstituting the real dimensions from the deformations of the resulting images, is essential. It will greatly improve the analysis and opens the perspective for an exact quantitative study of the variation in the contact angle with changing viscoelastic properties.

Part IV.

Debonding of Newtonian oils

10. The time evolution of the fingering pattern in a Newtonian oil

10.1. Introduction

If one confines a viscous liquid between two circular plates and lifts the upper plate, the liquid is sucked inwards and a fingering instability evolves. It has been shown by several authors that this instability is a variant of the classical *Saffman–Taylor* instability, if one accounts for the change in plate spacing with time [104, 10, 75]. The cell is then called lifted Hele–Shaw cell. A review of different variants of the Saffman–Taylor flow can be found in reference [78].

In the previous part of this thesis, we investigated the behavior of viscoelastic materials in such a cell. We were mostly interested in the first destabilizing wavelength and showed that the Saffman–Taylor prediction works fine for that situation. The subsequent pattern formation however is non-linear and not easy to describe. In this Chapter, we investigate the pattern formation as a function of time for Newtonian oils.

The Saffman–Taylor instability in a circular cell has first been investigated by Paterson [87], see Chapter 4. He showed that the linear destabilizing wavelength λ at the onset of the instability is given by

$$\lambda = \frac{2\sqrt{3}\pi R}{\sqrt{\frac{12 V_{\mathrm{R}} R^2 \eta}{b^2 \gamma} + 1}} \,. \tag{10.1}$$

Equation 10.1 tends to $\lambda = \pi b/\sqrt{Ca}$ for a large radius R. This equation is valid both for the case of outward fingering, where a less viscous fluid pushes a more viscous filling fluid from the center of the cell, and the case of inward fingering, where the surrounding less viscous liquid pushes the filling liquid towards the center. The subsequent scenario of pattern formation however is very different in both cases. In the outward fingering situation, the tips of each finger split up subsequently, so that fractal patterns occur (see for example reference [103]). In the inward fingering situation, a strong decrease in the number of fingers is observed. This coarsening of the pattern has been linked to the competition between fingers as the available space decreases when they are growing inwards (see for example Bohr *et al.* [13]). Shelley *et al.* discussed the respective influence of geometrical effects and changing control parameter [104], but a concluding answer to this question has not been given so far. In this thesis, we investigate in more detail how the changing control parameter influences the pattern formation.

In the following, we will speak in terms of *number of fingers* rather than in terms of wavelength. The reason therefor is that the radius R of the retracting circle is changing with time and the wavelength has to be calculated in reference to the perimeter. In such a situation, the number of fingers is intuitively more accessible than the wavelength. The number of fingers N represents the dimensionless wave vector $k' = kR$. This can be seen from

$$\lambda = \frac{2\pi R}{N} = \frac{2\pi}{k} \, . \tag{10.2}$$

Shelley *et al.* [104] and Ben Amar *et al.* [10] investigated theoretically the situation of a Newtonian oil in the lifted Hele–Shaw cell. They both introduced a dimensionless surface tension τ_0 that controls the number of fingers at the onset of the instability. We define the control parameter τ_0 as [104]

$$\tau_0 = \frac{\gamma {b_0}^3}{12 v_0 \eta {R_0}^3} \, . \tag{10.3}$$

Therein, γ is the surface tension between the filling and the surrounding liquid, b_0 the initial gap width, R_0 the initial radius of the oil blob corresponding to the radius of the Hele–Shaw cell, v_0 the constant lifting speed, and η the viscosity of the filling liquid. The surface tension between air and silicone oil is $\gamma = 20\,{}^{\mathrm{mN}}/_{\mathrm{m}}$.

The initial number of fingers $N_0 = 2\pi R_0/\lambda$, where λ is the fastest growing wavelength at the onset of the instability, is linked to τ_0 as

$$N_0 = \sqrt{\frac{1}{3}\left(1 + \frac{1}{2\tau_0}\right)} \, . \tag{10.4}$$

This equation is equivalent to equation 10.1.

Ben Amar *et al.* investigated the instability analytically for short times [10]. They also took into account the three dimensional shape of the meniscus between oil and air. Shelley *et al.* [104] performed numerical simulations of the Navier–Stokes equations in two dimensions for the complete debonding process. Lindner *et al.* compared numerical and experimental results [75]. They found that the number of fingers is controlled by τ_0, whereas the perimeter Γ, which is linked to the finger amplitude, varies with the exact experimental conditions. The influence of the fingers on the force that is needed to remove the two plates from each other remained unclear. Lindner *et al.* performed some experiments with different combinations of experimental parameters yielding the same τ_0, but no complete systematic study was conducted. In this Chapter, we focus on these open questions.

10.2. Materials and methods

In this section, we characterize first the materials and describe then the experimental protocol.

	Nominal viscosity	y_0	A	B
oil 100	100 Pa s	0	142.17 ± 1.29	0.0152 ± 0.0003
oil 10	10 Pa s	0	17.202 ± 0.246	0.0164 ± 0.0005

Table 10.1.: Fit parameters to an exponential law describing the temperature dependence of the viscosity for two Newtonian oil, see figure 10.2.

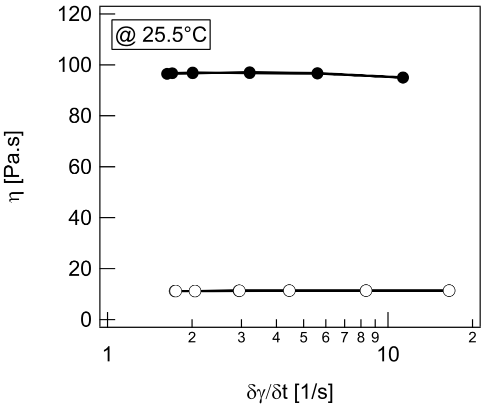

Figure 10.1.: The viscosity versus the shear rate for oil 100 ($\eta \approx 100\,\mathrm{Pa\,s}$) and oil 10 ($\eta \approx 12\,\mathrm{Pa\,s}$) at 25.5 °C.

10.2.1. Materials

We used two silicone oils (PDMS) with different viscosities. The oil called "oil 100" in the following had a nominal viscosity $\eta = 100\,\mathrm{Pa\,s}$, the oil called "oil 10" had a a nominal viscosity $\eta = 10\,\mathrm{Pa\,s}$. They were purchased at *Aldrich*.

Figure 10.1 shows the shear viscosity as a function of shear rate for both oils. The data was obtained in a *Haake RS 100 Rheostress* rheometer using a cone-plate geometry with diameter $d = 35\,\mathrm{mm}$ and an angle $\theta = 2^\circ$ at $T = 25.5\,^\circ\mathrm{C}$. The viscosity does not vary with the shear rate and is considered as constant in the experimentally relevant range of shear rates. A oscillatory frequency sweep revealed that $G'' \gg G'$ in this range of frequencies; the oils behave as Newtonian liquids.

However, the viscosity depends on the temperature. As we cannot control the temperature in the experimental setup, we determined η as a function of T between $T = 24\,^\circ\mathrm{C}$ and $T = 40\,^\circ\mathrm{C}$ at $\dot\gamma \approx 5\,{}^1\!/\mathrm{s}$. The data could be fitted with an exponential law

$$\eta(T) = y_0 + A\mathrm{e}^{-B\,T}\,, \tag{10.5}$$

see figure 10.2. The resulting values of the fit parameters are given in table 10.1.

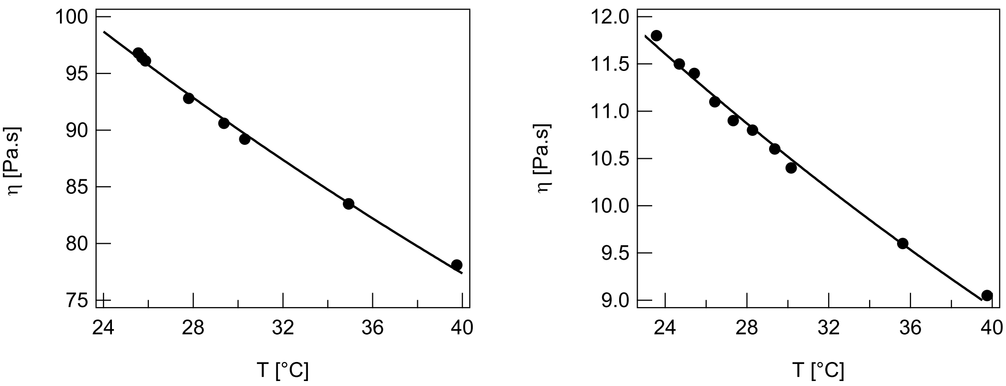

(a) Oil 100 at $\dot{\gamma} = 6\,\mathrm{s}^{-1}$.

(b) Oil 10 at $\dot{\gamma} = 4\,\mathrm{s}^{-1}$.

Figure 10.2.: Viscosity as a function of temperature. The solid line is a fit to an exponential law.

10.2.2. Experimental protocol

Experiments were performed in the μ-tack machine described earlier, yet with a slightly different experimental protocol. It was not possible to prepare samples of a given thickness on microscope glass slides as in the previous experiments, as the oil was flowing too fast. Instead, we proceeded in the following way.

The lifted Hele–Shaw cell consists in an upper microscope glass slide and a lower circular steel probe with a given radius R_0. The probe radius determines the size of the cell. The upper plate can be lifted at a defined speed. We used a thin PSA film on a microscope glass slide for a coarse alignment of probe and upper glass slide. Then we precleaned a microscope glass side with acetone and ethanol and put it into the apparatus. We approached the metal probe by hand slowly to the glass slide until contact was established and the force became non-zero. At the same time, interference fringes were observed upon contact through the camera mounted on the microscope. The final alignment was done at this moment by rendering the fringes as symmetric as possible. Once the alignment was satisfying, we moved the probe away from the glass slide in very small steps. We determined the zero position $b = 0\,\mu\mathrm{m}$ as the force became zero again and the interference fringes disappeared. Lowering the probe by several millimeters, a drop of silicone oil was then placed on the probe with a syringe. Finally, we brought the probe slowly into the desired position. A typical value was $b_0 = 100\,\mu\mathrm{m}$. The experiment itself started when we lifted the upper glass slide at a given speed v_0. During the experiment, images were taken by the digital camera, allowing for a good visualization of the emerging pattern and its evolution in time.

A crucial point in the course of an experiment was to have reproducible boundary conditions. It was impossible to put the exact volume of oil that corresponds to the initial cell volume onto the probe in the first place. Thus, we always had to remove an excess of oil at the borders of the probe when the probe arrived at its starting position. The borders had to be cleaned very properly with small instruments made for this purpose. Every small dust particle represents a perturbation of the boundary and disturbs the fingering pattern, and every extra amount of oil surrounding the probe introduces time shifts in the evolution of the finger pattern.

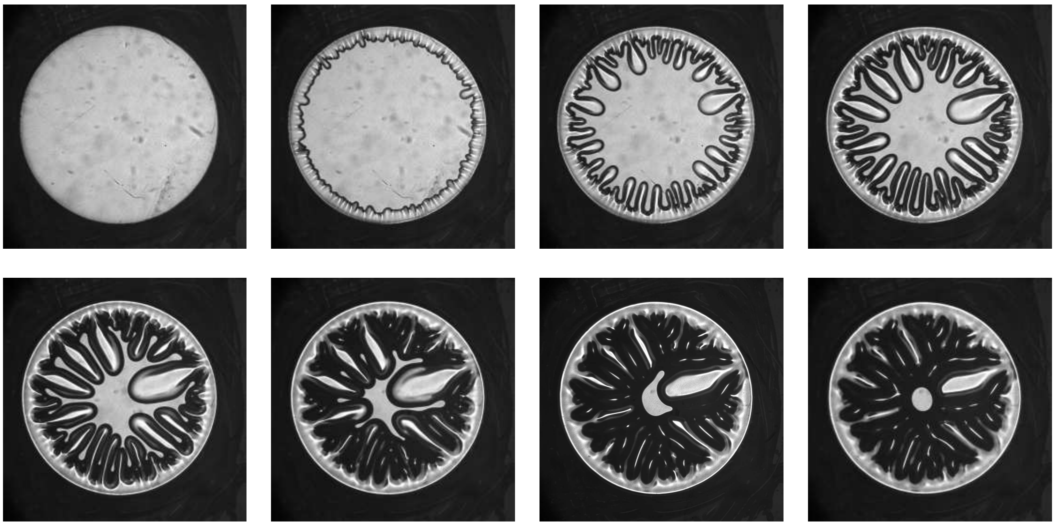

Figure 10.3.: The Saffman-Taylor instability at different times in the lifted Hele–Shaw cell. $R_0 = 3\,\mathrm{mm}$, $b_0 = 50\,\mu\mathrm{m}$, $v_0 = 8\,{}^{\mu\mathrm{m}}/_{\mathrm{s}}$, $\eta = 96\,\mathrm{Pa\,s}$.

Figure 10.3 shows a typical experiment in top view at different times. At the beginning, the system is at rest and the $2D$ projection of the interface between oil and air is ideally a perfect circle. The contact line is not visible as it lies on the border of the probe. The light area represents the metal probe covered with oil, the black line the interface between air and oil. At $t = 0$, the oil starts to flow inwards and the circular interface retracts as the upper glass plate moves upwards. The interface is soon destabilized and starts to undulate. The amplitude of these undulations increases and air fingers grow inwards. Figure 10.4 shows an overlay of the contact line for different times. Lighter colors correspond to later times. The finger amplitude can be strong or weak depending on the experimental parameters. The finger growth is very pronounced in figure 10.3. The number of fingers decreases with time. Finally all the fingers disappear, the interface becomes circular again, and one final fibril remains between glass plate and probe. Its stretching is dominated by material flow. It finally breaks up triggered by the Rayleigh–Plateau instability [90, 95], the test is stopped, and the glass plate and probe return to their initial position.

We investigate different realizations of the same control parameter τ_0. To do so, we change the initial gap width and the oil viscosity and adapt at the same time the lifting speed to keep τ_0 constant. As the temperature cannot be controlled in

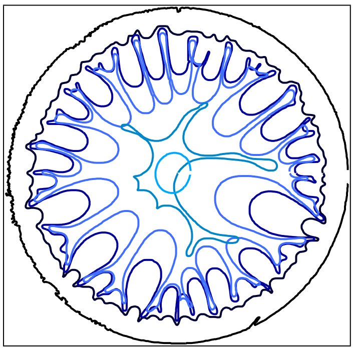

Figure 10.4.: Superposition of the contact lines from figure 10.3. Lighter colors correspond to later times.

our setup, we noted the temperature for each experiment and accounted for the change in the viscosity in the calculation of τ_0. We performed several experiments in one series, that is, with the same oil and different b_0. When an experiment at a certain initial gap width was completed, we returned to the starting position $b = b_0$. Then we moved the steel probe a little closer to the glass plate and proceeded to a second experiment. It is important to make sure that all traces from the previous experiments are deleted to exclude memory effects. The interface was again cleaned from excess oil and the next test was started. In this way, we performed three to four experiments in one series.

We checked that using several times the same oil is a valid protocol by performing experiments where fresh oil was used for every single experiment, including a new setting of the zero point. The results were in perfect agreement with the ones obtained from the protocol that uses several times the same oil.

Determination of t_0

A crucial point was the determination of the starting time $t_0 = 0$, that is the moment where the motors start to lift the upper glass plate and the oil starts to move. Normally, the experimental setup is equipped with a trigger that activates a timer at the moment the motors start to move. In this way, each image can be linked to a time stamp from the timer. However, technical problems due to an incompatibility of camera and trigger made it impossible to use the trigger. We decided instead to determine t_0 visually on the images. We started the camera before the actual experiment. The camera software automatically generates a time stamp T_i for each image i. The image on which the oil started to move could be determined from very small dust particles, which were always present in the oil and were visible on a zoom. We determined the time t_i of an image i relative to the moment where the oil first moved as

$@T = 25°\text{C}$	$\eta[\text{Pas}]$	$b_0[\mu\text{m}]$	$v_0[\mu\text{m/s}]$	$\eta[\text{Pas}]$	$b_0[\mu\text{m}]$	$v_0[\mu\text{m/s}]$
$\tau_0 \simeq 9.6 \times 10^{-6}$	97.2	100	66	11.4	75	238
	97.2	75	28	11.4	50	71
	97.2	50	8	11.4	35	24
	97.2	25	1	11.4	25	9

Table 10.2.: Different realizations of the control parameter $\tau = 9.6 \times 10^{-6}$.

$$t_i = T_i - T_{\text{first move}} + \frac{T_{\text{first move}} - T_{\text{last still}}}{2} \; . \tag{10.6}$$

T_i is the time stamp of image i. $T_{\text{first move}}$ and $T_{\text{last still}}$ denote the time stamps of the two images between which the oil started to move first. In this way, t_0 lies between the last image on which the oil did not move and the first image on which the dust particles changed their position. This method yields an uncertainty in the time of the order of the inverse frame acquisition rate of the camera.

10.3. The number of fingers in comparison to linear $2D$ theory

The number of fingers changes strongly as a function of time. In a first step, we chose the control parameter $\tau_0 = 9.6 \times 10^{-6}$. It yields strongly growing fingers, see figure 10.3, resulting in images that are easy to treat. Furthermore, our choice of τ_0 can be obtained with different parameter combinations within the experimental limitations. Table 10.2 gives the reference for the combination of parameters we used.

Experiments with different v_0 and b_0 can be compared as a function of the dimensionless time

$$t' = t \, \frac{v_0}{b_0} \tag{10.7}$$

with $t_0 = 0$ as defined in equation 10.6. Figure 10.5 shows the number of fingers N versus dimensionless time t' for a large number of experiments with different combinations of the experimental parameters. The scatter in the experimental data is large, the initial number of fingers can differ by up to a factor of 2. The decrease in N with t' is extremely pronounced for small times. The determination of N_0 is thus demanding in the case of a pure silicone oil: the amplitudes are very small and counting is difficult in a region where the number of fingers changes a lot.

Several processes can interfere in the decrease of the number of fingers. On the one hand, the control parameter is changing with time. This means that at each moment, a different wavelength is the wavelength with the highest growth rate in a sense of the linear stability analysis. On the other hand, geometrical effects can influence the fingering pattern. As the fingers are growing inwards, the available

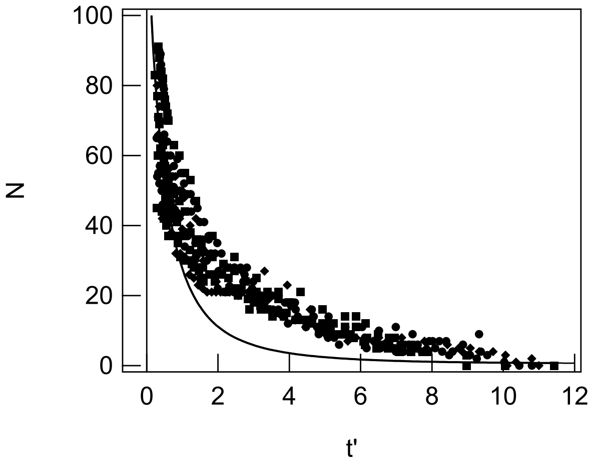

Figure 10.5.: N versus t' for $\tau_0 = 9.6 \times 10^{-6}$. The solid line corresponds to the theoretical prediction from linear stability analysis equation 10.9.

space is more and more restricted, their growth is hindered, and shielding effects are expected.

We concentrate now on the effect of the changing control parameter. To obtain τ as a function of t', one simply replaces all quantities in τ_0 by their time dependent analogue, see also section 4.2.2. The equation for the time dependent τ then reads [104]

$$\tau(t') = \frac{\gamma b(t')^3}{12 v(t') \eta R(t')^3} \ . \tag{10.8}$$

Hence follows a time dependence of the number of fingers

$$N(t') = \sqrt{\frac{1}{3}\left(1 + \frac{1}{2\tau_0 (1+t')^{9/2}}\right)} \ . \tag{10.9}$$

Note that for higher numbers of fingers, one can drop the 1 in equation 10.9, and the number of fingers depends on the time as a power law,

$$N^2 \propto (1+t')^{-9/2} \ . \tag{10.10}$$

This equation based on two dimensional linear stability analysis is the simplest way to approach the change in the number of fingers. One assumes a freshly starting experiment at each moment, albeit with an interface that is disturbed by the fingers that have evolved previously. The straight line in figure 10.5 corresponds to the theoretical prediction from equation 10.9 for $\tau_0 = 9.6 \times 10^{-6}$. At the beginning, the average number of fingers is of the same order of magnitude in experiments and theory. Subsequently, the number of fingers decreases much slower in the experiments than calculated and reaches zero at later times, so that the theoretical prediction

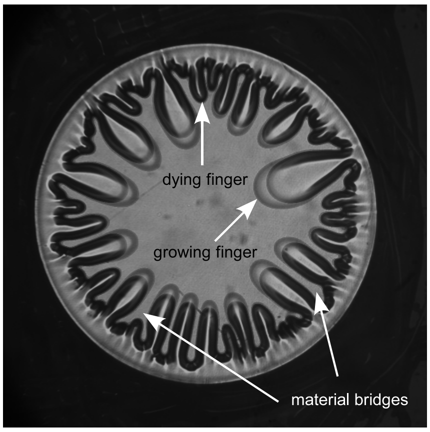

Figure 10.6.: Overlay of two images at different times. The lighter contact line corresponds to $t_2 > t_1$ (darker contact line).

always underestimates the actual number of fingers. This result has been described before. Lindner *et al.* compared the number of fingers from numerical experiments, laboratory experiments, and the linear theory [75]. They found that the number of fingers from experiments and simulations agreed, whereas they were always higher than the most unstable number of fingers from linear theory. In the following, we will discuss in more detail the origin of this deviation.

Growing and dying fingers

A closer look at the images of the experiments reveals that the decrease in the number of fingers is caused by a *dying out* of fingers. We understand thereby that a certain finger stops growing inwards at a certain time and stays fixed at its current position. From that moment on, only the surrounding fingers continue to move inwards and they outrun the fixed finger. The material bridges that are left between the air fingers, see figure 10.6, contract to the middle of the cell, so that a fixed finger finally disappears. The retraction of these bridges is clearly visible in figure 10.4. Figure 10.6 shows an overlay of two images at different times t'_1 and $t'_2 > t'_1$. The lighter, more transparent image has been taken at a later time. The finger labeled as “growing finger” is advancing between t'_1 and t'_2. On the contrary, the finger labeled as “dying finger” does not change its position. We call a finger on an image i *dying* (or stagnant), if its tip does not move towards the center of the cell between image i and image $i+1$. A dying finger can also be observed on the last two images of figure 10.3. This coarsening starts very early in the debonding process.

Figure 10.7 shows the number of growing fingers N_{grow} as a function of time. It is of course smaller than the total number of fingers N_{all}. At the very beginning, where the fingers are harder to distinguish, it is difficult to judge whether each finger is growing. Comparing the number of growing fingers to the linear prediction from equation 10.9, we find that the experimental results and the linear prediction agree surprisingly well. This is a startling result, as it implies that the system chooses the number of fingers corresponding to the linearly most unstable wavelength at every moment in time and makes them grow.

As the number of growing fingers is governed by the changing control parameter, we conclude that geometrical shielding effect play only a secondary role. To separate geometrical effects, it is necessary to perform an experiment at constant control parameter. The lifting speed has to be changed in such way that the variable gap distance is compensated and $\tau(t') = \tau_0$. A decrease in the finger number would then be caused by geometric constraints. Such an experiment could unfortunately not be realized in our setup.

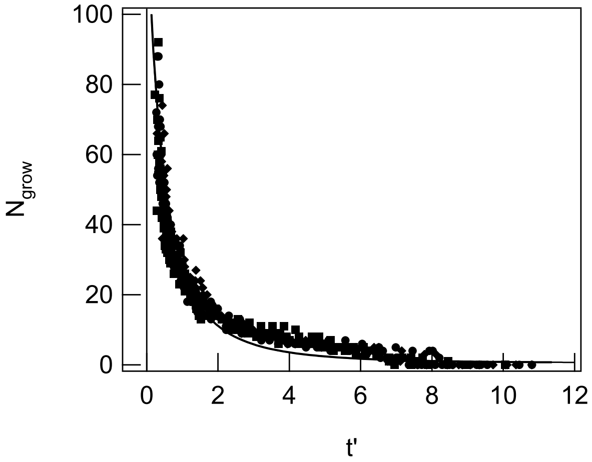

Figure 10.7.: The number of growing fingers versus t' in comparison to the linear theoretical prediction from equation 10.9 for $\tau_0 = 9.6 \times 10^{-6}$.

To conclude so far, the total number of fingers as a function of time exceeds the number of fingers predicted from linear theory. This result has been observed as well in a laboratory experiment (this thesis and reference [75]) as in numerical simulations based on the $2D$ Navier–Stokes equations [75]. The experimental situation can be depicted in the following way. Consider a number of fingers N_1 at $t' = t'_1$. At $t'_2 = t'_1 + \Delta t$, a number of fingers N_2 is growing. However, $N_1 - N_2$ "additional" fingers are present in the experiment. Even if they are not growing, they are contributing to the total number of fingers. The oil that remains between the air fingers retracts to the cell center subsequently and the stagnant fingers therefore die out.

The total number of fingers is imperatively higher than linear theory predicts, unless the material bridges contract very fast. In this case, the advancing finger base "keeps up" with the advancing finger tips and the finger amplitudes are vanishing. We have shown that the number of growing fingers is described by a time dependent control parameter derived from linear stability analysis.

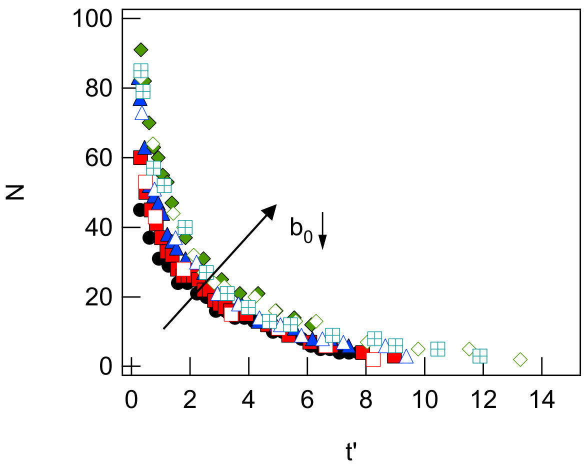

Figure 10.8.: N versus t'. Full symbols: $\eta = 95.6\,\mathrm{Pa\,s}$, open symbols: $\eta = 10.8\,\mathrm{Pa\,s}$. $b_0 = 100\,\mu\mathrm{m}$ (●), $b_0 = 75\,\mu\mathrm{m}$ (🟥), $b_0 = 50\,\mu\mathrm{m}$ (▲), $b_0 = 35\,\mu\mathrm{m}$(⊞), and $b_0 = 25\,\mu\mathrm{m}$ (◆).

C	R_0[mm]	b_0[µm]
30	5 ●	150
40		125
60		84
120		41

R_0[mm]	b_0[µm]
3 ■	100
	75
	50
	25

R_0[mm]	b_0[µm]
1.5 ◆	50
	38
	25
	13

Table 10.3.: The different realizations of the control parameter $\tau = 9.6 \times 10^{-6}$ for the same confinement $C = R_0/b_0$ and different radii.

10.4. Confinement dependence

In this section, we concentrate on the total number of fingers N for different realizations of τ_0. We represent eight different realizations in figure 10.8. Obviously, the data falls on a broad curve, but closer inspection reveals that the scatter is not arbitrary. Data with the exact same experimental conditions (same viscosity, gap width, and speed) are extremely reproducible. The number of fingers shows a clear tendency: the thinner the initial layer is, the higher the total number of fingers is.

The two different oils (open and full symbols) can obviously not be separated as they fall on the same curves in figure 10.8. As we kept the control parameter constant, we changed the initial gap width and the lifting speed simultaneously for one oil. However, a closer inspection of figure 10.8 shows that the effects of b_0 and v_0 can be separated. As an example, we compare the experiment with $\eta = 95.6\,\mathrm{Pa\,s}$, $b_0 = 75\,\mu\mathrm{m}$, $v_0 = 28\,\mu\mathrm{m/s}$ represented by red full squares 🟥, and the one with $\eta = 10.8\,\mathrm{Pa\,s}$, $b_0 = 75\,\mu\mathrm{m}$, $v_0 = 251\,\mu\mathrm{m/s}$ represented by red open squares □. Even though the speed and also the viscosity differ by about a factor of 9, the data fall very close to each other. This implies that the variation in the number of

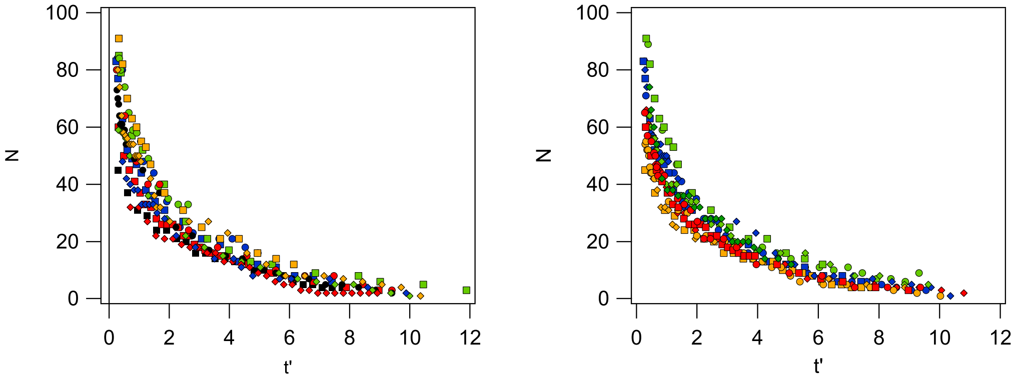

(a)

(b)

orange	$b_0 = 25\,\mu\mathrm{m}$
green	$b_0 = 35\,\mu\mathrm{m}$
blue	$b_0 = 50\,\mu\mathrm{m}$
red	$b_0 = 75\,\mu\mathrm{m}$
black	$b_0 = 100\,\mu\mathrm{m}$

orange	$C = 30$
red	$C = 40$
blue	$C = 60$
green	$C = 120$

Figure 10.9.: N versus t'. Circles correspond to $R_0 = 3\,\mathrm{mm}$, squares to $R_0 = 5\,\mathrm{mm}$, and diamonds to $R_0 = 1.5\,\mathrm{mm}$. Color code: left side b_0, right side C.

fingers cannot be attributed to the changed speed but to the difference in the initial gap width.

Naturally, we investigated whether this effect is governed by the absolute initial gap width or by the confinement (or aspect ratio) $C = R_0/b_0$. Therefore, we performed tests with three different probe radii: $R_0 = 1.5\,\mathrm{mm}$, $R_0 = 3\,\mathrm{mm}$, and $R_0 = 5\,\mathrm{mm}$. We realized different values of the confinement for all three probe sizes and compared as well different absolute thicknesses. The parameters for these experiments are given in table 10.3.

Figure 10.9(a) displays the results for different probe radii and different initial gaps. The speed is always adapted in such a way that the control parameter remains constant at $\tau_0 = 9.6 \times 10^{-6}$. The different radii are encoded by different symbols, the initial gap b_0 by different colors. Figure 10.9(b) shows the same data; again, different radii are encoded by different symbols, but the color encodes now different initial confinements C. Comparing figure 10.9(a) and 10.9(b), a tendency is manifestly distinguishable with the confinement, but not with the absolute gap distance. Obviously, a higher degree of confinement yields a higher number of fingers. The data for $R_0 = 1.5\,\mathrm{mm}$ and $C = 115$ represented by green diamonds ◆ do not scale well with the confinement. They rather fall onto the data with $C = 60$ (blue markers). This experimental condition however remains the only irregularity. It might be explained by the very small initial gap width ($b_0 = 13\,\mu\mathrm{m}$) that challenges the experimental resolution.

τ_0	b_0	η	R_0
9.6×10^{-6}	yes	yes	yes
4.5×10^{-6}	yes	no	no
3×10^{-5}	yes	yes	no

Table 10.4.: Changed parameters for each τ_0.

In total, we investigated several realizations of three different control parameters τ_0 ($4.5 \times 10^{-6} < 9.6 \times 10^{-6} < 3.0 \times 10^{-5}$). The changed experimental conditions for each τ_0 are displayed in table 10.4. Figure 10.10 displays images for 4.5×10^{-6} and 3.0×10^{-5} at time $t' = 2$.

Figure 10.11 shows N_{all} and N_{grow} as a function of t' for all three τ_0. The broad scatter in the total number of fingers due to different degrees of confinement is not observed in the number of growing fingers (exception made for the number of fingers at the very first moment). The results for all three τ_0 are in agreement: the more the system is confined, the more fingers appear. $N_{\text{grow}}(t')$ is well described by linear theory for each control parameter, at least for early times, and does not depend on the confinement. The confinement dependence of the total number of fingers is more or less pronounced depending on the control parameter. This is visible as well on the images at fixed time in figure 10.10 as in the number of fingers as a function of time in figure 10.11. The dependence on C is most pronounced for the smallest control parameter 4.5×10^{-6}. On the contrary, the influence of the confinement is harder to distinguish for the highest control parameter 3.0×10^{-5}. The finger amplitude is smaller for higher control parameters and counting becomes harder, see figure 10.10. This might explain why Lindner *et al.* found that the number of fingers does *not* depend on the exact experimental conditions [75]. They were working at higher control parameters (2.5×10^{-5}, 8.4×10^{-5}, and 2×10^{-4}), where the effect might not be clearly visible anymore.

(a) $b_0 = 120\,\mu\mathrm{m}$, $v_0 = 35\,{}^{\mu\mathrm{m}}\!/\!{}_{\mathrm{s}}$ (b) $b_0 = 100\,\mu\mathrm{m}$, $v_0 = 20\,{}^{\mu\mathrm{m}}\!/\!{}_{\mathrm{s}}$ (c) $b_0 = 75\,\mu\mathrm{m}$, $v_0 = 8.5\,{}^{\mu\mathrm{m}}\!/\!{}_{\mathrm{s}}$ (d) $b_0 = 55\,\mu\mathrm{m}$, $v_0 = 3.4\,{}^{\mu\mathrm{m}}\!/\!{}_{\mathrm{s}}$

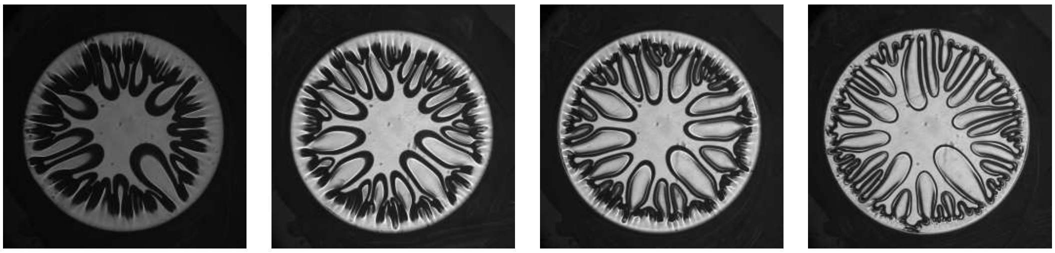

(e) $b_0 = 100\,\mu\mathrm{m}$, $v_0 = 137\,{}^{\mu\mathrm{m}}\!/\!{}_{\mathrm{s}}$ (f) $b_0 = 75\,\mu\mathrm{m}$, $v_0 = 58\,{}^{\mu\mathrm{m}}\!/\!{}_{\mathrm{s}}$ (g) $b_0 = 50\,\mu\mathrm{m}$, $v_0 = 17\,{}^{\mu\mathrm{m}}\!/\!{}_{\mathrm{s}}$ (h) $b_0 = 25\,\mu\mathrm{m}$, $v_0 = 2\,{}^{\mu\mathrm{m}}\!/\!{}_{\mathrm{s}}$

Figure 10.10.: Images at $\tau_0 = 3.0 \times 10^{-5}$ (top row) and $\tau_0 = 4.5 \times 10^{-6}$ (bottom row) and $t' = 2$. All experiments have been conducted with oil 100 and $R_0 = 3\,\mathrm{mm}$.

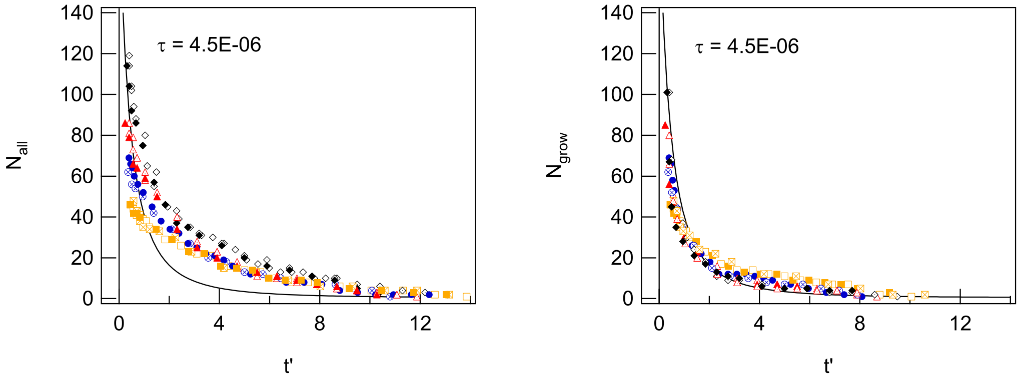

(a) N_{all} versus t', $\tau_0 = 4.5 \times 10^{-6}$. (b) N_{grow} versus t', $\tau_0 = 4.5 \times 10^{-6}$.

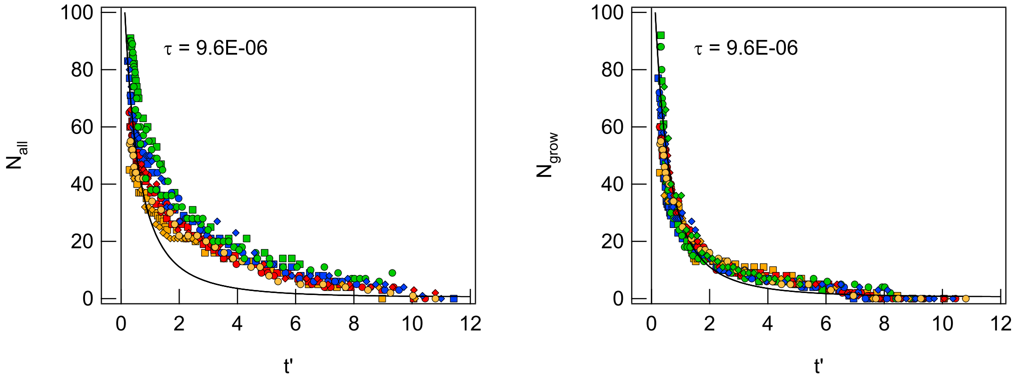

(c) N_{all} versus t', $\tau_0 = 9.6 \times 10^{-6}$. (d) N_{grow} versus t', $\tau_0 = 9.6 \times 10^{-6}$.

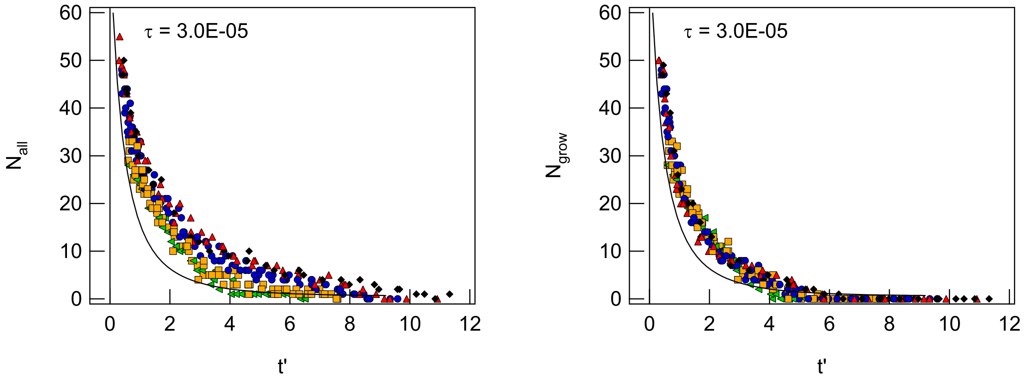

(e) N_{all} versus t', $\tau_0 = 3.0 \times 10^{-5}$. (f) N_{grow} versus t', $\tau_0 = 3.0 \times 10^{-5}$.

τ_0	Symbol	C	τ_0	Symbol	C	τ_0	Symbol	C
4.5×10^{-6}			9.6×10^{-6}			3×10^{-5}	◀	25
	■	30		orange	30		■	30
	●	40		red	40		●	40
	▲	60		blue	60		▲	54.5
	◆	120		green	120		◆	120

Figure 10.11.: The total number and number of growing fingers versus t', for $\tau_0 = 4.5 \times 10^{-5}$, $\tau_0 = 9.6 \times 10^{-6}$, and $\tau_0 = 3.0 \times 10^{-6}$ in comparison to the 2D theoretical prediction from equation 10.9.

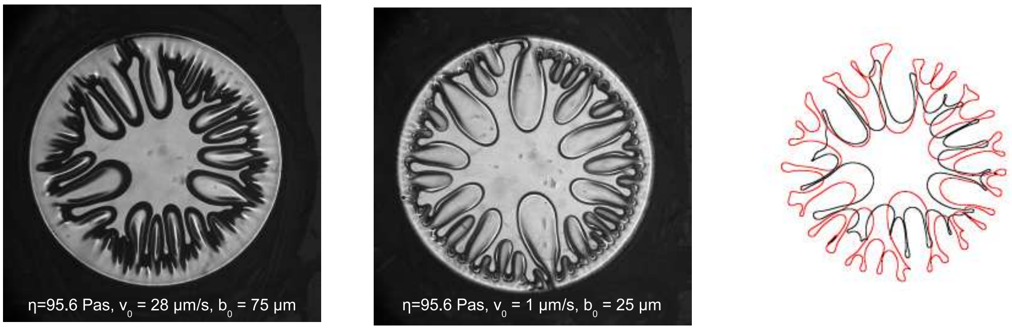

(a) (b) (c) Overlay of (a) and (b).

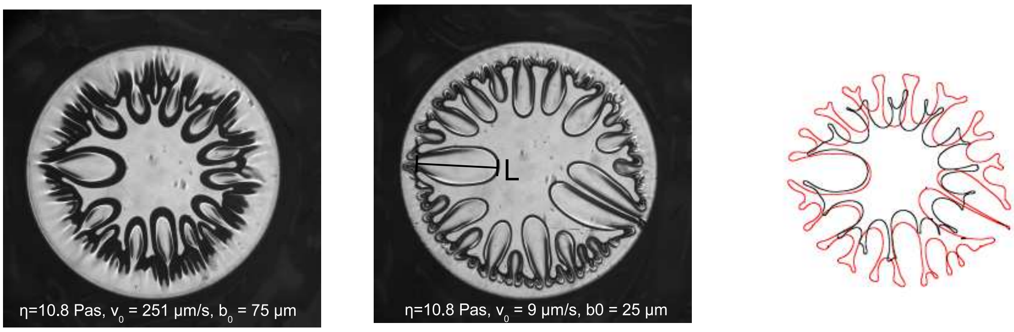

(d) (e) (f) Overlay of (d) and (e).

Figure 10.12.: Different realizations of $\tau_0 = 9.6 \times 10^{-6}$ at $t' = 2$. Upper row, oil 100, lower row, oil 10. For both oils, the finger amplitudes are higher at higher confinement.

10.5. Finger growth

In this section, we discuss in more detail the finger amplitude and its influence on the total number of fingers. Figure 10.12 shows a snapshot at $t' = 2$ of four different experimental conditions. The upper row shows experiments with oil 100 with initial gap width $b_0 = 75\,\mu\text{m}$ (a) and $25\,\mu\text{m}$ (b). The lower row represents experiments with oil 10, again with $b_0 = 75\,\mu\text{m}$ (d) and $25\,\mu\text{m}$ (e). The control parameter is $\tau_0 = 9.6 \times 10^{-6}$. Obviously, the finger amplitude, that is, the distance between finger tip and finger base designated with “L” in figure 10.12(e), depends strongly on the confinement, but not on the oil viscosity or speed. Higher confinements (in the middle) yield higher amplitudes. This tendency is as well clearly visible in figure 10.10. Overlays of the two confinements (red $b_0 = 25\,\mu\text{m}$, black $b_0 = 75\,\mu\text{m}$), are shown on the right side of figure 10.12 for each oil. This representation reveals clearly that the finger tips are at similar positions for each confinement. However, the position of the finger base varies strongly. In other terms, the higher the confinement is, the slower the material between the air fingers contracts to the cell center.

The perimeter as a measure for the finger growth

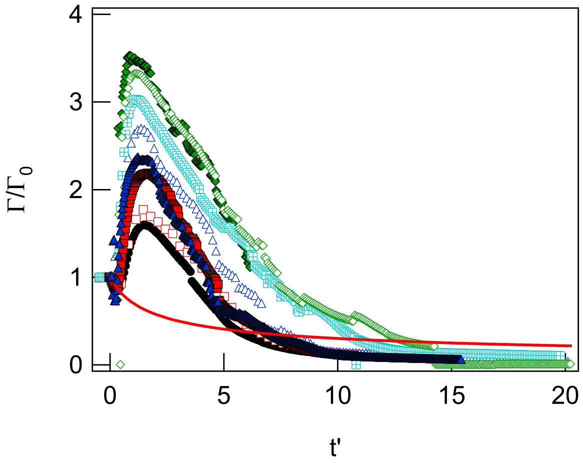

Figure 10.13.: The dimensionless perimeter as a function of dimensionless time for different realizations of $\tau_0 = 9.6 \times 10^{-6}$. $C = 30$ (Black circles), $C = 40$ (red squares), $C = 60$ (blue triangles), $C = 86$ (crossed squares), $C = 120$ (green diamonds). Full symbols refer to oil 100, open symbols to oil 10. The straight line is calculated from volume conservation (equation 4.34)

A quantitative measure of the finger growth is the perimeter Γ along the contact line. Higher finger amplitudes lead to a higher value of Γ. We have shown that the total number of fingers depends on the confinement. One tends to divide the perimeter by the notal number of fingers to have a measure for the finger shape. However, we have shown that all fingers are not growing alike. The main part of the perimeter is used by the growing fingers, the dying fingers only take a small amount. A correct measure therefore would be to sum up the outline of each growing finger and divide by the number of growing fingers. This was technically not doable. Arguing that the part of the perimeter occupied by the non growing fingers is small, we decided to consider the total circumference normalized by the initial circumference.

Figure 10.13 displays the perimeter Γ normalized by the initial perimeter $\Gamma_0 = 2\pi R_0$ as a function of dimensionless time. Black circles represent $C = 30$, red squares $C = 40$, blue triangles $C = 60$, crossed squares $C = 86$, and green diamonds $C = 120$. Full symbols represent oil 100, open symbols oil 10. The straight line corresponds to a retracting circle calculated from volume conservation (equation 4.34),

$$\frac{\Gamma(t')}{\Gamma_0} = \frac{1}{\sqrt{1+t'}} \,. \tag{10.11}$$

The general tendency in figure 10.13 is in agreement with the observations from images in figure 10.12: the perimeter is longer the more confined the system is. It can be up to a factor of 7 higher than the theoretical value for a circular interface.

When the fingers have died out or only a few fingers are left, the interface recovers the circular shape, see figure 10.3. Γ/Γ_0 recovers the shape of the curve for a retracting circle, however with an offset: the experimental values lie below theory. This is a sign of volume loss during the experiment, discussed at the very end of this chapter.

Linear growth rate

We have shown previously that the extent of finger growth depends on the control parameter: small values of τ_0 induce many fingers with high amplitudes, high values of τ_0 induce few fingers with small amplitudes. In the last section, we discussed the additional confinement dependence of the amplitudes. We investigate in the following the instantaneous linear growth rate σ to gain a better understanding of these effects. As we compare experiments as a function of reduced time t', we consider the dimensionless growth rate. σ' is non-dimensionalized in the same way as the time, that is, $\sigma' = b_0/v_0\,\sigma$. σ' at wave number k' has been calculated from linear stability analysis as a function of t' as [104]

$$\sigma'(k',t') = \frac{k'}{2}\frac{\dot{B}}{B} + \frac{B^2}{R^3}\tau(k' - k'^3)\,. \tag{10.12}$$

Therein, $B = b/b_0$, $\dot{B} = v/v_0$ and $R = R/R_0$. The dimensionless wave number k' is calculated in reference to the radius R_0, so $k' = kR_0$, $k = 2\pi/\lambda$. Equation 10.12 recovers the growth rate for the Saffman-Taylor instability in a linear channel, equation 4.20, at $t' = 0$ for $b_0 \ll R_0$.
The fastest growing wave number is

$$k'_{\max} = \frac{1}{\sqrt{3}}\sqrt{1 + \dot{B}R^3/2\tau B^3}\,. \tag{10.13}$$

At $t' = 0$, B, $\dot{B}$ and R are equal to 1 and equation 10.13 recovers the equation for the initial finger number equation 10.4.

The growth rate σ' as a function of k' at $t = 0$ is displayed in figure 10.14(a). It depends solely on τ_0. The fastest growing wave number at $t' = 0$ is

$$\sigma(k_{\max}, t' = 0) = \frac{k_{\max}}{2} + \tau_0(k_{\max} - k_{\max}^3) \tag{10.14}$$

$$= \frac{1}{2}\left[\frac{1}{3}(1 + \frac{1}{2\tau_0})\right]^{1/2} + \tau_0\left(\left[\frac{1}{3}(1 + \frac{1}{2\tau_0})\right]^{1/2} - \left[\frac{1}{3}(1 + \frac{1}{2\tau_0})\right]^{3/2}\right)\,. \tag{10.15}$$

The maximum growth rate varies with τ_0 (equation 10.15), displayed in figure 10.14(b). It has a minimum at $\tau_0 = 0.25$, corresponding to $N_0 = 1$. $N_0 < 1$ has no physical meaning. On the left side of the minimum, the growth rate is decreasing with increasing control parameter. The finger growth should thus be more pronounced for higher numbers of fingers or smaller control parameters, in

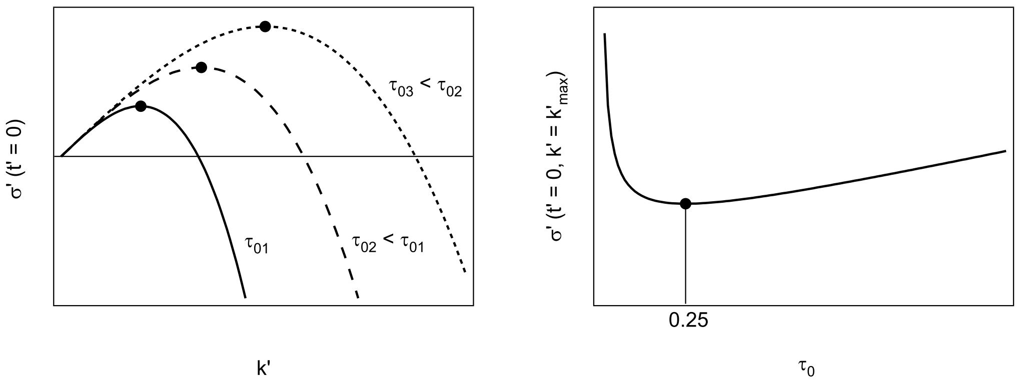

(a) Dimensionless growth rate versus dimensionless wave vector, calculated from equation 10.12.

(b) Maximum dimensionless growth rate versus τ_0, calculated from equation 10.15

Figure 10.14.: Growth rate and most unstable wave vector at $t' = 0$.

agreement with our experiments. However, the dependence on the confinement is not explained by the linear theory, as σ depends solely on τ_0.

Comparison to simulations

We compare now our experiments to simulations that are reported in references [104] and [75]. As the simulations are solely controlled by τ_0, it is not possible to test different realizations of a constant τ_0 as we did in our experiments. However, the initial perturbation can be varied in a controlled way. Lindner *et al.* found that a minimal amplitude of the initial perturbation is necessary to make fingers grow in the simulations [75]. They tested different initial perturbations for one control parameter ($\tau_0 = 8.4 \times 10^{-5}$): a large band of initial wavelengths with small amplitudes (case A), and a tighter band of high wave numbers with low initial amplitude (case B) and high initial amplitude (case C). Figure 10.15 shows the contact line for different times. In the upper row, our experiments with $C = 120$ (red line) and $C = 40$ (blue line) are displayed at $t' = 0.3$, $t' = 1$, and $t' = 2$. In the lower row, simulations with high initial amplitude (case C, red line) and low initial amplitude (case B, blue line) are given at $t' = 0$, $t' = 1$, and $t' = 2$. Note that τ_0 and thus the number of fingers differ in experiments and simulations.

Obviously, some qualitative features that we observed in our experiments are as well present in the simulations. First, the position of the finger tips is similar for different conditions (blue and red). Second, the oil between the air fingers contracts at different speeds for different conditions.

We have detailed in the previous section that a certain inertia of the material bridges is responsible for the fact that stagnant fingers survive during a certain time. The oil between the fingers retreats more slowly than the finger tips advance. Logically, a slower contraction of the bridges leads to a higher total number of fingers,

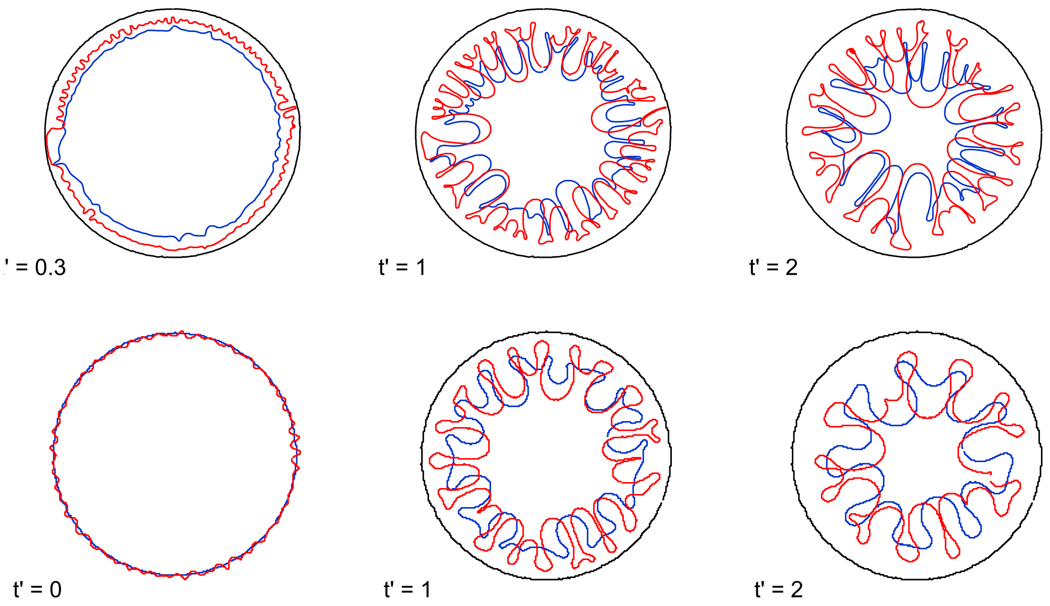

Figure 10.15.: The contact line at different times. *Upper row:* experiments. Red corresponds to $C = 120$, blue to $C = 40$. *Lower row:* simulations from reference [75]. Red corresponds to high initial amplitudes (case C), blue to low initial amplitudes (case B).

as stagnant fingers survive longer. This is in agreement with our experiments: in more confined situations, an increase in the total number of fingers and in the finger amplitude is observed. Now we investigate the total number of fingers from simulations for different initial conditions. In figure 10.16, taken from reference [75], different initial noise conditions are compared for one control parameter. Again, case A corresponds to a large band of initial wavelengths with small amplitudes. Cases B and C correspond to a tighter band of high wave numbers with low initial amplitude (B) and high initial amplitude (C). We focus on cases B and C. Although the number of fingers is roughly reproduced in both cases, especially at short times, a closer inspection of the curves reveals that the number of fingers in the case of lower amplitudes (B) lies below the number of fingers for higher amplitudes (C) from $t' = 0.5$ on. These observations are again in agreement with our experimental results. The control parameter in the simulations, $\tau_0 = 8.4 \times 10^{-5}$, is higher than the control parameters we used. We observed that the difference in the number of fingers decays with increasing control parameter. This could explain the only small effect in the simulations.

To summarize this section so far, we state that the oil bridges between the air fingers take more time to move towards the cell center for higher degrees of confinement. This slower contraction leads simultaneously to larger finger amplitudes and higher total numbers of fingers, as stagnant fingers persist longer. Comparison to numerical simulations indicates that the slower retraction and higher amplitudes

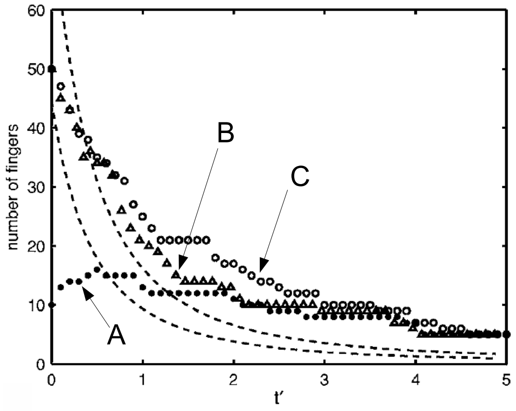

Figure 10.16.: The number of fingers versus the reduced time for different initial perturbations in simulations at control parameter $\tau_0 = 8.4 \times 10^{-5}$, taken from [75].

might be caused by the conditions in the underlying noise spectrum at the beginning. In simulations, higher amplitudes during the complete experiment were reproduced by higher amplitudes of the initial perturbation only. In the experiment, the origin of the different initial conditions however remains unclear so far.

We mention again that we observed an influence of the confinement R_0/b_0, but not of the viscosity or speed, on the total number of fingers. Note that we did not change the viscosity or speed independently of all other parameters, but kept the quantity $v_0\,\eta$ constant. It is worth mentioning that the capillary number contains the quantities R_0/b_0 and $v_0\,\eta$,

$$Ca = \frac{U_0\eta}{\gamma} = \frac{R_0 v_0 \eta}{2b_0\gamma}\ , \tag{10.16}$$

which might be a hint to an influence of the capillary number on the initial perturbations.

10.5.1. Controlled perturbation

In the previous section, we discussed the possible influence of the initial perturbation on the finger growth. To investigate this experimentally, we wanted to introduce controlled perturbations into the system. The idea was to produce probes with sinusoidal perturbations along the border. Cutting the perturbations directly into the steel probe with a mill turned out to be an inadequate method, as the perturbations were rather square instead of sinusoidal. In collaboration with D. Martina (PPMD-ESPCI), we adapted in a time-consuming process a soft lithography method to produce small pastilles with known perturbations at their margins. An overview over soft lithography methods can be found in the review article reference [124]. The technique we applied consists in covering a UV sensitive liquid polyurethane (NOA81, *Norland Products*) with a mask and curing it under UV radiation. The

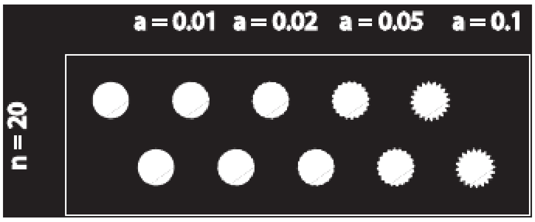

Figure 10.17.: Mask for the fabrication of pastilles with controlled sinusoidal perturbations. Here, 20 fingers are distributed along the circumference. The amplitudes range from 0.01 to 0.1 λ.

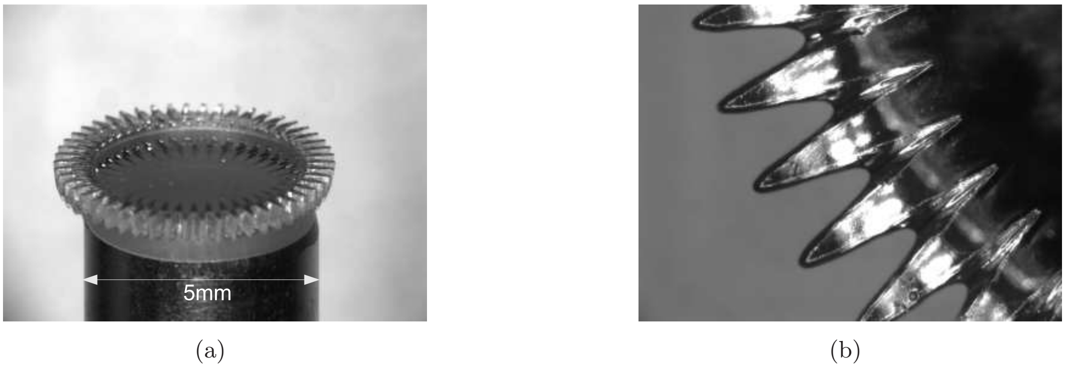

(a)

(b)

Figure 10.18.: Images of a cured polyurethane pastille glued on a steel probe.

mask is a plastic film covered with black printer's ink. An area of the wanted shape is spared and stays transparent for UV radiation. Figure 10.17 displays one of our masks. It consist in circles with a radius of 3 mm and sinusoidal undulations along the outline. The wavelength respectively the number of maxima are well defined, here $n = 20$. The controlled amplitude ranges from 0.01 to 0.1 λ.

The curing method is the following: One applies a layer of NOA81 to a microscope glass slide. The polyurethane (PU) is then covered with a second glass slide. The height of the liquid layer is controlled with spacers of known thickness. Then the mask is fixed on the upper glass slide, the assembly is placed under UV radiation, and the PU is cured. Once the piece of polyurethane with the desired shape is completely crosslinked, it is rinsed thoroughly with acetone and ethanol to remove remaining non-cured material. The resulting pastille is dried in an oven at 60 °C for several hours and then glued onto a steel probe. A second method consists in curing the polyurethane directly on the steel probe. Figure 10.18 shows images of the resulting probe with well controlled perturbations of the boundary.[1]

The aim of the controlled perturbations was to perform experiments at a control parameter τ_0 with very weak finger growth. Introducing successively initial perturbations with a wavelength that corresponds to τ_0 and with increasing amplitude, we

---

[1] Pastilles and images courtesy of David Martina, PPMD, ESPCI.

aimed to investigate whether we can stimulate the growth of fingers. Unfortunately, we were not able to transfer the perturbation of the probe's border to the contact line, as the oil was flowing into the grooves and the oscillations were smoothed out. A more extensive study of the amplitude and the wavelength of the perturbations could potentially yield experimental conditions that make it possible to perturb the contact line sufficiently. Then we could gain the desired information about the finger growth.

10.6. Lifting force

In this section, we discuss the force that is needed to separate the two plates during debonding. The question whether cavitation or the fingering instability have an influence on the force is of great interest, mostly for adhesives. The influence of the pattern formation on the lifting force has been studied by several groups. Tirumkudulu *et al.* showed that cavitation influences the force [113]. Poivet *et al.* studied cavitation and fingering in highly viscous oils [92]. They found that both mechanisms have an influence on the lifting force. However, Derks *et al.* found no or little influence on the force curves for low viscosity materials with yield stress [40]. Lindner *et al.* predicted an influence of the fingering for Newtonian oils from simulations, but could not confirm it in experiments [75].

The lifting force as a function of the time for a retracting oil circle is given as [12]

$$F_{\text{Newtonian}}(t) = \frac{3\pi\eta {R_0}^4 {b_0}^2 v}{2b(t)^5} \,. \tag{10.17}$$

Reformulating equation 10.17 as a function of the reduced time reveals that the force is proportional to $1/\tau_0$, provided that the plate radius R_0 and the surface tension γ are kept constant,

$$F_{\text{Newtonian}}(t) = \frac{\eta v {R_0}^3}{{b_0}^3} \frac{3\pi R_0}{2(1+t')^5} \,. \tag{10.18}$$

Therefore, the force should be controlled by the control parameter under the conditions of constant R_0 and γ.

The strain ϵ, a quantity that is typically measured in debonding experiments, corresponds to $t' = v_0 t/b_0$. Figure 10.19 shows the force-strain curves for different realizations of three control parameter values. Color encodes the initial confinement: black lines correspond to $C = 25$ ($b_0 = 120\,\mu\text{m}$), red to $C = 30$ ($b_0 = 100\,\mu\text{m}$), blue to $C = 40$ ($b_0 = 75\,\mu\text{m}$), orange to $C = 60$ ($b_0 = 50\,\mu\text{m}$), and green to $C = 120$ ($b_0 = 25\,\mu\text{m}$). Black dotted lines represent the force calculated from equation 10.18. All experiments have been carried out with oil 100, the radius of the Hele–Shaw cell was $R_0 = 3\,\text{mm}$. Sharp edges and peaks in the experimental data are caused by the restricted frequency of data acquisition.

Comparing the first three graphs in figure 10.19, it is obvious that the force prediction for a retracting circle works best for higher control parameters, that is, for less

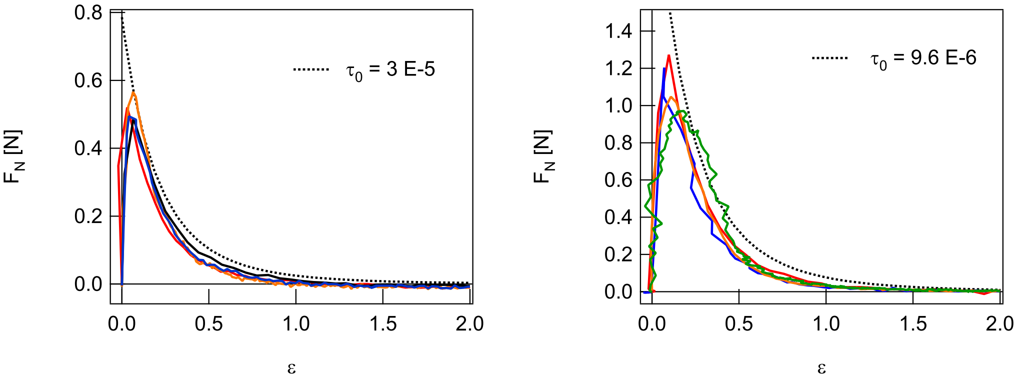

(a) $\tau_0 = 3.0 \times 10^{-5}$.

(b) $\tau_0 = 9.6 \times 10^{-6}$.

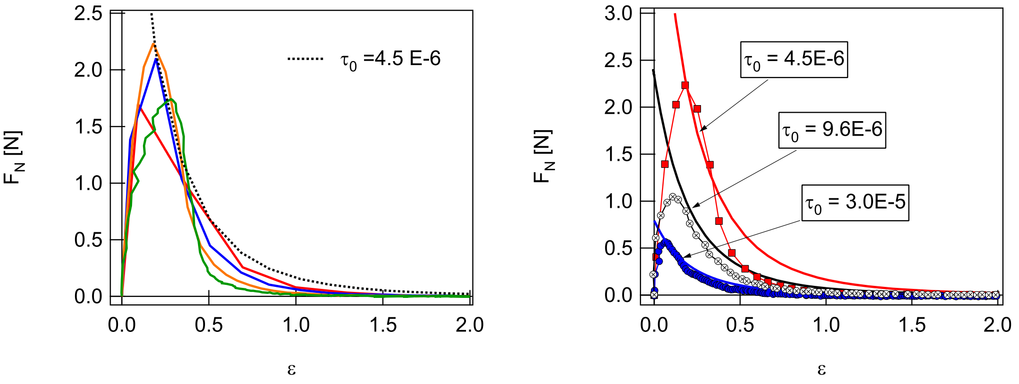

(c) $\tau_0 = 4.5 \times 10^{-6}$.

(d) Comparison of all control parameters at $C \approx 60$ ($b_0 \approx 50\,\mu\text{m}$).

Figure 10.19.: The normal force on the probe versus the strain during the debonding process. Different confinements for each control parameters at constant viscosity $\eta = 100\,\text{Pa s}$ and radius $R_0 = 3\,\text{mm}$. $C = 25$ (black), $C = 30$ (red), $C = 40$ (blue), $C = 60$ (orange), $C = 120$ (green). $C = 60$ on graph (d).

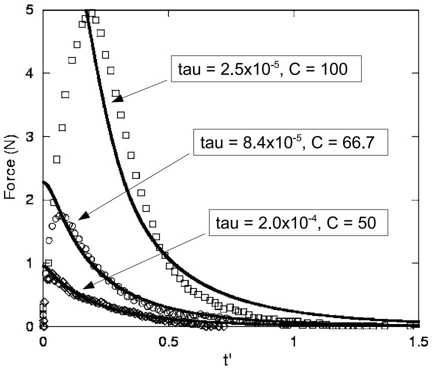

Figure 10.20.: Lifting force versus reduced time, taken from reference [75]. No or little influence of the fingering is observed.

fingers. In figure 10.19(a), the experimental results lie sightly below the calculated force, but the overall shape is well predicted. The measured force does not depend on the exact experimental conditions. Figure 10.19(b) displays the force for a lower control parameter. The measured force still lies slightly below the theoretically calculated force. For even higher numbers of finger [figure 10.19(c)], the gap between experimentally measured and calculated force becomes more important. Interestingly, some variation with the confinement is now observed. The more confined the system is, the higher the deviation is. For very confined systems, we observe a slight overshoot in the force, which can be attributed to the stretching of the apparatus. The confinement dependence of the force corresponds to the confinement dependence of the finger amplitudes and the number of fingers. We have shown that the finger amplitude is higher the more confined the system is. Thus, the parallel evolution of decreasing force and increasing finger amplitude indicates that the fingering process is indeed responsible for the decrease in the force, as predicted from simulations by Linder *et al.* [75].

Figure 10.19(d) displays the results for all three control parameters at constant confinement $C = 60$. Blue full circles represent $\tau_0 = 3.0 \times 10^{-5}$, black open circles $\tau_0 = 9.6\times10^{-6}$, and red squares $\tau_0 = 4.5\times10^{-6}$. Solid lines are again calculated from equation 10.18. This graph might be compared to results from reference [75], see figure 10.20. Lindner *et al.* observed a slight deviation from the retracting circle case only for the lowest control parameter $\tau_0 = 2.5\times10^{-5}$. They stated that this deviation might be linked to the fingering process. The influence disappears when increasing the control parameter, see figure 10.20. Our results on the lifting force complete this study, as we explore a supplementary region on the control parameter scale. We observed a slight deviation for $\tau_0 = 3.0 \times 10^{-5}$ that increases with decreasing control parameter. Additionally, we observed the confinement dependence that we attribute to an increasing finger amplitude. Note that the radius R_0 in figure 10.20 differs from our experiments, so that the absolute force values cannot be compared.

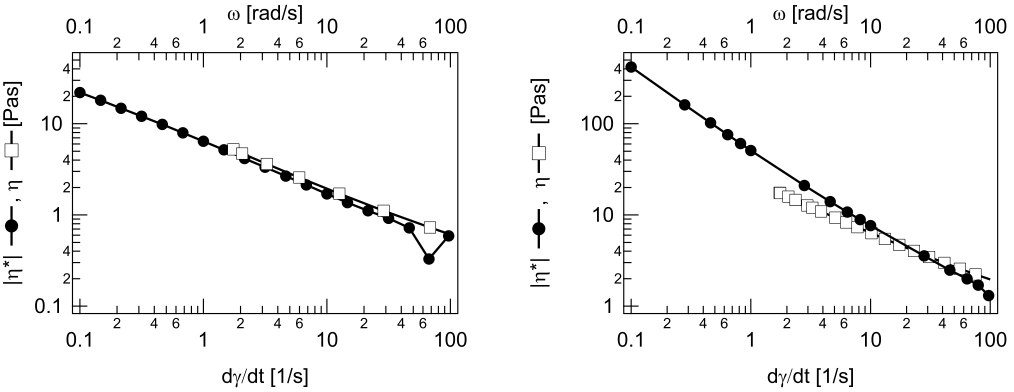

(a) 0.1% Carbopol solution

(b) 1% Carbopol solution

Figure 10.21.: Comparison of $|\eta^\star|$ versus ω and η versus $\dot{\gamma}$ for the Carbopol solutions.

10.7. A viscoelastic shear thinning liquid

In this section, we present observations from preliminary experiments with a shear-thinning viscoelastic liquid. We did not perform a systematic study but present here results on some individual experiments. The influence of shear thinning viscosity on the destabilizing wavelength has been discussed for example in references [61, 62, 120, 10]. Therein, no or only a slight influence is predicted.

The material we used is known under the name of *Carbopol*. It is a polymer with high molecular weight that forms a gel in an adequate solvent. In higher concentrations, it is used for experiments as a yield stress fluid, see for example reference [26]. At low frequencies, the elastic effects are negligible, thus it has been used as a shear thinning liquid with no elasticity [126]. In the concentrations we used, the liquid was shear thinning and viscoelastic, see figures 10.21 and 10.22, but showed only a very weak yield stress. It was not visible from the rheological measurements, but from small air bubbles that persisted in the container.

We prepared the Carbopol solutions as described in the following. We made a 0.1% and 1% solution of the polymer PAA (Poly(acrylic acid)) with a molecular weight of $M_\mathrm{W} = 1\,250\,000$ in Ethylene Glycol (EG). Percentages are calculated in reference to the total weight, thus, the 1% solution corresponds to 1.996 g of PAA in 198.01 g of EG. As the PAA forms lumps easily, the mixing is best done if one produces first a vortex by turning the EG with a magnetic mixer, and then sprinkles slowly the polymer on the turning EG. Thorough mixing during 24 to 48 h yields the swollen polymer, which is a cloudy solution. To dissolve the polymer properly, it is necessary to adjust the pH value. We did so by adding a few droplets of Triethylamine. All chemicals have been purchased from *Aldrich*. This procedure yielded liquids with the rheological properties described in the following.

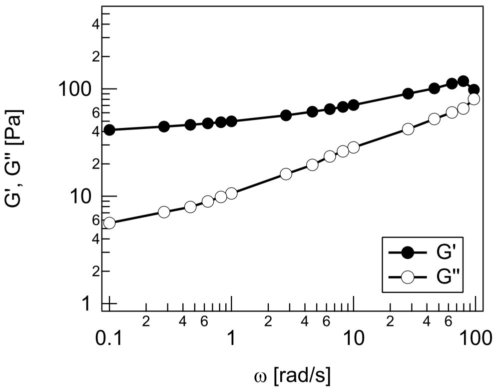

Figure 10.22.: G' and G'' versus ω for the 1% Carbopol solution.

Rheological characterization

We performed constant shear and oscillating frequency sweep tests on the Carbopol solutions with a *Haake RS 100 Rheostress* rheometer as described for the Newtonian oils. Following the *Cox–Merz* rule equation 7.3, the complex viscosity and the steady shear viscosity are linked via

$$|\eta^\star(\omega)| = \eta(\dot\gamma)|_{\omega=\dot\gamma} \; . \tag{10.19}$$

Figure 10.21 shows a comparison of the two functions $|\eta^\star|$ versus ω and η versus $\dot\gamma$ for two Carbopol solutions. Whereas the rule is perfectly confirmed for the less viscous solution, we observe a deviation for the 1% solution. However, the viscosity's order of magnitude is still well reproduced. Figure 10.22 shows the storage and loss modulus for the 1% Carbopol solution. In the experimental range of frequencies, the storage modulus is very low at values $< 100\,\mathrm{Pa}$, yet higher than the loss modulus. The initial experimental strain rates in the debonding tests were rather high at $60\,{}^1\!/\!{}_\mathrm{s}$ and $240\,{}^1\!/\!{}_\mathrm{s}$. The complex viscosity of the 1% solution could be fitted in the range of frequencies between $1\,{}^\mathrm{rad}\!/\!{}_\mathrm{s}$ and $100\,{}^\mathrm{rad}\!/\!{}_\mathrm{s}$ by the power law

$$|\eta^\star| = A\,\omega^B \tag{10.20}$$

with $A = 46.86 \pm 0.733$ and $B = -0.786 \pm 0.0099$.

Experimental observations

We performed experiments with both solutions. The amplitudes were very weak and virtually no fingers were formed with the 0.1% solution, so that results for the number of fingers are only shown for the 1% solution. However, we observed some interesting phenomena during the debonding of the thinner solution, see figure 10.23. From figure 10.23(b) on, one distinguishes a structured probe surface on the debonded part of the probe. This structure indicates wetting problems between the

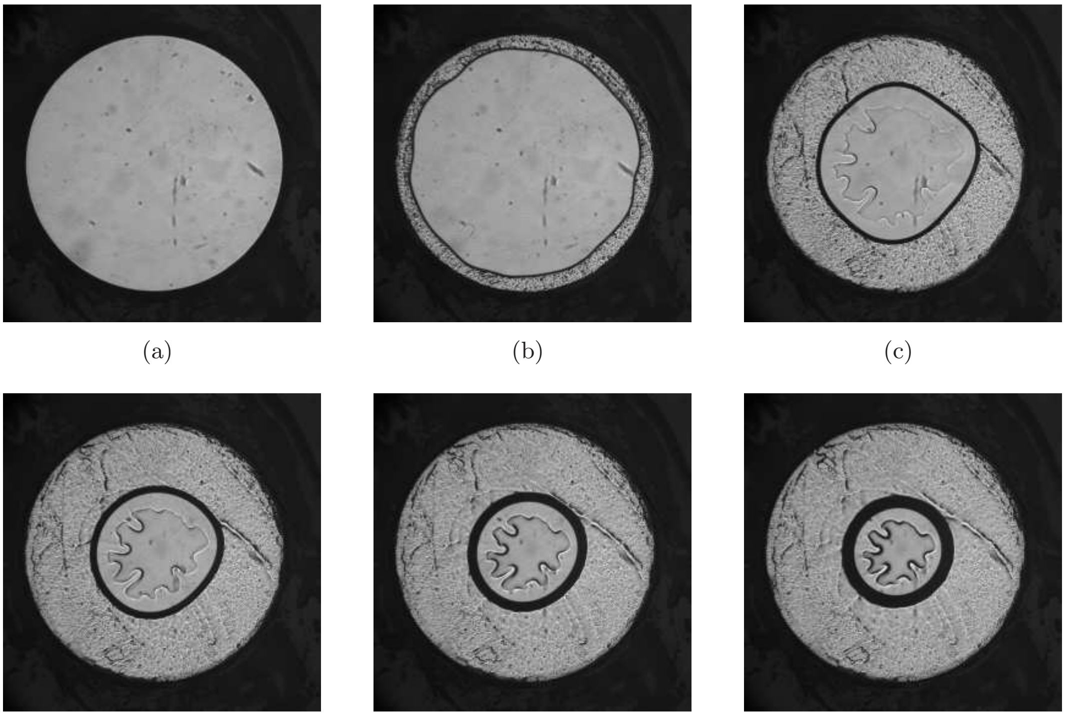

(a) (b) (c)

(d) (e) (f)

Figure 10.23.: 0.1% Carbopol solution in the lifted Hele–Shaw cell, $b_0 = 50\,\mu\mathrm{m}$, $v_0 = 100\,{}^{\mu\mathrm{m}}/_{\mathrm{s}}$. Wetting problems on the steel surface as well as "phase separation" phenomenon are visible on the top view images.

(a) (b) (c)

Figure 10.24.: 1% Carbopol solution in the lifted Hele–Shaw cell, $b_0 = 50\,\mu\mathrm{m}$, $v_0 = 100\,{}^{\mu\mathrm{m}}/_{\mathrm{s}}$.

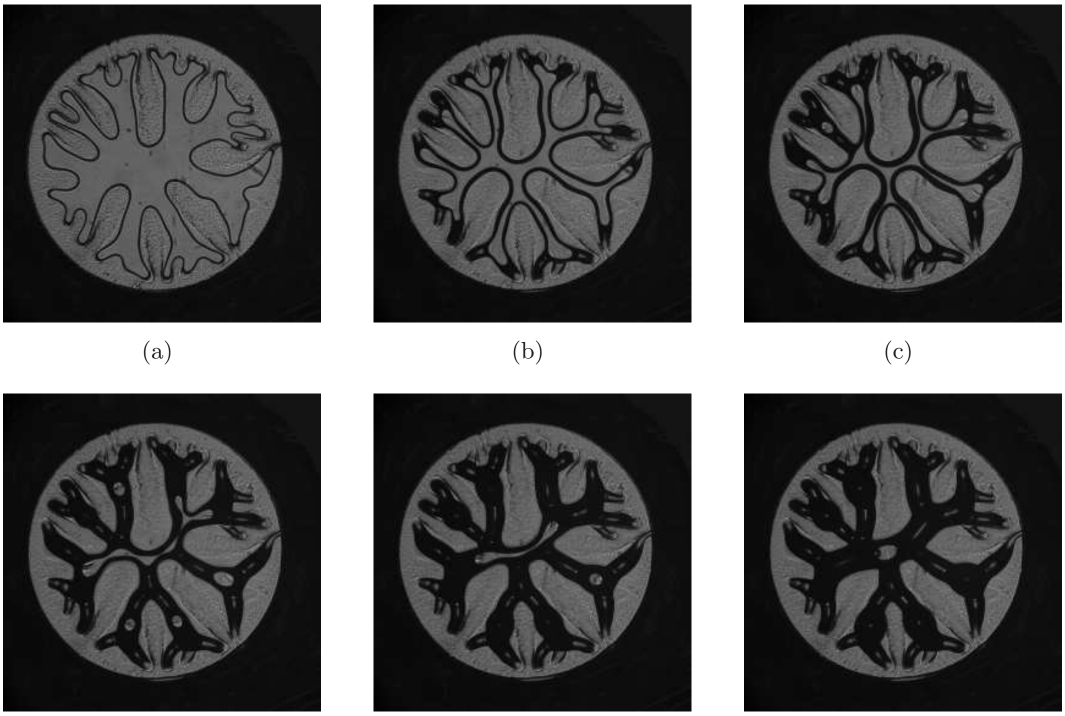

(a) (b) (c)

(d) (e) (f)

Figure 10.25.: 1% Carbopol solution in the lifted Hele–Shaw cell, $b_0 = 25\,\mu\mathrm{m}$, $v_0 = 100\,{}^{\mu\mathrm{m}}\!/\mathrm{s}$.

Carbopol solution and the steel surface. A second phenomenon becomes visible on image 10.23(c) and becomes stronger with the retraction of the circular liquid blob: Within the polymer solution, a distinct "inner" fingering phenomenon occurs. We are not able to explain properly this phenomenon, but it could be a phase separation in the polymer solution. The contact line between air and Carbopol shows only slight undulations and no proper fingering, and it becomes perfectly circular again on picture 10.23(e).

We restricted the image analysis to the thicker solution that showed a pronounced fingering instability, see figure 10.24 and 10.25. We observed as well a structuration of the debonded area, however weak, indicating some wetting problems, but we did not see the "phase separation" as in figure 10.23. An interesting feature are the branched traces left on the probe surface where the material bridges between the fingers were before the final break-up.

Comparison to linear theory

The control parameter τ_0 is calculated via

$$\tau_0 = \frac{\Gamma {b_0}^3}{12 v_0 \eta_0 {R_0}^3} , \tag{10.21}$$

with η_0 being the (complex) viscosity at shear rate $\dot{\gamma}_0$. Γ is here the surface tension between air and Carbopol, $\Gamma = 0.048\,{}^{\mathrm{N}}\!/\!{}_{\mathrm{m}}$. A new dependence on the time is introduced into the control parameter via the shear rate dependent viscosity, as the shear rate changes with time. $\tau(t')$ now reads

$$\tau(t') = \frac{\Gamma b(t')^3}{12 v(t') \eta(t') R(t')^3} = \frac{\Gamma b(t')^3}{12 v(t') A \dot{\gamma}(t')^B R(t')^3} . \tag{10.22}$$

We performed two tests with $v_0 = 100\,{}^{\mu\mathrm{m}}\!/\!{}_{\mathrm{s}}$, $b_0 = 25\,\mu\mathrm{m}$ and $b_0 = 50\,\mu\mathrm{m}$, giving $\tau_0 \approx 3.8 \times 10^{-5}$ and $\tau_0 \approx 1 \times 10^{-4}$, respectively. As for the Newtonian oil, we determined the total number of fingers and the number of growing fingers. The shear rate is estimated as

$$\dot{\gamma} = \frac{U(t')}{b(t')} = \frac{v_0 R(t')}{2 b(t')^2} = \frac{v_0 R_0}{2 {b_0}^2 (1 + t')^{5/2}} . \tag{10.23}$$

Figure 10.26 displays the total number of fingers and the number of growing fingers in comparison to the prediction from equation 10.22. As for the Newtonian oil, the total number of fingers is higher than the prediction from linear theory due to stagnant fingers as explained before. The number of growing fingers however is extremely well predicted by equation 10.22. At that point of the study we cannot judge if the confinement plays the same important rule as for the Newtonian oils.

As conclusion, as far as we can see from preliminary experiments, the number of growing fingers as a function of time is very well predicted from the classical *Saffman–Taylor* prediction using the adequate value of the (complex) viscosity. Thus

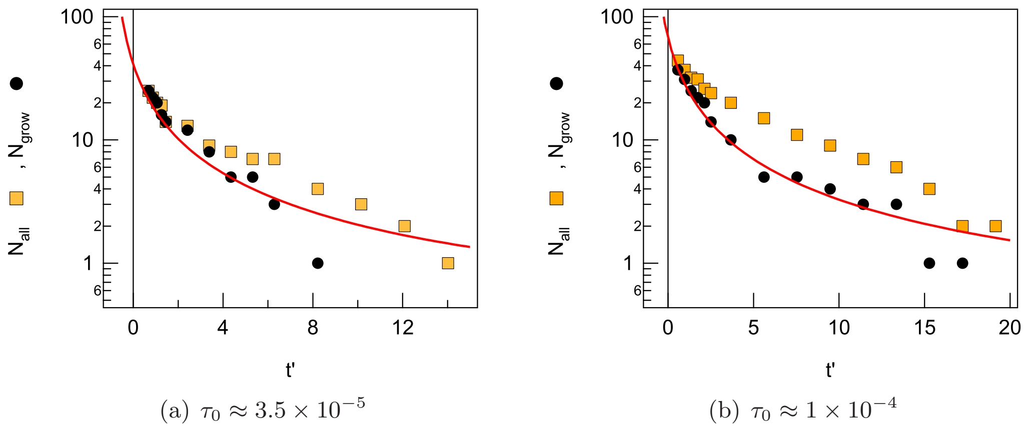

(a) $\tau_0 \approx 3.5 \times 10^{-5}$ (b) $\tau_0 \approx 1 \times 10^{-4}$

Figure 10.26.: Total number of fingers and number of growing fingers for the 1% Carbopol solution. The continuous line is calculated from equation 10.22.

we presume that the destabilizing wavelength can be calculated in the same manner as for a Newtonian oil. It would be very interesting to perform a complete study with different confinements, control parameters, and also different concentrations of PAA. Higher polymer concentrations form eventually gels with an important yield stress, making it possible to investigate the transition towards system with higher and higher values of the yield stress.

10.8. Conclusion

In this Chapter, we investigated the viscous fingering instability in a lifted Hele–Shaw cell filled with a Newtonian oil. We studied the coarsening of the fingering pattern, that is, its evolution with time over the complete debonding process. We concentrated on the question whether the number of fingers and the finger amplitude are solely determined by the control parameter τ_0 or whether the exact experimental parameters have an additional influence. The total number of fingers in each experiments exceeds the value that is predicted by linear stability analysis, as described previously [75]. We identify *dying* and *growing* fingers. Surprisingly, the number of growing fingers is at each moment well described by the prediction from linear theory. Therefore, geometric effects play only a secondary role in the coarsening process. The stagnant fingers do not disappear instantly and contribute thus to the total number of fingers. We demonstrate that the finger amplitudes are higher for higher confinement, due to a retarded contraction of the material left between the air fingers. The more a system is confined, the more slowly these oil bridges retreat to the cell center, and the longer the stagnant fingers persist. That is why we observe higher total numbers of fingers with higher confinement.

Comparison to numerical simulations [75] indicates that higher finger amplitudes can be linked to the initial conditions. In the simulations, higher amplitudes of the initial perturbations lead to higher amplitudes during the whole debonding process. Greater insight into the finger growth could be gained pursuing experiments with a sinusoidal perturbation of controlled wavelength and amplitude at the outline of the probe.

A second effect we studied in this Chapter is the influence of the fingering instability on the lifting force. This effect was unclear so far, as different working groups have found contradictory results [113, 92, 40, 75]. We showed that the force is at high control parameters well described by an equation for a retracting oil circle. We observed a visible influence of the fingering pattern only for small enough control parameters and strong finger amplitudes. Higher confinement, corresponding to higher amplitudes, leads to lower debonding forces.

Appendix to Chapter 10

In this Appendix, we discuss some possible additional effects on the number of fingers. First, we consider $3D$ effects and apply a theory that accounts for the different initial shape of the contact line. Second, we discuss a possible influence of volume loss during a test.

A $3D$ effect?

In the derivation of Darcy's law, the Hele–Shaw cell is approximated by a two dimensional system. Naturally, the lubrification approximation breaks down at some point with increasing cell thickness. Thus, we will discuss here some possible three dimensional effects.

Solving the full Navier-Stokes equations with free boundaries analytically in three dimensions is impossible [10]. Instead, Ben Amar *et al.* included three dimensional effects into their calculations by investigating the influence of the meniscus shape at the cell edge [10]. Comparing to experiments with different control parameters, the authors found that the influence of the meniscus shape is becoming more important for higher b_0. Reference [10] is to our knowledge the only study including $3D$ effects into the stability analysis. Thus we investigate here whether their theory can predict the influence of the confinement we observed.

The crucial parameter in the theoretical analysis is ρ, a parameter that measures the deviation of the initial viscous blob from a perfect cylindrical shape. At $t = 0$, it is defined as

$$\rho = \frac{4|R(b = b_0/2) - R(b = b_0)|}{b_0}. \tag{10.24}$$

R is the blob radius. ρ evolves with time during the experiment.

On the one hand, the authors derived limiting equations that are only valid in the case of very small or large ρ. On the other hand, they calculate an equation for arbitrary ρ that is valid for the boundary condition of an oscillating contact line. ρ discriminates in which regime the system falls. In our experiments, we estimate ρ as follows. We assume the silicone oil to be perfectly wetting and estimate therefore the initial curvature to be $b_0/2$. Thus, for very small times, equation 10.24 simplifies and reads

$$\rho = \frac{4|R_0 - b_0/2 - R_0|}{b_0} = 2\ . \tag{10.25}$$

ρ is of the order of 1 and we cannot use the limiting equations. Instead, we use the general equation for all ρ:

$$\begin{aligned} &N^2\left[\frac{1}{\rho}\operatorname{arctanh}\frac{\rho}{(1+\rho^2)^{1/2}}\right]+\frac{2}{3}\frac{\rho}{(1+\rho^2)^{3/2}}\frac{R_0^2 b_0}{b(t)^3}+\frac{L-1}{3\rho}\operatorname{arctanh}\frac{\rho}{(1+\rho^2)^{1/2}} \\ &-\frac{L}{3}\frac{1}{(1+\rho^2)^{1/2}}=\frac{1-\eta_{\mathrm{rel}}}{6T}\frac{v(t)}{v(0)}\left(\frac{b(0)^{5/2}R_0^2}{b(t)^{9/2}}\right)\,. \end{aligned} \tag{10.26}$$

The notations are the following: R_0 is the radius of the Hele–Shaw cell, b_0 and $b(t)$ the initial and changing gap width, respectively, $v(0)$ and $v(t)$ the initial (and possibly changing) lifting speed, T the control parameter $(b_0\gamma)/(12R_0\eta v(0))$, and γ the surface tension. L is the smallest radius of the viscous blob, that is, the radius at half the cell height. It is non-dimensionalized by R_0. η_{rel} is the ratio of the viscosities of surrounding and inner fluid, so that $1-\eta_{\mathrm{rel}}\approx 1$. In the following, we discuss small times t and estimate that

$$L=\frac{L(t)}{R_0}=\frac{L_0-b_0/2}{R_0}=1-\frac{b_0}{2R_0}\approx 1\,. \tag{10.27}$$

Thus equation 10.26 simplifies to

$$\begin{aligned} &N^2\left[\frac{1}{\rho}\operatorname{arctanh}\frac{\rho}{(1+\rho^2)^{1/2}}\right]+\frac{2}{3}\frac{\rho}{(1+\rho^2)^{3/2}}\frac{{R_0}^2 b_0}{b(t)^3}-\frac{1}{3}\frac{1}{(1+\rho^2)^{1/2}} \\ &=\frac{12R_0\eta v_0}{6b_0\gamma}\left(\frac{{b_0}^{5/2}{R_0}^2}{b(t)^{9/2}}\right)\,. \end{aligned} \tag{10.28}$$

At $t=0$, it reads

$$N^2\left[\frac{1}{\rho}\operatorname{arctanh}\frac{\rho}{(1+\rho^2)^{1/2}}\right]+\frac{2}{3}\frac{\rho}{(1+\rho^2)^{3/2}}\frac{{R_0}^2}{{b_0}^2}-\frac{1}{3}\frac{1}{(1+\rho^2)^{1/2}}=\frac{2{R_0}^3\eta v_0}{{b_0}^3\gamma}\,. \tag{10.29}$$

The $2D$ limit is recovered for $\rho\to 0$. Equation 10.28 can be solved numerically. We investigated the experimental parameters $\gamma=20\,\mathrm{mN/m}$, $R_0=3\,\mathrm{mm}$, and $\rho=2$. b_0, v_0, and η were varied according to each experiment.

Figure 10.27 compares the experimental results to linear $2D$ theory and numerical $3D$ predictions. Special care has to be taken considering the time dependence. Previously, we have shown that the number of fingers changes strongly, especially at the beginning of the experiment.

Graph 10.27(a) displays the number of fingers at the first moment we were able to count them, $t_{\text{first count}}$. We compare experimental results to predictions from linear $2D$ theory and to calculations from equation 10.28 at the corresponding time $t_{\text{first count}}$ for each experiment. The results all fall in the same range, but no clear tendencies are observed. The approximations concerning the shape of the viscous blob, that is, $L=1$ and $\rho=2$ might not be true anymore even at small times $t>0$.

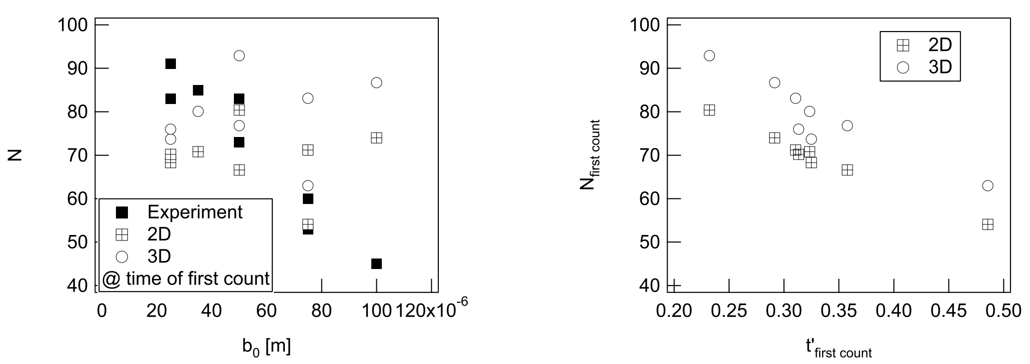

(a) $t' = t'_{\text{first count}}$

(b)

Figure 10.27.: The comparison of the number of fingers in the experiment (squares) to results from $2D$ and $3D$ theory (triangles and circles, respectively).

But the finger growth is not very developed at that point so that we consider these approximations still as reasonable.

The number of fingers predicted from both theories fluctuates strongly. Figure 10.27(b) displays the number of fingers versus the time $t_{\text{first count}}$ they are calculated at. The linear relation between number of fingers and time shows that these fluctuations can be attributed to the time dependence of the number of fingers. Even if the time of first count differs only a little ($0.23 < t' < 0.48$) and is small compared to the experimental duration ($t' \approx 15$), the number of fingers changes strongly at the initial stages of the experiment. We state that the number of fingers for different realizations of one control parameter is slightly increased when including the meniscus shape. However, the general tendency of increasing total finger number with increasing confinement is not reproduced by the $3D$ theory including the curvature effect.

Volume loss

In this section, we discuss the possible influence of volume loss on the control parameter.

A thin oil layer is left on the glass and the steel plate behind the advancing air fingers. The thickness of this draining film has first been studied by Bretherton [14] for air bubbles rising in capillary tubes. He found that its thickness varies like $Ca^{2/3}$. Tabeling *et al.* investigated the influence of this draining film on the finger selection in the linear Hele–Shaw cell [111, 112]. They showed that Bretherton's law breaks down for capillary numbers higher than 0.01. The layer thickness saturates at a value $0.1\, b_0$ that depends on the cell geometry. In our experiments, the capillary number is always higher than 0.01. Presuming a layer with thickness $0.1\, b_0$ on each wall of the cell and leads to an effective thickness $b_{\text{eff}} = 0.8\, b_0$ at early times. However, the control parameter is changed about the same percentage for different confinements

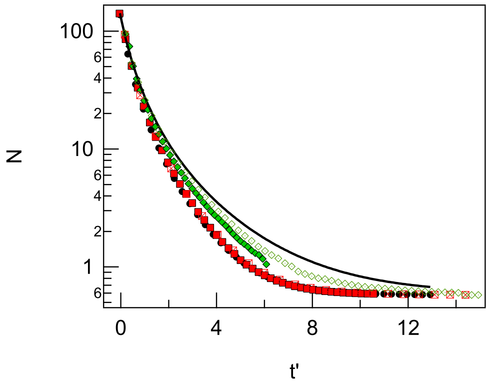

Figure 10.28.: Comparison between the number of fingers calculated from linear theory with volume conservation (solid line) and calculated from a mean radius determined experimentally from the pictures (markers). Filled symbols = oil 100, open symbols = oil 10. $C = 30$ (lack circles), $C = 40$ (red squares), $C = 120$ (green diamonds).

C. The draining film can hence not explain the confinement dependence.

A second origin for volume loss is material flow due to gravity. We checked whether the loss of oil volume affects the control parameter strongly enough to be reflected in the number of fingers. Therefore, we measured the contact area A during a test as a function of time. We calculated then an effective mean radius R_{eff} by approximating the measured area A with a circle. R_{eff} is given by

$$R_{\text{eff}} = \left(\frac{A}{\pi}\right)^{1/2} . \tag{10.30}$$

In equation 10.8, we replace $R(t)$ with $R_{\text{eff}}(t)$. It then reads

$$\tau(t) = \frac{\gamma b(t)^3}{12\eta v_0 R_{\text{eff}}(t)} = \frac{\gamma {b_0}^3 (1+t')^3}{12\eta v_0 R_{\text{eff}}(t)} . \tag{10.31}$$

Figure 10.28 displays the calculated number of fingers as a function of time. The solid line represents $N(t)$ as predicted from linear stability analysis. Markers correspond to calculations from equation 10.28. Filled symbols represent oil 100, open symbols oil 10. Black circles correspond to $C = 30$, red squares to $C = 40$, and green diamonds to $C = 120$.

Obviously, the deviation is only small. Note that N is plotted here on a logarithmic scale. Especially for small times, no influence is observed. In conclusion, the volume loss has no important influence on the control parameter at early times.

Part V.

Conclusions

11. Conclusion

In this thesis, we have investigated the debonding of soft viscoelastic materials in a probe tack geometry, focussing on the transition from a Newtonian liquid to a soft elastic solid.

Our model system consisted of Poly(dimethyl siloxane) with different degrees of crosslinking. We characterized the system with linear rheological measurements. In its non-crosslinked state, it behaves essentially as a Newtonian liquid. Adding a curing agent increases the number density of crosslink points and introduces viscoelasticity. The system reaches its gel point upon addition of only a small amount of curing agent, namely 1.1%. When increasing this amount, the material stops flowing since the polymeric network percolates. The more crosslinker is added, the more polymer chains contribute to the network elasticity, which increases thus strongly. The elastic modulus remains nearly independent of the frequency above a curing agent content of about 2%. The loss modulus increases however strongly with frequency.

The key results are summarized in the following.

We investigated the pattern formation occurring during debonding as a function of the material properties. We present for the first time a quantitative description of the destabilizing wavelength of the fingering instability within one material system spanning a large range of properties from a liquid to a solid. Changing the respective role of liquid and elastic properties of the system, we identified two different regimes. For only weakly crosslinked materials, the fingers are initiated in the bulk. Their wavelength depends on the layer thickness and on the material parameters. We have shown that it can be described by an equation that has been established for the Saffman-Taylor instability [98], if one replaces the viscosity η by the complex viscosity $|\eta^\star|$,

$$\lambda = \pi b / (U\eta/\gamma)^{1/2} \,. \tag{11.1}$$

b is the layer thickness, U the radial velocity, and γ the surface tension between air and PDMS. This equation holds for the Newtonian oil, very weakly crosslinked materials around the gel point, and for very weakly crosslinked viscoelastic solids.

For predominantly elastic materials however, the debonding is interfacial, and air fingers propagate at the interface between probe and polymer. In this case, the wavelength is independent of all system parameters and varies linearly with the film thickness as

$$\lambda = (2.27 \pm 0.1)\, b \,. \tag{11.2}$$

This result is in agreement with theory and experiments in the case of a static peeling geometry [47]. We showed that it holds over three decades in the elastic modulus. The transition between bulk deformation and interfacial regime is determined by an empiric dimensionless parameter that has been proposed for soft viscoelastic systems [36],

$$\frac{\mathcal{G}_0\, G''}{b\, G'^2} \,. \tag{11.3}$$

This parameter compares the energy per unit area that has to be provided to the system to make an interfacial crack move and the energy needed per unit area to deform a elastic layer with elastic shear modulus G'. This parameter had been tested previously for a restricted range of material properties. We confirmed on our model system that this parameter separates the regimes of interfacial and bulk debonding. Furthermore, we were able to switch the debonding mechanism from interfacial to bulk by changing the probe surface and thus the adhesion energy $\mathcal{G}_0$.

We investigated in more detail the complete debonding process exploiting stress-strain curves. The change in their shape with varying material properties reflects the different micromechanisms. Combining visual observation and stress-strain curves, we showed again that the finger pattern can be initiated at the interface or in the bulk. An initially interfacial mechanism will stay interfacial during the whole debonding process. An initiation of the debonding in the bulk however entails the formation of fibrils that finally can break up in the middle or detach from the probe.

The number of fingers decreases with time as the probe is removed from the layer. We investigated this coarsening process in more detail for a Newtonian liquid. The question of the respective importance of geometrical effects and changing control parameter in such a configuration had remained open so far [75, 10]. We answered this question by showing that at each moment, only a certain number of fingers is actually growing. This number is well described by linear stability analysis only, taking into account the time dependence of the control parameter. Geometrical effect thus are only secondary. Furthermore, we demonstrated that the total number of fingers as well as the finger amplitude depend on the cell aspect ratio. The influence of fingering on the force that is needed to pull the probe away was unclear in the past, as several researchers obtained contradictory results [92, 40]. We showed that the influence of the fingers is only important for stronger finger amplitudes and is barely distinguishable for small amplitudes or small numbers of fingers. Comparison between experiments and numerical simulations suggested that the dependence on the aspect ratio is linked to a variation of the initial conditions, more precisely to the amplitude of the initial perturbation [104, 75]. Thus, it is planned to investigate whether different amplitudes of an imposed initial perturbation can enhance the finger growth.

Based on the stress-strain curves, we investigated the adhesion energy for interfacial crack propagation on well crosslinked materials. We showed that the speed dependence of the adhesion energy is described by the frequency dependence of the bulk property $\tan\delta$. This empirical relationship, established in 1985 by Ramond *et al.* and tested on one material [94], has now been confirmed for the first time for elastomers whose elastic modulus spans two decades. While we could explain the speed dependence, the absolute value of the adhesion energy, which differs slightly for different materials, is not completely understood yet.

For a quantitative interpretation of the adhesion energy and for numerical or analytical modelling, the knowledge of the exact boundary conditions during crack propagation is crucial. So far, no technique was available to visualize directly the contact line between the viscoelastic material and the rigid probe. Based on a technique developed by Yamaguchi *et al.* [122], we presented here a new method that allows to visualize directly the advancing contact line between air, viscoelastic material, and rigid substrate in three dimensions. We revealed qualitatively the variation in the finger thickness and in the contact angle with changing material properties. Bulk fingering without direct air-probe contact and interfacial crack propagation with a contact angle close to 90° were clearly distinguished. We showed evidence for tip blunting with a contact angle that differs distinctly from 90° for intermediate degrees of crosslinking. In such way, we provided for the first time access to the actual boundary conditions. A future implementation of mathematical methods will provide means for extracting the real dimension from the deformed $3D$ images and for performing in this way quantitative measurements.

We believe that the results obtained in this study broaden the knowledge in the field of pattern formation in complex materials and in adhesive science, as they bridge the gap between liquids and solids. This thesis has inspired several ongoing projects in the laboratory. The $3D$ setup is being improved; debonding tests with structured probe surfaces are conducted to investigate their influence on the adhesion energy and on the destabilizing wavelength.

Résumé en Français

Introduction

Coller et décoller deux solides est une expérience très répandue dans la vie quotidienne. Une industrie immense développe et améliore les différentes sortes d'adhésifs. Les adhésifs qui adhèrent au substrat après application d'une pression légère, uniquement par des forces de van der Waals, sont appelés adhésifs sensibles à la pression, en anglais *pressure sensitive adhesives (PSA)*. Idéalement, ils se détachent du substrat sans laisser de trace. Les PSAs sont utilisés par example pour les rubans adhésifs ou les étiquettes.

Les PSAs sont des matériaux viscoélastiques très complexes. Ils doivent être assez liquides pour pouvoir former un bon contact entre les surfaces (rugueuses) qu'on veut coller ensemble, tout en gardant une résistance aux contraintes qui apparaissent lors du décollement. Ces dernières années, beaucoup de travaux fondamentaux ont été menés avec l'objectif d'approfondir la compréhension des mécanismes de décollement. D'une part, la performance adhésive a été caractérisée en termes d'énergie d'adhésion et de déformation maximale avant décollement ; D'autre part, un intérêt élevé a été apporté à la formation de structures observée lors du décollement.

Dans le domaine de la formation de structures ainsi que dans l'analyse quantitative du décollement, les concepts théoriques sont bien connus pour les fluides newtoniens et les solides élastiques. En revanche, les propriétés des PSAs se trouvent à la frontière entre ces deux limites. C'est pourquoi une étude approfondie de la transition entre liquide et solide apporte beaucoup à la fois à la science des adhésifs et à la compréhension de la formation de structures dans des matériaux complexes.

La viscoélasticité en général est une propriété mécanique très complexe qui peut avoir des origines physiques très différentes. Dans cette étude, nous travaillons avec des matériaux avec une élasticité d'origine entropique tels que des fluides viscoélastiques, des réseaux de polymère plus ou moins réticulés, et des élastomères. Le changement du mécanisme de décollement avec une variation des propriétés viscoélastiques a été étudié dans un grand nombre de cas pour des systèmes très spécifiques [102, 89, 96, 93, 113, 130, 48, 77].

La formation de structures est aussi importante d'un point de vue plus général. Elle se produit quand l'état homogène d'un système devient instable lorsqu'il est soumis à des perturbations ; le système passe ensuite dans un nouvel état avec formation de structures périodiques. Un grand nombre de systèmes dans la nature présentent ce phénomène. On peut notamment mentionner la formation de nuages, les structures sur la peau des animaux, ou encore certaines réactions chimiques. Récemment, la formation de structures pendant la déformation élongationnelle de couches confinées a attiré beaucoup d'intérêt. Dans le volume des matériaux, on observe la formation de doigts d'air, décrite par l'instabilité de Saffman-Taylor [98, 87, 75, 10]. Cette instabilité a été étudiée pour un grand nombre de matériaux complexes [71, 40, 85, 9]. Des instabilités avec digitation sont également connues pour des matériaux élastiques [42, 47, 109, 79, 1].

Plusieurs travaux se sont intéressés à la transition du liquide vers le solide vitreux [54, 128, 125]. Très récemment, la transition du liquide au solide élastique a été étudié a travers une instabilité de contact dans un champ électrique par Arun *et al.* [7].

En revanche, une étude de l'adhésion, des instabilités et des mécanismes de décollement allant du fluide newtonien jusqu'à l'élastomère n'a jamais été entreprise pour une seule famille de matériaux. Nous réalisons dans cette thèse une transition continue entre les différentes classes de matériaux en utilisant une famille de Poly(diméthyle siloxane) (PDMS) avec différents degrés de réticulation.

Matériaux et méthodes

Dans ce paragraphe, nous décrivons la préparation des échantillons et la caractérisation des matériaux. Le matériau que nous avons choisi comme système modèle est le produit *"Sylgard© 184 Silicone Elastomer Kit"* acheté chez *Dow Corning*. Il consiste en une huile silicone (Polydiméthyle siloxane, PDMS) et un agent de réticulation. Après avoir ajouté l'agent de réticulation à l'huile et avoir chauffé le mélange, des liaisons covalentes se forment entre les chaînes de polymère. Le nombre de ces points de réticulation augmente avec la proportion de réticulant ajoutée. Un réseau de chaînes de polymère se forme, et le matériau acquiert des propriétés viscoélastiques. A grande concentration de réticulant, on obtient finalement un élastomère mou.

Préparation des échantillons

Nous utilisons le PDMS avec différent taux d'agent de réticulation. Le pourcentage est calculé sur la masse totale selon

$$\% = 100 \frac{m[\text{réticulant}]}{m[\text{réticulant}] + m[\text{huile de silicone}]} \ . \tag{11.4}$$

Nous préparons le produit avec un certain degré de réticulation selon l'équation 11.4. 10% de réticulant permettent, selon le fabricant, de réticuler entièrement le PDMS. Après avoir bien mélangé les deux composants, nous mettons le produit sous vide pour le dégazer. Ensuite, nous préparons de fines couches sur des lames de microscope en verre de dimensions 10 cm × 2.6 cm × 0.2 cm à l'aide de différents applicateurs en métal. Nous réticulons les échantillons à l'étuve à 80 °C pendant 5 heures. Ainsi nous obtenons des couches dans une gamme d'épaisseur entre 100 µm et 500 µm.

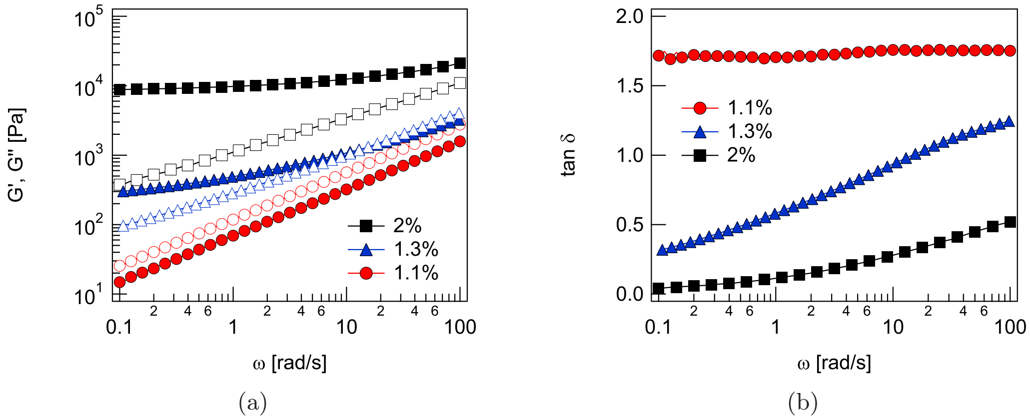

FIGURE 11.1.: Comparaison des modules de stockage et de perte G' (symboles pleins) and G'' (symboles ouverts), ainsi que de $\tan\delta$ en fonction de la fréquence de sollicitation pour des taux de réticulant différents.

Caractérisation des échantillons

Nous déterminons les propriétés viscoélastiques avec un rhéomètre *Haake RS 100 Rheostress* pour l'huile non réticulée et un rhéomètre *TA ARES* pour la famille de matériaux plus ou moins réticulés. Nous effectuons des tests de rhéométrie oscillatoire, technique consistant en l'application d'une déformation sinusoïdale $\gamma = \gamma_0 \sin \omega t$. La mesure de la contrainte résultante dans l'échantillon, qui montre un déphasage, permet d'accéder au module élastique G' et au module de perte G''. $\tan\delta = G''/G'$ est une mesure de l'importance relative de l'élasticité et de la dissipation dans un matériau. G' et G'' sont mesurés en fonction de la fréquence ω de la sollicitation.

Nous donnons ici une vue globale des propriétés viscoélastiques des échantillons en fonction du taux de réticulant. L'huile de PDMS est composée de chaînes de polymère courtes. Sans agent de réticulation, elle se comporte comme un liquide newtonien. Quand on rajoute du réticulant, un réseau est formé petit à petit, et on introduit de la viscoélasticité. Plus on rajoute de réticulant, plus la densité de points de réticulation augmente. Les modules de stockage et de perte, ainsi que $\tan\delta$, sont présentés figure 11.1 pour quelques pourcentages représentatifs. En ajoutant environ 1.1% d'agent de réticulation, le matériau se trouve très proche du point de gel, ce qui se traduit par le parallélisme des valeurs de G' et G'' sur toute la gamme de fréquence. En augmentant le taux de réticulant, le matériau ne coule plus. Le PDMS devient un réseau gonflé par de courtes chaînes de polymère. Plus on ajoute de réticulant, plus un nombre important de chaînes de polymère contribue au réseau et le module élastique croît de manière importante. En même temps, $\tan\delta$ décroît, la dissipation devient moins importante. A partir de 2% d'agent de réticulation, le module élastique ne dépend quasiment plus de la fréquence, le module de perte par contre continue a augmenter avec la fréquence.

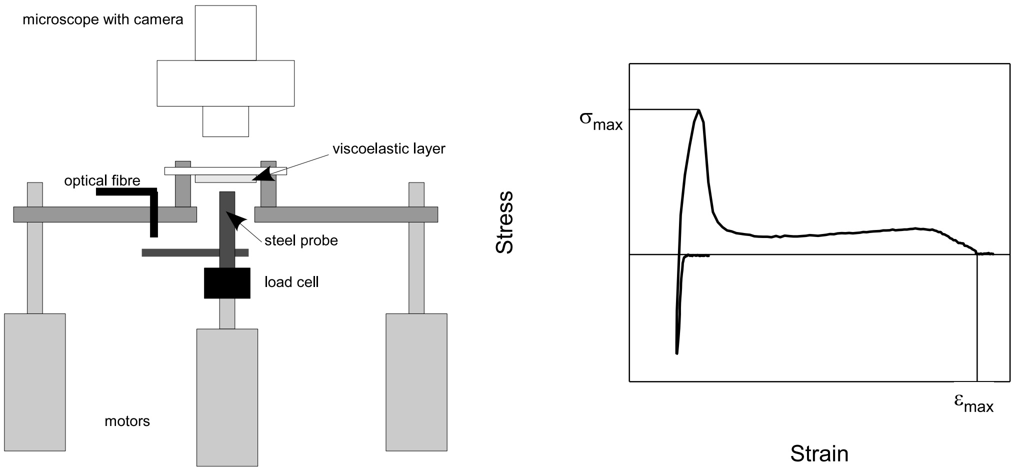

(a) Vue schématique du montage expérimental “probe tack”.

(b) Courbe de contrainte-déformation typique avec la définition de la contrainte et de la déformation maximale.

Figure 11.2.: Le probe tack test - schéma et courbe typique.

Montage expérimental

Nous utilisons un montage “probe tack”, expérience classique pour la caractérisation des adhésifs. Il consiste en un poinçon, c’est-à-dire un cylindre en métal avec une surface plane, qui peut être rapproché d’une couche d’un matériau viscoélastique. Après avoir établi un contact maximal, le poinçon est retiré de la couche à une vitesse bien contrôlée. Lors du test, la force normale sur le poinçon est enregistrée à l’aide d’une cellule de force, et le déplacement relatif entre le poinçon et la couche à l’aide d’une fibre optique. Une caméra montée sur un microscope permet d’observer en détail les mécanismes de décollement. Une vue schématique du montage expérimental ainsi qu’une courbe typique de contrainte-déplacement sont présentées figure 11.2. Quand on commence à tirer sur l’échantillon, l’appareil ainsi que le matériau sont étirés, et la force augmente. Lors du décollement, des structures sont formées dans le matériau : on observe typiquement la formation de cavités ou bien la formation de doigts d’air qui se propagent vers le centre du poinçon. Dans le cadre de cette étude, nous nous intéressons à la formation de doigts.

Résultats

La formation de structures

Nous effectuons des expériences en géométrie de “probe tack” décrite antérieurement. Nous utilisons du PDMS avec une proportion de réticulant variant de 0.9 à 6% de réticulant, c’est-à-dire une gamme de matériaux comprenant des liquides viscoélastiques, des matériaux autour du point de gel, des solides viscoélastiques et fi-

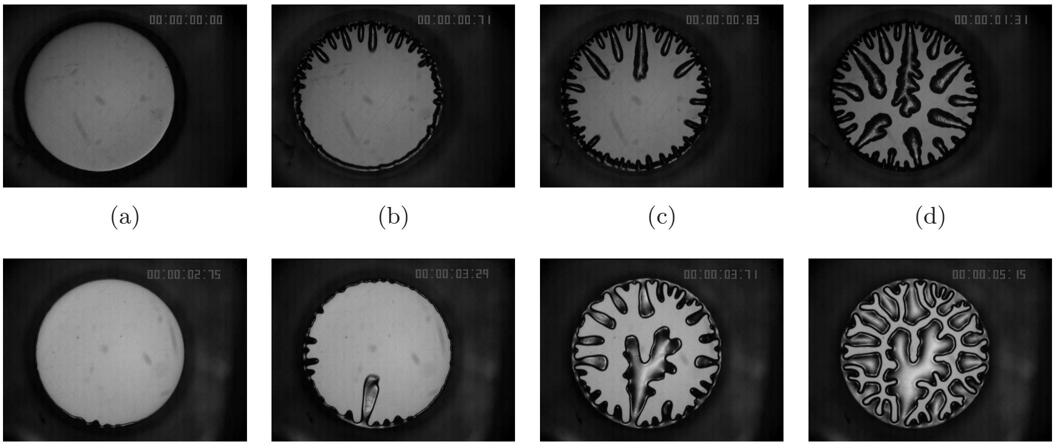

(a) (b) (c) (d)

(e) (f) (g) (h)

FIGURE 11.3.: Déstabilisation de la ligne de contact, initialement circulaire, par des ondulations et la croissance subséquente de doigts d'air. *Ligne supérieure :* 1.1% de réticulant, cas volumique. *Ligne inférieure :* 2.0% de réticulant, cas interfacial.

nalement des elastomères où la dissipation devient de moins en moins importante. Nous mesurons le nombre n de doigts qui apparaissent au début du décollement, voir figure 11.3. D'abord, la ligne de contact entre le polymère et l'air forme un cercle. Cependant, ce cercle est rapidement déstabilisé après le début de la traction, et la ligne de contact se met à onduler. Ensuite, l'amplitude des ondulations croît et des doigts d'air se forment. Nous calculons la longueur d'onde de la déstabilisation initiale $\lambda = 2\pi R/n$, R étant le rayon du poinçon. Changeant la hauteur b et les propriétés de la couche ainsi que la vitesse de décollement v, nous avons réussi à distinguer deux régimes de décollement.

Le premier de ces régimes présente une importante déformation du volume de l'échantillon, s'exprimant par la formation de fibrilles, c'est-à-dire des "ponts" de matériau qui s'étirent entre le poinçon et l'échantillon. Dans ce régime volumique, la longueur d'onde dépend de b, v, et du module complexe $|G^\star| = \left(G'^2 + G''^2\right)^{1/2}$. Nous comparons la longueur d'onde de cette instabilité à celle d'une instabilité volumique typique décrite pour les liquides (complexes), l'instabilité de *Saffman–Taylor* [98]. Pour cette instabilité, la longueur d'onde initiale a été calculée par analyse de stabilité linéaire et est donnée par

$$\lambda = \pi b/\sqrt{Ca}\,. \tag{11.5}$$

$Ca = U\eta/\gamma$ est le nombre capillaire, un nombre sans dimension qui compare les forces visqueuses aux forces capillaires. η est la viscosité, $\gamma = 20\,\mathrm{mN/m}$ la tension de surface entre le PDMS et l'air, et U la vitesse radiale de l'interface circulaire. Pour un liquide incompressible, elle peut être calculée à partir de la conservation du volume par $U = Rv/2b$.

Nous appliquons la formule de *Saffman-Taylor* équation 11.5 à notre système en remplaçant la viscosité newtonienne η par la viscosité complexe $|\eta^\star| = |G^\star|/\omega$ déterminée par des mesures de rhéologie. Nous trouvons que cette formule décrit l'instabilité initiale qualitativement et quantitativement dans les limites de la résolution expérimentale.

Le deuxième régime que nous observons est caractérisé par une propagation de doigts d'air à l'interface entre le polymère et le poinçon. Le volume de la couche n'est que peu déformé, et la longueur d'onde est indépendante de tous les paramètres de système sauf de l'épaisseur b. Dans ce régime, λ est décrite par une loi linéaire,

$$\lambda = (2.27 \pm 0.1)\, b \; . \tag{11.6}$$

Ce résultat est en accord avec des expériences et des calculs théoriques qui ont été effectués pour une situation semblables, c'est-à-dire pour le cas statique du pelage d'une lame de verre flexible d'une couche de PDMS [47].

Une théorie de l'adhérence établie pour des élastomères permet de déterminer un paramètre pertinent pour la transition entre les mécanismes de décollement interfacial et volumique. Il a été montré que le paramètre empirique

$$\mathcal{G}_\mathrm{c}/E \propto G''/{G'}^2 \tag{11.7}$$

prédit qualitativement la transition entre le mécanisme interfacial et le mécanisme volumique pour des adhésifs souples et viscoélastiques, si l'on considère la surface du poinçon et l'épaisseur de la couche constantes. $\mathcal{G}_\mathrm{c}$ est le taux de restitution d'énergie critique, une quantité qui mesure l'énergie à fournir par unité de surface pour faire propager une fissure interfaciale. E est le module élastique de la couche. En modifiant ce paramètre de telle manière qu'il puisse être appliqué à des surfaces avec différentes énergies d'adhésion $\mathcal{G}_0$ et à des couches avec différentes épaisseurs, nous construisons un nouveau paramètre

$$\frac{\mathcal{G}_0\, G''}{b\, {G'}^2} \; . \tag{11.8}$$

Nous montrons qu' à partir de ce paramètre, il est possible de tracer une "carte de mécanismes" engendrée par les quantités $\mathcal{G}_0 \tan\delta$ et $G'b$. $\mathcal{G}_0 \tan\delta$ est une approximation de $\mathcal{G}_\mathrm{c}$, donc de l'énergie nécessaire par unité de surface pour faire propager une fissure interfaciale. $G'b$ en revanche donne une estimation de l'énergie qu'il faut injecter dans le système par unité de surface pour déformer le volume de l'échantillon. Nous mettons en évidence que ces paramètres sont aptes à prédire le mécanisme de décollement pour notre système modèle.

Le processus de décollement non-linéaire

Après avoir étudié l'instabilité linéaire, nous consacrons le chapitre 8 à l'étude du processus de décollement complet. Nous étudions plus en détail les courbes de force ainsi que l'énergie d'adhésion.

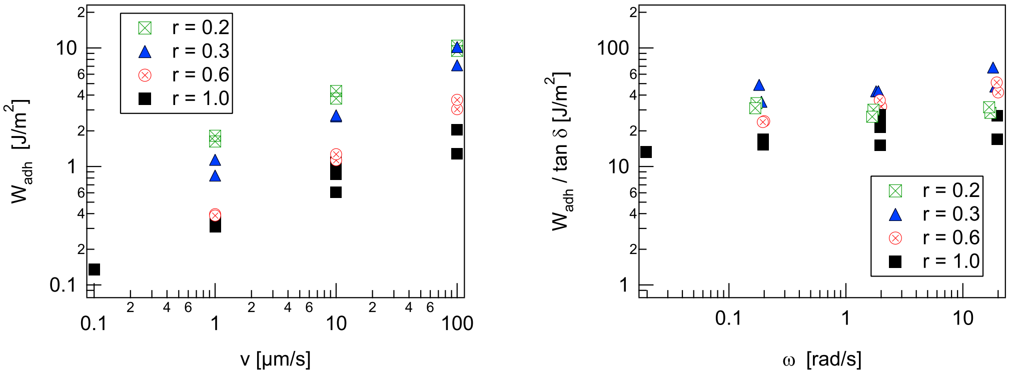

(a) L'énergie d'adhésion *versus* la vitesse de décollement.

(b) L'énergie d'adhésion divisée par tan δ *versus* la fréquence de sollicitation.

FIGURE 11.4.: La dépendance de l'énergie d'adhésion est décrite par la dépendance en vitesse de l'angle de perte.

La transition des propriétés du liquide vers le solide élastique se traduit également dans une modification de la forme des courbes contrainte-déformation. Nous entendons ici par contrainte la contrainte nominale, c'est-à-dire la force divisée par l'aire de contact maximale avant le début du décollement ; la déformation est calculée relativement à l'épaisseur initiale du film. Nous décrivons en détail les différentes courbes et l'évolution de leur forme caractéristique lors de la transition du liquide vers le solide élastique mou en passant par une gamme de matériaux viscoélastiques. En combinant l'étude des courbes et l'observation visuelle, nous révélons trois différents mécanismes de décollement. Premièrement, nous décrivons un mécanisme *cohésif*. Ce mécanisme, caractéristique des liquides, consiste en une formation très importante de fibrilles et une rupture finale en volume. Plus spécifiquement, les fibrilles cassent au milieu, et des traces du matériau restent sur la surface du poinçon. Nous observons ce mécanisme pour les taux de réticulant faibles, jusqu'à 1.2%. Pour des taux de réticulant intermédiaires, entre 1.3% et 1.6%, nous observons également une formation importante de fibrilles, donc une déformation du volume de la couche, par contre le décollement final se fait à l'interface. Les fibrilles se détachent de la surface du poinçon, et on ne trouve donc pas de traces du matériau sur le poinçon. Nous appelons ce mécanisme *adhésif-volumique*. Finalement, pour des taux de réticulant supérieurs à 1.6%, le processus reste interfacial : la déformation maximale avant décollement est inférieure à 100%. Il n'y a donc pas de fibrilles, et nous appelons ce mécanisme *adhésif-interfacial*.

Après avoir décrit la transition à travers les courbes contrainte-déformation, nous étudions plus en détail les différentes quantités qui caractérisent ces courbes. Typiquement, celles-ci sont la déformation maximale avant décollement et l'énergie d'adhésion. Cette dernière quantité est définie comme l'aire sous la courbe contrainte-déplacement et correspond à l'énergie nécessaire pour séparer deux plaques collées

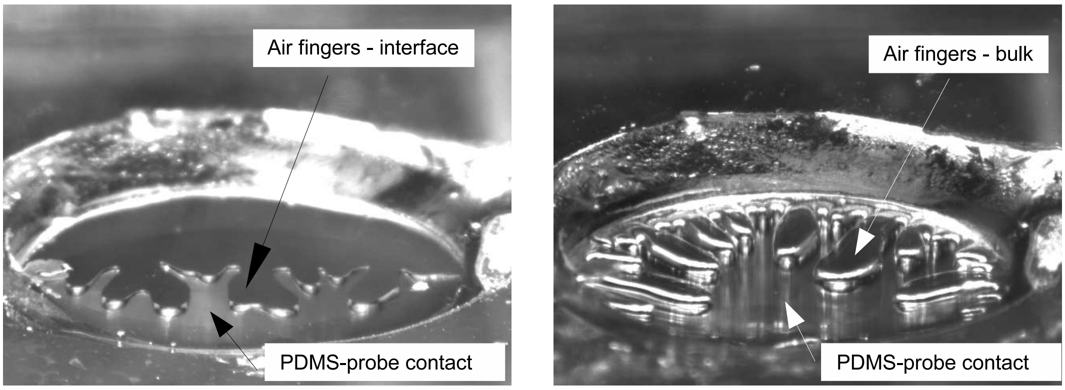

(a) Digitation interfaciale.

(b) Digitation en volume.

Figure 11.5.: Visualisation en $3D$

par le matériau viscoélastique. Traçant la déformation maximale en fonction du module élastique du matériau, on observe qu'elle diminue fortement. L'énergie d'adhésion par contre passe par un maximum. Dans la limite du liquide visqueux et du solide élastique très réticulé, on retrouve des valeurs proches de l'énergie thermodynamique. Plus un nombre élevé de points de réticulation est présent dans le matériau, moins la couche peut être facilement déformée. Par contre, le matériau est capable de dissiper de plus en plus d'énergie. La superposition de ces deux phénomènes résulte en un maximum dans l'énergie d'adhésion. Vers ce maximum, on retrouve normalement les adhésifs commerciaux. Par contre, il est important de noter que notre système de PDMS montre en général une trop faible énergie d'adhésion (due à une dissipation insuffisante) pour être utilisé comme adhésif.

Dans l'étape suivante, nous regardons plus en détail l'énergie d'adhésion pour les matériaux bien réticulés, c'est-à-dire pour les pourcentages d'agent de réticulation supérieurs à 2%. Nous observons qu'une dépendance entre l'énergie d'adhésion et la vitesse de propagation du front persiste jusqu'au matériau complètement réticulé (10% d'agent de réticulation). Un résultat surprenant donné par Ramond *et al.* [94] lie la dépendance en vitesse de l'énergie d'adhésion, propriété interfaciale, à la dépendance en fréquence de sollicitation de $\tan\delta$, propriété volumique. Ceci n'avait été vérifié que pour un seul matériau jusqu'ici. Nos résultats sur tous les élastomères de PDMS sont en bon accord avec ceux de Ramond *et al.* Nous traçons $W_{\mathrm{adh}}/\tan\delta$ en fonction de la fréquence de sollicitation et trouvons que cette quantité ne dépend plus de la fréquence, voir figure 11.4. Dans notre étude, le module varie sur deux ordres de grandeur.

La visualisation en $3D$

Dans beaucoup d'études s'intéressant aux énergies d'adhésion, il a été montré que les conditions aux limites au front de décollement jouent un grand rôle et ont une influence majeure sur l'énergie d'adhésion. En effet, les phénomènes de glissement à la ligne de contact résultent en une modulation de l'angle de contact. Malgré l'importance de la question, la forme exacte du front qui avance, c'est-à-dire la forme tridimensionnelle des doigts d'air, n'a jamais pu être éclaircie de manière satisfaisante. En nous basant sur une technique développée récemment au Japon [123], nous avons réussi à monter une expérience, en collaboration avec T. Yamaguchi et L. Sonnenberg, qui permet de visualiser pour la première fois en direct le front de décollement en trois dimensions. Pour cela, nous avons modifié le montage d'une machine qui est normalement utilisée en configuration de "tack" classique. Le poinçon habituel est remplacé par un disque en verre collé sur un prisme. Regarder à travers le prisme et le poinçon avec une caméra permet de visualiser *in situ* l'aire de contact entre le poinçon et la couche viscoélastique. Au moment du décollement, on obtient des images $3D$ de la ligne de contact qui avance. Bien que, pour l'instant, nous n'ayons pas encore mis au point les techniques de traitement d'image pour effectuer des mesures quantitatives sur les images déformées, nous arrivons à discerner clairement le décollement interfacial avec un contact direct entre l'air et le poinçon, et le décollement volumique ou l'on n'observe pas de contact, voir figure 11.5. Qualitativement, nous observons un changement dans l'angle de contact, qui est très proche de $90\,°$ dans les matériaux bien réticulés, et qui dévie nettement de l'angle droit dans les matériaux moins réticulés.

Le décollement d'une huile de silicone newtonienne

Dans le dernier chapitre de cette thèse, nous étudions plus en détail la formation de structures dans une huile newtonienne qui remplit une cellule de Hele-Shaw circulaire avec un entrefer variable $b(t) = b_0 + v_0 t$. Contrairement au chapitre 7, où nous nous sommes intéressés principalement à la première déstabilisation lors de la formation de structures, nous étudions dans le chapitre 10 l'évolution du nombre de doigts avec le temps. Comme nous l'avons vu auparavant, la formation de structures en montage de probe tack peut être décrite par l'instabilité de Saffman-Taylor, résultat obtenu par plusieurs groupes de recherche [104, 10, 75]. Le paramètre de contrôle qui détermine la longueur d'onde, ou, d'un autre point de vue, le nombre de doigts, est décrit par

$$\tau_0 = \frac{\gamma {b_0}^3}{12 v_0 \eta {R_0}^3} \,. \tag{11.9}$$

γ est la tension de surface entre le liquide dans la cellule et l'air ambiant, b_0 la valeur initiale de l'entrefer, R_0 le rayon de la tache d'huile correspondant au temps $t = 0$ au rayon du poinçon, v_0 est la vitesse de soulèvement de la plaque supérieure, et η dénomme la viscosité du liquide remplissant la cellule. La tension de surface entre air et huile de silicone est $\gamma = 20\,{}^{\mathrm{mN}}/_{\mathrm{m}}$.

Le nombre de doigts initial au moment de la première apparition de l'instabilité est lié à la longueur d'onde initiale par $N_0 = 2\pi R_0/\lambda$. λ est la longueur d'onde avec le plus grand taux de croissance au sens d'une analyse de stabilité linéaire. N_0 peut

Figure 11.6.: L'instabilité de Saffman–Taylor dans une cellule circulaire avec entrefer variable à temps différents. $R_0 = 3\,\mathrm{mm}$, $b_0 = 50\,\mu\mathrm{m}$, $v_0 = 8\,{}^{\mu\mathrm{m}}/_{\mathrm{s}}$, $\eta = 96\,\mathrm{Pa\,s}$.

être calculé à partir de τ_0 selon

$$N_0 = \sqrt{\frac{1}{3}\left(1 + \frac{1}{2\tau_0}\right)}\,. \tag{11.10}$$

Introduisant la dépendance de b et R en temps, respectivement en temps réduit $t' = v_0/b_0\,t$, dans l'équation 11.10, on obtient une formule qui décrit l'évolution du nombre de doigts avec le temps sans dimension :

$$N(t') = \sqrt{\frac{1}{3}\left(1 + \frac{1}{2\tau_0(1+t')^{9/2}}\right)}\,. \tag{11.11}$$

Cette formule est basée sur une analyse de stabilité linéaire en deux dimensions et néglige par conséquent tout effet non-linéaire ou tridimensionnel. Nous étudions dans cette thèse le nombre de doigts pour différentes réalisations du même paramètre de contrôle τ_0. Plus précisément, nous utilisons des systèmes plus ou moins confinés avec deux viscosités différentes, tout en adaptant la vitesse pour garder τ_0 constant. Nous comparons le nombre N expérimental au nombre N théorique calculé d'après l'équation 11.11 et nous trouvons que le nombre de doigts dans les expériences est toujours supérieur à la prédiction théorique. Ceci s'explique par la variation du paramètre de contrôle en fonction du temps. Nous observons qu'on peut distinguer à chaque instant des doigts en croissance, c'est-à-dire, des doigts qui avancent vers le centre de la cellule, et des doigts qui meurent. Ces doigts “morts” sont fixés à leur position actuelle, sont doublés par la ligne de contact qui avance et finissent par disparaître. Au moment t'_1, $\tau(t')$ excite un certain nombre de doigts N_1 à croître. Au moment $t'_2 + \delta t'$, ce nombre est égal à $N_2 < N_1$. Pourtant, N_1 doigts excités à t'_1 sont présents dans le système. Le nombre de doigts supérieur à la prédiction linéaire peut donc être attribué à l'inertie de la ligne de contact : L'huile qui reste entre les doigts d'air se retire avec une certaine inertie et les doigts stagnants ne disparaissent pas instantanément. Nous avons pu montrer que le nombre de doigts croissant est très bien décrit par l'équation 11.11, donc par une analyse de stabilité linéaire à chaque instant. En outre, nous mettons en évidence que le nombre de doigts total dépend fortement du confinement du système. Plus le système est confiné, plus on observe de doigts en total. Nous attribuons cette observation au fait qu'à un temps donné, l'amplitude des doigts est d'autant plus grand que le système est confiné. Ainsi, une plus grande amplitude engendre un plus grand temps de vie des doigts, c'est-à-dire l'huile se retire moins rapidement vers le centre. les doigts stagnants contribuent donc plus longtemps au nombre total de doigts. La question de savoir pourquoi l'amplitude dépend du confinement du système reste ouverte pour l'instant. Une comparaison avec des simulations numériques [75] indique pourtant une relation avec l'amplitude de la perturbation initiale.

Dans l'étape suivante, nous nous sommes intéressés à l'influence des doigts sur la force pendant le processus de décollement, une question qui a été étudiée par différents groupes de recherche et qui est cruciale pour la compréhension de la performance des adhésifs. Il a été démontré que la formation de cavités a une influence sur la force dans des huiles [113, 92]. Pour la digitation visqueuse en revanche, des observations contradictoires ont été décrites [92, 40, 75]. Dans le cadre de cette thèse, nous présentons des résultats montrant que l'influence des doigts dépend fortement du paramètre de contrôle, c'est-à-dire du nombre et de l'amplitude des doigts. Pour une digitation faible, nous n'observons quasiment pas d'influence des digitations sur la force de décollement en la comparant avec la force calculée pour un cercle d'huile qui se rétracte de façon homogène. Pour des valeurs plus faibles du paramètre de contrôle, qui engendrent la formation de plus de doigts, nous observons que la force mesurée reste inférieure à la force calculée. Le fait que l'influence des digitations sur la force est plus importante pour des amplitudes de doigts plus prononcées nous amène à dire que la diminution de la force est réellement liée à la digitation. Dans ce contexte, il est intéressant de mentionner que la valeur des amplitudes dépend, elle aussi, du paramètre de contrôle. Un petit τ engendre un grand nombre de doigts avec une croissance importante, un grand τ entraîne la formation de peu de doigts avec une faible croissance. Ceci est d'ailleurs un des facteurs limitants pour les expériences : un τ trop grand rend impossible le comptage des doigts qui croissent à peine et sont donc difficilement distinguables.

Conclusion

En conclusion, dans le cadre de cette thèse, nous avons étudié la transition d'un liquide newtonien vers un solide élastique mou lors du décollement en géométrie de probe tack. Nous avons trouvé que le décollement d'un matériau viscoélastique peut être amorcé par la formation de doigts à l'interface ou en volume. Un mécanisme qui est initialement interfacial le restera pendant tout le décollement. Dans ce cas, la longueur d'onde ne dépend que de l'épaisseur de la couche, en accord avec une instabilité interfaciale observée dans une géométrie de pelage statique [47]. En revanche, un amorçage du décollement en volume engendre la formation de fibrilles qui peuvent se casser au milieu ou bien se détacher du poinçon. Dans ce cas, la longueur d'onde initiale est décrite par l'équation établie dans le cas de l'instabilité de Saffman-Taylor [98]. La transition entre les mécanismes volumiques et interfaciaux est décrite par un paramètre sans dimension [36]. Ce paramètre a été établi à partir des propriétés viscoélastiques linéaires du matériau et de l'énergie d'adhésion entre la couche viscoélastique et le poinçon.

Le montage de probe tack peut être décrit comme une cellule de Hele-Shaw circulaire avec entrefer variable [104, 10]. Pour compléter l'étude de la formation de structures, nous avons étudie une huile newtonienne dans une telle cellule. Nous avons expliqué le processus de "coarsening" que les structures subissent au cours du temps par analyse de stabilité linéaire. Nous avons également mis en évidence l'influence du confinement sur l'amplitude des doigts et sur la force normale pendant le décollement.

Nous présentons des résultats concernant la dépendance de l'énergie d'adhésion avec la vitesse pour des élastomères. Nous confirmons que la dépendance en vitesse de l'énergie d'adhésion est lié directement à la dépendance en fréquence de sollicitation de $\tan \delta$. C'est la première fois que cette théorie, établie par Ramond *et al.* en 1985 [94], a pu être vérifié sur une large gamme du module élastique.

La connaissance des conditions aux limites pendant la propagation d'une fracture est cruciale pour toute interprétation quantitative de l'énergie d'adhésion et pour toute modélisation numérique ou analytique. Basé sur une technique développé par Yamaguchi *et al.* [122], nous présentons une nouvelle méthode de visualisation en trois dimensions. Cette technique nous permet pour la première fois de visualiser directement la ligne de contact entre le matériau viscoélastique et le poinçon rigide et d'acceder ainsi au conditions aux limites lors du décollement.

Les résultats que nous avons obtenus sont d'une grande utilité pour l'amélioration des adhésifs, matériaux très complexes, ainsi que pour la compréhension fondamentale de la formation de structures dans des matériaux viscoélastiques.

Deutsche Zusammenfassung

Das Zusammenkleben und Ablösen zweier Gegenstände ist ein alltägliches Phänomen. Klebstoffe, die nach Anwendung eines leichten Druckes nur anhand der van-der-Waals-Kraft kleben, heißen „pressure sensitive adhesives“(PSAs). Typische Anwendung sind Klebstreifen und Etikette. Die Eigenschaften der PSAs liegen zwischen denen reiner Flüssigkeiten und reiner Festkörper. Im Rahmen dieser experimentellen Doktorarbeit untersuchen wir anhand des Ablöseprozesses den Übergang von einer viskosen Flüssigkeit über viskoelastische Materialien hin zum elastischen weichen Festkörper. Dabei untersuchen wir verschiedene Aspekte dieses fundamentalen Problems in der so genannten „Probe-Tack-Geometrie“.

Als Modellsystem mit einem kontinuierlichen Übergang zwischen den verschiedenen Substanzklassen verwenden wir ein kommerzielles Produkt (*„Sylgard© 184 Silicone Elastomer Kit“* von *Dow Corning*). Das Kit enthält ein Silikonöl (Polydimethyl Siloxan, PDMS) und einen so genannten *Crosslinker*. Das reine Silikonöl besteht aus kurzen Polymerketten und verhält sich wie eine Newtonsche Flüssigkeit. Unter Zugabe des Crosslinkers und unter Hitzeeinwirkung bilden sich kovalente Bindungen zwischen den einzelnen Polymerketten aus und es entsteht ein Netzwerk. Die Materialien charakterisieren wir in einem Rheometer. Wir bestimmen den Speichermodul G', der die elastischen Eigenschaften des Materials quantifiziert, sowie den Verlustmodul G'', der ein Maß für den viskosen Anteil der Materialeigenschaften ist. Je nach zugegebener Menge des Crosslinkers erhält man eine viskoelastische Flüssigkeit, ein Material am Gelpunkt oder einen viskoelastischen Festkörper, dessen elastischer Modul mit einer weiteren Erhöhung des Crosslinker-Anteils weiter ansteigt und dessen dissipativer Anteil dabei geringer wird.

Beim Probe-Tack-Test [129, 58] wird ein zylindrischer Metallstempel (Radius 3 mm) mit flacher Oberfläche einer 50 µm bis 500 µm dicken Schicht eines viskoelastischen Materials angenähert. Nach Erreichen des Kontakts wird der Stempel mit kontrollierter Geschwindigkeit von der Schicht abgelöst. Dabei werden die Normalkraft auf den Stempel sowie seine Entfernung von der PDMS-Schicht gemessen. Während des Ablösens entstehen durch in die Klebeschicht eindringende Luft verschiedene Strukturen. Diese Strukturbildung beobachten wir in einer Draufsicht mit einer Kamera durch ein Mikroskop.

In Kapitel 7 untersuchen wir die Strukturbildung während des Ablöseprozesses. Beim Ablösen dringt Luft seitlich entweder in den Bulk der viskoelastischen Schicht oder an der Grenzfläche zwischen Polymer und Stempel ein. Die Kontaktlinie zwischen Luft und viskoelastischem Material ist anfänglich kreisförmig. Beim Ablösen wird sie jedoch instabil und beginnt sich zu wellen. Je weiter der Stempel abgezogen wird, desto stärker wächst die Amplitude der Wellen. Schließlich bilden sich Luftfinger, die sich zur Mitte des Stempels hinbewegen. Hierbei identifizieren wir zwei verschiedene Mechanismen: einerseits ein Entkleben an der Grenzfläche zwischen Stempel und PDMS, andererseits einen Mechanismus, der sich im Bulk des viskoelastischen Materials abspielt. Der Fall des Entklebens an der Grenzfläche zeichnet sich durch schnelles Ausbreiten der Luftfinger an der Grenzfläche aus, ohne das Material selbst stark zu deformieren. Im Fall des Entklebens im Bulk bilden sich so genannte Fibrillen, das heißt „PDMS-Brücken“ zwischen dem Stempel und der Polymerschicht. Hierbei wird das Volumen des Materials sehr stark verformt. Wir charakterisieren die Strukturen in beiden Fällen durch ihre Wellenlänge im Moment der Destabilisierung. Sie berechnet sich aus der Anzahl der Finger und dem Umfang des Stempels. Hierbei konnten wir die Wellenlänge sowohl für das Grenzflächenregime als auch für das Bulkregime quantitativ und qualitativ bestimmen. Wir zeigen, das die Wellenlänge im Bulkregime durch die Saffman-Taylor-Theorie beschrieben wird [98], und im Grenzflächenregime den Gleichungen gehorcht, die für eine elastische Oberflächeninstabilität auf gestellt wurden [47]. Weiterhin schlagen wir einen empirischen Parameter vor, der den Übergang zwischen Grenzflächen- und Bulkmechanismus beschreibt. Diese Resultate wurden 2008 publiziert [81].

In Kapitel 8 konzentrieren wir uns auf die Spannungs-Belastungskurven während des gesamten Entklebeprozesses. Wir beschreiben die Änderung der Kurvenform, wenn das Material von der Flüssigkeit zum Festkörper übergeht, und quantifizieren diesen Übergang anhand der typischen Parameter Adhäsionsenergie und maximale Deformation vor dem vollständigen Ablösen. Die Adhäsionsenergie repräsentiert die Energie, die nötig ist, um den Stempel von der Polymerschicht abzulösen. Wir identifizieren drei verschiedene Mechanismen in Abhängigkeit von den Materialeigenschaften. Für sehr schwach vernetzte Materialien finden wir einen kohäsiven Volumenmechanismus, das heißt, dass die Fibrillen am Ende des Entklebeprozesses in der Mitte durchreißen und somit Überreste des Polymers auf dem Stempel vorzufinden sind. Für mittlere Vernetzungsgrade finden wir einen adhäsiven Volumenmechanismus, bei dem das Entkleben im Volumen initiiert wird und Fibrillen entstehen, diese sich jedoch ohne Überreste vom Stempel ablösen. Für stark vernetzte, überwiegend elastische Materialien schließlich finden wir einen adhäsiven Grenzflächenmechanismus, bei dem sich der gesamte Entklebeprozess an der Oberfläche abspielt und der Bulk der Schicht kaum deformiert wird. Für die vorwiegend elastischen Materialen untersuchen wir die Adhäsionsenergie genauer. Dabei zeigen wir, dass es möglich ist, die Geschwindigkeitsabhängigkeit der Adhäsionsenergie durch die Geschwindigkeitsabhängigkeit rheologischer Materialeigenschaften zu erklären [94].

Kapitel 9 stellt eine neue Technik vor, die es erstmals erlaubt, die Kontaktlinie zwischen Luft und Polymer in drei Dimensionen abzubilden. Aufbauend auf einer Technik, die von T. Yamaguchi *et al.* entwickelt wurde [123], nutzen wir die Totalreflexion in einem Prisma und beobachten durch einen Glasstempel hindurch direkt den Kontakt Stempel-PDMS-Luft. In ersten Versuchen zeigen wir, dass sich verschiedene Materialien sowohl in der Dicke der Luftfinger als auch im Kontaktwinkel qualitativ unterscheiden. Damit ist es uns zum ersten Mal gelungen, die Kontaktlinie und ihre Destabilisierung beim Entkleben *in situ* abzubilden. Dies ermöglicht erstmals eine direkte Bestimmung der Randbedingungen zwischen viskoelastischem Material und festem Substrat und liefert damit die Grundlage für Modellierung.

Kapitel 10 schließlich widmet sich der detaillierten Untersuchung der Strukturbildung beim Entkleben einer Newtonschen Flüssigkeit in einer kreisförmigen Zelle. Wir betrachten eine dünne Schicht eines Silikonöls zwischen einer Glasplatte und einem Metallstempel. Dabei ist die Schichtdicke b_0 sehr klein gegenüber dem Stempelradius R_0. Zieht man den Stempel mit der Geschwindigkeit v_0 ab, bilden sich Luftfinger im Volumen. Diese Instabilität ist eine Variante der *Saffman-Taylor-Instabilität* [98, 104, 10]. Die destabilisierende Wellenlänge wurde durch lineare Stabilitätsanalyse bestimmt und wird von dem Parameter $\tau_0 = \gamma {b_0}^3/12 v_0 \eta {R_0}^3$ kontrolliert, wobei γ die Oberflächenspannung zwischen Luft und Öl und η die Viskosität des Öls ist [104, 10]. Mit wachsendem Abstand der Platten verringert sich die Fingeranzahl deutlich *(Coarsening)* [75]. Einerseits wurden hierfür geometrische Effekte verantwortlich gemacht, da den Fingern zur Mitte hin immer weniger Platz zur Verfügung steht, andererseits die Änderung im Kontrollparameter $\tau(t)$, der mit wachsendem Plattenabstand $b(t)$ zunimmt. Es ist uns gelungen, das Coarsening der Strukturen dadurch zu erklären, dass wir die Finger in wachsende und stagnierende Finger einteilen. Wachsende Finger bewegen sich zur Mitte des Stempels, während stagnierende Finger auf ihrer Position verharren und schließlich aussterben. Wir zeigen, dass die Anzahl wachsender Finger auch zu fortgeschrittenen Zeiten durch lineare Stabilitätsanalyse vorhergesagt werden kann, und geometrische Effekte somit nur eine untergeordnete Rolle spielen. Weiterhin zeigen wir, dass die Kraft, die benötigt wird, um die Platten zu trennen, durch die Fingerinstabilität beeinflußt wird: Je größer das Aspektverhältnis R_0/b_0 ist, desto größer ist die Fingeramplitude und desto kleiner wird die Kraft.

Die Ergebnisse, die in dieser Dissertation vorgestellt werden, ermöglichen ein tieferes Verständnis der Strukturbildung in viskoelastischen Materialien. Speziell die Frage des Übergangs von flüssig zu fest ist einerseits für die Verbesserung und Entwicklung von Klebstoffen, andererseits für das grundlegende Verständnis von Strukturbildung in Materialien mit komplexen Eigenschaften von großer Bedeutung .

Bibliography

[1] M. Adda-Bedia and L. Mahadevan: *Crack-front instability in a confined elastic film.* Proceedings of the Royal Society A - Mathematical, Physical, and Engineering Sciences, **462**, 3233 (2006) 1, 4.3, 4.3, 7.3.2, 7.3.2, 11

[2] D. Ahn and K. R. Shull: *JKR studies of acrylic elastomer adhesion to glassy polymer substrates.* Macromolecules, **29**, 4381 (1996) 1

[3] D. Ahn and K. R. Shull: *Effects of methylation and neutralization of carboxylated poly(n-butyl acrylate) on the interfacial and bulk contributions to adhesion.* Langmuir, **14**, 3637 (1998) 3.3

[4] J. J. Aklonis and W. J. MacKnight: *Introduction to Polymer Viscoelasticity* (Wiley-Interscience, 1983), second edition 2.1, 2.2, 2.2

[5] N. Amouroux: *Etude des méchanismes de modulation de l'adhérence entre un élastomère silicone et un adhésif acrylique.* Ph.D. thesis, Université Paris VI (1998) 5.1

[6] N. Amouroux, J. Petit, and L. Leger: *Role of interfacial resistance to shear stress on adhesive peel strength.* Langmuir, **17**, 6510 (2001) 8.4.3, 9.1

[7] N. Arun, A. Sharma, P. S. G. Pattader, I. Banerjee, H. M. Dixit, and K. S. Narayan: *Electric field induced patterns in soft visco-elastic films: From long waves of viscous liquids to short waves of elastic solids.* to be published in Physical Review Letters (2009) 1, 2, 11

[8] H. A. Barnes: *Shear-thickening ("dilatancy") in suspensions of nonaggregating solid particles dispersed in newtonian liquids.* Journal of Rheology, **33**, 329 (1989) 2.2(b), 2.1

[9] Q. Barral, G. Ovarlez, X. Chateau, J. Boujlel, B. Rabideau, and P. Coussot: *Adhesion energy of soft-jammed systems.* to be published (2009) 1, 11

[10] M. Ben Amar and D. Bonn: *Fingering instabilities in adhesive failure.* Physica D - Nonlinear Phenomena, **209**, 1 (2005) 1, 4.2.2, 10.1, 10.1, 10.1, 10.7, 10.8, 11, 11, 11, 11, 11

[11] L. Benyahia, C. Verdier, and J. M. Piau: *The mechanisms of peeling of uncross-linked pressure sensitive adhesives.* Journal of Adhesion, **62**, 45 (1997) 1

[12] J. J. BIKERMAN: *The fundamentals of tackiness and adhesion.* Journal of Colloid Science, **2**, 163 (1947) 8.4.3, 10.6

[13] J. BOHR, S. BRUNAK, and T. NORRETRANDERS: *Viscous trees and Voronoi-structure formation in expanding systems.* Europhysics Letters, **25**, 245 (1994) 10.1

[14] F. P. BRETHERTON: *The motion of long bubbles in tubes.* Journal of Fluid Mechanics, **10**, 166 (1961) 10.8

[15] X. Q. BROWN, K. OOKAWA, and J. Y. WONG: *Evaluation of polydimethylsiloxane scaffolds with physiologically-relevant elastic moduli: interplay of substrate mechanics and surface chemistry effects on vascular smooth muscle cell response.* Biomaterials, **26**, 3123 (2005) 5.3

[16] C. CARELLI, F. DEPLACE, L. BOISSONNET, and C. CRETON: *Effect of a gradient in viscoelastic properties on the debonding mechanisms of soft adhesives.* Journal of Adhesion, **83**, 491 (2007) 3.3, 7.3.1

[17] E. P. CHANG: *Viscoelastic windows of pressure-sensitive adhesives.* Journal of Adhesion, **34**, 189 (1991) 1, 3.3

[18] E. P. CHANG: *Viscoelastic properties of pressure-sensitive adhesives.* Journal of Adhesion, **60**, 233 (1997) 3.3

[19] A. CHICHE: *Décollement d'un adhésif souple : rupture et cavitation.* Ph.D. thesis, Université Paris VII (2003) 4.3, 6.1

[20] A. CHICHE, J. DOLLHOFER, and C. CRETON: *Cavity growth in soft adhesives.* European Physical Journal E, **17**, 389 (2005) 6.1, 8.4.1

[21] A. CHICHE, P. PAREIGE, and C. CRETON: *Role of surface roughness in controlling the adhesion of a soft adhesive on a hard surface.* Comptes Rendus De L'Academie Des Sciences Série IV: Physique Astrophysique, **1**, 1197 (2000) 6.1, 8.4.1

[22] R. L. CHUOKE, P. VANMEURS, and C. VANDERPOEL: *The instability of slow, immiscible, viscous liquid-liquid displacements in permeable media.* Transactions of the American Institute of Mining and Metallurgical Engineers, **216**, 188 (1959) 4.2

[23] R. COMBESCOT, T. DOMBRE, V. HAKIM, Y. POMEAU, and A. PUMIR: *Shape selection of Saffman-Taylor fingers.* Physical Review Letters, **56**, 2036 (1986) 4.2

[24] Y. COUDER: *Viscous fingering as an archetype for growth patterns.* In *Perspectives in Fluid Dynamics. A collective Introduction to Current Research* (G. K. BATCHELOR, H. K. MOFFATT, and M. G. WORSTER, editors), chapter 2 (Cambridge University Press, 2000) 4.2.3

[25] P. Coussot: *Saffman-Taylor instability in yield-stress fluids.* Journal of Fluid Mechanics, **380**, 363 (1999) 4.2.3

[26] P. Coussot, L. Tocquer, C. Lanos, and G. Ovarlez: *Macroscopic vs. local rheology of yield stress fluids.* Journal of Non-Newtonian Fluid Mechanics, **158**, 85 (2009) 10.7

[27] W. P. Cox and E. H. Merz: *Correlation of dynamic and steady flow viscosities.* Journal of Polymer Science, **28**, 619 (1958) 7.3.1

[28] C. Creton, J. Hooker, and K. R. Shull: *Bulk and interfacial contributions to the debonding mechanisms of soft adhesives: Extension to large strains.* Langmuir, **17**, 4948 (2001) 1

[29] C. Creton and H. Lakrout: *Micromechanics of flat-probe adhesion tests of soft viscoelastic polymer films.* Journal of Polymer Science Part B-Polymer Physics, **38**, 965 (2000) 3.3

[30] C. Creton and L. Leibler: *How does tack depend on time of contact and contact pressure?* Journal of Polymer Science Part B-Polymer Physics, **34**, 545 (1996) 3.3

[31] A. J. Crosby, K. R. Shull, H. Lakrout, and C. Creton: *Deformation and failure modes of adhesively bonded elastic layers.* Journal of Applied Physics, **88**, 2956 (2000) 3.3

[32] A. J. Crosby, K. R. Shull, Y. Y. Lin, and C. Y. Hui: *Rheological properties and adhesive failure of thin viscoelastic layers.* Journal of Rheology, **46**, 273 (2002) 1

[33] C. A. Dahlquist: *Pressure-senistive adhesives.* In *Treatise on Adhesion and Adhesives* (R. L. Patrick, editor), volume 2, 219–260 (Dekker, 1969) 3.3

[34] P. G. deGennes: *Fracture of a weakly crosslinked adhesive.* Comptes Rendus De L'Académie Des Sciences Serie II, **307**, 1949 (1988) 1

[35] P. G. deGennes: *Soft adhesives.* Langmuir, **12**, 4497 (1996) 1

[36] F. Deplace: *Waterborne nanostructured adhesives.* Ph.D. thesis, Université Paris VI (2008) 3.3, 3.3, 3.3, 7.4, 11, 11

[37] F. Deplace, C. Carelli, S. Mariot, H. Retsos, A. Chateauminois, K. Ouzineb, and C. Creton: *Fine tuning the adhesive properties of a soft nanostructured adhesive with rheological measurements.* The Journal of Adhesion, **85**, 18 (2008) 8.1

[38] F. Deplace, M. A. Rabjohns, T. Yamaguchi, A. B. Foster, C. Carelli, C. H. Lei, K. Ouzineb, J. L. Keddie, P. A. Lovell, and

C. Creton: *Deformation and adhesion of a periodic soft-soft nanocomposite designed with structured polymer colloid particles*. Soft Matter, **5**, 1440 (2009) 1, 8.3

[39] C. Derail, A. Allal, G. Marin, and P. Tordjeman: *Relationship between viscoelastic and peeling properties of model adhesives. Part 1. Cohesive fracture*. Journal of Adhesion, **61**, 123 (1997) 1, 8.4.3

[40] D. Derks, A. Lindner, C. Creton, and D. Bonn: *Cohesive failure of thin layers of soft model adhesives under tension*. Journal of Applied Physics, **93**, 1557 (2003) 1, 1, 8.3, 8.4.3, 10.6, 10.8, 11, 11, 11

[41] D. Dillard and A. Pocius (editors): *The Mechanics of Adhesion*, volume 1 of *Adhesion science and engineering* (Elsevier, 2002), first edition 3, 3.1

[42] R. J. Fields and M. F. Ashby: *Finger-like crack growth in solids and liquids*. Philosophical Magazine, **33**, 33 (1976) 1, 11

[43] B. A. Francis and R. G. Horn: *Apparatus-specific analysis of fluid adhesion measurements*. Journal of Applied Physics, **89**, 4167 (2001) 6.1, 8.3, 8.4.1

[44] A. N. Gent: *Adhesion and strength of viscoelastic solids. is there a relationship between adhesion and bulk properties?* Langmuir, **12**, 4492 (1996) 1, 3.3, 8.4.3

[45] A. N. Gent and R. P. Petrich: *Adhesion of viscoelastic materials to rigid substrates*. Proceedings of the Royal Society of London Series a-Mathematical and Physical Sciences, **310**, 433 (1969) 1, 8.4.3

[46] A. Ghatak and M. K. Chaudhury: *Adhesion-induced instability patterns in thin confined elastic film*. Langmuir, **19**, 2621 (2003) 1, 4.3, 4.8, 4.3

[47] A. Ghatak, M. K. Chaudhury, V. Shenoy, and A. Sharma: *Meniscus instability in a thin elastic film*. Physical Review Letters, **85**, 4329 (2000) 1, 4.3, 4.7(a), 7.3, 7.3.2, 11, 11, 11, 11, 11

[48] A. Ghatak, L. Mahadevan, and M. K. Chaudhury: *Measuring the work of adhesion between a soft confined film and a flexible plate*. Langmuir, **21**, 1277 (2005) 1, 4.3, 8.4.3, 11

[49] F. X. Gibert, G. Marin, C. Derail, A. Allal, and J. Lechat: *Rheological properties of hot melt pressure-sensitive adhesives based on styrene-isoprene copolymers. Part 1: A rheological model for [SIS-SI] formulations*. Journal of Adhesion, **79**, 825 (2003) 1

[50] N. J. Glassmaker, C. Y. Hui, T. Yamaguchi, and C. Creton: *Detachment of stretched viscoelastic fibrils*. European Physical Journal E, **25**, 253 (2008) 8.3, 8.3

[51] D. S. GRAY, J. TIEN, and C. S. CHEN: *Repositioning of cells by mechanotaxis on surfaces with micropatterned Young's modulus.* Journal of Biomedical Materials Research Part A, **66A**, 605 (2003) 5.3

[52] A. A. GRIFFITH: *The phenomena of rupture and flow in solids.* Philosophical Transaction of the Royal Society London A, **221**, 163 (1921) 3.3

[53] F. H. HAMMOND: *Polyken probe tack tester.* ASTM Special Technical Publication, **360**, 123 (1964) 6.1

[54] J. A. F. HARVEY and D. CEBON: *Failure mechanisms in viscoelastic films.* Journal of Materials Science, **38**, 1021 (2003) 1, 11

[55] D. C. HONG and J. S. LANGER: *Analytic theory of the selection mechanism in the Saffman-Taylor problem.* Physical Review Letters, **56**, 2032 (1986) 4.2

[56] K. L. JOHNSON, K. KENDALL, and A. D. ROBERTS: *Surface energy and contact of elastic solids.* Proceedings of the Royal Society of London Series a-Mathematical and Physical Sciences, **324**, 301 (1971) 3.3

[57] G. JOSSE: *De l'adhérence à l'anti-adhérence à travers le Probe Tack.* Ph.D. thesis, Université Paris VI (2001) 4.3, 6.1

[58] G. JOSSE, P. SERGOT, C. CRETON, and M. DORGET: *Measuring interfacial adhesion between a soft viscoelastic layer and a rigid surface using a probe method.* Journal of Adhesion, **80**, 87 (2004) 6.1, 6.1, 8.1, 8.3, 11

[59] D. H. KAELBLE: *Theory and analysis of peel adhesion - rate-temperature dependence of viscoelastic interlayers.* Journal of Colloid Science, **19**, 413 (1964) 3.3

[60] K. KENDALL: *Adhesion and surface energy of elastic solids.* Journal of Physics D-Applied Physics, **4**, 1186 (1971) 3.3

[61] L. KONDIC, P. PALFFY-MUHORAY, and M. J. SHELLEY: *Models of non-Newtonian Hele-Shaw flow.* Physical Review E, **54**, R4536 (1996) 10.7

[62] L. KONDIC, M. J. SHELLEY, and P. PALFFY-MUHORAY: *Non-Newtonian Hele-Shaw flow and the Saffman-Taylor instability.* Physical Review Letters, **80**, 1433 (1998) 10.7

[63] M. A. KRENCESKI and J. F. JOHNSON: *Shear, tack, and peel of polyisobutylene - effect of molecular-weight and molecular-weight distribution.* Polymer Engineering and Science, **29**, 36 (1989) 1

[64] V. R. KRISHNAN and C. Y. HUI: *Large deformation of soft elastic materials in adhesive contact with a rigid cylindrical flat punch.* Soft Matter, **4**, 1909 (2008) 9.2, 9.1

[65] H. Lakrout, C. Creton, D. C. Ahn, and K. R. Shull: *Influence of molecular features on the tackiness of acrylic polymer melts*. Macromolecules, **34**, 7448 (2001) 1, 8.4.3

[66] H. Lakrout, P. Sergot, and C. Creton: *Direct observation of cavitation and fibrillation in a probe tack experiment on model acrylic pressure-sensitive-adhesives*. Journal of Adhesion, **69**, 307 (1999) 6.1, 8.3, 9.1, 9.2

[67] L. Landau and E. Lifschitz: *Lehrbuch der Theoretischen Physik*, volume VI (Akademie-Verlag Berlin, 1991), fifth edition 4.2

[68] L. Leger and N. Amouroux: *Modulation of adhesion at silicone elastomer-acrylic adhesive interface*. Journal of Adhesion, **81**, 1075 (2005) 5.1

[69] L. Leger and C. Creton: *Adhesion mechanisms at soft polymer interfaces*. Philosophical Transactions of the Royal Society a-Mathematical Physical and Engineering Sciences, **366**, 1425 (2008) 1, 8.3

[70] L. Leger, E. Raphael, and H. Hervet: *Surface-anchored polymer chains: Their role in adhesion and friction*. In *Polymers in Confined Environments*, volume 138 of *Advances in Polymer Science*, 185–225 (1999) 1

[71] H. Lemaire, Y. Ould Mohamed Abdelhaye, J. Larue, R. Benoit, P. Levitz, and H. Van Damme: *Pattern formation in noncohesive and cohesive granular media*. Fractals, **1**, 968 (1993) 1, 11

[72] A. Lindner, D. Bonn, and J. Meunier: *Viscous fingering in a shear-thinning fluid*. Physics of Fluids, **12**, 256 (2000) 4.2.3, 7.3.1

[73] A. Lindner, D. Bonn, E. C. Poire, M. Ben Amar, and J. Meunier: *Viscous fingering in non-Newtonian fluids*. Journal of Fluid Mechanics, **469**, 237 (2002) 4.2.3, 7.3.1

[74] A. Lindner, P. Coussot, and D. Bonn: *Viscous fingering in a yield stress fluid*. Physical Review Letters, **85**, 314 (2000) 4.2.3, 7.3.1

[75] A. Lindner, D. Derks, and M. J. Shelley: *Stretch flow of thin layers of Newtonian liquids: Fingering patterns and lifting forces*. Physics of Fluids, **17**, 072107 (2005) 1, 4.2.2, 10.1, 10.1, 10.3, 10.3, 10.4, 10.5, 10.15, 10.16, 10.6, 10.20, 10.6, 10.6, 10.8, 11, 11, 11, 11, 11

[76] A. Lindner, B. Lestriez, S. Mariot, C. Creton, T. Maevis, B. Luhmann, and R. Brummer: *Adhesive and rheological properties of lightly crosslinked model acrylic networks*. Journal of Adhesion, **82**, 267 (2006) 1, 7.3.1

[77] D. Maugis and M. Barquins: *Fracture mechanics and adherence of viscoelastic bodies*. Journal of Physics D-Applied Physics, **11**, 1989 (1978) 1, 3.3, 3.3, 7.4, 8.4.3, 11

[78] K. V. McCloud and J. V. Maher: *Experimental perturbations to Saffman-Taylor flow*. Physics Reports-Review Section of Physics Letters, **260**, 139 (1995) 10.1

[79] W. Monch and S. Herminghaus: *Elastic instability of rubber films between solid bodies*. Europhysics Letters, **53**, 525 (2001) 1, 4.7(b), 4.3, 11

[80] H. K. Mueller and W. G. Knauss: *Crack propagation in a linearly viscoelastic strip*. Journal of Applied Mechanics, **38**, 483 (1971) 1

[81] J. Nase, A. Lindner, and C. Creton: *Pattern formation during deformation of a confined viscoelastic layer: From a viscous liquid to a soft elastic solid*. Physical Review Letters, **101**, 074503 (2008) 1, 11

[82] B. M. Z. Newby and M. K. Chaudhury: *Effect of interfacial slippage on viscoelastic adhesion*. Langmuir, **13**, 1805 (1997) 8.4.3, 9.1

[83] B. M. Z. Newby and M. K. Chaudhury: *Friction in adhesion*. Langmuir, **14**, 4865 (1998) 8.4.3, 9.1

[84] B. M. Z. Newby, M. K. Chaudhury, and H. R. Brown: *Macroscopic evidence of the effect of interfacial slippage on adhesion*. Science, **269**, 1407 (1995) 9.1, 9.1

[85] R. M. Oliveira and J. A. Miranda: *Stretching of a confined ferrofluid: Influence of viscous stresses and magnetic field*. Physical Review E, **73**, 036309 (2006) 1, 11

[86] P. Oswald: *Rhéophysique Ou comment coule la matière* (Belin, 2005), first edition 2.1, 2.4, 2.4

[87] L. Paterson: *Radial fingering in a Hele Shaw cell*. Journal of Fluid Mechanics, **113**, 513 (1981) 1, 4.2.1, 4.2.1, 4.5, 4.2.1, 7.3.1, 10.1, 11

[88] G. Petitet and M. Barquins: *Matériaux caoutchouteux* (Presses polytechniques et universitaires romandes, 2008), first edition 3.3

[89] J. M. Piau, G. Ravilly, and C. Verdier: *Peeling of polydimethylsiloxane adhesives at low velocities: Cohesive failure*. Journal of Polymer Science Part B-Polymer Physics, **43**, 145 (2005) 1, 11

[90] J. Plateau: *Statique expérimentale et théorique des liquides soumis aux seules forces atomiques* (1873) 8.3, 8.3, 10.2.2

[91] A. V. Pocius: *Adhesion and Adhesives Technology* (Hanser, 2002), second edition 3

[92] S. Poivet, F. Nallet, C. Gay, and P. Fabre: *Cavitation-induced force transition in confined viscous liquids under traction*. Europhysics Letters, **62**, 244 (2003) 6.1, 10.6, 10.8, 11, 11

[93] S. Poivet, F. Nallet, C. Gay, J. Teisseire, and P. Fabre: *Force response of a viscous liquid in a probe-tack geometry: Fingering versus cavitation.* European Physical Journal E, **15**, 97 (2004) 1, 1, 8.4.1, 11

[94] G. Ramond, M. Pastor, D. Maugis, and M. Barquins: *Mesure du module complexe par poinçonnement.* Cahiers du Groupe Français de Rhéologie., **6**, 67 (1985) 3.3, 7.4, 8.4.3, 11, 11, 11, 11

[95] L. Rayleigh: *On the instability of jets.* Proceedings of the London Mathematical Society, **10**, 4 (1879) 8.3, 8.3, 10.2.2

[96] A. Roos, C. Creton, M. B. Novikov, and M. M. Feldstein: *Viscoelasticity and tack of poly(vinyl pyrrolidone)-poly (ethylene glycol) blends.* Journal of Polymer Science Part B-Polymer Physics, **40**, 2395 (2002) 1, 11

[97] M. Rubinstein and R. Colby: *Polymer Physics* (Oxford University Press, 2003), first edition 2.2, 2.2

[98] P. G. Saffman and G. Taylor: *The penetration of a fluid into a porous medium or Hele-Shaw cell containing a more viscous liquid.* Proceedings of the Royal Society of London Series a-Mathematical and Physical Sciences, **245**, 312 (1958) 1, 4.2, 4.2, 4.2, 7.3.1, 7.3.1, 11, 11, 11, 11, 11

[99] D. Satas (editor): *Handbook of pressure sensitive adhesive technology* (Van Nostrand Reinhold, New York, 1989), 2nd edition 3

[100] R. Sattler, C. Wagner, and J. Eggers: *Blistering pattern and formation of nanofibers in capillary thinning of polymer solutions.* Physical Review Letters, **100**, 164502 (2008) 1, 1.1(a)

[101] F. Saulnier, T. Ondarcuhu, A. Aradian, and E. Raphael: *Adhesion between a viscoelastic material and a solid surface.* Macromolecules, **37**, 1067 (2004) 1, 3.3, 8.4.3

[102] R. Schach and C. Creton: *Adhesion at interfaces between highly entangled polymer melts.* Journal of Rheology, **52**, 749 (2008) 1, 11

[103] E. Sharon, M. G. Moore, W. D. McCormick, and H. L. Swinney: *Coarsening of fractal viscous fingering patterns.* Physical Review Letters, **91**, 205504 (2003) 10.1

[104] M. J. Shelley, F. R. Tian, and K. Wlodarski: *Hele-Shaw flow and pattern formation in a time-dependent gap.* Nonlinearity, **10**, 1471 (1997) 1, 4.2.2, 10.1, 10.1, 10.1, 10.1, 10.3, 10.5, 10.5, 11, 11, 11, 11

[105] V. Shenoy and A. Sharma: *Pattern formation in a thin solid film with interactions.* Physical Review Letters, **86**, 119 (2001). Times Cited: 50 1, 4.3

[106] B. I. Shraiman: *Velocity selection and the Saffman-Taylor problem.* Physical Review Letters, **56**, 2028 (1986) 4.2

[107] K. R. Shull: *Contact mechanics and the adhesion of soft solids.* Materials Science & Engineering R-Reports, **36**, 1 (2002) 9.1

[108] K. R. Shull and C. Creton: *Deformation behavior of thin, compliant layers under tensile loading conditions.* Journal of Polymer Science Part B-Polymer Physics, **42**, 4023 (2004) 1, 3, 7.1

[109] K. R. Shull, C. M. Flanigan, and A. J. Crosby: *Fingering instabilities of confined elastic layers in tension.* Physical Review Letters, **84**, 3057 (2000) 1, 4.2.4, 7.3.1, 11

[110] S. Sinha, T. Dutta, and S. Tarafdar: *Adhesion and fingering in the lifting Hele-Shaw cell: Role of the substrate.* European Physical Journal E, **25**, 267 (2008) 1

[111] P. Tabeling and A. Libchaber: *Film draining and the Saffman-Taylor problem.* Physical Review A, **33**, 794 (1986) 10.8

[112] P. Tabeling, G. Zocchi, and A. Libchaber: *An experimental study of the Saffman-Taylor instability.* Journal of Fluid Mechanics, **177**, 67 (1987) 4.2, 4.2, 4.4, 10.8

[113] M. Tirumkudulu, W. B. Russel, and T. J. Huang: *On the measurement of "tack" for adhesives.* Physics of Fluids, **15**, 1588 (2003) 1, 10.6, 10.8, 11, 11

[114] M. F. Tse and L. Jacob: *Pressure sensitive adhesives based on Vector (R) [SIS] polymers I. Rheological model and adhesive design pathways.* Journal of Adhesion, **56**, 79 (1996) 1

[115] Y. Urahama: *Effect of peel load on stringiness phenomena and peel speed of pressure-sensitive adhesive tape.* Journal of Adhesion, **31**, 47 (1989) 3.2, 3.1, 4.3

[116] H. Vandeparre and P. Damman: *Wrinkling of stimuloresponsive surfaces: Mechanical instability coupled to diffusion.* Physical Review Letters, **101**, 124301 (2008) 8.5

[117] C. Wagner, H. W. Müller, and K. Knorr: *Faraday waves on a viscoelastic liquid.* Physical Review Letters, **83**, 308 (1999) 1, 1.1(b)

[118] R. E. Webber, K. R. Shull, A. Roos, and C. Creton: *Effects of geometric confinement on the adhesive debonding of soft elastic solids.* Physical Review E, **68**, 021805 (2003) 1, 3.3, 8.3, 8.4.3

[119] M. L. WILLIAMS, R. F. LANDEL, and J. D. FERRY: *The temperature dependence of relaxation mechanisms in amorphous polymers and other glass-forming liquids.* Journal of the American Chemical Society, **77**, 3701 (1955) 2, 3.3

[120] S. D. R. WILSON: *The Taylor-Saffman problem for a non-Newtonian liquid.* Journal of Fluid Mechanics, **220**, 413 (1990) 10.7

[121] H. H. WINTER and F. CHAMBON: *Analysis of linear viscoelasticity of a cross-linking polymer at the gel point.* Journal of Rheology, **30**, 367 (1986) 5.2.2

[122] T. YAMAGUCHI, K. KOIKE, and M. DOI: *In situ observation of stereoscopic shapes of cavities in soft adhesives.* EPL, **77**, 64002 (2007) 1, 9.3, 9.1, 11, 11

[123] T. YAMAGUCHI, H. MORITA, and M. DOI: *Modeling on debonding dynamics of pressure-sensitive adhesives.* European Physical Journal E, **20**, 7 (2006) 8.4.1, 11, 11

[124] G. M. W. YOUNAN XIA: *Soft lithography.* Angewandte Chemie International Edition, **37**, 550 (1998) 5.1, 10.5.1

[125] H. ZENG, Y. TIAN, B. ZHAO, M. TIRRELL, and J. ISRAELACHVILI: *Transient surface patterns and instabilities at adhesive junctions of viscoelastic films.* Macromolecules, **40**, 8409 (2007) 1, 11

[126] R. ZENIT: private communication (2007) 10.7

[127] S. Z. ZHANG, E. LOUIS, O. PLA, and F. GUINEA: *Linear stability analysis of the Hele-Shaw cell with lifting plates.* European Physical Journal B, **1**, 123 (1998) 8.4.3

[128] B. X. ZHAO, H. B. ZENG, Y. TIAN, and J. ISRAELACHVILI: *Adhesion and detachment mechanisms of sugar surfaces from the solid (glassy) to liquid (viscous) states.* Proceedings of the National Academy of Sciences of the United States of America, **103**, 19624 (2006) 1, 11

[129] A. ZOSEL: *Adhesion and tack of polymers - influence of mechanical properties and surface tensions.* Colloid and Polymer Science, **263**, 541 (1985) 6.1, 11

[130] A. ZOSEL: *Effect of cross-linking on tack and peel strength of polymers.* Journal of Adhesion, **34**, 201 (1991) 1, 8.3, 11

Hiermit versichere ich an Eides statt, dass ich die vorliegende Arbeit selbstständig und ohne Benutzung anderer als der angegebenen Hilfsmittel angefertigt habe. Die aus anderen Quellen oder indirekt übernommenen Daten und Konzepte sind unter Angabe der Quelle gekennzeichnet. Die Arbeit wurde bisher weder im In- noch im Ausland in gleicher oder ähnlicher Form in einem Verfahren zur Erlangung eines akademischen Grades vorgelegt.